Correcting for Parity-Violating and Parity-Conserving Asymmetries from Pions in the MOLLER Experiment

by

Fatemeh (Elham) Gorgannejad

A Thesis submitted to the Faculty of Graduate Studies of
The University of Manitoba
in partial fulfillment of the requirements of the degree of

DOCTOR OF PHILOSOPHY

Department of Physics and Astronomy
University of Manitoba
Winnipeg

Abstract

The Measurement of a Lepton-Lepton Electroweak Reaction (MOLLER) experiment, approved and scheduled to be conducted at the Thomas Jefferson National Accelerator Facility (JLab), aims to provide a high-precision measurement of the parity-violating asymmetry in the scattering of longitudinally polarized electrons off an unpolarized liquid hydrogen target. Utilizing an 11 GeV upgraded beam, the MOLLER experiment will measure the asymmetry with a precision of 2.4% at an average Q^2 of 0.0056 GeV^2. This experiment is expected to probe new physics beyond the Standard Model of particle physics and provide significant new details on the electroweak world, particularly the weak mixing angle.

To achieve the expected precision, corrections must be applied to the Møller signal for background processes characterized by background asymmetries and fractional dilution factors. Significant contributions to these experimental signal corrections come from pion asymmetries and pion dilution factors, which will be measured using a dedicated pion detector system. The design, development, and prototyping of the pion detector system for the MOLLER experiment are the primary objectives of this thesis. To confirm the effectiveness of the detector system, the outcomes from simulations, cosmic testing carried out at the University of Manitoba, and beam testing carried out at MAMI B microtron in Mainz, Germany, will be compared.

Furthermore, this thesis introduces Bayesian analysis as a novel approach for applying non-experimental signal corrections to experimental values. Serving as a complement to the commonly used frequentist methods, Bayesian analysis is explored for its potential to refine experimental results. By employing Bayesian analysis, the

accuracy of corrections applied post-measurement is aimed to be enhanced, thereby improving the overall precision of the MOLLER experiment. The benefits and implications of using Bayesian analysis for theoretical corrections in Parity-Violating Electron Scattering (PVES) experiments are thoroughly examined.

The results provided in this work emphasize the importance of fully understanding and controlling the parity-violating and parity-conserving asymmetries for pions to achieve the required precision in the MOLLER experiment. The effectiveness of the MOLLER experiment and its potential to improve our understanding of the electroweak interaction and the Standard Model are significantly affected by the results of this research, which includes the development of the pion detector system and the study of Bayesian analysis for non-experimental signal corrections.

Acknowledgements

Firstly, I express my deepest gratitude to my supervisor, Dr. Wouter Deconinck, for his unwavering support, patience, and guidance throughout my Ph.D. journey. His expertise, dedication, and encouragement have been invaluable to my academic and personal growth. Also, I appreciate the constructive comments and feedback from my committee members, Dr. Gerald Gwinner, Dr. Michael Gericke, and Dr. Jim Napolitano, during the annual progress report meetings and on my thesis. Their insights have significantly contributed to the quality of my work. Special thanks go to Dr. David S Armstrong, who provided invaluable advice and assistance throughout my research. Although not officially my co-supervisor, his mentorship and collaboration have profoundly impacted my work. Dr. Michael Gericke, Dr. Dustin McNulty, and Dr. Krishna Kumar were instrumental in helping during the test beam data-taking. At the same time, Dr. James Fast and Dr. Dustin McNulty contributed valuable input during the weekly meetings. Their expertise and collaboration have been essential to the success of this project. I am grateful for the support and guidance from the department's administrative staff, Susan Beshta, Milijana Prstojevic, Aymsley Bishop Mahon, Robyn Beaulieu, and Maiko Langelaar, who helped me navigate various aspects of the department. I acknowledge the support of the Natural Sciences and Engineering Research Council of Canada (NSERC), Canada Foundations for Innovation (CFI), and the Canadian Institute of Nuclear Physics (CINP). Finally, I wish to extend my thanks to my family for their love, support, and encouragement during the difficult days.

Contents

List of Figures

List of Tables

Chapter 1

Introduction

Parity-Violating Electron Scattering (PVES) experiments have provided a broad knowledge of electroweak interactions, nucleon structure, and weak force properties. This chapter discusses the significance of PVES experiments, with an emphasis on the MOLLER experiment as a promising initiative. To facilitate navigation through the dissertation, a document roadmap is provided at the end of this chapter.

1.1 Overview of Parity Violation in Electron Scattering

The Standard Model of particle physics is the main model that describes fundamental particles, their interactions and their symmetries. The most relevant force and symmetry to this research are the weak force and parity. Additionally, one class of low-energy measurements of particular interest to us involves scattering longitudinally polarized electrons from unpolarized targets. When a longitudinally polarized electron beam is scattered off an unpolarized target, it can interact electromagnetically by exchanging a photon and weakly by exchanging a Z^0 boson. Electromagnetic interactions conserve parity, while electroweak interactions violate it. In fact, among the four fundamental interactions, the only one that violates parity is the weak interaction [1]. Parity violation is observed due to the interference between electromagnetic and weak

components of the electroweak interactions [2]. It can be measured by comparing the cross sections for left- and right-handed electrons scattered from unpolarized targets. This asymmetry can be written as:

$$A_{PV} = \frac{\sigma_R - \sigma_L}{\sigma_R + \sigma_L}, \tag{1.1}$$

where σ_R and σ_L are the cross sections for incident right-handed and left-handed electrons, respectively. Through this measurement, the parameters of the Standard Model, especially the couplings of the Z boson, can be precisely determined [3]. Additionally, it allows for exploring new parity-violating interactions beyond the Standard Model [4] and enables the accurate study of nuclear properties [5]. A number of novel experimental techniques have been developed to measure small asymmetries; the experiments utilizing these techniques will be reviewed.

In 1978, Prescott et al. published the first observation of parity violation in electron scattering through the pioneering E122 experiment conducted at the Stanford Linear Accelerator Centre (SLAC) [6]. This marked the establishment of the field of PVES. This experiment measured parity violation in the inelastic scattering of longitudinally polarized electrons from deuterium and hydrogen targets. The asymmetry measured was a small fraction of the cross-section, 10^{-4}. Experimental improvements have been necessary to measure asymmetry with this precision, some of which are ongoing. Developing a polarized electron source based on photoemission from GaAs was the most important. The beam's helicity could be reversed without significantly impacting the source's intensity or the beam's other characteristics, such as position, angle, or energy. Also, a set of precision beam monitors needed to be developed to ensure the beam was precisely reversed. Following the Prescott experiment, two PVES experiments [7],[8], utilizing nuclei as targets, were conducted. These experiments aimed to measure even smaller asymmetries and then assess the Standard Model predictions. These experiments will be referred to as Generation I PVES experiments.

In 1989, the question of the role of strange quarks in the nucleon was raised by the appearance of the spin crisis [9]. Data on the proton's spin-structure functions showed that the proton's spin was not simply the sum of the spins of the valence

quarks [10]. In addition, PVES was described as a useful method for determining the strangeness content of nucleon elastic form factors. As a result, the Generation II PVES experiments, conducted across four programs in three labs, came next. SAMPLE in the MIT Bates laboratory [11], HAPPEX at JLab [12], G0 at JLab [13], and A4 program at Mainz [14] were the experiments.

The success of the strange form factor program laid the groundwork for a series of more challenging experiments, advancing the precision of Standard Model testing. Examples include SLAC E158 [15], which measured the weak mixing angle in Møller scattering, Qweak at JLab [16], which determined the weak charge of the proton, and the PREx experiment [17], which used PVES on ^{208}Pb to calculate the charge radius of the neutron distribution. These experiments along with PREx-II [18] and CREx measurements [19] are Generation III PVES experiments.

The P2 experiment at Mainz [20], the MOLLER [21], and the SoLID experiments at JLab [22] are among a number of more challenging Generation IV PVES experiments that have been proposed. These experiments will push the boundaries of how precisely and how small an asymmetry can be measured. Figure 1.1 provides a summary of the precision of the various PVES experiments.

Overall, the advancements in PVES experiments have improved our knowledge of parity violation and the fundamentals of particle dynamics. Among PVES experiments, the MOLLER experiment, which holds significant potential for probing the fundamental physics of electron scattering, will be the focus of this research. To better understand its significance, the physics motivation behind this experiment is explored in the next section.

1.2 Physics Motivation

The motivation of the MOLLER experiment [21] is searching for new dynamics beyond the Standard Model of electroweak interactions from low energy levels (100 MeV) to high energy levels (multi-TeV). MOLLER will measure parity-violating asymmetry in the scattering of longitudinally polarized electrons from unpolarized target electrons to an accuracy of 2.4% using an 11 GeV beam in Hall A at Jlab. In

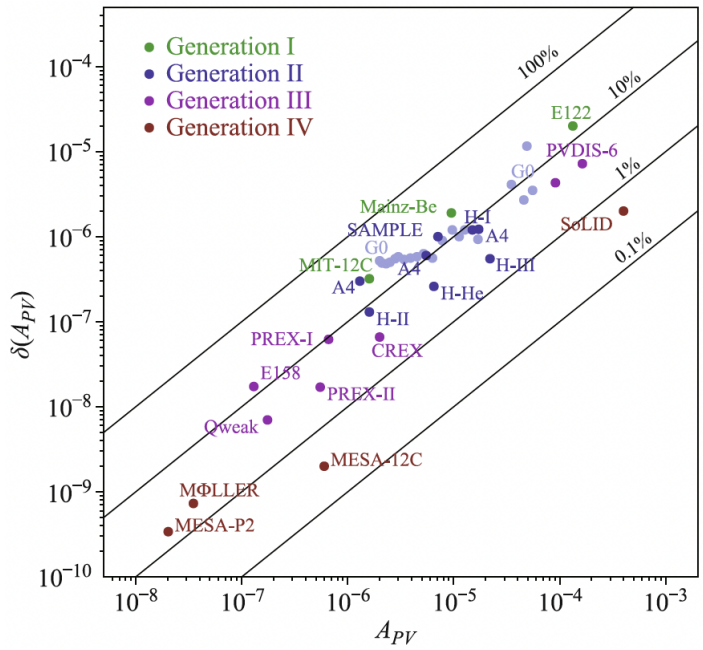

Figure 1.1: Overview of past and future PVES experiments at SLAC, Bates, Mainz, and Jlab [20]. The horizontal axis is the measured value of the asymmetry (A_{PV}). The vertical axis is the total experimental uncertainty ($\delta(A_{PV})$). The diagonal lines show the fractional uncertainty in the measurements (0.1%-100%).

Møller scattering, the name was given to electron-electron scattering; as a result of the interference between the photon and Z^0 boson exchange, parity-violating asymmetry is directly proportional to the weak charge of the electron (Q_W^e) by the following formula

$$A_{PV} = mE\frac{G_F}{\sqrt{2}\pi\alpha}\frac{4sin^2(\theta)}{(3+cos^2(\theta))^2}Q_W^e = mE\frac{G_F}{\sqrt{2}\pi\alpha}\frac{2y(1-y)}{1+y^4+(1-y)^4}Q_W^e, \tag{1.2}$$

where α is the fine structure constant, G_F is the Fermi constant, m is the mass of the electron, θ is the scattering angle in the center of mass frame, $y = 1 - \frac{E'}{E}$ is the fractional energy loss of the incident electron with E and E' the energy before and after scattering. Finally, Q_W^e is related to the electroweak mixing angle (θ_W),

$$Q_W^e = 1 - 4sin^2(\theta_W). \tag{1.3}$$

The relation between the weak charge of the electron and the electroweak mixing

angle is verified by SLAC experiment E158 [15] as the first experiment using Møller scattering to measure parity-violating asymmetry. MOLLER proposes to measure this quantity using Møller scattering with more than a factor of five improvements in fractional precision. The prediction for measured parity-violating asymmetry in the MOLLER experiment is 33 ppb with a total uncertainty of 0.8 ppb to achieve 2.4% accuracy in the Q_W^e measurement. Applying higher-order loop radiative corrections [23] causes a dependency of Q_W^e to the energy scale of the measurement experiment (μ). The weak mixing angle in terms of energy scale is compared for some experiments in Figure 1.2. The plot shows the anticipated accuracy of the MOLLER experiment

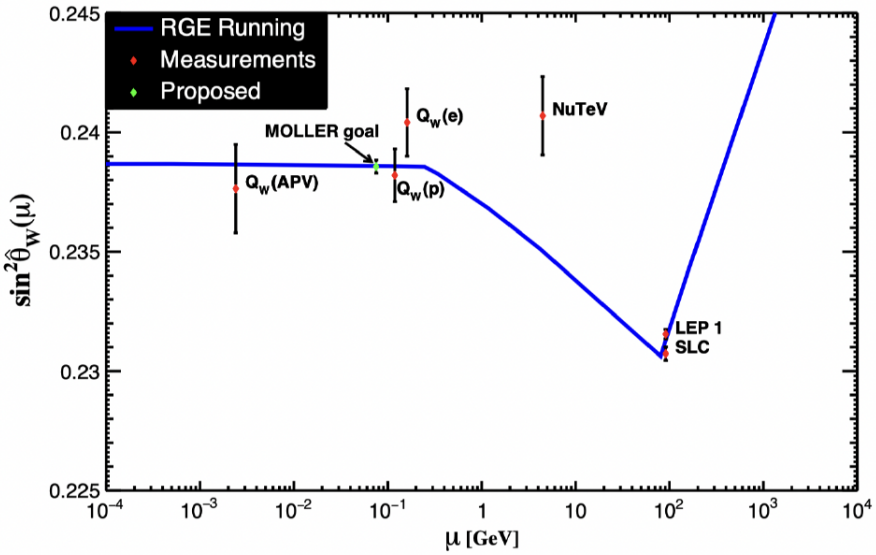

Figure 1.2: Precise measurements of the weak mixing angle versus the energy scale are shown as red dots with error bars; the blue line shows the theoretical prediction of the weak mixing angle in the Standard Model as a function of energy scale (μ) and the black error bars show the uncertainty of the measurements. The existing measurements are from atomic parity violation (Q_W^{APV}) [24], Qweak experiment (Q_W^p) [16], SLAC E-158 (Q_W^e) [15], NuTeV experiment (NuTev) [25], and Z^0 pole asymmetries ($LEP + SLC$) [26]. The proposed MOLLER measurement [21] is shown, and the central value of the proposed error bar is the nominal Standard Model prediction.

within the broader context of past and proposed experiments, highlighting its potential to advance our understanding of electroweak interactions.

Building on this foundation, there are two main aspects to the physics motivation of

the MOLLER experiment:

1. **Ranging from low energy levels (100 MeV) to high energy levels (multi-TeV):**
   At low energies, effective four-fermion interactions, represented by the ratio Λ/g, are used to characterize new neutral current interactions. The interaction strength is denoted by g, and Λ denotes the scale of the recently introduced dynamics. The measurement of the parity-violating asymmetry in the MOLLER experiment with 2.4% uncertainty is sensitive to interaction amplitudes of 1.5×10^{-3} times the Fermi constant, G_F. As a result, It is possible to measure the resulting sensitivity to amplitudes for new four-electron contact interactions as follows

$$\frac{\Lambda}{\sqrt{|g_{RR}^2 - g_{LL}^2|}} = \frac{1}{\sqrt{\sqrt{2}G_F|\Delta Q_W^e|}} \simeq \frac{246.22\,GeV}{\sqrt{0.024 Q_W^e}} = 7.5\,TeV. \tag{1.4}$$

   A coupling strength of approximately one allows for probing the TeV scale. On the other hand, when Λ is around 100 MeV, there is an extraordinary level of sensitivity approaching 10^{-3} times the fine-structure constant, α_{QED}. The MOLLER experiment is an excellent complement to existing precise low-energy experiments and the energy frontier projects, including those conducted at the Large Hadron Collider (LHC). If the LHC continues to agree with the predictions of the Standard Model of particle physics while operating at its maximum energy of 14 TeV with high luminosity, then the MOLLER experiment will play an important part in a comprehensive plan to discover evidence of various physics phenomena that might escape detection at the LHC.

2. **Precision Goal:** In experiments with very high rates, high-precision measurements of very small polarization-dependent scattering asymmetries rely on the flux integration technique, depending on the detector choice. To isolate the elastic scattered events onto a detector, which yields a response that is strictly proportionate to the amount of electrons observed, this technique uses a magnetic spectrometer. The spectrometer must spatially separate elastic scattered

events since it is impossible to distinguish elastic scattering from other types of scattering using characteristics of the individual recorded electrons (e.g., time, amplitude, energy, tracking information). With a fixed beam polarization, the response of the detectors is integrated over time. The objective is to compare integrated flux measurements with opposing beam polarization to make a measurement. The scattering asymmetry is measured for a pair of windows with right- (left-) handed polarization, with the integrated signal corresponding to the detected flux rate, F, in a particular time window,

$$A_i^{raw} = (\frac{F_R - F_L}{F_R + F_L})_i \simeq (\frac{\Delta F}{2F})_i. \tag{1.5}$$

Rapid helicity reversal of 1.92 kHz is used to prevent experimental condition changes that may otherwise make it more challenging to understand the integrated signal by altering its proportionality to the measured flux rate. The electron beam trajectory, energy, and intensity are three factors that might change quickly during these measurements; these conditions must be averaged over the same integration periods and utilized to adjust the detected asymmetry for the changing conditions

$$A_i = (\frac{\Delta F}{2F} - \frac{\Delta I}{2I})_i - \sum_j (\alpha_j (\Delta X_j)_i), \tag{1.6}$$

where I is the time-averaged beam intensity throughout a helicity window, X_j are corresponding average beam trajectory parameters derived from judiciously placed beam position monitors, and $\alpha_j \equiv \frac{\partial F}{\partial X_i}$ are coefficients that depend on the scattering kinematics as well as the details of the spectrometer and detector geometry. The uncertainty in this rapid measurement, A_i, will approximately reflect the counting statistics of the measured flux in a well-designed experiment. The experiment's total statistical uncertainty is determined by averaging many of these measurements, assuming independence. The average measurement $\bar{A}$

and its standard deviation $\sigma_{\bar{A}}$ are given by:

$$\bar{A} = \frac{1}{N}\sum_{i=1}^{N} A_i \quad ; \quad \sigma_{\bar{A}} = \frac{\sigma_{A_i}}{\sqrt{N}}. \tag{1.7}$$

In summary, the MOLLER experiment is poised to push the boundaries in the field of PVES, primarily due to its unprecedented precision and advanced measurement techniques. Unlike previous experiments, MOLLER targets a significant advance in accuracy and sensitivity, proposing to measure the parity-violating asymmetry with over five-fold improvement in fractional precision compared to past efforts. This enhancement originates from innovative approaches in beam monitoring, data collection, and reduction of systematic uncertainties. Such advancements in methodology are expected to provide clearer insights into electroweak interactions and offer a more rigorous examination of the Standard Model's predictions. By setting new standards for precision, MOLLER contributes to the immediate field of PVES and extends its impact to the broader scope of experimental physics, potentially uncovering phenomena that have so far evaded observation.

1.3 Document Roadmap

Chapter 1 sets the foundation for the thesis, introducing the primary focus and establishing the overall context. Section 1.1 has presented an overview of PVES experiments, offering essential background on this research area. In Section 1.2, the physics motivation behind the research is explored. The chapter concludes with Section 1.3, which provides a structured roadmap of the thesis, guiding readers through the subsequent chapters and summarizing their content.

Chapter 2 outlines the theoretical framework critical to the MOLLER experiment. Section 2.1 introduces the Standard Model of particle physics, highlighting the fundamental particles and forces relevant to the study, detailing the building blocks of the universe, the forces between them, and the discrete symmetries. Section 2.2 discusses helicity and the violation of parity within the electroweak theory, concepts

central to understanding parity-violating asymmetries. The focus shifts in Section 2.3 to Møller scattering, which is central to measuring the electron's weak charge. Section 2.4 examines electron-proton scattering processes and their importance in pion productions. Section 2.5 considers the impact of electron polarization on asymmetry measurements. Section 2.6 investigates how charged particles interact with materials, a key aspect for detection in the MOLLER experiment. Section 2.7 introduces cosmic and beam testing as methods for validating the results of the pion detector in the MOLLER experiment. The chapter concludes with Section 2.8, presenting *remoll*, the simulation that employs Geant4 and ROOT for the experimental modelling. This chapter provides a clear path from the core theories of particle physics to the expected outcomes of the experiment, setting the stage for the detailed discussions to follow in the thesis.

Chapter 3 transitions into a detailed examination of the MOLLER experiment, highlighting the facilities and equipment involved. Section 3.1 begins with the polarized beam, monitoring, and control, offering an in-depth look at the polarized electron source and elaborating on the specific MOLLER beam requirements. A comprehensive overview of the target system is covered in Section 3.2. Section 3.3 focuses on the spectrometer system, discussing the open spectrometer concept and detailing the distribution on the detector plane. The mechanisms of the detector system are described in Section 3.4, starting with the main integrating detectors, moving to the tracking detectors, and concluding with an in-depth analysis of the auxiliary detectors. Section 3.5 summarizes the components of data collection, experiment initiation, and data interpretation, detailing data collection, trigger, and analysis. Overall, the chapter provides a thorough understanding of the MOLLER experiment's setup and processes, laying the foundation for the methodology, procedures, and results presented in subsequent chapters of this thesis.

Chapter 4 presents the comprehensive development of the pion detector system, elucidating its principles and practical applications. Section 4.1 commences with exploring the system's physics and mechanisms, beginning with the criteria for selecting the active medium, followed by the requirements for choosing PMTs. The focus then shifts to the optimization process of the system in Section 4.2, detailing the strategies

and algorithms employed. Section 4.3 presents an examination of the mechanical design of the system, discussing its structural and functional aspects. The verification of simulation results is addressed in Section 4.4 through cosmic testing, with subsections dedicated to the setup for cosmic testing, and the simulation of these tests. This is followed by Section 4.5, which outlines the beam testing verification, describes the beam testing setup, and concludes with a comparative analysis of results from simulations, cosmic, and beam testings. Overall, the chapter provides an intricate and detailed account of the pion detector system's development, from its theoretical underpinnings to its practical implementation, setting the stage for further discussion on its applications and significance in the field.

Chapter 5 explores Bayesian statistical analysis and its application to PVES experiments like Qweak and MOLLER. It examines integrating prior knowledge with observed data to enhance measurement precision, as explained in the introductory section 5.1. The theoretical basis of Bayesian analysis, including the derivation of Bayes' theorem and its components, is addressed in Section 5.2. The practical application of Bayesian methods to the Qweak experiment and comparing this approach with Monte Carlo minimization is discussed in Section 5.3. Lastly, Section 5.4 focuses on adapting this method to the MOLLER experiment, highlighting the generation of mock data and the prediction of experimental outcomes. This chapter reinforces the significance of Bayesian analysis in interpreting experimental data and showcases its potential to yield precise insights into the fundamental interactions investigated by PVES experiments. Chapter 6 concludes the thesis by summarizing the key findings from the MOLLER experiment and outlining future research directions. Section **??** provides a detailed summary of the experiment's objectives, methodologies, and significant results, emphasizing the precision achieved in measuring parity-violating asymmetry and the techniques used for signal correction and background differentiation. The chapter continues with Section 6.2, which discusses potential advancements in the pion detector system and Bayesian analysis methodologies. This section proposes enhancements to experimental setups and statistical models, aiming to refine data analysis and improve the precision of future measurements. The chapter serves to bridge the comprehensive research presented in the previous chapters with forth-

coming initiatives that could further advance the field of particle physics.

Chapter 2

Theory and Methodology

This chapter discusses the theoretical aspects underlying the MOLLER experiment. Starting with the Standard Model of particle physics, the chapter examines the fundamental particles and interactions that are key to the experiment. This is followed by exploring parity symmetry violation, a central aspect of electron scattering driven by weak interactions. The chapter then focuses on the process of pion-production through inelastic electron-proton scattering, emphasizing the importance of detecting these signals for the experiment's objectives.

Furthermore, the chapter addresses the interaction of charged particles with matter. This section is critical for understanding how particles such as pions, muons, and electrons interact with the various materials used in the experiment, influencing their detection and analysis.

Finally, the chapter concludes with an overview of the MOLLER experiment simulation, known as *remoll*. This simulation, utilizing Geant4 and ROOT, is instrumental in modeling the experiment and understanding the expected outcomes. This comprehensive chapter lays the theoretical and practical foundation for the MOLLER experiment, guiding the reader through the complex physics and simulations that form the foundation of this research.

2.1 The Standard Model of Particle Physics

Through the theories and research of thousands of physicists since the 1950s, it has been discovered that the universe is comprised of a few basic building blocks known as fundamental particles governed by four fundamental forces. The Standard Model of particle physics, as shown in Figure 2.1, incorporates our current understanding of the interactions between these particles and three of the forces. It was created in the early 1970s and has predicted a wide range of phenomena while successfully explaining nearly all experimental data. The following subsections explain the es-

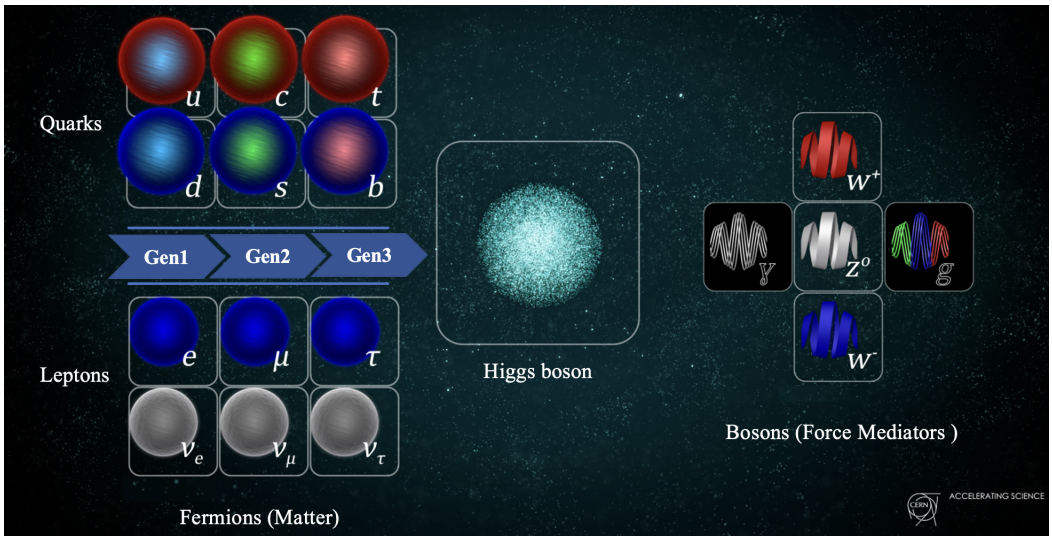

Figure 2.1: The Standard Model of particle physics [27].

sential components of the Standard Model of particle physics. Subsection 2.1.1 will introduce the elementary particles, fermions, and bosons, which are the universe's building blocks. Following this, subsections 2.1.2 and 2.1.3 will discuss the forces that bind these particles and explore the discrete symmetries that form the basis for the laws governing their interactions. This examination will prepare us to understand complex phenomena such as helicity and parity-violating asymmetry, which will be further expanded upon in subsequent sections.

2.1.1 Particles of Matter

The two categories of elementary particles in the Standard Model are fermions and bosons. Particles with integer spin are known as bosons. They act as force carriers and mediate particle interactions. Fermions, with a spin of $\frac{1}{2}$ integer, are divided into six quarks and six leptons. Quarks compose protons, neutrons, and other exotic particles, while leptons include electron-like particles and neutrinos. Quarks and leptons are paired or arranged in generations of six to correlate.

The first generation comprises the lightest and most stable particles, whereas the second and third generations comprise heavier and less stable particles. While the first generation of particles forms all stable matter in the universe, any heavier particles rapidly decay into more stable ones. The three generations of the six quarks are composed of the up quark (u) and down quark (d), as the first generation, the charm quark (c) and strange quark (s), as the second generation, and the top quark (t) and bottom (b) (or beauty) quark, as the third generation. Additionally, there are three different colors of quarks, and they only combine in ways that produce colorless objects. The three generations of the six leptons are composed of the electron (e) and electron neutrino (ν_e), the muon (μ) and muon neutrino (ν_μ), and the tau (τ) and tau neutrino (ν_τ) that are similarly ordered. While the neutrinos are electrically neutral and have very little mass, the electron, muon, and tau, all have an electric charge and a sizable mass.

2.1.2 Carrier Particles and Forces

Four fundamental forces govern the universe: the strong force, the weak force, the electromagnetic force, and the gravitational force. They each work within different constraints and have unique strengths. The gravitational and electromagnetic forces have an infinite range; the former is the weakest force, and the latter is far stronger. The weak and strong forces dominate only at the level of subatomic particles and are only effective across very small distances. Over larger distances, the weak force is significantly weaker than the electromagnetic and strong forces, it is still much stronger than the gravitational force. As its name suggests, the strongest of the four

fundamental interactions is the strong force. All four fundamental forces are mediated by the exchange of force-carrier particles. Each force is associated with a specific boson: the gluon (g) for the strong force, the photon (γ) for the electromagnetic force, and the W and Z bosons for the weak force. Although it has not yet been identified, the graviton is hypothesized to be the carrier of the gravitational force.

The electromagnetic, strong, and weak forces, along with all of their carrier particles, are included in the Standard Model of particle physics, explaining how these forces interact with every matter particle. The most common force in our daily lives, gravity, is not included in the Standard Model since it has been shown to be difficult to incorporate gravity into this framework. The primary challenge in unifying the general theory of relativity and quantum theory lies in the theoretical inclusion of gravity, as no complete framework currently exists to reconcile gravity with quantum mechanics.

The Higgs boson is a major element of the Standard Model associated with the Higgs field. This field gives mass to other fundamental particles such as electrons and quarks. In 2012, the existence of the Higgs boson, predicted by the theory, was confirmed by experiments. The European Organization for Nuclear Research (CERN) built a high-energy collider called the Large Hadron Collider (LHC) to discover the Higgs particle. Inside two detectors (ATLAS [28] and CMS [29]), two very energetic proton beams collide. Each time a proton from one beam collides with another proton from the other beam, additional particles are created, including the Higgs boson. Some of the produced particles can be observed and measured in the detectors. The Higgs boson decays into other Standard Model particles very quickly and cannot be directly recognized, but detectors can detect the byproducts of the decay. The Higgs boson could decay through a variety of mechanisms. Based on the discovered collision byproducts, the decay process can be reconstructed.

Even though the Standard Model provides an accurate description of particle interactions, it is still insufficient. It might only be a small component of a larger picture that also incorporates novel physics buried deep inside the universe. We will be able to fill in more of these blanks with the help of new findings from experiments like the one described here and other future PVES experiments.

2.1.3 Discrete Symmetries

Symmetry in physics implies that a transformation of the coordinate system does not affect the Lagrangian representing the system being studied, and an observed or intrinsic feature of the system remains invariant under that transformation. The Standard Model of particle physics describes the particles and their interactions based on underlying symmetries. Charge, parity, and time reversal are discrete symmetries in particle physics that the Standard Model may or may not satisfy.

Parity is the most relevant symmetry to this research, representing a spatial inversion through the origin. When parity is applied twice, the initial state is restored. In contrast to electromagnetic and strong interactions, which do not violate parity, weak interactions do. The initial verification of parity violation was found in the investigation of β decay of polarized ^{60}Co [30], where it was shown that the electron was preferentially emitted in the direction opposing the nucleus' spin. The distribution of the electrons that decay can be characterized as:

$$\frac{dN}{d\Omega} = 1 - \frac{\vec{\sigma} \cdot \vec{p}}{E}. \tag{2.1}$$

The $\vec{\sigma} \cdot \vec{p}$ term is parity-violating, as will be detailed in the next section. When parity is violated, the weak interaction exhibits a preferred spatial direction. The next section provides a more detailed discussion of helicity, electroweak theory, and the formalism of parity-violating asymmetry, both conceptually and mathematically.

2.2 Theoretical Formalism of Helicity and Parity-Violating Asymmetry

In particle physics, an understanding of the fundamental properties and interactions of elementary particles necessitates an exploration of their intrinsic characteristics and the symmetries that influence their behavior. This section introduces the theoretical formalisms of helicity and electroweak theory to establish the foundation for explaining parity-violating asymmetry in subsequent sections.

2.2.1 Helicity

A particle's helicity is determined by the angle (cosine) between its spin and momentum directions. The definition of the helicity operator is:

$$\vec{\Sigma} \cdot \hat{p} = \begin{pmatrix} \vec{\sigma} \cdot \hat{p} & 0 \\ 0 & \vec{\sigma} \cdot \hat{p} \end{pmatrix}, \tag{2.2}$$

where $\hat{p} = \vec{p}/|\vec{p}|$ is the unit vector pointing in the direction of a particle's momentum and $\vec{\sigma} = (\sigma^1, \sigma^2, \sigma^3)$ are the 2×2 Pauli matrices. For massless particles, right-handed particles (or particles with positive helicity) have their spin and momentum aligned, while left-handed particles (or particles with negative helicity) have their spin and momentum anti-aligned, as shown in Figure 2.2.

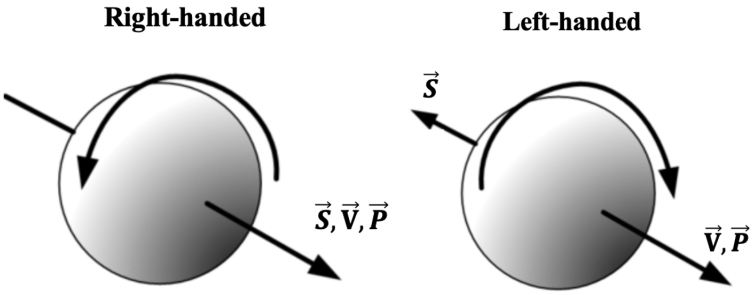

Figure 2.2: Right-handed and Left-handed particles. $\vec{S}$ shows the direction of the spin, $\vec{V}$ and $\vec{P}$ show the direction of the motion [31].

For a massless particle, all reference frames will have the same value for its helicity, implying that helicity is an intrinsic property of the particle. In contrast, helicity is not an inherent property for a particle with mass. This is because different observers can measure varying left- or right-helicity values based on their specific reference frames. Helicity is, therefore, not a fundamental characteristic of most particles. The concept of helicity remains applicable for relativistic electrons interacting via weak interaction. Thus, the electrons are considered left-handed if their spin and momentum directions are anti-aligned and right-handed if their spin and momentum directions are aligned. When the parity operator mentioned in 2.1.3 is applied to an electron, the spin is unaffected, but the momentum is reversed under spatial inversion.

2.2.2 Electroweak Theory

Following the first observation of parity violation in the weak interaction [30], several theories and models were developed to explain the phenomenon. The Glashow-Weinberg-Salam (GWS) theory was one of these frameworks [32]. It predicts the existence of a new electrically neutral boson, Z^0, and leads to the unification of the electromagnetic and weak interactions. The electroweak symmetry is mathematically described by an $SU(2) \times U(1)$ gauge group, which formalizes the operations that can be applied to the electroweak gauge fields without affecting the system's dynamics. The electroweak gauge fields include the weak isospin fields W_1, W_2, W_3, and the weak hypercharge field B. The $W^{\pm}$ and Z^0 bosons, as well as the photon, emerge from the Standard Model's spontaneous symmetry breaking of the electroweak symmetry $SU(2) \times U(1)$ to $U(1)_{\text{em}}$. This symmetry breaking is induced by the Higgs mechanism, a complex quantum-field-theoretic phenomenon that spontaneously alters the system's symmetry and reorganizes the degrees of freedom [33].
The Lagrangian for the electroweak interaction after spontaneous symmetry breaking is given by [34]:

$$\begin{aligned} \mathcal{L} = & \mathcal{L}_{\text{gauge}} + \mathcal{L}_{\phi} + \sum_r \overline{\psi}_r \left(i\partial - m_r - \frac{m_r H}{\nu} \right) \psi_r \\ & - \frac{g}{2\sqrt{2}} \left(J_W^{\mu} W_{\mu}^{-} + J_W^{\mu\dagger} W_{\mu}^{+} \right) \\ & - e J_Q^{\mu} A_{\mu} - \frac{g}{2\cos\theta_W} J_Z^{\mu} Z_{\mu}, \end{aligned} \tag{2.3}$$

where $\mathcal{L}_{\text{gauge}}$ represents the kinetic energy and self-interactions of the gauge bosons, while $\mathcal{L}_{\phi}$ includes the kinetic and potential energy of the Higgs field, describing its self-interactions. The fermion kinetic and mass terms, $\sum_r \overline{\psi}_r \left(i\partial - m_r - \frac{m_r H}{\nu} \right) \psi_r$, represent the kinetic energy of the fermions and their interactions with the Higgs field. The charged current interaction term, $-\frac{g}{2\sqrt{2}} \left(J_W^{\mu} W_{\mu}^{-} + J_W^{\mu\dagger} W_{\mu}^{+} \right)$, describes the interaction of fermions with the W bosons, where J_W^{μ} represents the weak isospin current. The electromagnetic interaction term, $-eJ_Q^{\mu}A_{\mu}$, represents the interaction of fermions with the photon field A_{μ}, J_Q^{μ} being the electromagnetic current. Finally, the

neutral current interaction term, $-\frac{g}{2\cos\theta_W} J_Z^\mu Z_\mu$, describes the interaction of fermions with the Z boson, considering J_Z^μ as the neutral weak current.

The symmetry breaking not only reveals the mass generation for the $W^\pm$ and Z^0 bosons but also determines the relationships among the weak isospin, weak hypercharge, and electromagnetic interactions, leading to the formation of electric charge and the associated currents. Weak hypercharge (Y_w) and the T_3 component of weak isospin combine in a specific linear manner to form the electric charge, $Q = T_3 + \frac{1}{2}Y_w$, and the associated current, $J_Q = J^3 + \frac{1}{2}J^Y$. The W_3 and B bosons mix to form two distinct physical bosons with different masses, the Z^0 boson and the photon (γ), as a result of the aforementioned spontaneous symmetry breaking:

$$\begin{pmatrix} \gamma \\ Z^0 \end{pmatrix} = \begin{pmatrix} \cos\theta_W & \sin\theta_W \\ -\sin\theta_W & \cos\theta_W \end{pmatrix} \begin{pmatrix} B \\ W_3 \end{pmatrix}, \tag{2.4}$$

where the weak mixing angle is denoted by θ_W. In the (W_3, B) plane, the particle representation axes are effectively rotated by the angle θ_W. Consequently, there is a mismatch between the masses of the Z^0 and the W particles, denoted as m_Z and m_W, respectively:

$$m_Z = \frac{m_W}{\cos\theta_W}. \tag{2.5}$$

The charged massive bosons $W^\pm$ are created by the combination of the W_1 and W_2 bosons:

$$W^\pm = \frac{1}{\sqrt{2}}(W_1 \mp iW_2). \tag{2.6}$$

The weak isospin, hypercharge, and electromagnetic couplings are related by $g\sin\theta_W = g'\cos\theta_W = e$. The Z boson interactions can be separated into right-handed couplings from J^{EM} and left-handed couplings from J^3:

$$g_L = T_3 - Q\sin^2\theta_W, \quad g_R = -Q\sin^2\theta_W. \tag{2.7}$$

These couplings can be written as vector and axial couplings g_V and g_A:

$$g_V = g_L + g_R = T_3 - 2Q\sin^2\theta_W, \quad g_A = g_L - g_R = T_3. \tag{2.8}$$

The weak neutral current couplings predicted by electroweak theory depend on the type of fermion, as listed in Table 2.1. According to GWS theory, all spin-1/2 par-

Table 2.1: The weak neutral current couplings for different fermion types.

Lepton	$2g_V$	$2g_A$	Quark	$2g_V$	$2g_A$
ν_e, ν_μ, ν_τ	1	1	u, c, t	$1 - \frac{8}{3}\sin^2\theta_W$	1
e, μ, τ	$-1 + 4\sin^2\theta_W$	-1	d, s, b	$-1 + \frac{4}{3}\sin^2\theta_W$	-1

ticles carry both axial (g_A) and vector (g_V) couplings. The neutral-weak interaction strength for the left- and right-handed states of spin-1/2 particles differs according to the axial coupling, whereas the vector coupling defines the average of the two. For pure virtual photon exchange, since there is no difference between left- and right-handed particles, the only coupling that exists is a vector coupling that is equivalent to the particle's electrical charge. The Z boson can interact with both left- and right-handed fermions.

In summary, the electroweak theory, mainly through the framework of the GWS model, provides a comprehensive explanation of the weak neutral current couplings, distinguishing between the interactions of left- and right-handed fermions. This understanding forms the cornerstone for investigating intricate particle interactions, such as electron-electron and electron-proton scattering, detailed in sections 2.3, 2.4, and 2.5.

2.3 Electron-Electron Scattering and Parity-Violating Asymmetry

Electron-electron scattering, represented by the notation $e^-e^- \to e^-e^-$, is known as Møller scattering. The leading order Feynman diagrams related to Møller scattering, including both interfering direct and exchange diagrams, are shown in Figure 2.3. To write the cross section for this process, the amplitude for the electromagnetic interaction, A_γ, as well as the amplitude for the weak interaction, A_{Z^0}, should be considered:

$$\sigma_{R(L)} = |A_\gamma \pm A_{Z^0}|^2 = |A_\gamma|^2 \pm 2\Re(A_\gamma A^*_{Z^0}) + |A_{Z^0}|^2. \tag{2.9}$$

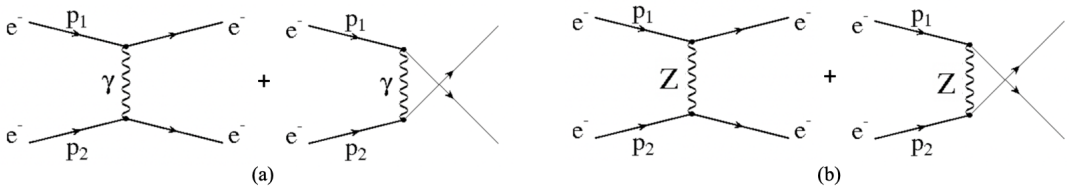

Figure 2.3: Feynman diagrams for Møller scattering at tree level, a) electromagnetic interaction, b) electroweak interaction [23].

The parity-violating asymmetry arises from the interference of electromagnetic and weak interactions. The weak interaction mediator Z^0 does not couple with left- and right-handed fermions with equal strength, leading to a differential cross-section that depends on the electron's helicity. This dependency reflects the parity-violating nature of the neutral current, and thus, the parity-violating asymmetry is defined as the normalized difference in the helicity-correlated scattering cross-section:

$$A_e^L = \frac{(\frac{d\sigma_R}{d\Omega} - \frac{d\sigma_L}{d\Omega})}{(\frac{d\sigma_R}{d\Omega} + \frac{d\sigma_L}{d\Omega})} \propto \frac{2\Re(A_\gamma A_{Z^0}^*)}{|A_\gamma|^2}, \tag{2.10}$$

It can be obtained as [35]:

$$A_e^L = mE\frac{G_F}{\sqrt{2}\pi\alpha}\frac{4\sin^2(\theta)}{(3+\cos^2(\theta))^2}Q_W^e, \tag{2.11}$$

where $\frac{d\sigma_R}{d\Omega}$ and $\frac{d\sigma_L}{d\Omega}$ represent differential cross-sections for right-handed and left-handed scattering processes, respectively, α is the fine structure constant, G_F is the Fermi constant, m is the mass of the electron, θ is the scattering angle in the center of mass frame, and Q_W^e is the weak charge of the electron. The weak charge of the electron is proportional to the product of the electron's vector and axial couplings to the Z^0 boson, $Q_W^e = 2g_V^e \times 2g_A^e = 1 - 4\sin^2(\theta_W)$, as mentioned in Section 1.2.

Measuring the parity-violating asymmetry in Equation 2.11 is the main objective of the MOLLER experiment. However, both other parity-violating and parity-conserving asymmetries contribute to the main measurement. This is because, in the scattering of longitudinally polarized electrons from unpolarized targets, processes other than Møller scattering are possible, such as electron-proton scattering. There-

fore, the impact of these parity-violating and parity-conserving asymmetries should be considered. Only longitudinal electron parity-violating asymmetry was covered in this section, and additional parity-violating and parity-conserving asymmetries are addressed in the following sections.

Given the potential contributions of other scattering processes to these asymmetries, it is crucial to explore three types of electron-proton scatterings: elastic, inelastic, and deep inelastic scatterings. The inelastic and deep inelastic scattering types, enabled by electron beams with energies of 11 GeV, will be considered to construct the theoretical framework for the proposed research project. In inelastic scattering, protons and neutrons transition into excited states. Upon decaying back into their stable states, they produce particles other than electrons such as pions ($\pi^{\pm}, \pi^{0}$). Deep inelastic scattering involves a high-energy electron beam knocking out the quarks of a proton, potentially yielding a variety of hadrons, primarily pions. Furthermore, in the deep inelastic scattering processes, combinations of quarks and anti-quarks can constitute the pions. This research focuses on detecting π^{-}; the reasons for this will be explained in Chapter 3, where the experimental apparatus, designed to bend the electrons, is discussed. The following section discusses electron-proton scattering in more detail, focusing on the mathematical aspects.

2.4 Electron-Proton Scattering and Parity-Violating Asymmetry

The investigation of electron-proton scattering, denoted as $e^{-}p \rightarrow e^{-}p$, is essential in advancing our understanding of particle interactions and the parity-violating and parity-conserving asymmetry. This field of study provides insights into the fundamental properties of protons and a framework for evaluating theoretical models in particle physics. Building on the electroweak theory principles discussed in section 2.2.2, this section probes how these theories are demonstrated in the complex dynamics between electrons and protons, illuminating the more intricate aspects of parity violation in these interactions.

The outcome of $e^- p \rightarrow e^- p$ scattering depends on the effective wavelength, $\lambda = hc/E$. When the electron energy is extremely low, and the wavelength significantly surpasses the proton's radius ($\lambda \gg r_p$), the proton can be approximated as a point-like particle, simplifying our understanding of the scattering process. At low electron energies, where the wavelength is comparable to the proton's radius ($\lambda \sim r_p$), the proton's extended charge distribution becomes significant, altering the scattering dynamics. High electron energies, characterized by wavelengths shorter than the proton's radius ($\lambda < r_p$), allow us to probe the proton's substructure, revealing the interactions with its constituent quarks. In the regime of extremely high electron energies, where the wavelength is much smaller than the proton's radius ($\lambda \ll r_p$), the scattering interactions predominantly occur with a sea of gluons and quarks, providing a more detailed view of the proton's internal structure. The MOLLER experiment would align most closely with scenarios where the electron energy is high or extremely high. In other words, the MOLLER experiment operates in a regime where the electron's energy and corresponding wavelength are sufficiently high to probe subatomic details, including the electroweak interaction between electrons and the quark substructure of protons.

As we get deeper into the complexities of electron-proton scattering, it becomes necessary to consider the structural characteristics of protons that influence these interactions. This is where form factor theory comes into play. Form factors, which are the Fourier transform of the matter density of a proton, explain how the interior structure of the proton influences the scattering process [36]. Form factors allow us to determine exact details like the distribution of the electric charge within the proton and its recoil during scattering events by bridging our theoretical models with experimental facts [37].

In the following subsections, a deeper look into specific scattering scenarios starts with elastic electron-proton scattering in 2.4.1. Subsection 2.4.2 focuses on inelastic electron-proton scattering, where the effects of higher energy impacts and proton recoil are crucial. This will detail how the proton's structure, represented by form factors, affects the high-energy interactions. Subsection 2.4.3 will also cover deep inelastic scattering, revealing insights into the formation of hadronic jets and their role

in understanding quark behavior. Subsection 2.4.4 will integrate these scattering concepts into the context of parity-violating and parity-conserving asymmetries in deep inelastic electron-proton scattering. Emphasizing practical experimental considerations, this section will discuss the need for adjustments due to pion background signals in the MOLLER experiment and explore the expected results based on theoretical models.

2.4.1 Elastic Electron-Proton Scattering

Figure 2.4 illustrates the Feynman diagram for elastic electron-proton scattering. The diagram represents the exchange of a virtual photon (denoted by q) between an incoming electron (with momentum p_1) and a proton (with momentum p_2), resulting in an outgoing electron (with momentum p_3) and proton (with momentum p_4). The vertices represent the interaction points where the electromagnetic force acts between the particles. Notably, the diagram includes a blob at one vertex to indicate the complex interaction between the virtual photon and the proton. The differential cross-

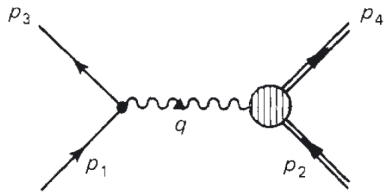

Figure 2.4: Feynman diagram of elastic electron-proton scattering, illustrating the exchange of a virtual photon, denoted as q, between an incoming electron (p_1) and a proton (p_2). The interaction results in outgoing electron (p_3) and proton (p_4) particles. The shaded blob represents complex interactions at the vertex, indicating factors not explicitly detailed in the diagram [1].

section in elastic electron-proton scattering, denoted by $\frac{d\sigma}{d\Omega}$, describes the probability density that a scattering event will occur under a specific solid angle. The formula for this differential cross-section is given by [1]:

$$\frac{d\sigma}{d\Omega} = \left(\frac{\alpha\hbar}{4ME\sin^2\left(\frac{\theta}{2}\right)} \right)^2 \frac{E'}{E} \left[2K_1 \sin^2\left(\frac{\theta}{2}\right) + K_2 \cos^2\left(\frac{\theta}{2}\right) \right], \tag{2.12}$$

where E and E' represent the energies of the electron before and after the scattering event, respectively. The variable M denotes the proton mass, and θ is the scattering angle. The terms K_1 and K_2 are coefficients that include the form factors depending on the square of the momentum transfer, q^2. The outgoing electron energy, E', is not an independent variable; it is kinematically determined by E and θ:

$$E' = \frac{E}{1 + \left(\frac{2E}{Mc^2}\right) \sin^2\left(\frac{\theta}{2}\right)}. \tag{2.13}$$

By counting the number of electrons scattered in a given direction for a range of incident energies, $K_1(q^2)$ and $K_2(q^2)$ can be determined experimentally. Instead of working directly with these quantities, the electric and magnetic form factors, $G_E(q^2)$ and $G_M(q^2)$, are derived as follows:

$$K_1 = -q^2 G_M^2, \quad K_2 = \frac{(2Mc)^2 G_E^2 - \left(\frac{q}{2Mc}\right)^2 G_M^2}{1 - \left(\frac{q}{2Mc}\right)^2}. \tag{2.14}$$

G_E and G_M are related to the proton charge and magnetic moment distributions, respectively. This formulation is essential for understanding the scattering dynamics as it incorporates the cross-section's dependency on the electron's initial and final energies and the angle of deflection.

2.4.2 Inelastic Electron-Proton Scattering

While elastic scattering of electrons by protons at modest energies results in the recoil of the proton retaining its identity, inelastic scattering processes at higher energies can produce a variety of particles. When the incident electron has sufficient energy, it can excite the proton into a higher energy state, leading to the emission of pions, kaons, deltas, and other particles as part of the reaction products. This is depicted in the inelastic scattering process $e + p \rightarrow e + X$, where X represents the array of possible particles produced, referred to as hadronic jets. Figure 2.5 illustrates a typical Feynman diagram for such an inelastic scattering process. The diagram shows an electron scattering off a proton, where the proton transitions into

a state characterized by multiple particle emissions. These emissions are represented by several outgoing lines, indicating the variety of hadronic jets resulting from the proton's disintegration in a higher energy state. The non-perturbative vertex in the

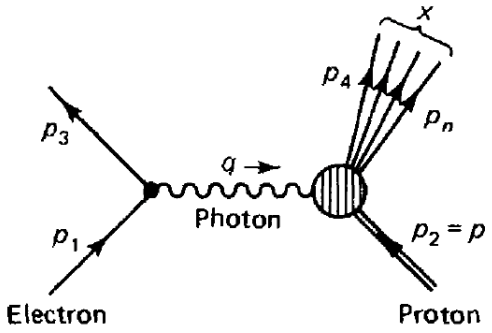

Figure 2.5: Feynman diagram illustrating inelastic electron-proton scattering. An incoming electron (p_1) exchanges a photon (q) with a proton (p_2), leading to an outgoing electron (p_3) and resulting hadronic jets (p_4, p_n). The shaded blob at the vertex represents the non-perturbative and not fully understood photon-proton interaction. The diagram also depicts the formation of hadronic jets from the excited proton [1].

diagram, often represented as a shaded or filled blob, symbolizes the current limits of our understanding regarding the detailed photon-proton interactions at these energy levels.

In the inelastic electron-proton scattering experiments, the inclusive cross section is measured instead of recording the momentum of the scattered electron (p_3). The inclusive cross-section can be derived by summing over X and integrating over $p_4, p_5, \ldots, p_n$. In this case, unlike elastic scattering, the outgoing electron's energy, E', does not depend solely on the initial energy E and the scattering angle θ since the outgoing hadrons can absorb a wide range of energy values. The total hadronic momentum $p_{\text{tot}} = p_4 + p_5 + \ldots + p_n$ is not bound by the condition $p_{\text{tot}}^2 = M^2c^2$. Consequently, Equation 2.13 no longer applies. The differential cross-section for scattering under these more generalized conditions incorporates the modified kinematic factors:

$$\frac{d\sigma}{dE'd\Omega} = \left(\frac{\alpha\hbar}{2E\sin^2(\theta/2)}\right)^2 \left[2W_1 \sin^2(\theta/2) + W_2 \cos^2(\theta/2)\right]. \tag{2.15}$$

The structure functions, W_1 and W_2, depend on two independent variables given a

specific incident energy E. While experimentalists utilize E' and θ, theorists would generally prefer to use the Lorentz-invariant quantities q^2 and $q \cdot p$. Additionally, as will be detailed in the subsequent section, theorists favor q^2 and x, where $x = -\frac{q^2}{2q \cdot p}$. By contrast, the elastic form factors (K_1 and K_2) depend on a single variable (θ for the experimentalist, q^2 for the theorist). In this scenario, E' is determined by equation 2.13 and x is fixed ($x = 1$). Formally, elastic scattering can be seen as a special case of inelastic scattering, where an additional constraint ($p_{\text{tot}}^2 = M^2c^2$) is imposed on the outgoing hadron momenta. It can be verified that [1]:

$$W_{1,2}(q^2, x) = -\frac{K_{1,2}(q^2)}{2Mq^2}\delta(x - 1). \tag{2.16}$$

This formulation effectively bridges the theoretical models between elastic and inelastic scattering phenomena.

2.4.3 Deep Inelastic Electron-Proton Scattering

During the late 1960s, Bjorken postulated that at extremely high energies, the dependency of inelastic structure functions on q^2 diminishes, essentially transforming them into functions solely of $x = -\frac{q^2}{2q \cdot p}$, which he named the Bjorken variable. More precisely, he suggested that

$$MW_1(q^2, x) \to F_1(x), \tag{2.17}$$

$$-\frac{q^2}{2Mc^2}W_2(q^2, x) \to F_2(x). \tag{2.18}$$

In what is known as the deep inelastic scattering regime, where both $-q^2 = (4EE'/c^2)\times \sin^2(\theta/2)$ and $q \cdot p = M(E - E')$ are significantly large but their ratio, $2x = -q^2/(q \cdot p)$, remains fixed. This concept is illustrated by the cross-section data for inclusive inelastic electron-proton scattering shown in Figure 2.6, which plots the cross-section as a function of the missing mass ($W = \sqrt{p_{\text{tot}}^2}/c$). The peak at $W = M$ has been scaled down to better fit within the graph. Further theoretical insights by Callan and

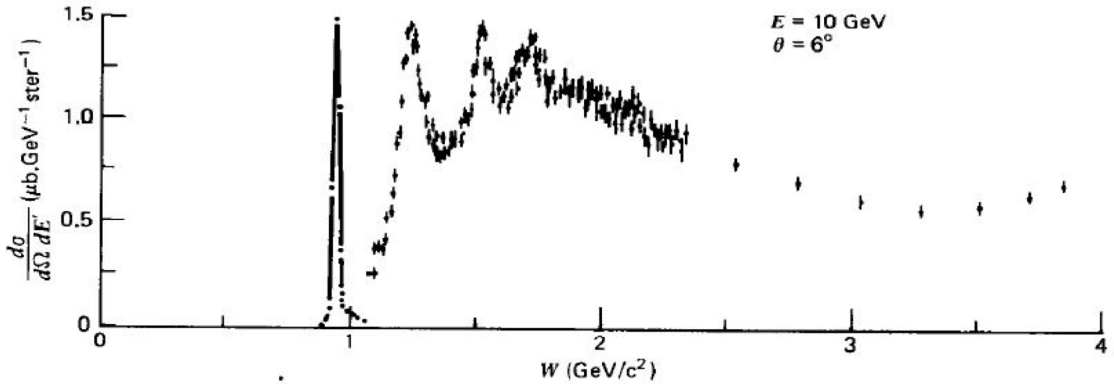

Figure 2.6: The cross-section for inclusive inelastic electron-proton scattering as a function of missing mass (W), illustrates the reduction in dependency on q^2 at higher energies. The distinct peak corresponds to the elastic scattering, reduced for clarity [1].

Gross in 1969 [38] proposed a relationship between these scaling functions:

$$2xF_1(x) = F_2(x), \tag{2.19}$$

which has also been validated through experiments [39]. The Callan-Gross relation [38] implies that the charged constituents of the proton are fermions with spin $\frac{1}{2}$, as a spin 0 prediction would lead to $2xF_1/F_2 = 0$, clearly inconsistent with the observed data. The experimental confirmation of Bjorken scaling and the Callan-Gross relation in deep inelastic scattering provides robust evidence for the existence of quarks. To derive Equations 2.17, 2.18, and 2.19, the reader is referred to Reference [1]. By substituting these three Equations to Equation 2.15, it can be found

$$\frac{d\sigma}{dE'd\Omega} = \frac{F_1(x)}{2M}\left(\frac{\alpha\hbar}{E\sin\left(\frac{\theta}{2}\right)}\right)^2\left[1 + \frac{2EE'}{(E-E')^2}\cos^2\left(\frac{\theta}{2}\right)\right]. \tag{2.20}$$

The formula above shows how the deep inelastic scattering process depends on both the energy of the incoming electron and the scattering angle, thereby affecting the distribution and characteristics of the reaction products. By experimentally measuring $\frac{d\sigma}{dE'd\Omega}$, researchers can derive insights into the proton's behavior under high-energy impacts, specifically regarding how its constituent quarks redistribute energy and

momentum.

Generated hadrons through deep inelastic electron-proton scattering include two main categories: baryons and mesons. Baryons, typically composed of three quarks, include stable particles like protons and neutrons and more exotic forms such as delta baryons and hyperons. Delta baryons, or Δ resonances, such as Δ^{++}, Δ^{+}, Δ^{0}, and Δ^{-}, also typically decay into nucleons and pions, e.g., Δ^{+} decaying into a proton and π^{0} or a neutron and π^{+}, and Δ^{0} decaying into a proton and π^{-}. Hyperons, which contain at least one strange quark, encompass particles like Lambda (Λ), Sigma (Σ), Xi (Ξ), and Omega (Ω) baryons, and typically decay into nucleons and pions. For instance, the Lambda (Λ) baryon often decays into a proton and a π^{-} or a neutron and a π^{0}, while the Sigma (Σ) baryon can decay into a neutron and a π^{+} or a proton and a π^{0}, among other decay modes. Mesons, consisting of a quark and an antiquark, include particles such as pions, the lightest and most broadly studied mesons. Consequently, the production of pions can occur directly from deep inelastic electron-proton interactions or indirectly from the decay of resonance states.

The purpose of this section was to explain how pion signals are produced in the MOLLER experiment. Deep inelastic electron-proton scatterings and consequent pion generations are enabled using electron beams with energies of 11 GeV. It is important to recall that the MOLLER experiment's primary signal comes from electron-electron scattering. Nevertheless, charged pions are important in determining the background fraction and signal asymmetry. To effectively correct the primary signal for the background, the effects of pion parity-violating and parity-conserving asymmetries, which we will further investigate experimentally in chapters 3 and 4, should be considered. The pion parity-violating asymmetry's mathematical formalism is examined in the following subsection.

2.4.4 Deep Inelastic Electron-Proton Scattering and Parity-Violating Asymmetry

In the context of the Standard Model of particle physics, parity-violating pion asymmetry in deep inelastic electron-proton scattering in a $Q^2 \ll M_Z^2$ region with

one photon or one Z^0 exchange between the electron and the target can be expressed as:

$$A_\pi^L = \frac{G_F Q^2}{4\sqrt{2}\pi\alpha}[a_1(x) + a_3(x)\frac{1-(1-y)^2}{1+(1-y)^2}], \tag{2.21}$$

where G_F is the Fermi constant, Q^2 is the squared momentum transfer to the electron, α is the electromagnetic fine structure constant, x is the Bjorken variable, and y is the fractional energy loss of the incident electron. a_1 and a_3 are

$$a_1(x) = 2g_A^e \frac{F_1^{\gamma Z}}{F_1^\gamma}, \quad a_3(x) = g_V^e \frac{F_3^{\gamma Z}}{F_1^\gamma}. \tag{2.22}$$

$\gamma - Z$ interference structure functions are characterized by $F_{1,3}^{\gamma Z}$ functions and are dependent on the vector and axial coupling of the electrons and quark.

It is important to note that this formula for pion parity-violating asymmetry in deep inelastic scattering is not the sole contributor to the observed effects in practical experimental setups, such as the MOLLER experiment and other PVES experiments. In other words, the pion parity-violating asymmetry can be zero or very small in value, indicating that pion production at this stage is primarily parity-conserving. As discussed in Section 2.4.3, delta baryons and hyperons can decay into nucleons and pions. These decays involve weak interactions that can introduce parity-violating effects, potentially complicating the interpretation of experimental results. The parity-violating and parity-conserving asymmetry values resulting from these pion productions should be considered when measuring the Møller parity-violating asymmetry. From an experimental perspective, it is necessary to measure both the pion parity-violating asymmetry and the pion dilution factor using the dedicated pion detector system (refer to section 3.4.3.2) and then to correct the Møller signal for the pion background signal.

The hypothesis in the simulations of the MOLLER experiment assumes a purely longitudinally polarized beam. However, the actual experiment may only partially align with this theoretical prediction. The following section will discuss how the transverse polarization component of the beam affects both Møller and pion asymmetry.

2.5 Transverse Asymmetry

In the MOLLER experiment, the electron beam produced by the source is designed to have purely (maximum possible) longitudinal polarization at the MOLLER target, aligning the spin of the electrons along their direction of motion. In this scenario, no transverse components of polarization are expected to be measured. However, slight deviations in the beam's spin alignment due to imperfections in the source, accelerator, or even external magnetic fields can result in transverse components of polarization. A transverse component of beam polarization would create an azimuthal modulation in the scattering rate asymmetry. Asymmetries arising from transverse polarization are called beam-transverse single-spin asymmetries (BTSSA), which describe the asymmetry when the electron's spin lies within the scattering plane but is oriented perpendicular to the incoming electron's momentum. So, when we talk about the asymmetry components in all the subsequent sections, it means the asymmetry which have been arisen from the polarization components.

In the following subsections, two cases of BTSSA relevant to this research are studied: transversely polarized Møller scattering and transversely polarized electron-proton scattering.

2.5.1 Transverse Asymmetry in Electron-Electron Scattering

In the process of transversely polarized Møller scattering, $e^{-\uparrow}e^- \to e^-e^-$, most of the data from PVES experiments utilized primarily longitudinal polarization of the electron beam, a fraction is conducted using primarily transverse electron polarization, thus facilitating the analysis of azimuthal asymmetry,

$$A_e^T(\phi) \equiv \frac{2\pi \frac{d(\sigma_R - \sigma_L)}{d\phi}}{\sigma_R + \sigma_L}. \tag{2.23}$$

The derivation of $A_e^T(\phi)$ for transversely polarized Møller scattering in the leading one-loop order was conducted by Barut and Fronsdal in 1960 [40], and by DeRaad and Ng in 1974 [41]. Note that ϕ here is the azimuthal angle of the scattered electron. This calculation is crucially influenced by the absorptive component of the scattering

amplitude, which necessitates an s-channel cut to account for the real, on-shell particle states. Consequently, only the box Feynman diagram and the diagram where the two indistinguishable outgoing electron legs are exchanged are relevant. These diagrams are essential as they capture both the direct and exchanged interactions between the electrons, including higher-order loop effects that contribute to azimuthal asymmetry in the scattering process. These considerations are illustrated in Figure 2.7, highlighting the unique contributions of these diagrams to the observable under study.

Figure 2.7: Left: Tree-level Feynman diagrams for transversely polarized electron-electron scattering, showing the basic exchange processes. Right: One-loop Feynman diagrams, contributing to the azimuthal asymmetry in transversely polarized Møller scattering. The absorptive components are highlighted by the dashed red line (s-channel cuts). These diagrams focus solely on box contributions to observe the effects of transverse spin, which are marked by arrows on the incoming electron lines [42].

At the percent level of precision, it becomes crucial to investigate the next-to-leading order radiative corrections to $A_e^T(\phi)$. The detailed theoretical calculation of these radiative corrections are beyond the scope of this research thesis and this section. The primary focus of this subsection, and the subsequent one, is to underscore the significance of transverse asymmetry and the necessity of incorporating corrections into the primary signal. For comprehensive details, the reader is referred to Reference [42]. Considering the radiative corrections but omitting the detailed steps results in the following expression for transverse asymmetry:

$$A_e^T = \frac{1}{\sin\phi} \frac{d\sigma^\phi/d\Omega}{d\sigma_{\text{Born}}/d\Omega}, \tag{2.24}$$

where the Born-level differential cross section for Møller scattering, derived from the

tree diagrams on the left side of Figure 2.7, is

$$\frac{d\sigma_{\text{Born}}}{d\Omega} = \frac{\alpha^2}{2s}\left(\frac{t^2+tu+u^2}{tu}\right)^2. \tag{2.25}$$

The dominant term in the cross-section, which contains azimuthal dependence, arises at the order α^3 (where α is the fine structure constant) due to the interference between the tree diagrams on the left side of Figure 2.7 and the box diagrams on the right side of Figure 2.7. The dependence on ϕ at this level is given by [42]:

$$\begin{aligned}\frac{d\sigma^{\phi}}{d\Omega} = &-\frac{\alpha^3 m_e}{8\sqrt{s}}\sin\theta\sin\phi \\ &\times\left[\frac{1}{t^2u^2}\left(3s(t(u-s)\ln\left(\frac{-t}{s}\right)+u(t-s)\ln\left(\frac{-u}{s}\right))-2(t-u)\frac{tu}{s}\right)\right].\end{aligned} \tag{2.26}$$

In the equation above, $s = 2m_eE$, where m_e is the electron mass and E is the energy. The variables t and u are described by $t = -2EE_{\text{lab}}(1-\cos\theta_{\text{lab}}) = -\frac{s}{2}(1-\cos\theta)$ and $u = -2m_eE_{\text{lab}} = -\frac{s}{2}(1+\cos\theta)$, respectively. Here, E_{lab} represents the lab frame energy and is calculated as $E_{\text{lab}} = \frac{E}{2}(1+\cos\theta)$, and $\cos\theta_{\text{lab}}$ is given by $1-\frac{m_e}{E}(1-\cos\theta)$, with θ being the center-of-mass (CM) frame polar scattering angle.

Note that A_e^T demonstrates odd symmetry with respect to $\theta \leftrightarrow \pi-\theta$, or equivalently, Equation 2.26 exhibits odd symmetry under $t \leftrightarrow u$. This symmetry arises due to two identical electrons in the final state configuration. In the CM frame, if one electron is positioned at (θ,ϕ), the other, according to leading order calculations, appears at $\pi-\theta, \phi+\pi$. Given that $\sin\phi$ changes sign under the transformation $\phi \leftrightarrow \phi+\pi$, the coefficient A_e^T is similarly odd with respect to the transformation $\theta \leftrightarrow \pi-\theta$. Such behavior significantly affects the integrated asymmetry that an experiment observes, especially when integrating over a range of θ and ϕ, because it is highly sensitive to the exact experimental acceptance. As a summary, symmetric forward-backward acceptance in the CM frame, as elaborated in Chapter 3 for the MOLLER experiment, results in a very small, yet non-negligible, Møller transverse asymmetry.

2.5.2 Transverse Asymmetry in Inelastic Electron-Proton Scattering

In this section, the BTSSA in electron-proton inelastic scattering is studied when a pion is observed in the final state. To compute the BTSSA, the differential cross section is first determined for cases where both the electron and the pion are observed. Figure 2.8 illustrates the various parameters involved in the interaction. Here, k_i and

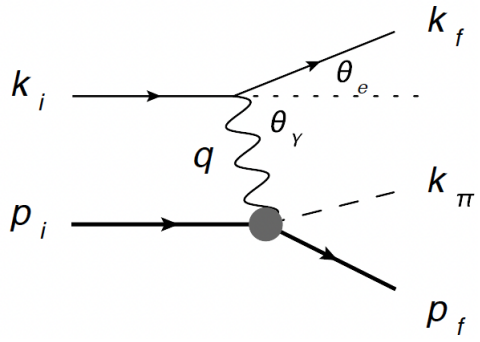

Figure 2.8: Diagram of the electron proton interaction, which decays into a nucleon and a pion [43].

k_f denote the momentum of the incoming and outgoing electrons, respectively. The symbol q represents the momentum transferred from the electron to the proton (defined by $q = k_i - k_f$), while k_π indicates the momentum of the pion. The variables p_i and p_f represent the momenta of the incoming and outgoing nucleons, respectively. Additionally, θ_e signifies the polar angle of the outgoing electron (its angle in the scattering plane), and θ_γ indicates the angle between the incoming electron and the photon. The pion emerges at angles θ_π and ϕ_π. According to a standard approximation ([44] and [45]), the complete differential cross section for single-pion creation in the one-photon exchange is [43],

$$\frac{d\sigma}{d^3k_f d\Omega_\pi^{CM}} = \epsilon_f^2 \Gamma \frac{d\sigma_v}{d\Omega_\pi^{CM}}, \tag{2.27}$$

where

$$\Gamma = \frac{\alpha^2}{2\pi} \frac{\epsilon_f}{\epsilon_i} \frac{W^2 - m_p^2}{2m_p Q^2} \frac{1}{1-\epsilon}, \tag{2.28}$$

ϵ_i and ϵ_f are the energies of the incident and outgoing electrons, respectively, W is the final state hadron mass, m_p is the mass of the proton, $Q^2 = -q^2$, and ϵ represents the photon polarization parameter (Appendix A of Reference [43]) and defined as:

$$\frac{1}{\epsilon} = 1 + 2\left(1 + \frac{\omega_\gamma^2}{Q^2}\right)\tan^2\frac{\theta_e}{2}, \tag{2.29}$$

$$\omega_\gamma = \epsilon_i - \epsilon_f,\ \tan^2\frac{\theta_e}{2} = \frac{Q^2}{4\epsilon_i\epsilon_f - Q^2}. \tag{2.30}$$

This parameter is provided in terms of the photon lab energy and electron lab scattering angle. The cross-section denoted as $d\sigma_v/d\Omega_\pi^{CM}$ refers to the production of a pion from a virtual photon ($p_i \to p_f k_\pi$). Typically, when the beam electron is polarized perpendicular to its direction of momentum, its spin orientation is determined by an azimuthal angle $\phi_{\rm Se}$. Under these conditions, the differential cross-section can be expressed as follows:

$$\frac{d\sigma_v}{d\Omega_{\rm CM}} = \frac{d\sigma_v^{\rm unpol}}{d\Omega_{\rm CM}} + \sin\phi_{\rm Se}\frac{d\sigma_v^n}{d\Omega_{\rm CM}} + \cos\phi_{\rm Se}\frac{d\sigma_v^s}{d\Omega_{\rm CM}}. \tag{2.31}$$

The pion transverse asymmetry becomes

$$A_\pi^T = \frac{d\sigma_v^s/d\Omega_{\rm CM}}{d\sigma_v^{\rm unpol}/d\Omega_{\rm CM}}. \tag{2.32}$$

The equation for the unpolarized cross section, which can be found in numerous sources, such as [44] and [46], is

$$\frac{d\sigma_v^{\rm unpol}}{d\Omega_{\rm CM}} = A + eB + eC\sin^2\theta_{\rm CM}^\pi\cos 2\phi_{\rm CM}^\pi + \sqrt{2e(1+e)}D\sin\theta_{\rm CM}^\pi\cos\phi_{\rm CM}^\pi. \tag{2.33}$$

The cross sections with transverse beam polarizations are,

$$\begin{aligned}\frac{d\sigma_v^n}{d\Omega_{\rm CM}} &= \frac{2m_e}{Q}(1-e)D'\sin\theta_{\rm CM}^\pi\cos\phi_{\rm CM}^\pi,\\ \frac{d\sigma_v^s}{d\Omega_{\rm CM}} &= \frac{2m_e}{Q}(1-e)E'\cos\theta_{\rm CM}^\pi\sin\phi_{\rm CM}^\pi\sin\phi_{\rm CM}.\end{aligned} \tag{2.34}$$

Explanation for constants A, B, C, D, D', and E' can be found in references [44] and [46]. Clearly, Equation 2.32 involves a complex formulation with numerous variables. Consequently, transverse asymmetry in inelastic electron-proton scattering is not addressed; instead, an alternative approach is introduced in the following subsection to incorporate pion transverse asymmetry into the simulations for the MOLLER experiment.

2.5.3 Implementing Transverse Asymmetries in the MOLLER's Simulation

To implement the asymmetry values for the simulation purposes, Equation 2.11 is used as the longitudinal Møller asymmetry, and Equation 2.24 is used as the transverse Møller asymmetry with the vertical and horizontal components in the azimuthal plane as follow:

$$\begin{aligned} A_e^{TV}(\phi) &= A_e^T \sin(\phi), \\ A_e^{TH}(\phi) &= A_e^T \sin\left(\phi - \frac{\pi}{2}\right). \end{aligned} \tag{2.35}$$

For the longitudinal and transverse pion asymmetries, due to the incompleteness of Equation 2.21 and the complexity of Equation 2.32, as explained previously, the findings from the Qweak experiment [47] and their associated uncertainties are implemented. As it is detailed in Section 5.3.1, in an ancillary measurement of the Qweak experiment, the beam energy was increased to 3.35 GeV to measure a small (approximately 0.1%) contamination from pions and other charged hadrons at higher energies. In this particular measurement, the value for the longitudinal pion asymmetry is 25.4 ± 9.0 part per million (ppm), and for the transverse pion asymmetry, it is 60.1 ± 19.3 ppm. The dependency of these asymmetry values on the polar angle θ is defined as:

$$\begin{aligned} A_\pi^L &= (25.4 - 9.0) + 2 \times 9.0 \times \left(\frac{\theta - \theta_{\min}}{\theta_{\max} - \theta_{\min}}\right) ppm, \\ A_\pi^T &= (-60.1 - 19.3) + 2 \times 19.3 \times \left(\frac{\theta - \theta_{\min}}{\theta_{\max} - \theta_{\min}}\right) ppm, \end{aligned} \tag{2.36}$$

where A_π^L is the longitudinal pion asymmetry, and A_π^T is the transverse pion asymmetry. $\theta_{\min}$ is zero degrees, and $\theta_{\max}$ is two degrees, both measured with respect to the beam direction, defining the acceptance of the experiment for the pions. The dependency on the azimuthal angle ϕ is defined as:

$$\begin{aligned} A_\pi^{TV}(\phi) &= A_\pi^T \times \sin(\phi), \\ A_\pi^{TH}(\phi) &= A_\pi^T \times \sin\left(\phi - \frac{\pi}{2}\right), \end{aligned} \tag{2.37}$$

where A_π^{TV} is the vertical component, and A_π^{TH} is the horizontal component of pion asymmetry in the azimuth plane. All these modifications and implementations are available in the development branch of the *remoll* repository [48]. The rationale for defining the asymmetry values according to Equation 2.36 is to select a model consistent with the Qweak experiment within the acceptance range of the MOLLER experiment. This model is entirely arbitrary because we do not have information about the kinematic dependence of the pion asymmetries.

The dynamics of the transverse asymmetry were briefly examined, focusing on the crucial role of electron polarization orientation. Building upon this foundation, a Bayesian analysis method is introduced in Chapter 5. This method will be applied to extract components of the Møller asymmetry and pion asymmetry, along with their associated uncertainties, considering the effect of transverse components of the polarization.

To this end, the focus has been on the theoretical aspects of particle interactions before they reach the detection system. This exploration has included helicity, electroweak theory, and various scattering processes, emphasizing their roles in understanding parity violation. As we move from this theoretical groundwork, the next section will direct our attention to how these particles interact with matter. We will investigate how charged particles traverse through materials, a key aspect for advancing our understanding of particle detectors and interpreting experimental data.

2.6 Passage of Charged Particles through Matter

Following the discussion on the theoretical aspects of particle interactions before reaching the detection system in the previous section, the focus now is on the subsequent stage of these interactions: the passage of charged particles through matter. This process is crucial for particle detection, as it involves the interaction of particles with a detector medium, leading to energy transfer that can be observed and quantified. As a particle traverses through matter, there is a certain probability that it will interact with either the nuclei or the electrons present in that material. This probability is proportional to the thickness of the material and the number of target particles per unit volume within it. Additionally, the nature of the interaction will also influence this probability.

In the context of heavy charged particles, such as charged pions, which have a mass greater than that of an electron, their traversal through matter is predominantly influenced by ionization energy loss. Although nuclear interactions are also possible, they are not the focus of this discussion. As these heavy charged particles move through a material, they encounter the electromagnetic fields of electrons and nuclei, leading to collisions. The nature of these interactions varies depending on whether the particle collides with an electron or a nucleus. When a charged particle interacts with a nucleus, it primarily changes trajectory due to transferring some of its energy to the nucleus. This interaction often results in minimal energy loss for the particle but can significantly alter its path, sometimes causing a pronounced deflection. In contrast, interactions with electrons typically involve the transfer of a larger portion of the particle's momentum to the electron, leading to considerable energy loss. However, these interactions usually have a relatively minor effect on the particle's trajectory. This contrast highlights the different roles electrons and nuclei play in the passage of a charged particle through matter. While ionization is the primary energy loss, collisions with nuclei are responsible for the most significant changes in the particle's path. As a result of these interactions, the movement of a charged particle through the material leaves a trail of excited atoms and free electrons. While most of these electrons receive only momentum, a fraction of them,

known as δ-electrons, acquire enough momentum to travel noticeable distances within the material. These δ-electrons, characterized by their significant energy, can further excite or ionize surrounding atoms.

The primary energy loss for a high-energy charged particle in such interactions, predominantly with electrons, is often described as ionization energy loss. This concept will be further explored in subsection 2.6.1. Additionally, multiple scattering, which arises from the unpredictable deviation in a particle's path due to collisions with anything, will be examined in subsection 2.6.2. Furthermore, bremsstrahlung, electromagnetic radiation emitted when a charged particle accelerates or decelerates in the field of another charged particle, and Cherenkov radiation, produced when charged particles move through a material faster than the speed of light in that medium, will be discussed in subsections 2.6.3 and 2.6.4, respectively. Finally, subsection 2.6.5 examines the interactions of charged particles with a lead absorber, referred to as the Lead donut in the MOLLER experiment, with additional discussions in Sections 3.4 and 4.1.

2.6.1 Ionization

As mentioned before, in the interaction of charged particles with matter, one of the key phenomena is ionization energy loss. The Bethe-Bloch equation, which represents mathematically the energy loss caused by a charged particle due to its interactions with electrons in the material, is essential in understanding this process. This equation [49], is presented below:

$$-\frac{dE}{dx} = \rho K \frac{Z}{A} \frac{z^2}{\beta^2} \left(\frac{1}{2} \ln \left(\frac{2m_e c^2 \beta^2 \gamma^2 T_{max}}{I^2} \right) - \beta^2 \right), \tag{2.38}$$

where $\frac{dE}{dx}$ is the average energy loss of the particle per unit path length in the medium, ρ is the material density in g/cm^3, K is a constant equal to 0.307 MeV cm^2/g, Z is the dimensionless charge of the nuclei, A is the relative atomic weight, z is the charge of the particle in units of the electron charge e, β is the velocity of the particle in units of the speed of light, γ is the Lorentz factor, given by $\gamma = \frac{1}{\sqrt{1-\beta^2}}$, m_e is the

electron rest mass, T_{max} is the maximum energy transfer to an electron, and I is the mean excitation energy of the material. For a detailed derivation of this equation, see the calculations provided in [50]. For all incoming particles, excluding the electron, $T_{max} \approx 2\beta^2\gamma^2 m_e c^2$. In the case of electrons, the most significant energy transfer occurs through Møller scattering (Section 2.3) from atomic electrons. Given that this involves the scattering of identical particles, the maximum energy transfer is half that of the maximum transfer for heavier particles, $T_{e,max} = \frac{1}{2}T_{max}$.

The simplified or classic form of the Bethe-Bloch formula has been included. To consider various effects, the equation for the energy loss rate of charged particles in a medium has been expanded to include corrections and terms [51]. Several of these corrections consist of:

1. **Density Effect:** Particles moving rapidly through a medium at high energies can induce polarization in the medium. At extremely high energies, this polarization reduces the particle's effective electric field, consequently reducing energy loss.

2. **Shell Corrections:** The free-electron model of atomic electrons is the one used in the condensed Bethe-Bloch formula. In reality, electrons are bound within atomic shells, which impacts how they react to a passing particle. This correction accounts for the fact that electrons are not free to move around but are bound within specific atomic shells.

3. **Barkas and Bloch Corrections:** These corrections consider the particle's charge, illustrating why electron-electron interactions cause negatively charged particles to traverse through a material slightly differently compared to positively charged particles. The Barkas correction is particularly important when the particle's velocity is comparable with the speed of orbital electrons of the target material.

4. **Violation of the Born Approximation:** The Born approximation's assumptions, which were used to derive the Bethe-Bloch equation, break down at very

high energies, requiring corrections. This is particularly true for light particles, such as electrons or positrons at very high energy, where bremsstrahlung emission represents the primary energy loss mechanism.

5. **Spin Effects:** Additional corrections are required for spin-half particles, such as electrons, due to the quantum mechanical properties associated with their spin. This is particularly important for particles with a small mass, such as electrons, which can be significantly deflected due to a single collision.

In addition to the general principles of ionization energy loss discussed above, it is insightful to consider a specific example, the energy loss rate ($-\frac{dE}{dx}$) of muons as they travel through water (H_2O). This example demonstrates the application of the Bethe-Bloch equation in a real-world context. It illustrates how these principles are relevant to the study of cosmic rays, as will be further discussed in Section 4.4.1. The discussion here is focused on a muon traveling through H_2O ($\rho = 1.0\,\mathrm{g/cm^3}$). However, the energy loss can be scaled to another material by simply multiplying by the density (in $\mathrm{g/cm^3}$) of the material. As shown in Figure 2.9, there are three regions for a muon traveling in water. The first region is the sub-relativistic region: $E_k < mc^2$, the second one is the ionization region: $E_k > mc^2$ and $E < 400\,\mathrm{GeV}\,m^2/m_\mu^2$, and the last one is the radiation region: $E > 400\,\mathrm{GeV}\,m^2/m_\mu^2$. In the sub-relativistic domain (Muon: $E_k < 100$ MeV), the rate at which particles lose energy per unit of distance increases. This means that particles rapidly decelerate upon entering this zone. In the high-energy radiation domain (Muon: $E_k > 400$ GeV), energy loss occurs through processes such as bremsstrahlung, pair production, and nuclear interactions, as discussed in the subsequent subsections. In the ionization region, most of the energy of cosmic ray muons is observed, where they possess a mean energy of approximately 4 GeV at sea level [53], as indicated by a blue marker in Figure 2.9. This region is of particular interest as the rate of energy loss is almost steady (it ascends logarithmically), maintaining an average energy loss rate of $2.2\,\mathrm{MeV/cm}$ in a substance with a density of $1.0\mathrm{g/cm^3}$, across numerous magnitudes. The minimum here, represented by a red star in Figure 2.9, denotes the point where the muon becomes a minimum ionizing particle (MIP) and achieves peak penetrative capacity.

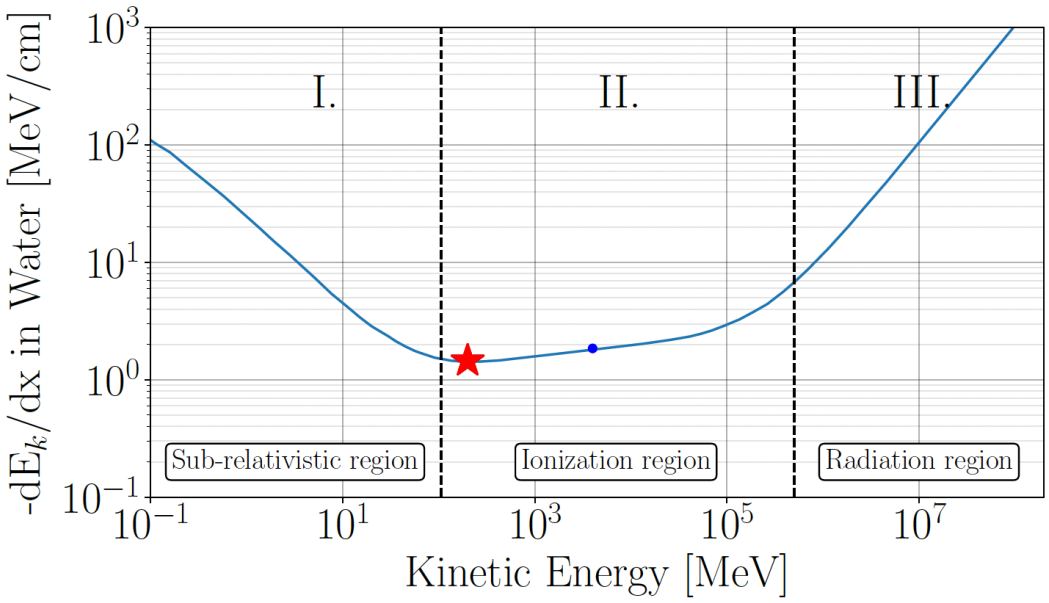

Figure 2.9: Energy loss per centimeter for a muon passing through water (H_2O, with a density of $1.0\,g/cm^3$). The blue dot signifies the average energy level of cosmic ray muons at sea level, 4 GeV, while the red star marks the point at which the muon exhibits minimum ionization [52].

To estimate the penetration depth of a standard cosmic ray muon, one can divide the energy by $2.2\,MeVcm^2/g$ and multiply by the absorber's density. This calculation method will be used in Section 4.4.1, where cosmic ray testing is discussed more thoroughly.

This exploration of ionization energy loss, particularly through the application of the Bethe-Bloch equation and its adaptations, underscores the intricate nature of particle interactions in various materials. The specific case of muons in water exemplifies these principles and is a foundational reference for further detailed studies in cosmic ray testing, as discussed in Section 4.4.1.

2.6.2 Multiple Scattering

Transitioning from the study of ionization, which is concerned with energy loss, multiple scattering is characterized by changes in the direction of particle movement. Multiple scattering occurs when charged particles interact with the nuclei in a ma-

terial, leading to a series of deflections. For minor angular deviations, these changes in trajectory typically follow a Gaussian distribution. The root mean square of the scattering angle, denoting the average directional change for a particle traversing a given material thickness L, is mathematically represented as follows[54]:

$$\begin{aligned} \sqrt{<\Theta^2>} &= \frac{z}{pc\beta}(20MeV)\sqrt{\frac{L}{X_0}}, \\ \frac{1}{X_0} &\approx 4\alpha r_0^2 \frac{\rho N_A}{A_r} Z(1+Z)\ln\left(\frac{183}{\sqrt[3]{Z}}\right). \end{aligned} \tag{2.39}$$

In the provided equation, Θ represents the scattering angle relative to the incoming particle direction, measured in radians. The term p denotes the momentum of the incoming particle, while X_0, known as the radiation length, indicates the material's thickness where the energy of the charged particle decreases by a factor of e, characterizing the depth of interaction of charged particles within a material. The material's density and nuclear charge significantly influence X_0. Additionally, N_A is Avogadro's number, α is the fine structure constant (approximately 1/137), and r_0 is the classical electron radius (2.82×10^{-15} meters). These parameters, combined in the equations, quantify the deflection of charged particles as they interact with nuclei, providing a statistical measure of multiple scattering effects in terms of angular deviations, which typically follow a Gaussian distribution. A more detailed representation of radiation length, beyond the rough approximation given in Equation 2.39, can be found in [51], which offers a more precise but complex form.

2.6.3 Braking Radiation (Bremsstrahlung)

Following the exploration of ionization and multiple scattering, breaking radiation is another critical phenomenon in interacting charged particles with matter, commonly known as bremsstrahlung. This electromagnetic radiation is produced when a charged particle is accelerated or decelerated in the field of an atom or nucleus. Bremsstrahlung occurs due to collisions between charged particles and nuclei, leading to deviations in their trajectories and the emission of radiation. While any accelerated charged particle can produce bremsstrahlung, it is predominantly observed and

more intense for lighter particles such as electrons and positrons [55]. In other words, except in cases of extremely high energies, the radiation released by particles other than electrons or positrons is negligible. As shown in Equation 2.39, the radiation length (X_0) determines the radiation that electrons and positrons emit. As a result of bremsstrahlung, an electron's average energy loss is given by:

$$E(x) = E_0 e^{-\frac{x}{X_0}}. \tag{2.40}$$

It has been found that the energy of the charged particle is directly related to the energy loss from bremsstrahlung. Above a certain threshold energy, E_C, the energy reduction caused by bremsstrahlung exceeds the energy reduction caused by ionization for electrons. This threshold energy can be estimated by $E_C = \frac{800\,\mathrm{MeV}}{Z+1.2}$ and is affected by the charge of the atomic nuclei in the material. Bremsstrahlung decreases by a factor of $(m_{\mathrm{electron}}/M)^2$ for particles of mass M that are different from electrons. Therefore, bremsstrahlung is negligible for particles other than electrons and positrons at energies below 1 TeV.

2.6.4 Cherenkov Radiation

When charged particles traverse a material at velocities exceeding the speed of light in that medium, they emit Cherenkov radiation. This radiation is visually evident as a distinct blue or ultraviolet cone of light because the emitted light is in the visible and ultraviolet spectrum, where shorter wavelengths (blue and ultraviolet) dominate due to the higher energy of the emitted photons [56]. As these particles move through the medium, they induce polarization due to their electric field. After their passage, the medium depolarizes, reverting to its initial state. This shift in polarization produces an electromagnetic disturbance that propagates at light speed. This rapid polarization and subsequent depolarization leads to the emission of Cherenkov photons. Figure 2.10 depicts two distinct behaviors of charged particles:

1. **Particle's Speed < Speed of Light in Medium:** Electromagnetic disturbances, originating from the medium's polarization and subsequent depolariza-

tion, travel faster than the particle. At distances far from the particle's path, these disturbances often cancel each other out due to the symmetric distribution of the emitted waves. However, if the particle is moving near the speed of light in the medium or if the medium has significant inhomogeneities, the disturbances may not cancel out completely, leading to detectable effects.

2. **Particle's Speed > Speed of Light in Medium:** The electromagnetic disturbances travel more slowly than the particle, converging into a unified wavefront. These disturbances synchronize in phase, producing a noticeable perturbation wave. The direction of this wave is determined by the particle's velocity and the speed of light within the medium.

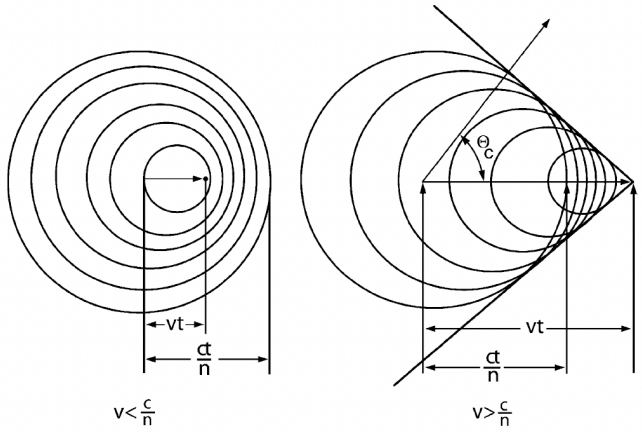

Figure 2.10: Left: The particle moves at a velocity below the medium's speed of light. Right: The particle moves at a velocity exceeding the medium's speed of light [54].

Given the geometric context of the situation, the angle between the particle's path and the wavefront can be readily calculated. Refer to the right triangle depicted on the right side of Figure 2.10, where the two sides of this triangle are given lengths of ct/n and vt. The Cherenkov angle, θ_c, can be derived as follows:

$$\cos(\theta_c) = \frac{(c/n)t}{vt} = \frac{c}{nv}. \tag{2.41}$$

Therefore, the Cherenkov effect is the emission of optical photons caused by the energy deposited from the charged particles in the direction indicated by Equation

2.41. The strength of the Cherenkov effect can be determined using fundamental principles by resolving the Maxwell equations with appropriate boundary conditions [54]. This results in:

$$\begin{aligned} \frac{d^2E}{d(\hbar\omega)dx} &= \hbar\omega\frac{z^2\alpha}{\hbar c}\left(1-\frac{c^2}{n^2v^2}\right) = \hbar\omega\frac{z^2\alpha}{\hbar c}\sin^2(\theta_c) && \text{for } v > \frac{c}{n} \\ \frac{d^2E}{d(\hbar\omega)dx} &= 0 && \text{for } v < \frac{c}{n}, \end{aligned} \tag{2.42}$$

where E represents the total energy radiated as Cherenkov photons, $\hbar\omega$ denotes the energy of a single Cherenkov photon, z is the charge of the particle, α is the fine-structure constant (approximately 1/137), $\hbar c$ is a physical constant with a value of $197 \times 10^{-9}\,\mathrm{eV\,m}$, c is the speed of light in a vacuum, n is the refractive index of the medium, and v is the particle's speed. The term $\sin^2(\theta_c)$ highlights why Cherenkov radiation is a visually evident continuous spectrum, but rises toward the UV, as it relates to the angle and intensity of emitted photons detected by PMTs in particle detectors. It is evident that Cherenkov radiation is emitted when $v > \frac{c}{n}$. Derived from this condition, the threshold kinetic energy, beyond which Cherenkov radiation becomes possible, is defined as:

$$E_{\text{threshold}} = mc^2\left(\sqrt{\frac{n^2}{n^2-1}}-1\right). \tag{2.43}$$

This threshold signifies the point where the particle's kinetic energy becomes sufficient to enable the emission of Cherenkov radiation. By dividing Equation 2.42 by $\hbar\omega$, the number of Cherenkov photons emitted per energy interval of the photon and for each unit of length is determined. Thus, the number of Cherenkov photons produced by a charged particle in one centimeter of a material within the visible range is given by:

$$N = \frac{z^2\alpha}{\hbar c}\sin^2(\theta_c)\int_{1.65\mathrm{eV}}^{3.26\mathrm{eV}} dE \int_{0\mathrm{m}}^{10^{-2}\mathrm{m}} dx. \tag{2.44}$$

Once the number of Cherenkov photons produced per unit length of the particle's path in the medium has been calculated using Equation 2.44, the next step is estimat-

ing the total energy loss due to Cherenkov radiation. This is achieved by multiplying the number of photons by the average energy of a single Cherenkov photon in the visible range. The average energy of photons in the visible spectrum is approximately 2.44 eV, $E_{\text{average}} = \frac{E_{\text{violet}}+E_{\text{red}}}{2}$. This value represents the typical energy carried by a single photon emitted due to the Cherenkov effect within the visible light range. The total energy loss due to Cherenkov radiation, E_{loss}, over a given path length L in the medium, can be estimated by the following calculation:

$$E_{\text{loss}} = N \times E_{\text{average}} \times L, \tag{2.45}$$

where N is the number of Cherenkov photons produced per unit length as calculated from Equation 2.44, E_{average} is the average energy of a Cherenkov photon (2.44 eV), and L is the path length of the particle in the medium. This equation provides a means to quantify the energy loss of a charged particle as it traverses a material. It is important to note that this energy loss is typically a small fraction of the particle's total kinetic energy. Still, it's crucial to understand the Cherenkov effect and its applications in particle detection.

2.6.5 Interactions of Charged Particles with a Lead Absorber

As the final discussion of this section, the interactions of charged particles with a lead absorber, known as the Lead donut in the MOLLER experiment, are examined. Section 3.4 describes the placement of the Lead donut following the main detector system and preceding the pion detector, functioning to filter out both high- and low-energy electrons, thereby selectively allowing pions to enter the pion detector. Section 4.1 explores optimizing the geometry and placement of the Lead donut to enhance the pion detector system's performance. Here, to visually complement the theoretical discussion of particle interaction in the lead, Figure 2.11 depicts the various interaction mechanisms experienced by electrons and positrons in the lead [57]. The plot demonstrates that ionization is the predominant energy loss mechanism for electrons and positrons at lower energies, while bremsstrahlung becomes more sig-

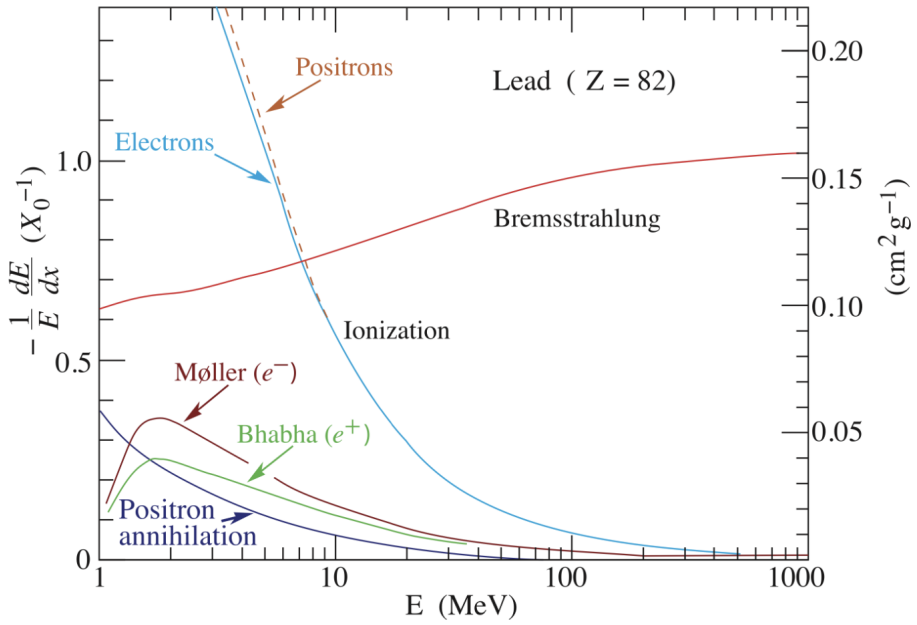

Figure 2.11: Energy loss mechanisms for electrons and positrons in lead are shown as fractional energy loss per radiation length. The x-axis represents the kinetic energy in Mega-electron Volts (MeV), and the y-axis shows the normalized energy loss $-\frac{1}{E}\frac{dE}{dx}$. Ionization (red curve) dominates at lower energies, while bremsstrahlung (blue curve) prevails at higher energies, with additional processes like Møller scattering for electrons (dark green curve), Bhabha scattering for positrons (light green curve), and positron annihilation (brown curve) also illustrated [57]

nificant at higher energies. For instance, electrons with an energy level of 11 GeV within the Lead donut undergo substantial energy loss due to bremsstrahlung, obstructing most electrons from penetrating the pion detector system. This justifies the theoretical placement of a Lead donut ahead of the pion detection system, as it effectively stops low-energy electrons through ionization and high-energy electrons through bremsstrahlung.

After discussing the theoretical foundations of charged particle interactions with matter and understanding the various phenomena such as ionization, multiple scattering, bremsstrahlung, and Cherenkov radiation, it becomes essential to explore the selection criteria for the active medium of the pion detector, as well as the methods for detecting and analyzing the interactions. The discussion of the active medium for the pion detector and the PMTs, which are designed to convert the physical phenomena

described earlier into measurable electrical signals, is deferred to Chapter 4 for consistency, as all aspects of the pion detector are explained in that chapter. Subsection 4.1.1 focuses on the specific requirements and properties that make UV-transparent acrylic (Lucite) an optimal choice for the pion detector in the MOLLER experiment. Subsection 4.1.2 Covers the PMTs, detailing their critical role in the detection process, the necessary characteristics, and the rationale for selecting the ET Enterprise 9125B model [58] as the PMT for the pion detector in the MOLLER experiment.

As in any research process, following the theoretical groundwork (Chapter 2) and the design and simulations (Chapter 4), the next step involves verifying the simulation results. In this study, the verification of the optimized pion detector design is carried out through cosmic testing and beam testing. The introduction to these tests, along with the underlying physics, is explained in the next section. If you are familiar with the field, you may skip the section. However, if you are new to the field, it is recommended to read it for a better understanding.

2.7 Verifying the Simulation Results: Cosmic Testing and Beam Testing

This section introduces cosmic testing and beam testing in validating theoretical models and simulations against experimental data, particularly within the pion detector of the MOLLER experiment. Section 2.7.1 provides a historical background and an overview of the fundamental principles underlying cosmic rays. In Subsection 2.7.2, the focus is on the Mainz Microtron (MAMI), an electron beam accelerator. A historical and technical overview of the MAMI facility is provided, with particular attention given to the MAMI B stage, which hosted the beam tests for this research.

2.7.1 Cosmic Rays and Cosmic Testing

The foundation of cosmic ray research was established in the early 20th century, significantly influenced by Victor Hess's experiments in 1912 [59]. Hess discovered a notable correlation between altitude and the rate of ionizing radiation in the Earth's

atmosphere. During his ascension in a balloon, he observed an increased discharge frequency in his electroscope, leading him to conclude that higher altitudes were associated with higher radiation levels. This observation ultimately led to his recognition with the Nobel Prize in physics in 1936 for the discovery of cosmic rays [60].

The Earth continuously receives a stream of particles known as cosmic rays. Around 74% of these particles consist of ionized hydrogen or protons. A further 18% originates from helium nuclei, which include two protons and two neutrons, while heavier elements makeup just a small fraction [53]. Most cosmic rays that we detect on Earth are of such high energy that their kinetic energy far exceeds their rest mass energy (with $\frac{E_k}{mc^2} > 1$), classifying them as relativistic. When a cosmic ray of primary origin strikes an atomic nucleus in the Earth's upper atmosphere, typically oxygen or nitrogen, the collision energy can be significant enough to disrupt the incoming particle and the nucleus via a nuclear interaction. This collision often results in the creation of transient particles known as mesons [61], predominantly pions (π^+, π^-, π^0) and kaons (K^+, K^-, K^0). The charged pions (π^+) undergo decay within ten nanoseconds [62], yielding muons of the same electric charge and neutrinos. The decay of charged kaons (K^+) into pions or directly to muons is somewhat more complex. Neutral mesons (π^0, K^0) decay almost instantaneously (on the order of 10^{-17} seconds) into gamma rays. Given their ability to cover more distance prior to decay compared to their neutral counterparts, charged mesons can engage in further interactions with atmospheric molecules. Such interactions may trigger additional nuclear reactions, which, governed by the strong force due to the quark content of mesons, could lead to generating even more mesons, thereby amplifying the particle shower initiated by the initial cosmic ray collision. Despite the shielding provided by the atmosphere, which largely blocks primary cosmic rays from reaching the surface, the secondary particles produced can occasionally descend through the atmosphere to the ground. A depiction of cosmic ray interaction is provided in Figure 2.12.

Cosmic ray muons ($\mu^{\pm}$) are produced from the decay of charged mesons. When a charged pion decays, it almost always generates a muon of the same charge (and a muon-neutrino) with a likelihood of 99.98%, as shown in Equation 2.46, while a charged kaon converts into a muon (and a muon-neutrino) 63.5% of the time, as

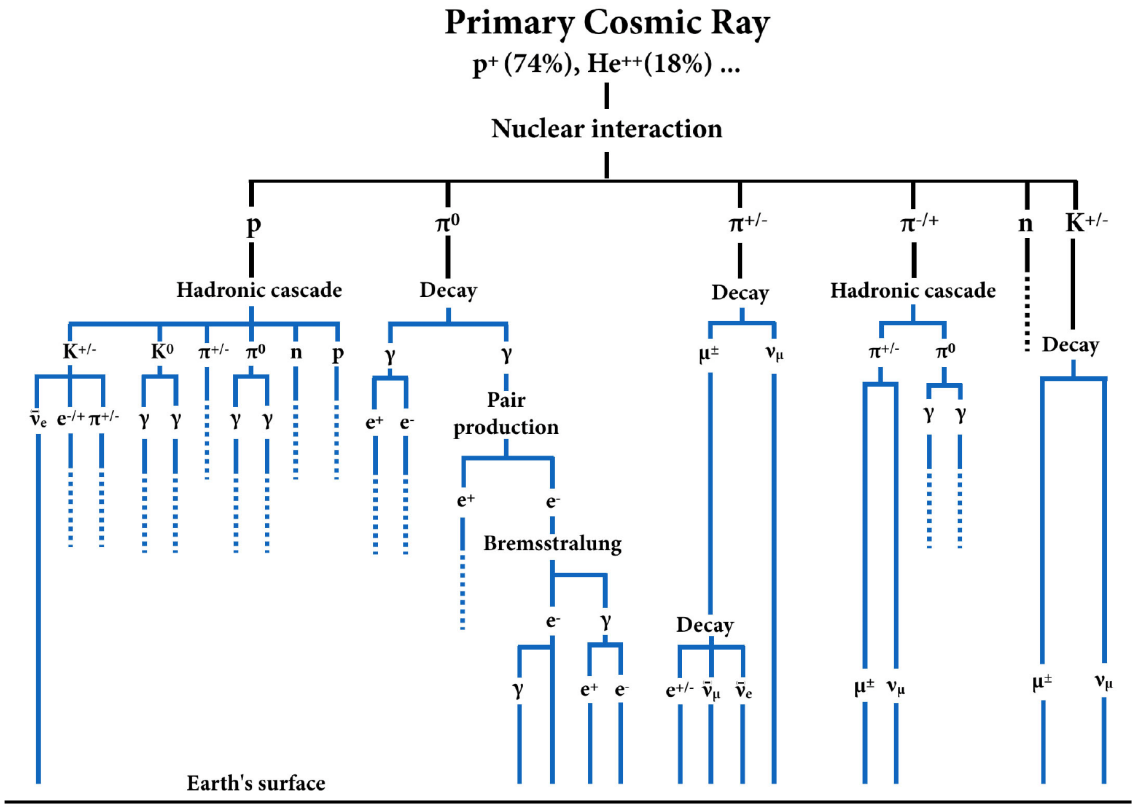

Figure 2.12: A schematic illustration of the various decay processes and interaction sequences occurring from the interaction of a cosmic ray with Earth's atmosphere [52].

indicated in Equation 2.47 [63].

$$\pi^{\pm} \rightarrow \mu^{\pm} + \nu_{\mu}(\overline{\nu}_{\mu}) \quad (99.98\%) \tag{2.46}$$

$$K^{\pm} \rightarrow \mu^{\pm} + \nu_{\mu}(\overline{\nu}_{\mu}) \quad (63.5\%) \tag{2.47}$$

Between 80% to 90% of the muon flux at the Earth's surface at energies of interest (GeV to TeV scale) originates from pion decay, with the remainder from kaon decay [64]. Muons, having a mass of 105.65 MeV, are highly penetrating particles that primarily interact through ionization (2.6.1) as they traverse the atmosphere. This characteristic allows them to reach the Earth's surface in significant numbers. The average muon energy at the Earth's surface is expected to be more than a few GeV,

often cited as approximately four GeV [53]. Muons that reach the Earth's surface without decaying contribute to the low-energy electromagnetic component of cosmic ray showers at sea level. Note that when cosmic ray muons enter the Earth's atmosphere at steeper angles relative to the vertical, they have to cover a substantially increased distance and consequently pass through more material before being detected at the Earth's surface. Therefore, it is anticipated that the intensity of cosmic ray muons will depend on the square of the cosine of that angle [53].

The energy loss rate of a muon traveling through H_2O was thoroughly discussed in Section 2.6.1. As mentioned, to estimate the penetration depth of a standard cosmic ray muon, the energy is divided by $2.2\,\mathrm{MeVcm^2/g}$ and multiplied by the absorber's density. For instance, a 10 GeV muon will traverse around 17 m of concrete ($\rho = 2.7\,\mathrm{g/cm^3}$). However, what of other massive charged particles like protons, pions, and kaons? Though these are subject to energy loss through ionization, their quark composition allows for interaction via the strong force, causing significant nuclear collisions that influence the particle's path and energy trajectory. Muons are distinctive in that they lose energy through ionization and do not engage in strong nuclear interactions like protons or pions. This enables them to penetrate materials with minimal energy loss due to collisions with electrons in the absorbers and minimal deviation in their path.

The conclusion of the discussions in this subsection leads to the understanding that cosmic testing involves the detection of muons with an energy of approximately 4 GeV. To validate the experimental setup, simulations can be conducted using this specific particle and energy level.

2.7.2 Mainz Microtron (MAMI) and Beam Testing

To ensure the robustness and reliability of the results from the cosmic testing phase, a series of beam tests were performed. This subsection focuses on the Mainz Microtron (MAMI), an electron beam accelerator. A historical and technical overview of the MAMI facility is provided, with particular attention given to the MAMI B stage, which hosted the beam tests for this research. The Mainz Microtron (MAMI)

is an advanced electron beam accelerator at the Institute for Nuclear Physics at the University of Mainz [65], primarily used for hadronic physics experiments. The facility has seen several upgrades and expansions since its inception, leading to different stages known as MAMI A, MAMI B, and MAMI C.

In 1976, a race track microtron (RTM 1) was proposed as the initial stage of a planned cascade of three microtrons to deliver a particle beam with an energy of up to 855 MeV. The RTM 1, with an extraction energy of 14 MeV, was completed in 1979. By 1983, the RTM 2, also known as MAMI A, was finished, delivering 180 MeV. The next stage, RTM 3 (MAMI B), which provided 855 MeV, became operational in 1990 as part of a Collaborative Research Centre (CRC 201). MAMI B was unique in delivering a continuous particle beam of exceptional quality, never before achieved in that energy range, with transverse emittances at 100 µA: horizontal 8π nmrad, vertical 0.5π nmrad, and an energy width of 13 keV. The installation of RTM 3 marked the mechanical limit of the race track microtron concept, as any further energy increase would require extremely large bending magnets. However, in 1979, a solution was proposed, explored in the late 1990s and led to the 1999 proposal of the harmonic double-sided microtron (HDSM) at 1.5 GeV, known as MAMI C.

Figure 2.13 depicts the Mainz Microtron (MAMI), illustrating its three main stages: MAMI A, MAMI B, and MAMI C, along with associated experimental setups. MAMI A begins the acceleration process, where electrons are initially accelerated to 180 MeV. MAMI B further enhances the electron energy to 855 MeV, highlighted by its capacity to deliver continuous, high-quality beams. The most advanced stage, MAMI C, achieves up to 1508 MeV, incorporating a Harmonic Double-Sided Microtron (HDSM) that surpasses previous energy limits. Additionally, the diagram includes experimental areas like the Spectrometer Hall, which has setups for various physics experiments. The beam testing related to this research was conducted at MAMI B, and a red star marks the test placement. The test played a crucial role in gathering essential data for developing and calibrating the pion detector. More detailed information and technical data are available in [67].

Before exploring the details of the facility and apparatus of the MOLLER experiment in chapter 3, the next section will discuss the MOLLER experiment simulation

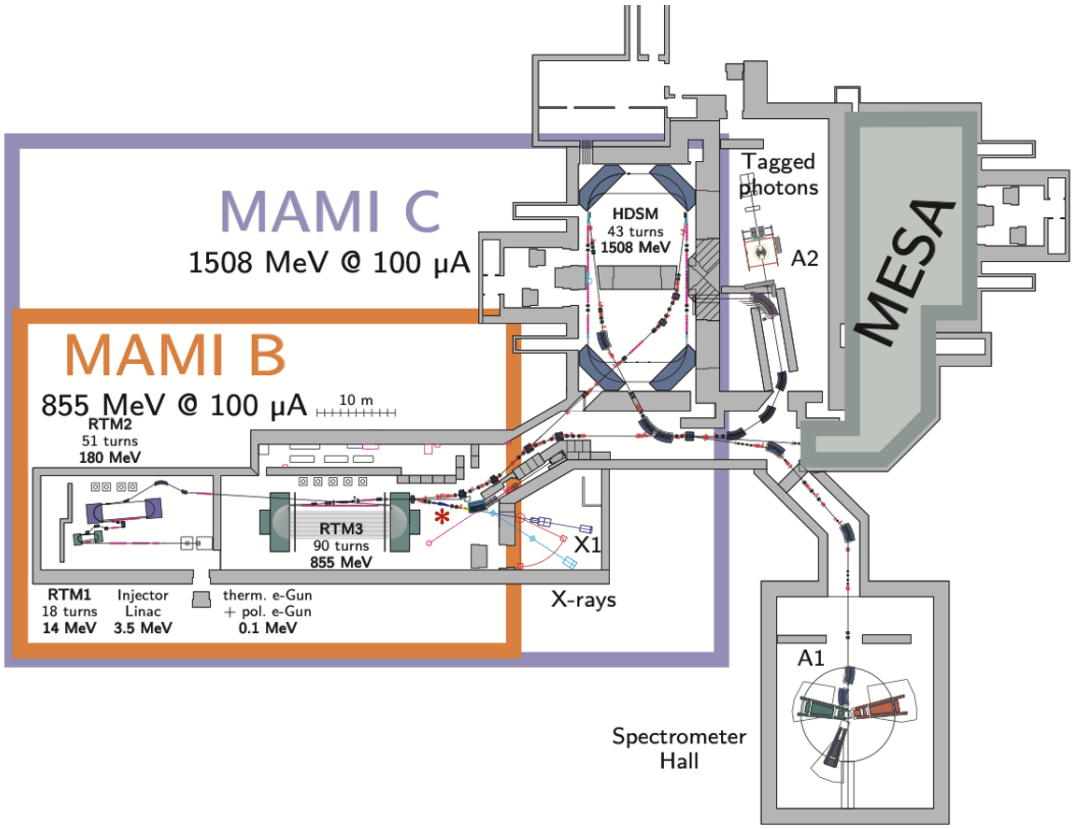

Figure 2.13: The floor plan of the MAMI facility, highlighting MAMI B and MAMI C, and the location of the pion detector prototype beam tests are indicated by a red star. This diagram illustrates the configuration and key components of the facility, including the different stages of the microtron and experimental areas [66].

which is called *remoll* and available in reference [68].

2.8 MOLLER Experiment Simulation (*remoll*)

The simulation tool for the MOLLER experiment, known as *remoll*, is accessible by compiling the source code. The most up-to-date branch is the develop branch, which consolidates all modifications and, as of the date of this thesis, contains the latest design updates for all subsystems.

In the remoll directory, two subdirectories are particularly important in the context of this thesis:

1. ***remoll/src*:** The src directory contains all source codes for various generators such as beam, Møller electron, pion, elastic, inelastic, aluminum, etc. It also includes codes for generating events specific to these generators. For this thesis, the pion and Møller generators are primarily used, while the elastic and inelastic generators are utilized at certain points for more accurate calculations (Section 4.2).

2. ***remoll/geometry*:** This directory houses the designs of all subsystems. Key areas focused on in this thesis include `geometry/detector/ThinQuartz/DetectorArray` for the main detector (Section 3.4.1), `geometry/showermax` for the shower-max detector (Section 3.4.3.1), `geometry/donut` for the Lead donut, and `geometry/pion/Lucite` for the pion detector system (Section 3.4.3.2). The pion detector system (Section 3.4.3.2) has seen significant design and modification efforts within `geometry/pion/Lucite`. The `geometry/showermax` has been utilized to address low-energy particle showering issues (Section 4.2) and its impact on the pion detector system (Section 3.4.3.2). Moreover, all simulation results for the main detector, as discussed in Section 3.4.1, which are used in the Bayesian analysis in Chapter 5, are extracted from `geometry/detector/ThinQuartz/DetectorArray`.

In the *remoll* simulations and designs, the identification numbers for detectors and particles are other essential aspects. For the pion detector, the active detector with a detector ID of 8000 corresponds to the photo-cathode area of the PMT, which is instrumental in detecting photo-electrons generated within the pion detector system. The detector ID 8001 also represents the Lucite (pion detector's medium 4.1), allowing for calculating different particle rates within this area. Concerning particle identification, *remoll* simulations employ the Monte Carlo particle numbering scheme [69] to distinguish various particle types, such as electrons (-11), positrons (+11), pions (-211 and +211), and muons (-13 and +13). These particles are the primary focus when calculating rates for different generators in Lucite (detector 8001). Furthermore, the output tree variables in *remoll* [70] facilitate the generation of diverse histograms. The installation and loading of the Geant4 and ROOT analysis packages

enable all of these processes.

The CERN-developed Geant4 [71] simulation is a widely recognized toolbox for simulating the passage of particles through materials. With a wide range of physics models and a reputation for adaptability and precision, Geant4 simulates detailed physical interactions and processes. These models apply to various experimental conditions, from high-energy physics to medical physics. The accurate estimation of energy deposition and secondary particle tracking is made possible by Geant4's thorough modelling of detector design and materials.

The ROOT analysis package [72], another essential tool in this study, is developed at CERN and serves as a powerful computing framework specifically designed for data analysis in particle physics. ROOT provides functions that enable researchers to manage and interpret massive datasets. ROOT specializes in data storage, statistical analysis, and visualization.

While the simulation tools provided by Geant4 and ROOT are indispensable for a broad spectrum of particle interactions, this thesis necessitates a particular emphasis on the pion generator. Our primary focus is the pion detector system, so a detailed understanding and accurate modelling of this generator are essential. Therefore, the specifics of the pion generator, central to simulating the interactions we aim to detect and analyze, will be thoroughly explored. To describe the cross-section of the pion generation in the context of virtual photon-nucleon interactions, Dr. Martin D. Wiser brought a model in the 1970s [73]. This model, now referred to as the Wiser parameterization, changed how we interpret these interactions. Including basic parameters like energy, momentum transfer, and pion angles was one of Wiser's notable characteristics in parameterization. The model describes pion production as a two-step, sequential process. Initially, the incoming photon triggers an excitation within the nucleon, causing it to transition into a delta resonance. Subsequently, this resonance decays, resulting in the generation of a nucleon and a pion. Initially, the Wiser parameterization was a semi-empirical formula carefully calibrated to match the experimental data available. It has ever been widely used in electron scattering experiments for modeling the background pion contributions.

The Geant4 simulation, the Wiser parameterization model, and the ROOT pack-

age will all be used in the framework of this thesis to improve the design and optimization of the pion detector system in chapter 4. Before exploring the details of the pion detector system in chapter 4, which is the main focus of this research, the next section will discuss the MOLLER experiment facilities and apparatus and show the role of the pion detector system.

Chapter 3

The MOLLER Experiment: Facility and Apparatus

An overview of the MOLLER subsystems and their operational requirements is provided in this chapter. The functional specifications define the performance and functionality required to fulfill the MOLLER science objectives that are outlined in Section 1.2. The goal of the experiment is to measure a very small parity-violating asymmetry which requires measurement of the scattered electron flux at high rate and attention to the statistical errors. The components of the MOLLER apparatus are arranged as follows:

1. **Liquid Hydrogen Target** utilizes cryogenic liquid hydrogen as the primary target for the MOLLER device.

2. **Spectrometer** consists of two seven-fold symmetry toroidal magnets and collimators designed to maximize the signal-to-background ratio and define experimental acceptance.

3. **Integrating Detectors** comprises a set of quartz Cherenkov detectors, which function as the primary detector elements for conducting high-rate, high-statistics measurements in the experiment.

4. **Tracking Detectors** operates in a low-rate counting mode to calibrate the

primary detectors, spectrometer optics, and background processes across the full radial and azimuthal ranges.

5. **Auxiliary Detectors** includes additional shower-max detectors for redundancy, pion detectors for background asymmetry monitoring, beam scattering monitors for detecting false asymmetries, and scanner detectors for precision alignment verification and background differentiation in asymmetry measurements.

6. **DAQ and Trigger** integrates beam diagnostic monitors and facilitates data acquisition readout in both high-rate (integrating) and low-rate (counting) modes.

Figures 3.1 and 3.2 show the MOLLER apparatus that will be installed in Hall A at Jefferson Lab (JLab). This section provides a brief explanation of each subsystem's design, along with the functional requirements necessary to achieve the performance and functionality needed to meet the MOLLER science goals, as detailed in Section 1.2.

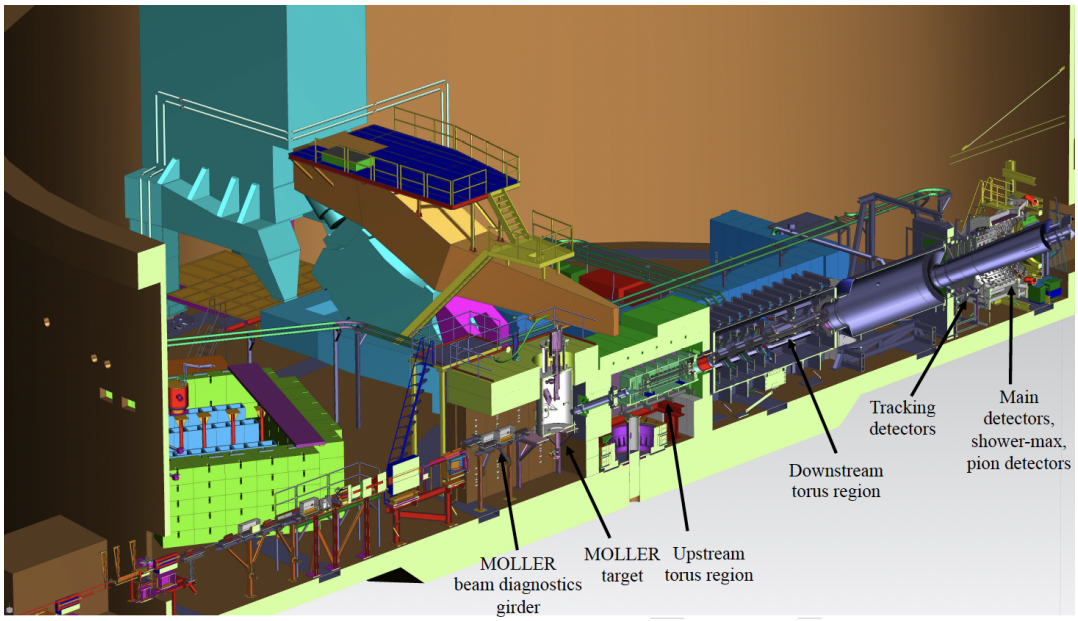

Figure 3.1: A cutaway picture of the MOLLER experimental setup in Hall A with some shielding removed. The beam direction is from left to right [74].

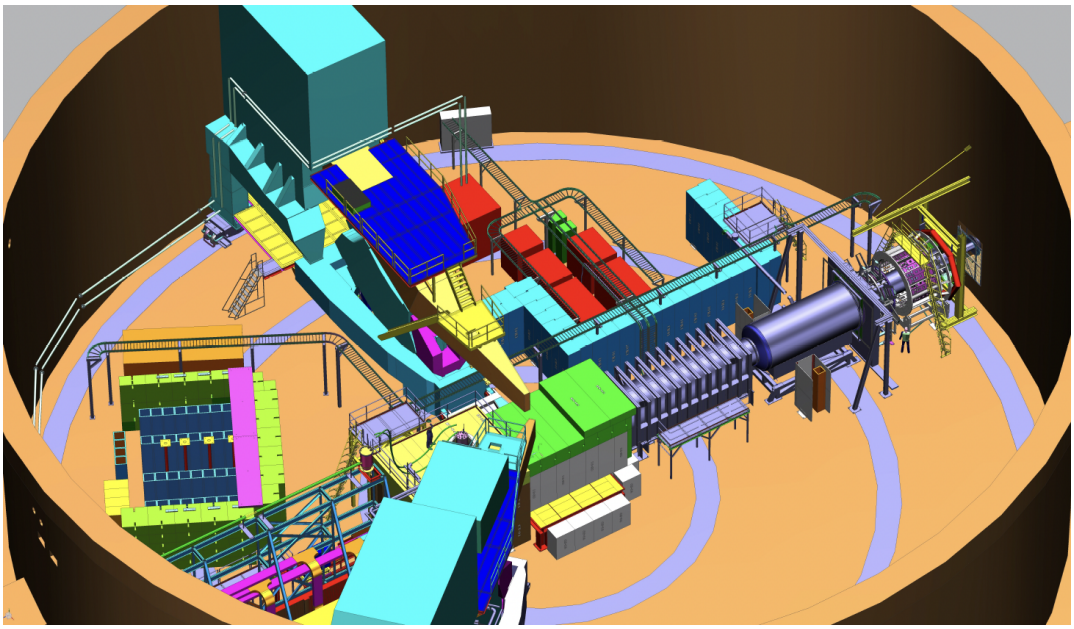

Figure 3.2: An overview of the shielding enclosures for the MOLLER experimental apparatus in Hall A. The beam direction is from left to right [74].

The coordinate system in use in Hall A is right-handed, with the positive Z axis running parallel to the electron beam axis, the Y axis pointing vertically up, and the positive X axis positioned beam left when looking at the detector system. The origin of the experimental coordinate system is located at the hall center. The MOLLER hydrogen target's center is about 0.450 m upstream at (0,0,-0.450).

3.1 Polarized Beam, Monitoring, and Control

The MOLLER experiment requires up to 70 μA of an 11 GeV electron beam, which is 90% polarized and aligned in the longitudinal direction. By employing photoemission from circularly polarized laser light that hits a doped gallium arsenide photocathode, the polarized electron beam is produced [75]. Time windows are created within the electron bunch train at a frequency of 1.92 kHz, with the beam's longitudinal polarization in each window assigned pseudo-randomly following a predetermined 32-window-pair pattern optimized to suppress 60 Hz noise. Window pairs are formed by adjacent time windows with opposite helicities. The time-averaged responses of

beam position monitors are used to determine the beam trajectory and energy for each window. For a range of nuclear physics research with different requirements on beam characteristics, the Continuous Electron Beam Accelerator Facility (CEBAF) at JLab typically runs with $> 100\mu A$ electron beam currents and $> 85\%$ beam polarization in four experimental halls [76]. Even though the specific requirements for the electron beam for MOLLER are similar to those of earlier parity-violation measurements carried out at JLab, the increased experimental precision goal leads to more demanding allowances for the stability of the beam under rapid helicity reversal and control of the beam polarization. The technology used at JLab to meet these needs is explained below.

3.1.1 Polarized electron source at CEBAF

As described previously and shown in Figure 3.3, the polarized electron beam is generated through the photoemission of electrons induced by circularly polarized light interacting with a doped gallium arsenide (GaAs) photocathode (Clayburn et al., 2013). The electron beam's polarization is determined by the polarization of the incident laser light. Light from the 780-850 nm laser is linearly polarized and then passes through the RTP Pockels cell. The Pockels cell receives a randomized helicity signal and converts the linearly polarized light into circularly polarized light of opposite helicities based on the sign of the input signal state. The generated circularly polarized light then interacts with the GaAs photocathode, where the symmetric response of the photocathode to the circularly polarized light ensures that the electron beam's transmission through the accelerator and into Hall A is unaffected by the polarization of the electrons. The voltage delivered to the Pockels cell is crucial, as it must be precisely controlled to correlate directly with any helicity-related asymmetry observed in the electron beam. A precision asymmetry measurement requires a strong and quick polarization reversal, which is only produced by the Pockels cell, even if photocathode technology is an important part of creating the polarized electron beam. The Pockels cell has been upgraded from a KD*P (potassium di-deuterium phosphate) cell to an RTP (rubidium titanyl phosphate) Pockels cell at JLab, enabling the fast

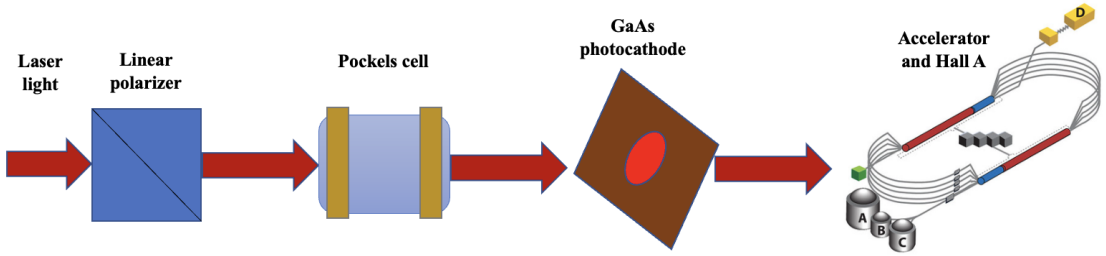

Figure 3.3: Diagram of the laser transport line that enables rapid electron beam polarization reversal, modified from [74].

flip rates needed for MOLLER [77]. Also, a more stable source configuration will be possible because the stronger electric field has been demonstrated to increase the activated photocathode's lifetime [78]. MOLLER experiment will benefit from these source enhancements [79] as well as other improvements [80].

3.1.2 MOLLER Beam Requirements

The MOLLER experiment represents the continuation of a series of high-precision parity-violation experiments that typically operate at small scattering angles and measure very small asymmetries. These investigations' challenges are variations in the beam's intensity, position, or profile, which will change the scattered flux that is being detected. The final result reflects small parity-violating asymmetries if the variations in the beam have a correlation to the electron helicity. Despite the fact that changes are frequently measured and corrected, there is a finite precision associated with these corrections, which could be a potential source for a false asymmetry or systematic error. Therefore, helicity-correlated beam asymmetries (HCBA) form a potential systematic error, and extremely strict HCBA control is necessary for the precise measurement that is under consideration. Table 3.1 displays the beam performance requirements for MOLLER to accomplish its scientific objectives. Table 3.2 compares the conditions for HCBA during MOLLER with those found in earlier studies. The HAPPEX [12], Qweak [16], PREX-II [18], and CREX [19] experiments are a few examples of earlier parity studies. The MOLLER goals are expected to be achievable given the plans for the new Pockels cell, among other crucial factors and technological

advancements.

Table 3.1: Performance objectives for MOLLER's parity quality beams [74].

Beam Property	Defining Equation	Required 960Hz pair random fluctuations	Cumulative Helicity Correlation (full dataset)
Intensity	$A_q \equiv \frac{I_0 - I_1}{I_0 + I_1}$	< 1000 ppm	< 10 ppb
Energy	$A_E \equiv \frac{E_0 - E_1}{E_0 + E_1} = \frac{\Delta E}{2E}$	< 110 ppm	< 1.4 ppb
Position	$D_x = \Delta x \equiv x_0 - x_1$	< 50 μm	< 0.6 nm
Angle	$\Delta\theta \equiv \theta_0 - \theta_1$	< 10 μrad	< 0.12 nrad
Spot-size	$\Delta\sigma/\sigma \equiv \frac{\sigma_0 - \sigma_1}{\frac{1}{2}(\sigma_0 + \sigma_1)}$	-	$< 10^{-5}$

Table 3.2: Comparison of MOLLER beam asymmetry requirements with the approximate average magnitudes of asymmetries achieved in previous experiments [74].

	HAPPEX-2 (achieved)	Q_{weak} (achieved)	PREX-II (achieved)	CREX (achieved)	MOLLER (required)
Intensity asymmetry	400 ppb	30 ppb	25 ppb	-88 ppb	< 10 ppb
Energy asymmetry	0.1 ppb	0.4 ppb	0.8 ± 1 ppb	0.1 ± 1.0 ppb	< 1.4 ppb
Position differences	1.7 nm	4.4 nm	2.2 ± 4 nm	-5.2 ± 3.6 nm	< 0.6 nm
Angle differences	0.2 nrad	0.1 nrad	$< 0.6 \pm 0.6$ nrad	-0.26 ± 0.16 nrad	< 0.12 nrad
size asymmetry (quoted)	-	$< 10^{-4}$	$< 3 \times 10^{-5}$	$< 3 \times 10^{-5}$	$< 10^{-5}$

3.2 Target System

Using a liquid hydrogen (LH_2) target will enable the necessary rate of Møller scattered electrons to be produced. The ideal target is LH_2 because it provides a substantial areal density (mass per unit area) of electrons for the minimum radiation length, essential for effective interactions with incident particles. LH_2 concentrations greater than 8.5 g/cm^2, representing this areal density, are required to reach the

necessary scattering rate. The target will, therefore, be 125 cm long and require a cryogenic system with a handling capability of 4.0 kW to maintain the system at low temperatures and remove heat. The LH_2 target will be the most powerful ever constructed. The suppression of density fluctuations at the timescale of the helicity flip rate is a critical design aspect from a physics perspective. Target density variation must be less than 30 ppm at 0.96 kHz to avoid variation in the number of scattered events. The target system's design is grouped into six subsystems: vacuum system, hydrogen gas service system, cryogenic helium service, target loop, motion system, and control system.

Figure 3.4 displays the vacuum, cryostat, and motion systems. A system of vac-

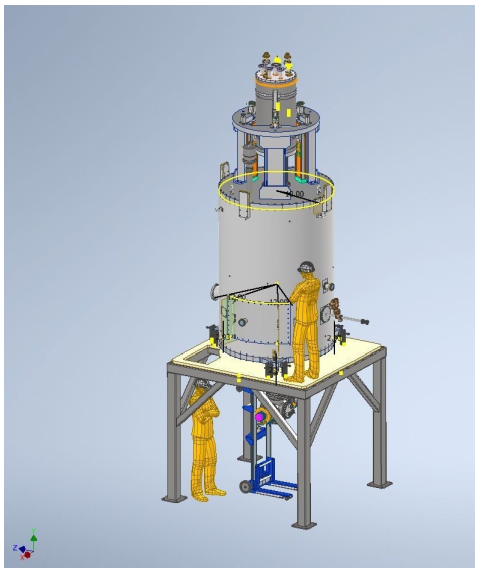

Figure 3.4: Cryostat, motion, and target vacuum systems. The scale model is a 6-foot-tall person [74].

uum pumps installed under the chamber maintains the target chamber's vacuum. The chamber has a platform that supports it on the beamline in Hall A. The cryogenic target loop is located inside the target vacuum chamber. The liquid hydrogen pump, the high-power heater, the Helium-hydrogen counterflow heat exchanger, and the cell are the major elements of the target loop. Most of the target loop's components are located on top of the target chamber outside the vacuum space, and the target loop is held inside the target chamber by a vertical motion mechanism. Helium and

hydrogen gases are supplied to the target loop through separate closed gas circuits. Instrumentation is installed on the target system to track it. Both hardware and software tools are used to control the target.

A solid target ladder will be thermally coupled to the LH_2 target cell's bottom to satisfy the requirements for beam alignment, backgrounds, and optical studies for the MOLLER apparatus. A vertical lifter will supply a single-axis motion mechanism during beam operations to place each necessary target on the beam line. The vertical lifter will also provide a "no target in beam" setting for accelerator beam studies.

3.3 Spectrometer System

The acceptance of the experiment is determined by the spectrometer system, which is optimized to maximize the signal-to-background ratio. It consists of two toroidal magnet assemblies with seven-fold symmetry and a series of collimators, as shown in Figure 3.5. Four collimators are positioned between the upstream and downstream torus magnets: 1, 2, 4, and 5. Note that collimator 3 is not present; it has been removed. These collimators ensure that only the scattering angles and azimuthal angles that pass through collimator 2 are considered without variation from other openings during the experiments. Upstream of collimator 1, there are also two septant blockers, numbers 6 and 7. Additionally, some lead lintels are spaced farther apart in radius and located at the same z-axis position as collimator 5. The magnets provide the kinematic separation of the scattered electrons and distribute them across the focal plane, which is crucial for determining the Møller asymmetry accurately. Moving from the structural setup to the functional dynamics of the spectrometer, the focus shifts to how its open design contributes to experimental efficacy.

3.3.1 Concept of the Open Spectrometer

The MOLLER spectrometer is an open type, which means it is not focused on high resolution but on moving electrons away from the beamline. This design helps to separate the electrons based on the different processes they undergo in the tar-

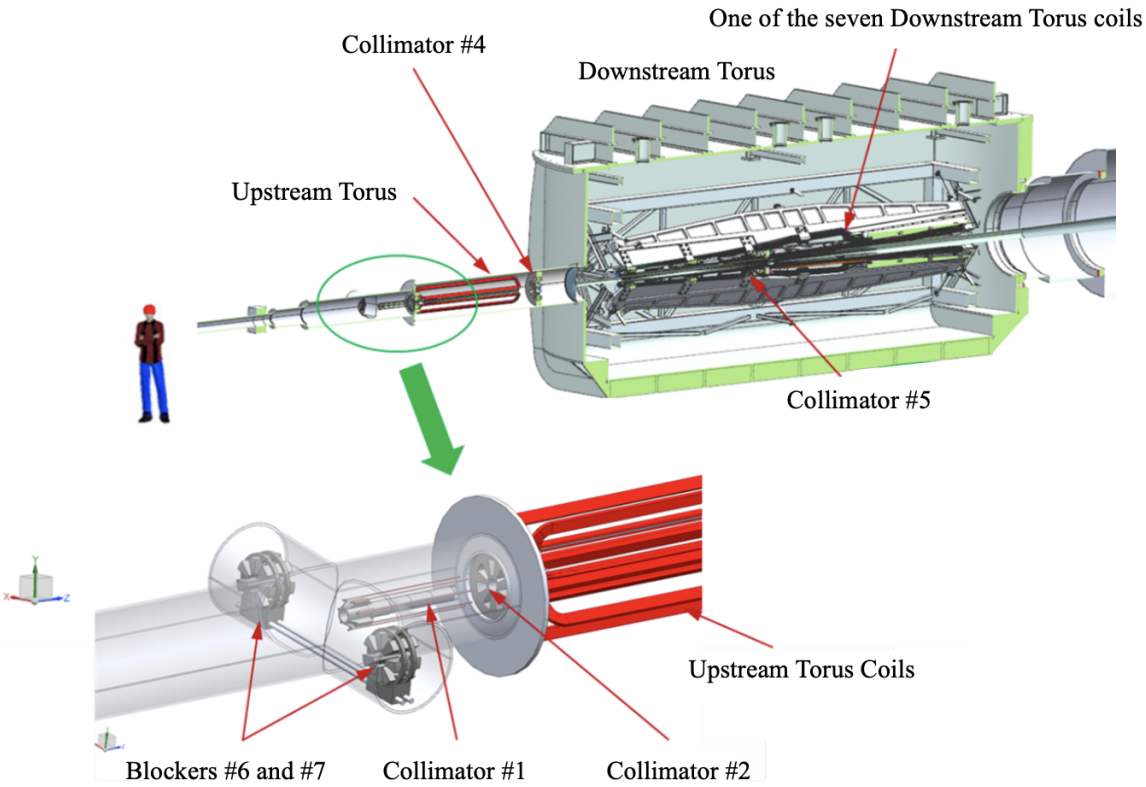

Figure 3.5: Locations of collimators in relation to the toroids upstream and downstream [74].

get, allowing for the identification of Møller electrons specifically. Møller scattering involves identical particles. Thus, the spectrometer can capture a full range of azimuthal angles even if part of the azimuth is blocked, as seen in Figure 3.6. Each forward-scattered electron on one side of the beamline corresponds to a backward-scattered electron on the opposite side in the laboratory frame. This configuration ensures that all forward and backward scattered electrons on one side of the beamline are captured, uniformly covering angular ranges around 90° in the center of mass (COM) frame.

The lab scattering angles for MOLLER range from 6 to 21 mrad, corresponding to COM angles between 60° and 120°, as illustrated in Figure 3.7. This configuration allows for a large energy range for the scattered Møllers, from 2 to 8 GeV. The left two graphs in Figure 3.7 show a one-to-one correlation between COM and scattered electron energy.

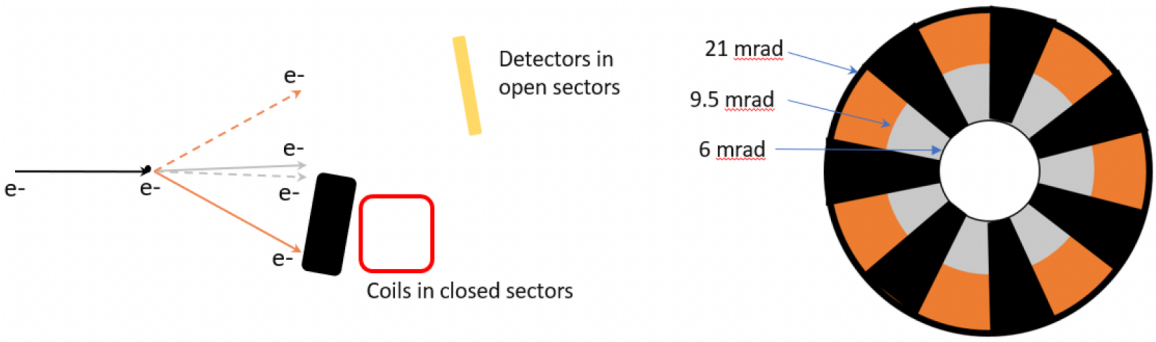

Figure 3.6: A scattering diagram on the left displays the scattered electrons from two scattering events. The electrons with dashed lines come from one event, and the straight lines belong to another. The closed sector, shown by the black trapezoids on the right, receives one electron from each event, and the open sector, represented by the grey and orange regions, receives the other electron from each event. Backward scattered electrons are indicated by the orange color, whereas forward scattered electrons are indicated by the grey color [74].

A deeper understanding can be gained by examining the primary acceptance collimator design depicted on the right of Figure 3.7 and comparing it with the design in Figure 3.6. Both figures illustrate the segmented approach to capturing scattered electrons. In Figure 3.6, the diagram highlights how different sectors (both open and closed) are strategically used to capture electrons from two scattering events, illustrating the physical layout of the acceptance collimator. Conversely, Figure 3.7 provides a view of how the spectrometer aligns with theoretical predictions of electron scattering angles and energies, ensuring that the device optimally separates forward from backward scattering within the specified energy and angular ranges.

Having established how the spectrometer's design optimally guides electrons through its acceptance collimators, the next focus is on observing outcomes on the detector plane. The precise engineering of the spectrometer not only enhances the capture and separation of scattered electrons but also significantly influences their distribution as they reach the detector plane. The following section will explore how the varying energies and angles of scattered electrons manifest in distinct spatial patterns on the detector plane, ultimately assisting in the deconvolution of the Møller asymmetry from background processes.

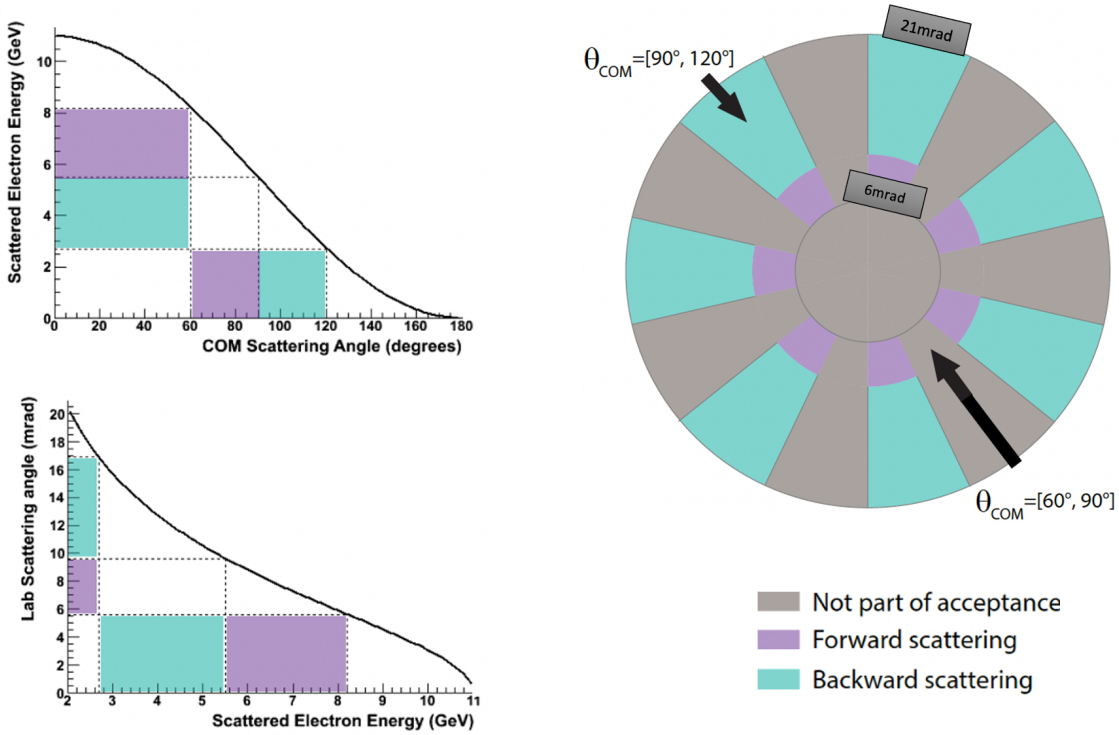

Figure 3.7: For $E_{beam} = 11GeV$, the two figures on the left show the correlation between the lab and COM angles. The ranges of each quantity for the forward and backward scattered electrons are shown by the colored bands in the θ_{COM} *vs.* E'_{lab} and E'_{lab} *vs.* θ_{lab} plots. The corresponding design for the primary acceptance collimator is shown on the right [35].

3.3.2 Distribution on the Detector Plane

The distribution of various particle envelopes at the detector plane provides the deconvolution of the Møller asymmetry. The collimators define angular acceptance, and due to distinct energy-angle correlations among various processes, these result in peaks appearing at separate radial distances following their kinetic separation by the magnets. Additionally, the magnets influence the azimuthal particle distribution. Electrons that travel downstream through the inner segments of the coils experience azimuthal focusing. They become azimuthally defocused if they go through the space between the coils' outer legs. When the lower-energy Møllers are defocused until the azimuth is filled, the rate density on the detector plane is decreased. The particle distributions are illustrated in a single septant and across different radial ranges at

the detector plane in Figure 3.8. The figure also shows the detector array concept (see Section 3.4). The deconvolution of the asymmetries from the various background processes is made possible by the segmentation of the detector array, which enables varying ratios of Møllers to backgrounds in each of the detectors.

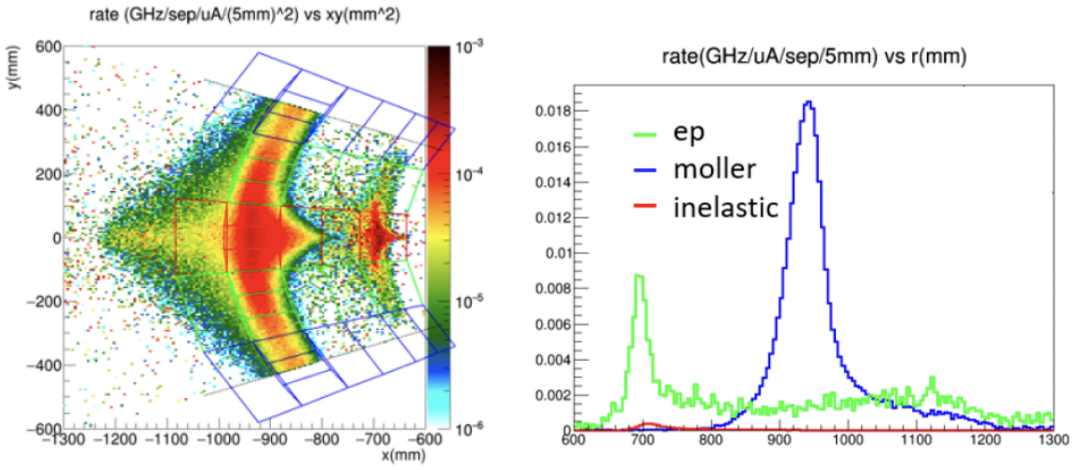

Figure 3.8: Left: Two-dimensional rate-weighted particle distributions within a single septant. The beam center ($x = 0, y = 0$) is offset to the right of the plot. The lines represent the quartz pieces in the detector array design, with open (red), closed (blue), and transition (green) sectors denoting the quartz regions entirely within open or closed sectors or partially spanning both. Particle distributions peak in ring 2 (ep particles) and ring 5 (Møller particles) from the center. Møller electrons are distributed across the full azimuth, extending into adjacent septants. Right: Radial rate-weighted distributions of Møller (blue), ep (green), and inelastic (red) particles at the detector plane, showing their respective contributions to the overall rate [74].

3.4 Detector System

In the MOLLER experiment, a sophisticated detection system is utilized, as shown in Figure 3.9. This system is designed to deliver high-precision measurements of the scattered electron flux and comprises the main detector system, a tracking detector system, and auxiliary detector systems.

In conducting such a precision experiment, the integration mode is predominantly utilized, where signals are integrated over helicity time window to measure the scattered electrons at a high rate in the order of MHz. The main integrating detector is

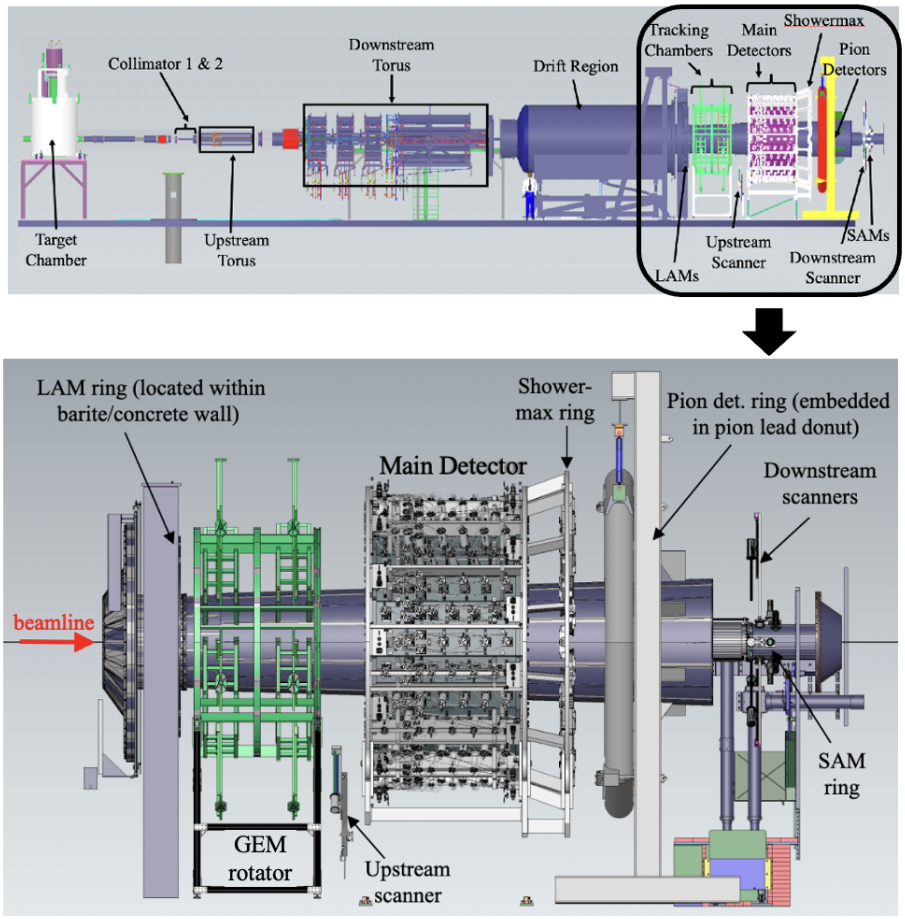

Figure 3.9: CAD layout of the MOLLER experiment apparatus highlighting the detector system [74].

optimized to integrate the incident signal rather than track individual electrons, as the high event rate makes implementing a finely granulated detector system for event-by-event detection expensive. The measured asymmetry value requires corrections before it can be interpreted as a measure of parity violation in Møller scattering. These corrections account for background effects from other scattering processes, specifically accommodating dilution factors and asymmetries, which are obtained using low beam current in the counting mode. These measurements are performed using both tracking and auxiliary detectors.

Tracking detectors calibrate the main detectors and the spectrometer optics using Gas Electron Multiplier (GEM) detectors and trigger scintillators. The shower-max

detector and the pion detector serve as auxiliary detectors, aiding in studying neutral and low-energy backgrounds and determining background fractions. Additionally, scattered beam monitors and scanner detectors, which are auxiliary detectors, are utilized to monitor the flux of scattered particles. The subsequent sections will thoroughly discuss each of these detector systems.

3.4.1 Main Integrating Detectors

The main detector is the center of focus in the MOLLER detector system. Instead of counting individual electrons as is usually done, this detector integrates the incident signal. A quartz Cherenkov detector is connected to a light guide in each main detector element. A PMT will then detect the Cherenkov light once it has been transported.

Six concentric rings are formed by radial segmentation around the beamline [74]. Five are divided into 28 detector elements around the azimuth, and the Møller ring (ring 5) is divided into 84 detector elements. Each ring's azimuthal segmentation is categorized as open, transition, and closed sectors, shown as different colors (red, green, and blue, respectively) in Figure 3.8 in Section 3.3.2. The open sectors are positioned along the mid-planes of the open acceptance semi-septants, while the closed sectors are situated along the mid-planes of the closed semi-septants. The transition sectors are located between these two areas. Consequently, each ring contains 28 segments. Specifically, ring 5 is further subdivided by a factor of three, resulting in 21 open sector modules, 21 closed sector modules, and 42 transition modules. In contrast, the remaining rings each consist of 7 open modules, 7 closed modules, and 14 transition modules.

The CAD model for the main detector system is shown in Figure 3.10. The purpose of dividing the main detector system into radial and azimuthal segments is to measure the Møller distribution and evaluate the contributions from elastic and inelastic scattering. As mentioned earlier in this section, to achieve the goal of precision in measuring the small Møller asymmetry in ring 5, a significant number of statistical data is needed, which implies extremely high event rates in the detectors. While

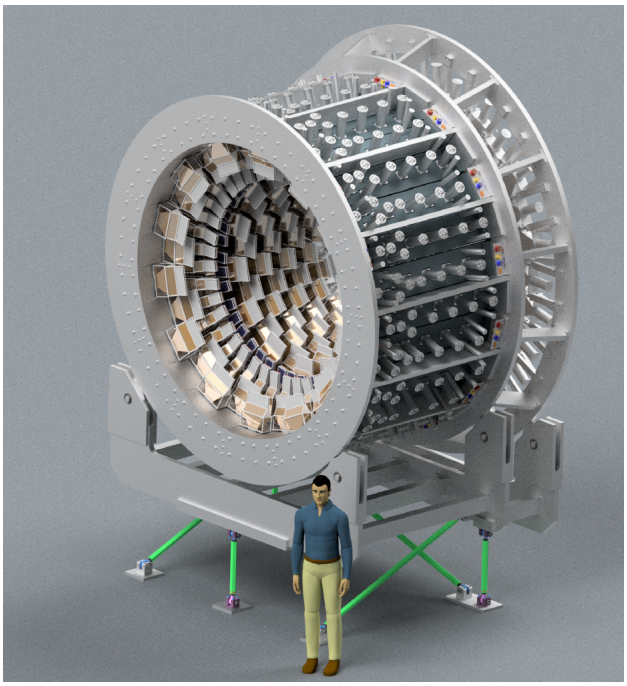

Figure 3.10: CAD representation of the full main integrating detector array, which includes 224 thin quartz detectors (shown in the front barrel) and the shower max detectors (depicted in the back barrel flare) [74]. The latter is thoroughly explained in Section 3.4.3.1.

the average electron rate for all detectors is approximately 50 kHz/mm^2, the peak electron rate for the Møller ring can reach 1 MHz/mm^2 in regions of the integrating detectors [74]. This calls for the integration of a large number of overlapping pulses. These considerations led the MOLLER experiment to select Cherenkov detectors that are radiation-resistant, highly linear, and have a comparatively large active area (approximately 100 cm^2). The most active detector sectors operate at average rates ranging from one to several GHz. As a result of these high rates, it is impossible to count individual pulses. Hence, integration mode operation is required. A continuous current is produced at the photo-cathode in this mode as a result of complete individual pulse overlap. In contrast to pulse mode, this mode is sometimes called current mode detection. Although the main detectors are primarily designed to operate in integration mode, they also operate in the standard event-counting mode for tracking and diagnostic needs. In this mode, tracking chambers are located immediately

upstream, and calibration tests with low beam current can be carried out to confirm the detector's alignment, acceptance, and response functions.

Understanding the segmentation and location of the main detector is essential to understanding the functionality of the subsequent detectors in the system. As the most important part of the system, the main detector is designed with specific segmentation that is compatible with other detectors and the spectrometer system. In Figure 3.11, the segmentation and z positioning are shown, with the left side showing the segmentation and the right showing the z positioning. Six radial areas, known as rings, and 28 azimuthal segments make up the active area of the main detector. Eight detector modules are housed in each segment, although three are found in ring 5. On the right plot of Figure 3.11, the position and orientation of the detector modules with respect to the segment plates and the direction of the beam are depicted. To

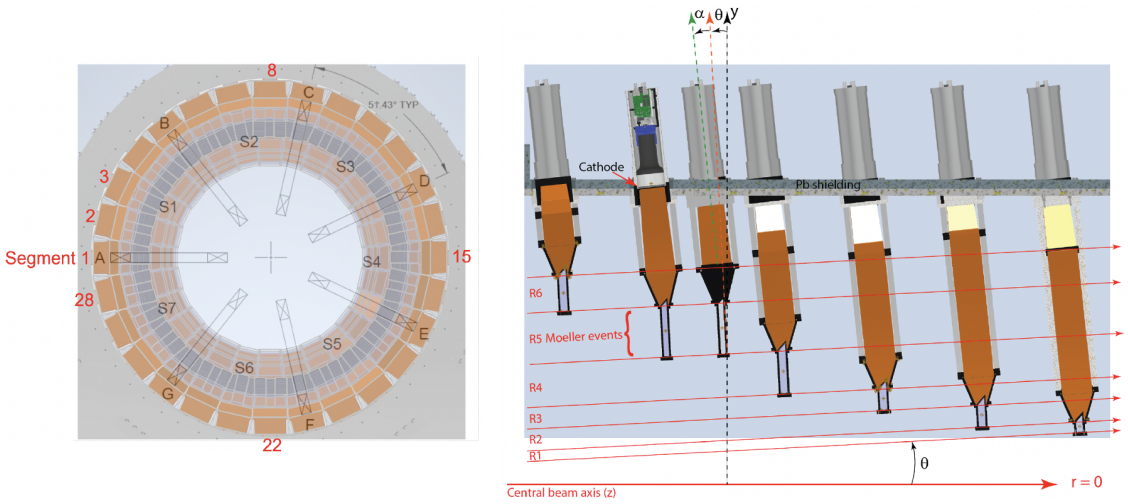

Figure 3.11: Left: Frontal view of the main detector array, with the beam directed toward the page. It comprises 28 azimuthal segments, marked in red and numbered 1 (to the left of the beam) through 28 (to the right of the beam). The septant zones are denoted by the numbers S1 through S7, and the spectrometer coils are labeled from A to G. Segment 1 aligns with spectrometer coil A and the initial segments of the other detectors. Right: The front-aligned segment plate configuration of the detector modules. The length of each module is adjusted to the placement of the sector, which covers the designated radial region of the scattered profile, and the position of the PMTs [74].

align the front sector orthogonal to the mean momentum direction of the scattered

electron profile in the detector plane, the quartz sectors are tilted at an angle of 3° with respect to the vertical (y) axis. Due to an additional tilt of the light guides, which are inclined at an angle of 3° relative to the quartz, the entire module is rotated by 6° with respect to the vertical axis. The light guides are rotated more than the quartz sector, a strategic adjustment designed to reduce the background amplitude from tracks passing through the light guides.

3.4.2 Tracking Detectors

The MOLLER experiment requires a tracking system to ensure accurate measurements of the parity-violating Møller asymmetry and for diagnostic and calibration purposes. A total of 28 identical Gas Electron Multiplier (GEM) detectors form the MOLLER tracking system, which comprises four layers of GEM detectors in each of the seven sectors discussed in Section 3.4.1. The system is located upstream of the main integrating detectors and downstream of the drift region, as shown in Figure 3.9. There will be 14 identical scintillators in total, divided across two layers of plastic trigger counters in each sector. The trackers are placed on a GEM Rotator that enables the array to rotate around the azimuth for the measurements throughout the full azimuthal acceptance. The tracking system verifies the optical properties and acceptance of the spectrometer system, and the acceptance of the quartz detectors, and measures the position-dependent light-output response of the quartz detectors. Additionally, it studies the radial and azimuthal distributions of incident electrons and neutral and soft backgrounds in the integrating detectors. It also helps identify pion events with pion detectors, shower-max, and main detectors. The tracking system operates primarily in counting mode during dedicated low-beam-current runs, as opposed to the usual integrating method of asymmetry data collection.

3.4.2.1 GEM detectors

The MOLLER system requires extremely accurate mapping of particle pathways, even when dealing with many particles spread across a large region. The Gas Electron Multiplier (GEM) technology, created by F. Sauli [81] in 1997, offers a useful and

economical method. This method uses small holes etched onto a Kapton foil coated on both sides with copper and uses a gas-based amplification technique. Rapid signals are produced by this amplification, or avalanche, which is constrained inside these holes. To obtain high amplification and consistent performance, many GEM layers, or amplification stages, can be arranged in a series. The operations of a triple (three-foil) GEM chamber are shown in Figure 3.12. The result is a system with incredible resolution, as good as 70 μm, with the ability to handle extremely high particle rates of over 100 MHz per cm^2.

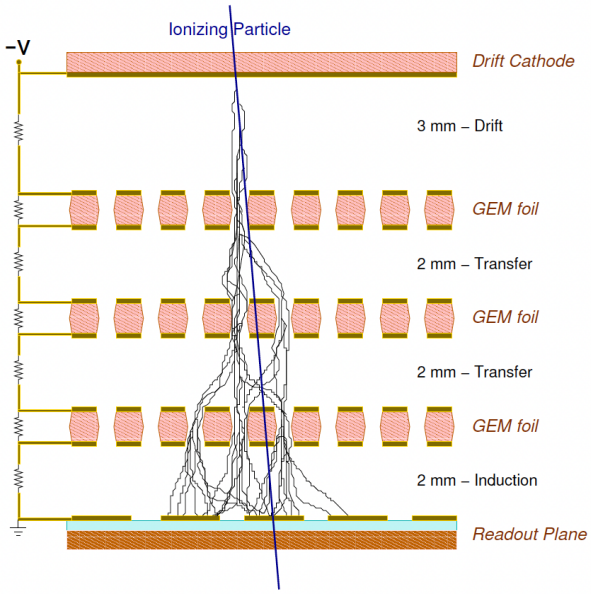

Figure 3.12: A triple GEM detector's operating mechanism [74].

The Geant4 simulation (Section 2.8) was used to determine the coverage area needed for each GEM detector or tracking wheel, defined by its location along the particle beam's path. This considers electrons that scatter inside the target due to Møller and electron-proton interactions and reach the quartz detectors. In the simulation, the electrons that arrive at a specific sector at the nominal location of the quartz detectors are selected, and their paths through each of the GEM layers are tracked backward. Determining the required sizes of different GEM layers is straightforward with backward tracking.

3.4.2.2 Trigger Scintillators

In order to ensure full coverage of GEMs, the MOLLER experiment has 14 plastic scintillator trigger counters that mimic the geometric layout of the GEM detectors. These scintillators are made of EJ-208, an Eljen Technology product chosen for its outstanding light output and absorption length. Regarding placement, the upstream scintillator is positioned upstream of the first GEM, while the downstream scintillator comes before the fourth GEM on the same frame. Although a time resolution of at least 2ns is preferred, the scintillators are not required to meet strict timing specifications due to the readout from the tracking GEMs, which employs a 25ns time binning. The requirement for a uniform detection efficiency for minimum ionizing particles at the 2% level over the GEMs active region is the scintillators' key performance characteristic. By achieving this level of uniformity, any trigger biases in the reconstruction of the track distribution at the main detectors and during the calibration of the spectrometer's optics are reduced. Above 98% is the desired overall efficiency in the active region.

3.4.3 Auxiliary Detectors

Additional detector systems are used to assess neutral, low-energy, and pion backgrounds inside the main detection region. These systems allow for quantifying the ratio, asymmetry, and optical response of charged pions in integrating detectors. They also evaluate the spectrometer's operation and provide sensitivity for identifying unexpected background sources. Figure 3.9 shows that auxiliary systems consist of the shower-max detector ring, pion detector ring, beam scattering monitors, and scanner detectors. The ultimate goal of each system's design and operation is to reduce systematic error in the core integrating detector ring 5 asymmetry measurement.

The shower-max and pion detector rings are situated to intercept the maximum Møller scattered flux after it has passed through the ring 5 detectors. To capture the scattered flux at the outer edge of the collimated primary flux envelope, the Large Angle Monitor (LAM) is positioned upstream of the GEM rotator. The Small Angle Monitor (SAM), located symmetrically around the beamline next to the Hall

A beam dump entrance, is set up to track the flux scattered from the target at very small angles (about 0.1°). A small upstream (US) 2-D scanner and four downstream (DS) linear scanners are also installed upstream of the SAM and the main detector. The primary function of the DS scanner is to validate the spectrometer's baseline optics, including the placement, angular alignment, and functionality of the magnet coils and collimator systems. The purpose of the US scanner is to map out the event distribution that affects the main detector array in two dimensions during the integrating mode.

3.4.3.1 Shower-max

The shower-max detector is a group of quartz-tungsten electromagnetic sampling calorimeters designed to measure energy. It is farther away from the thin quartz detector array and encounters the same particle flux as the central Møller ring 5. With lower sensitivity to hadronic and low-energy charged backgrounds, it provides an additional, energy-weighted measurement of the Møller signal. The azimuthal segmentation in these thick quartz detectors is lower than in thin quartz detectors because of the lateral dispersion of the showers. Each segmented section requires an energy resolution of at least 25% when interacting with electrons between 3 and 8 GeV to avoid significant statistical accuracy loss; this requires at least four tungsten and quartz layers that alternate to reduce sampling variances. The shower-max detectors, like the main detectors, have two operational modes: integrating mode and counting mode.

As discussed in Section 3.4.1 and shown in Figure 3.10, the main detector barrel structure's downstream end incorporates the shower-max ring support structure. It is centred on the beamline and has a z-location roughly 1.7 m downstream of ring 5. Full azimuthal coverage is provided by the 28 separate shower-max detectors instrumented around the ring, shown on the left plot in Figure 3.13. Each shower-max module covers the acceptance of three neighboring ring 5 modules in either an open, closed, or transition semi-sextant zone, shown on the left plot in Figure 3.13. However, the azimuthal segmentation of the shower-max ring is reduced by three

times compared to ring 5. The design and material construction is the same for each of the 28 detector modules. Each module comprises alternating layers of quartz and tungsten, which together create the "stack" structure. As the electromagnetic shower grows, a greater proportion of its charged, relativistic particles travel through the progressively thicker layers of quartz and produce Cherenkov light. The resulting Cherenkov light cone is efficiently directed into the light guide volume by the quartz layers using total internal reflection. Most of the light is directed to the PMT by the light guide in a single reflection.

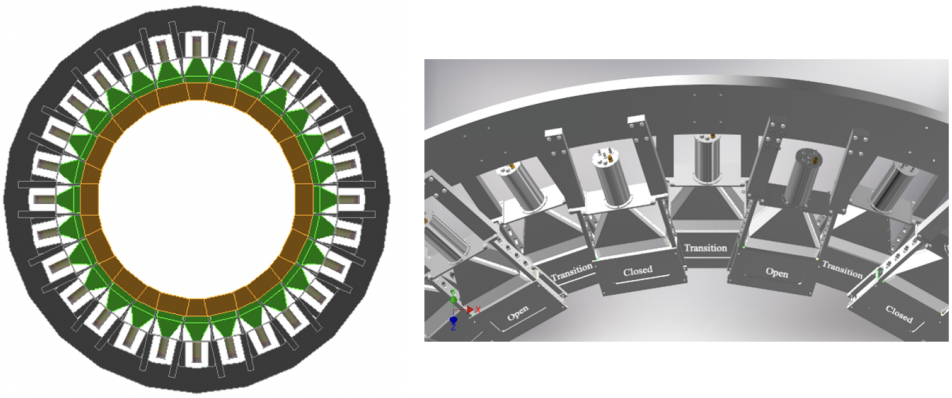

Figure 3.13: Left: Geant4 simulation model for the shower-max detector ring with support framing, left-side view. Right: The shower-Max ring structure in CAD. A view of the shower-max ring from downstream, showing the modules' attachment to the ring and aluminum support components. The open and closed Semi-Septant detectors are located upstream of the transition detectors. To avoid gaps, adjacent detectors have a small triangular region of overlap.[74].

3.4.3.2 Pion Detector

Near the Møller peak, there is a potential for a small contamination of approximately 0.1% from pions and other charged hadrons. This contamination, originating from processes with a very small cross-section but a very high analyzing power, could cause a significant background asymmetry. It is important to directly determine the dilution fraction and the asymmetry of this background. According to Geant4 simulations (Section 2.8) based on the Wiser parameterization for pion production [73], the pion-to-Møller scattered electron flux ratio for the main detectors will be around

10^{-3}. Any background asymmetry caused by these pions and their in-flight decay into muons must be identified and corrected. Assuming the simulation result is correct, the pion fraction equals 10^{-3} of the Møller electron flux, the MOLLER experiment aims to quantify the pion asymmetry with a statistical precision of 100 ppb over an estimated data collection duration of 50 days.

The pion detector system is made up of 28 matching acrylic Cherenkov detectors, situated downstream of the shower-max detectors and housed within a lead (Pb) absorbing donut, shown in the left plot of Figure 3.14 The system's design requires a

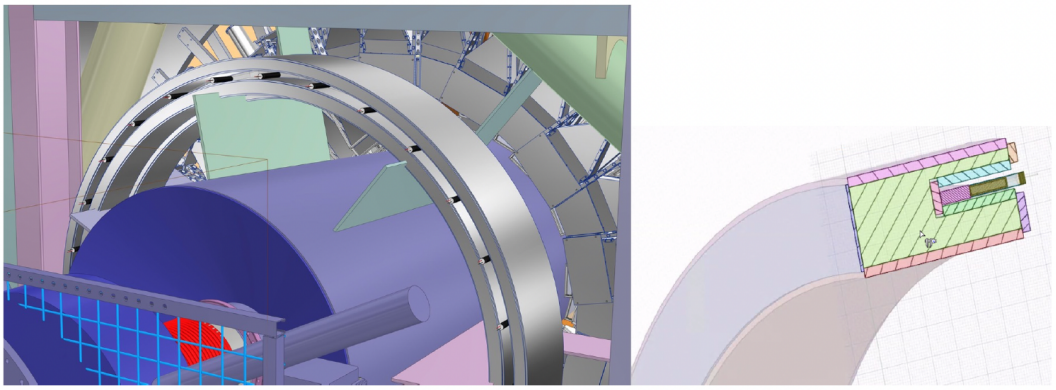

Figure 3.14: Left: The Pion Detector System integrated into the Pb (lead) Donut. Right: Section view of the Pb (lead) Donut.[74].

reduction in the impact of Møller electrons by more than a factor of 1000 while still capturing a substantial proportion of the incoming pions. This allows the detectors to measure the asymmetry in a sample that contains roughly equal amounts of pions and Møller electrons based on the predicted initial pion-to-electron ratio. The lead donut helps achieve this goal. In the initial design, Section 4.2, the lead donut and the pion detector system were distinct entities. However, these two components have been integrated into a unified system in the final design. The comprehensive documentation of the optimization steps and their implications can be found in chapter 4, which forms a core topic in this work.

The radial coverage of the pion detectors needs to adequately provide a sampling of the main detector ring 5 because measuring the pions interacting with the Møller ring is necessary. Due to the combination of small transverse beam polarization and

potential large single-spin asymmetries in pion production 2.5, there may be noticeable azimuthal variation in the measured pion asymmetries. The pion asymmetry must, therefore, be measured by this detector across the entire azimuth. It is possible to observe variations in pion asymmetry based on kinematics by dividing the pion detectors along the azimuthal direction. To distinguish the open, closed, and transition portions of ring 5's acceptance for each semi-septant, the pion detector system is segmented into 28 sections in azimuth. It is sufficient to measure the fraction of pion background in counting mode in one semi-septant of each type (open, closed, and transition), as no substantial fluctuation in the pion flow along the azimuthal direction is anticipated. The active volume of each detector is a rectangular shape of UV-Transparent (UVT) acrylic, see Section 4.1.1, read out optically by a PMT, see Section 4.1.2, which is attached to the center of the downstream side of the acrylic. For each pion detector, a light-tight enclosure, Figure 4.9, is constructed within an area on the downstream side of the lead donut.

3.4.3.3 Scattered Beam Monitors

Scattered Beam Monitors (SBM) are positioned at multiple points to detect any potential false asymmetries caused by irreducible background interactions from scattered beams interacting with collimators, beam pipes, and shielding. These include small and large-angle scattered beam monitors (SAM and LAM), also known as luminosity monitors, positioned where the scattering rates are likely equal to or greater than those observed in the main Møller rate. Unlike the Møller rate, the expected asymmetry is smaller. The detectors will be equipped with quartz Cherenkov detectors and air-core aluminum light guides that channel the light to PMT. Diffuse scattered beam monitors (DBM) are placed where secondary interactions from the primary target are expected to produce scattered rates. These detectors consist of PMTs connected directly to quartz Cherenkov detectors.

3.4.3.4 Scanner Detectors

Small, adjustable detectors capable of operating in both integrating and event modes for tracking measurements will be utilized at two different points in the experiment. The upstream scanner, positioned between the GEM detector array and the main detector array as seen in Figure 3.9, comprises two tiny, closely spaced fused-silica radiators that are coupled to air light guides and read out by a PMT. To remove background events that produce Cherenkov and scintillation light in the air, the tube enclosing the air light guide will be evacuated using a roughing pump during the scanner's operation.

The downstream scanners, positioned between the SAM and pion detectors as seen in Figure 3.9, differ from the upstream scanning detectors only in the size of the air light guide. These detectors, which will be read out only in the integrating mode, consist of four radially scanning linear scanners placed in exposed areas. Their purpose is to verify the beam-based alignment of collimator 2 with 1-mm precision.

3.5 Data Acquisition, Trigger, and Analysis

The primary high beam-current integrating mode and the low beam-current counting mode are the two modes in which the trigger and data acquisition (DAQ) systems are designed to operate. When collecting high beam current data, the integrating mode DAQ system mainly works with integrating analog to digital converter (ADC) modules to take signals from detectors and beam monitors. This system synchronizes the integration periods of the main detectors, beam monitors, and auxiliary detectors using custom-built, low-noise ADC modules. The counting mode DAQ is used for measurements with a low beam current where individual electron scattering events can be observed. Combinations of the main detector components and scintillators placed close to the GEMs tracking detectors are used to construct triggers. The GEM, trigger scintillators, main quartz detectors, and auxiliary shower max, pion, and scanner detectors will all benefit from this system's accurate timing and pulse size records. The MOLLER experiment will use a significant amount of JLab's sci-

entific computer capabilities, but it will also rely on an additional analytic cluster to guarantee the required data analysis throughput. This is an essential element for keeping track of the setup's effectiveness. The DAQ, trigger, and analysis systems are required to conform to the following requirements:

1. The network and event-building systems must accommodate a data rate of roughly 130 MB/s during integration production operation. This guarantees a throughput of 100% without downtime when data is being collected in production integration mode.

2. The counting mode trigger must be able to make decisions based on input rates between 10 kHz and 300 kHz. The ability to produce triggers from the specific scintillator triggers or any combination of the quartz detector signals should be provided.

3. During production at 1.92 kHz, the feedback and real-time analyzers must run at almost 100% throughput without affecting the data acquisition dead time.

4. The concurrent processes that can run on the online analysis cluster should sufficiently analyze 100% of the data flow quickly. Correlation analysis and adjustments are part of this.

5. The local disc storage must have enough space to hold complete analysis output files for evaluation and several days' worth of raw data files ready to be staged to the mass storage system.

Chapter 4

Development of the Pion Detector System: From Principles to Practice

To correct the observed asymmetry in ring 5 and showermax for the background contribution from pions (3.4.3.2), it is crucial to determine the flux and asymmetry of pions (and their subsequent decay muons). This chapter details the pion detector system, which was specifically designed and developed over the course of my graduate research project. It begins with a comprehensive examination of the fundamental physics and processes essential for pion detection. I discuss the optimization strategies implemented in the simulation and then proceed to verify these strategies through both cosmic and beam testing. Building on the insights gained from these experiments, the chapter further details the selection of the Photomultiplier Tube (PMT). The conclusion provides a comprehensive overview of the mechanical design, highlighting the careful design considerations and engineering expertise that underpin the project. This emphasizes my direct involvement and contributions to each development phase.

4.1 Pion Detector System: Physics and Mechanisms

Particle detectors are essential tools in physics for identifying and characterizing particles [82]. One such detector is the pion detector used in the MOLLER experiment. Like many others, this detector operates based on two critical components: the active medium and the PMT. Subsection 4.1.1 explores the selection criteria for the active medium, focusing on the specific requirements and properties that make UV-transparent acrylic (Lucite) an ideal choice for the pion detector in the MOLLER experiment. Subsection 4.1.2 is dedicated to the PMTs, crucial components in the detection process. This part elaborates on the necessary characteristics and minimum requirements of PMTs, emphasizing their various parameters, such as spectral range, quantum efficiency, cathode, and anode currents.

4.1.1 Active Medium Selection Criteria

The active medium is crucial as it interacts with incoming particles, resulting in the emission of light. For the pion detector in the MOLLER experiment, a UV-transparent acrylic [83] known as Lucite is employed as the active medium. Lucite, technically referred to as Poly(methyl methacrylate) (PMMA), is a synthetic polymer derived from methyl methacrylate. This transparent thermoplastic is also known under various brand names, including Plexiglas, Crylux, Hesalite, Acrylite, and Perspex. Despite the low expected interaction rate of charged particles with the pion detectors, only about 0.1% of the rate for the ring 5 integrating detectors, the pion detectors are required to withstand a radiation dose of 0.2 MRad without significant performance degradation [74]. This requirement is much less than that for integrating detectors due to the filtration of electrons by the showermax detector and the lead donut. Historically, UV-transparent acrylics have been successfully used in past experiments such as HAPPEX-I [12] and HAPPEX-III [84] at JLab. Eljen UV-transparent acrylic (BC-800) [85] is particularly notable, maintaining over 50% optical transmission even after receiving a radiation dose of 5 MRad, which is 25 times the anticipated total

dose in MOLLER pion detector. The transmission curve in Figure 4.1 illustrates the optical transparency of Lucite as a function of wavelength for different thicknesses (2.54 cm, 7 cm, and 21 cm), based on measurements conducted at JLab. It demonstrates that even at substantial thicknesses, Lucite maintains high transmission above 300 nm, ensuring efficient detection of Cherenkov photons, which predominantly fall in the UV and visible spectrum. However, the 7 cm thickness is particularly important for the MOLLER pion detector design, as it represents the planned thickness of the active medium. This transmission range, combined with its radiation tolerance, establishes Lucite as a suitable choice for the active medium in the pion detector.

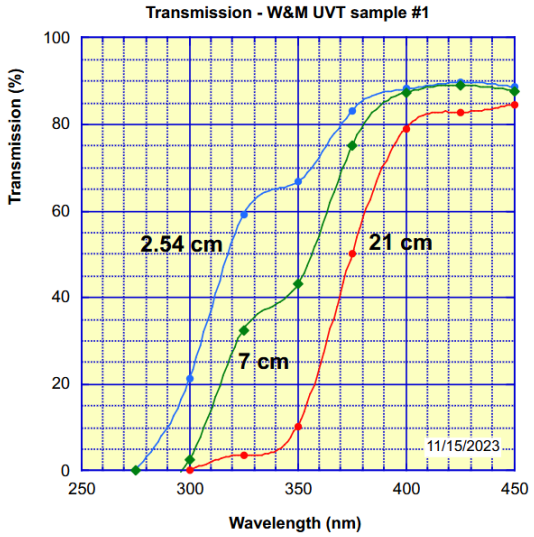

Figure 4.1: Transmission curves of UV-transparent acrylic (Lucite) samples of varying thicknesses (2.54 cm, 7 cm, and 21 cm), based on measurements conducted at JLab, showing optical transmission in the wavelength range relevant for Cherenkov radiation detection.

As discussed in Section 2.6.4, when charged particles traverse a material at velocities exceeding the speed of light in that medium, they emit Cherenkov radiation. There is a threshold kinetic energy beyond which Cherenkov radiation becomes possible. This threshold signifies the point where the particle's kinetic energy becomes sufficient to enable the emission of Cherenkov radiation. Given Lucite's refractive index of 1.5 and the pion mass ($m_\pi c^2$) of 139.570 MeV, the threshold kinetic energy for producing Cherenkov radiation is 48 MeV, as calculated using Equation 2.43. This

suggests that pions with kinetic energies above 48 MeV can generate Cherenkov radiation in Lucite. The Cherenkov angle (θ_c) in Lucite, derived from Equation 2.41, is approximately 48°. According to Equation 2.44, 817 Cherenkov photons are emitted when a single pion travels through one centimetre of Lucite. The total energy loss due to Cherenkov radiation over this distance can be estimated using Equation 2.45 by multiplying the number of Cherenkov photons by the average energy of each photon, 2.44 eV. This results in a total energy loss of approximately 0.002 MeV per centimetre, much lower than other energy loss mechanisms, such as ionization. As shown in Figure 4.1, the optical transmission of Lucite ensures that a significant portion of the emitted Cherenkov photons can be efficiently detected, further validating Lucite as an appropriate choice for the active medium in a pion detector due to its low energy loss and high photon generation efficiency.

4.1.2 Photomultiplier Tubes (PMTs) Selection Criteria

Following the light generation within the active medium, detecting and converting it into an electrical signal is crucial for further analysis. PMTs surpass other kinds of detectors in detecting photons emitted from phenomena such as Cherenkov radiation and processes like ionization and bremsstrahlung. These processes involve energy loss that often results in photon emission. PMTs are designed to convert these photons into electrical signals efficiently, enabling detailed analysis of underlying particle interactions.

When photons generated in the medium enter the PMT through a window, which is transparent to specific wavelengths, they strike the photocathode. This interaction results in the emission of photoelectrons due to the photoelectric effect, as shown in the schematic of Figure 4.2. These photoelectrons are then accelerated by an applied electric field, through a focusing electrode that guides them toward the electron multiplier section. This section consists of a series of dynodes, which are coated electrodes designed to amplify the signal by emitting multiple secondary electrons for each incoming electron. These secondary electrons are then accelerated to the next dynode, continuing the multiplication process until an avalanche of secondary

electrons is emitted from the last dynode. Finally, the electrons are collected by the anode at the end of the multiplier section, producing a current proportional to the intensity of the initial light signal.

The structural integrity of the PMT, along with its electrical connectivity to the outside circuitry, is maintained through the stem, which is a non-conductive glass or ceramic material that holds the internal elements in place. The stem pins, which are conductive elements extending from the stem, provide the necessary electrical connections from the internal components of the PMT, such as the dynodes and anode, to the external electronic circuitry. This connection ensures that the amplified electrical signal generated by the incident photons can be accurately transmitted and subsequently digitized and processed using specialized software. To optimize

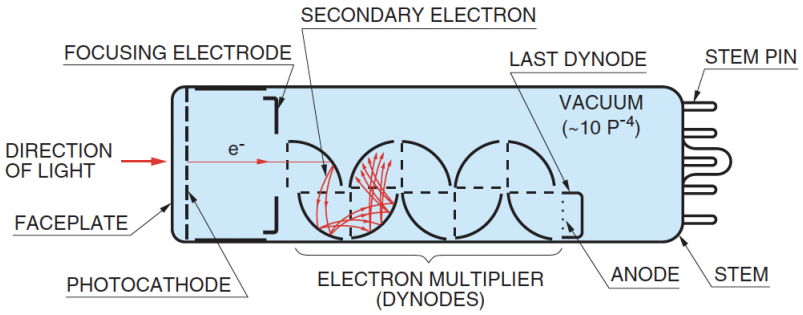

Figure 4.2: Construction of Photomultiplier Tubes [86].

the performance of the particle detectors, it is crucial to select PMTs that satisfy several key characteristics and minimum requirements. These include the spectral range, quantum efficiency, cathode current, anode current, linearity, PMT bases, dark current, time response, and lifetime. Each characteristic directly impacts the PMT's ability to detect and amplify the light signals into electrical signals accurately.

The remainder of this subsection details the necessary PMT characteristics and the rationale behind the selection of ET Enterprise 9125QB [58], with an overall size of 29 mm (1.13 inches) and an active diameter of 25 mm, as a suitable PMT for the pion detector of the MOLLER experiment. The PMT characteristics and minimum requirements are as follows:

Spectral Range: The spectral range defines the wavelengths that the PMT win-

dow can effectively transmit. For the pion detector, the optimal range is between 200 and 800 nm, which aligns with Lucite's transmission region, as shown in Figure 4.1. This ensures efficient transmission of light signals generated during experiments. The ET Enterprise 9125QB models, equipped with fused silica windows, further extend the spectral range to 160–630 nm, as illustrated in Figure 4.3. This extended range provides the necessary sensitivity and performance required for the experiment while maintaining compatibility with the detector's optical properties.

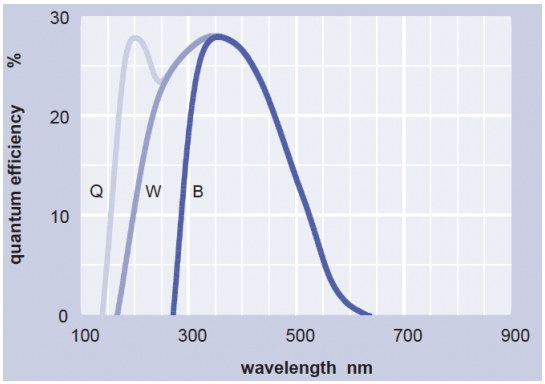

Figure 4.3: Quantum efficiency versus wavelength for different PMT window materials. "B" corresponds to borosilicate glass, "W" to UV glass, and "Q" to fused silica. The ET Enterprise 9125QB PMTs utilize fused silica windows, covering range of 160-630 nm, making them suitable for the pion detector in the MOLLER experiment. [58].

Quantum Efficiency: Quantum efficiency refers to the effectiveness of PMTs in converting incident photons into photoelectrons and is highly dependent on the wavelength, as shown in Figure 4.3. The ET Enterprise 9125QB model, equipped with fused silica window, achieves a maximum quantum efficiency of approximately 28%, which aligns well with the peak wavelength emission from the Lucite active volume. A quantum efficiency peaking at around 30% is ideal for enhancing photoelectron detection and facilitating high-precision measurements in high-energy physics applications, making this model well-suited for our requirements.

Cathode Current: The cathode current in PMTs is due to the rate of electrons emitted by the photocathode as a result of the photoelectric effect induced by photons hitting the PMT. This current is calculated by multiplying the number of

photoelectrons per event, the event rate, and the electron charge. In our application, derived from simulations, the event rate was determined using a beam current of $70\,\mu$A and a rate of $0.565 \times 10^{-4}\,$GHz/μA, resulting in an approximate event rate of 4 MHz. So, approximately 140 photoelectrons are generated per event. From these calculations, an expected cathode current of approximately 90 pA is obtained. The ET Enterprise 9125QB models, allowing a maximum cathode current of 50 nA, are found to be suitably equipped for the specific requirements of our application.

Anode Current: The anode current in PMTs is the current that flows at the anode due to the collection of photoelectrons. The average anode current can be calculated from the current-to-voltage (I-to-V) preamplifier gain and the PMT's operating conditions. Assuming that the Analog-to-Digital Converter (ADC) is equipped with a preamplifier gain of 1 MΩ and a dynamic range of $2\,V_{pp}$, an anode current of $2\,\mu A$ is required for optimal operation. Therefore, the ET Enterprise 9125QB, with an anode current capacity of $100\,\mu A$, is an appropriate choice for our application, ensuring the accurate transformation of photon signals into electrical signals for digital analysis.

Linearity: Linearity is important for ensuring the PMT's output signal is directly proportional to the incident light intensity, preventing signal distortion and providing accurate light intensity representation. This linearity is key to ensuring that the output current accurately reflects the amount of incident light, a fundamental requirement in precise measurement scenarios. The ET Enterprise 9125QB is known for its comparably good linearity, making it a suitable choice for such applications. However, further testing is required, and at the time of this thesis project, no specific plan had been established for this. **PMT Bases:** A B14B hardpin base with a C637A voltage divider [58] is the default one. The voltage divider configuration has a high-voltage input (T_1), requiring an SHV jack bulkhead mount connector [87] for connecting to the high voltage. Conversely, the signal output (T_4) necessitates a BNC female bulkhead mount connector [88] for connecting to a digitizer. However, the final prototyping phase of the pion detector of the MOLLER experiment employs PMT bases with switchable options between counting and integrating data-taking modes, as well as 12 dynode stages identical to those in the main detectors (Section 7.4 of [74]). This approach ensures compatibility and seamless integration with the

pion detector. However, as of the time of this thesis, a specialized switchable base design for the pion detector has yet to be developed. Transitioning from the 3-inch switchable base in the main detector to a 1-inch switchable base for the pion detector requires a new design. This design task, falling outside the scope of this project. The characteristics of the ET Enterprise 9125QB series are summarized in Table 4.1.

Table 4.1: Summary of ET Enterprise 9125QB Characteristics

Characteristic	**Unit**	**Minimum**	**Typical/Maximum**
Active Diameter	mm	-	25
Quantum Efficiency at Peak	%	-	28
Spectral Range (Fused Silica)	nm	160	630
Dark Current at 20°C	nA	0.2	5
Cathode Current (Max)	nA	-	50
Anode Current (Max)	μA	-	100
Linearity (Pulsed, -5% Deviation)	mA	25	100

4.2 Pion Detector System: Optimization Process

In the design and optimization process of the pion detector system, the Geant4 simulation toolkit and the ROOT analysis package were utilized for simulating the passage of particles through matter and for further analysis, as explained in Section 2.7. This section provides a comprehensive description of the process that led to the modification and finalization of the initial geometry and design of the pion detector system. The evolution of the system concludes with the finalized design presented in Figure 3.14. In this design, the pion detector system and the lead donut system are integrated to form a unified system called the pion donut system. This integration primarily arises from the need for the lead donut to shield the pion detector system against the flux of secondary particles. As a result, all optimization processes aimed to prevent these secondary particles from impacting the pion detector system. The optimization was carried out in three main steps:

1. Relocating and modifying the geometry of the pion detector system.

2. Rotating the entire pion detector system by 90°.

3. Integrating the pion detector system with the lead donut system.

To better understand the impact of integrating the pion detector system with the lead donut system (Figure3.14) and other initial optimization steps, refer to Figure 4.4. The left plot illustrates the original location, geometry, and design of the pion detector in relation to the lead donut and showermax systems. The right plot, on the other hand, shows the initial geometry of each module within the pion detector system. The initial pion detector system consisted of 14 Lucite detectors. Each Lucite

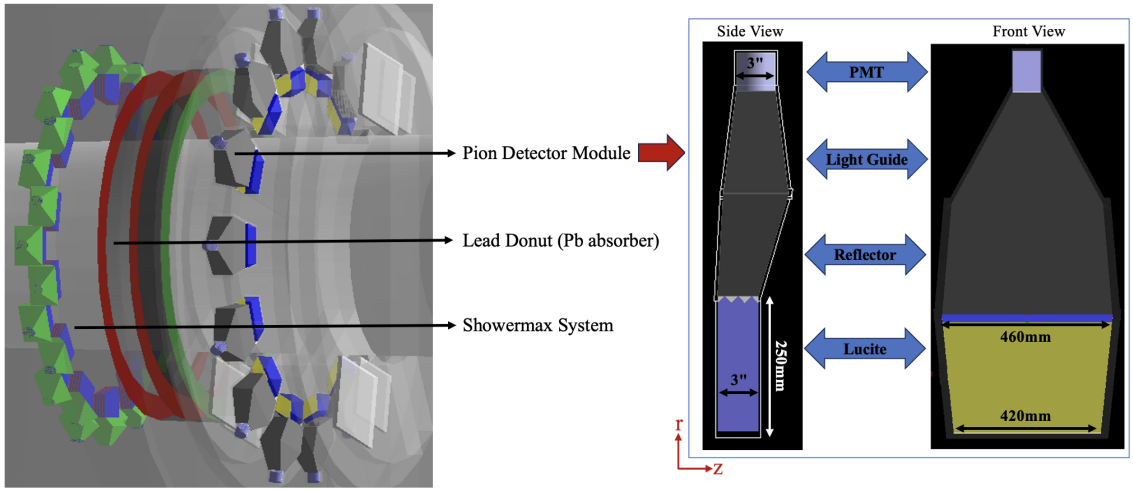

Figure 4.4: Left: Initial location of the pion detector system, aligned with the lead donut and showermax systems. Right: Initial geometry of each module within the pion detector system.

detector was trapezoidal in shape and was optically read out by a PMT via an air-core light guide. The light guide consisted of an air-core channel with walls made from high-reflectivity material. Each module's side and front views are shown on the right of Figure 4.4. Each module includes three 1-inch Lucite pieces connected to a 3-inch PMT (side view). The trapezoidal Lucite features a top side measuring 460 mm and a bottom side of 420 mm in the azimuthal direction (front view). It has a thickness of 3 inches along the z-axis and a radial length of 250 mm. At the top of each Lucite piece, there are wedges designed to break total internal reflection and couple the light from the Lucite to the air core light guide.

In contrast, the finalized pion detector system (Figure 3.14) consists of 28 Lucite detectors. Each detector has a rectangular shape. It measures 210 mm in the azimuthal direction for its length, 25.4 mm (1 inch) radially for its width, and 70 mm in depth along the z-axis, consistent with a 90° rotation. It is coupled directly to a 1-inch PMT using a glue layer without a light guide. Additionally, the wedges at the top of each Lucite have been removed. Simulations indicated that direct coupling of the PMT to the Lucite positively impacts the functionality of the pion detector system more than using wedges for total internal reflection.

Figure 4.5 illustrates the evolution of each module from its initial design to its final form. The leftmost plot illustrates the primary module from 2020. Moving to the

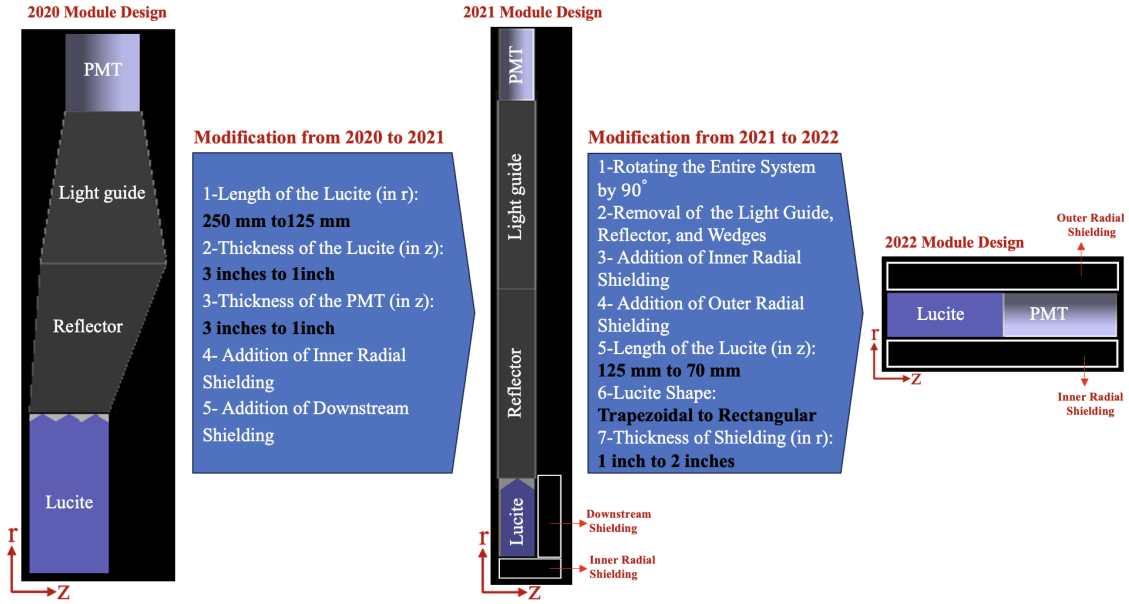

Figure 4.5: Left: Initial design of the pion detector module in 2020. Middle: Modified geometry of the pion detector module from 2021. Right: Finalized design of the pion detector module from 2022.

central plot, the 2021 modified version shows a reduction in the radial dimension of the Lucite from 250 mm to 125 mm and a decrease in the thickness of both the Lucite and the PMT from 3 inches to 1 inch. Furthermore, inner radial and downstream lead shielding were added to enhance the protection of the Lucite detector from low-energy secondary particle showers, while the light guide, reflector, and wedges

remained unchanged. The rightmost plot illustrates the most important step in the optimization process: rotating the pion detector system by 90°. Better coupling of particles to the PMT requires positioning the PMT in the direction of the primary particles rather than perpendicular to it. In the subsequent development of the pion detector system, several modifications were made following its rotation. The light guide, reflector, and wedges were removed, and shielding layers were added to both the inner and outer radial edges of the system. Further enhancements to the rotated version of the pion detector system led to significant improvements. These included increasing the thickness of both the inner and outer radial shielding from 1 inch to 2 inches, reducing the azimuthal thickness of the Lucite from 125 mm to 70 mm, and changing the Lucite shape from trapezoidal to rectangular. At this stage, the pion detector and lead donut systems remained separate entities. To provide context for the design changes to the pion detector system, the initial and finalized geometries of the individual modules and the entire system have been discussed. However, the reasoning behind these modifications still needs to be addressed.

Figure 4.6 illustrates the origin locations (r, z) of secondary particles from the Møller generator that interact with the pion detector to clarify these changes. All three 2-D plots illustrate the positions of the pion detector system, showermax, lead donut, and beam pipe. Numerous tracks hitting the Lucite detector originate from sources such as the beam pipe, the inner edge of the lead donut, the upstream side of the lead donut, or the showermax, all indicative of secondary particle effects.

The top plot represents the initial 2020 design, established when research on the pion detector system began. Within this design, the ratio of photoelectrons generated from pions to those generated from Møller electrons (π/e ratio) was 0.1%. The location of hits in the top plot prompted us to infer that these are not exclusively secondaries from the showermax, but also secondaries induced by those initial secondary particles within the showermax. While these secondary particles might not hit the Lucite in this particular sector, they are likely to impact the Lucite in other sectors. As a result, the design was subjected to modifications to better shield the Lucite detector from secondary particles, ensuring that the light at the PMT predominantly originates from primary particles. The middle plot shows the 2021 modified

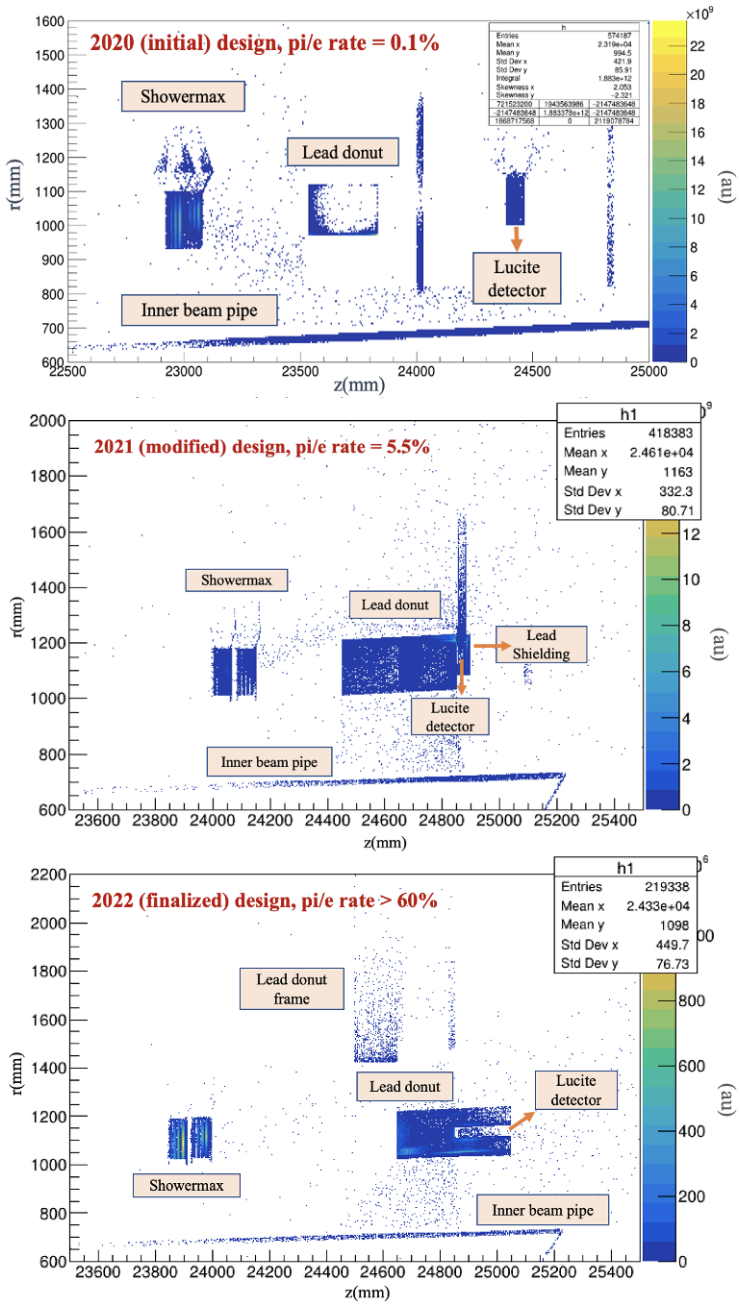

Figure 4.6: Top: Initial design of the pion detector system in 2020, aligned with the lead donut and showermax systems, featuring a π/e ratio of 0.1%. Middle: Modified geometry of the pion detector system from 2021, coordinated with the lead donut and showermax systems, boasting a π/e ratio of 5.5%. Bottom: Finalized design of the pion detector system from 2022, integrated into the lead donut, achieving a π/e ratio of $> 60\%$. Note that all plots are generated using the Møller generator.

design, which resulted in an increase of the π/e ratio from 0.1% to 5.5%. The Lucite detector has been optimally positioned close to the lead donut, with reductions in both thickness and length. This updated geometry efficiently prevents the penetration of showermax secondaries into the Lucite in adjacent sectors. Subsequently, the bottom plot illustrates the optimized 2022 design, which not only achieves a π/e ratio in excess of 60% but also meets the critical design objective of attaining roughly equal numbers of pions and Møller electrons, as detailed in Section 3.4.3.2. At this stage, the pion detector system was integrated with the lead donut structure to realize this improvement. Table 4.2 shows the impact of optimization steps in terms of the percentage of the π/e ratios.

Table 4.2: Optimization Steps.

Optimization Steps	π/e (Photoelectrons)
Initial Geometry (2020)	$0.10\% \pm 0.01\%$
Updated Geometry without Shielding (2021)	$2.5\% \pm 0.1\%$
Updated Geometry with Shielding (2021)	$5.5\% \pm 0.3\%$
Pion Detector System Rotation and Lucite's Direct Coupling to PMT (2022)	$16.8\% \pm 0.6\%$
Addition of Shielding to Rotated System (2022)	$49.1\% \pm 1.4\%$
Adjustment of Radial Position for Lucite (2022)	$51.8\% \pm 1.5\%$
Modification of Lucite Shape (2022)	$55.8\% \pm 1.6\%$
Integration of System into Lead Donut (2022)	$61.5\% \pm 1.7\%$

So far, the approach to obtaining the π/e ratio has involved using Møller and pion generators in Geant4 simulations (Section 2.8). This approach is expanded for further investigation by incorporating the impacts of both the elastic and inelastic generators. It is achieved by adding the rate of photoelectrons generated from these generators to the existing data obtained from the Møller generator. Therefore, the parameter under evaluation transformed from being the ratio of the pion-generated photoelectron rate over the Møller-generated photoelectron rate (π/e) to a ratio where the denominator also includes contributions from the elastic and inelastic generators ($\pi/(e + elastic + inelastic)$). It was observed through simulations that the photoelectron rate from the inelastic generator had a negligible impact. However, the photoelectron rate from the elastic generator significantly influenced the outcome, accounting for about

half of the photoelectron rate derived from the Møller generator. Consequently, the ratio decreased substantially from approximately 60% (π/e) to around 40% ($\pi/(e + elastic + inelastic)$).

Examining the underlying physics of the MOLLER experiment led us to conclude that the secondary particles observed in the inner radial region of the Lead donut and Lucite originated from elastic proton scattering signals. Due to the higher mass of protons, the electrons exhibited more forward scattering, which resulted in smaller scattering angles. This suggested that electrons would traverse a narrower radius, moving closer to the inner side of the donut, thereby increasing the likelihood of impacting the inner radial side of the donut. To address this, the design was revised to extend the radial thickness of the Lead donut from 16 cm to 21 cm and to enhance the inner radial shielding thickness from 2 inches to 4 inches. Simulations run with the modified geometry yielded a π/e ratio of $102.65\% \pm 2.5\%$ and a $\pi/(e + elastic + inelastic)$ ratio of $63.8\% \pm 1.8\%$. The finalized design incorporated these adjustments, featuring a Lead donut with a radial extension of 21 cm, shielding thicknesses of 2 inches for the outer radial, and an increased shielding thickness of 4 inches for the inner radial portions.

In collaboration with engineers at JLab, the finalized design was subjected to further technical and mechanical evaluations. Ultimately, we agreed on a design featuring approximately 0.935-inch thickness for the outer radial shielding, down from the initial 2 inches, and 4.21-inch thickness for the inner radial shielding, slightly exceeding the initially proposed 4 inches. While the updated geometry diverged from the original plan, new simulations of the modified geometry validated its efficacy. The revised design met the project's objectives, achieving a $\pi/(e+elastic+inelastic)$ ratio greater than 60%. The key point is that our design remained robust; the alterations made during the engineering phase remained consistent with the project's objectives.

Detailed information on the geometry and dimensions of the Lead donut and the pion detector system can be found in Table 4.3. Furthermore, Figure 4.7 provides additional insights into the pion donut system, a term designated for the pion detector system integrated with the lead donut system.

In both Table 4.3 and Figure 4.7, dimensions are presented in both millimetres and

Table 4.3: Lead Donut and Pion Detector Dimensions.

Parameter	Value (mm)	Value (inch)
Lead Donut Inner Diameter	1941.83	76.45
Lead Donut Outer Diameter	2438.15	95.99
Lead Donut Length	200.00	7.87
Lead Donut Thickness	210.06	8.27
Lead Donut Aluminum Thickness	19.05	0.75
Pion Detector Radial Position	1132.45	44.59
Pion Detector Inner Shielding Length	180.00	7.09
Pion Detector Outer Shielding Length	180.00	7.09
Pion Detector Inner Shielding Thickness	106.93	4.21
Pion Detector Outer Shielding Thickness	23.75	0.94
Pion Detector Slot	41.28	1.63
Pion Detector Length	210.00	8.27
Pion Detector Thickness	25.40	1.00
Pion Detector Depth	70.00	2.76

inches to accommodate the conventions of different disciplines involved in the design and implementation of the detector system. In engineering practices, certain components such as PMTs are commonly manufactured to inch-based specifications, and materials like Lucite are often referred to by their inch measurements. Conversely, the scientific community, particularly in the field of physics, frequently employs the metric system for precision and standardization. Providing both units allows for clarity and ease of reference for all collaborators, from manufacturers to researchers, ensuring that the specifications are universally understood and applicable.

Figure 4.7 illustrates the pion donut system from different angles to provide a complete understanding of its design. A front view is presented in the top left with labelled technical details. This is complemented by a side view in the top right, highlighting various other parameters. The bottom left gives an overview and a sectional view to visualize the structure. The bottom right contains a legend that pairs parameters with specific part numbers. Colour coding helps distinguish different parts: orange for aluminum components, blue for lead components, and purple for pion detector modules.

Following the finalization of the lead donut and pion detector module geometries,

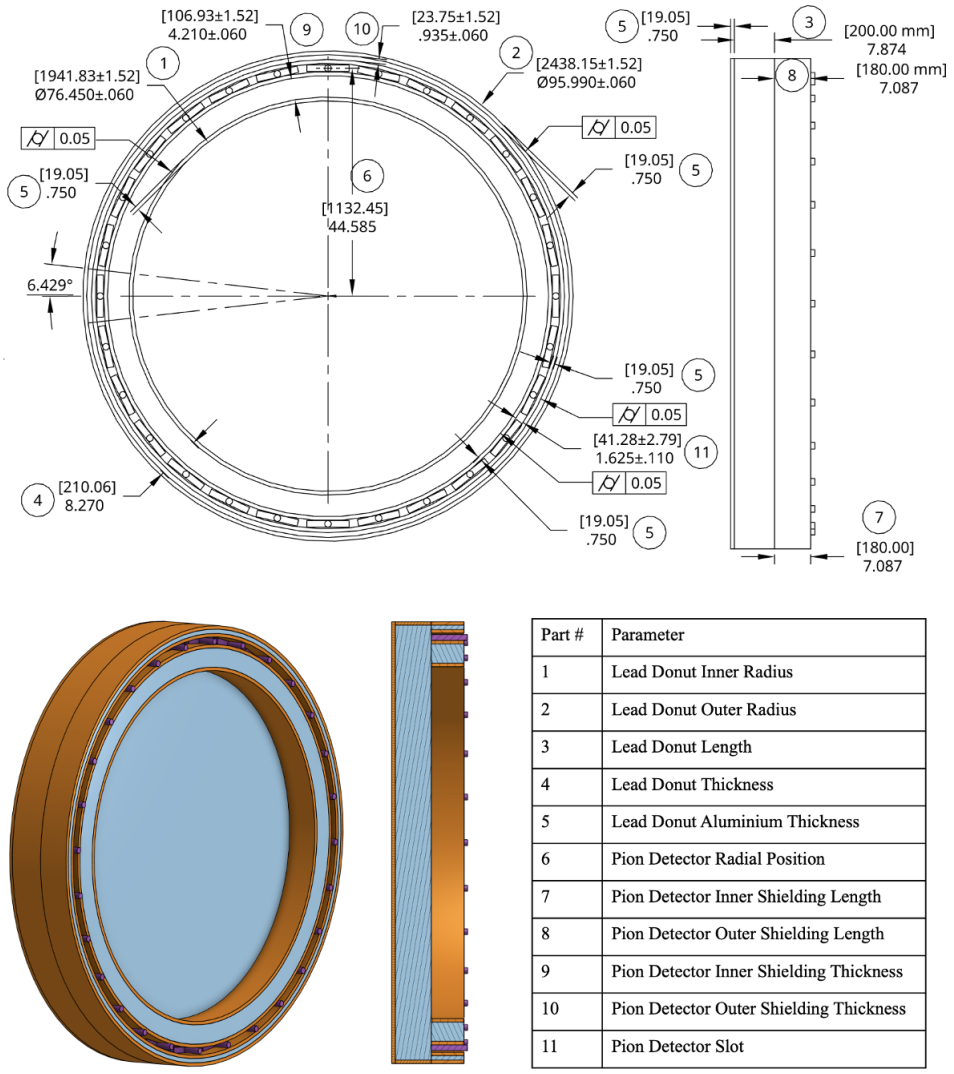

Part #	Parameter
1	Lead Donut Inner Radius
2	Lead Donut Outer Radius
3	Lead Donut Length
4	Lead Donut Thickness
5	Lead Donut Aluminium Thickness
6	Pion Detector Radial Position
7	Pion Detector Inner Shielding Length
8	Pion Detector Outer Shielding Length
9	Pion Detector Inner Shielding Thickness
10	Pion Detector Outer Shielding Thickness
11	Pion Detector Slot

Figure 4.7: Top left: Detailed drawing showing the front view of the pion donut system, labelled with specific technical details. Top right: Detailed drawing showing the side view of the pion donut system, labelled with specific technical details. Bottom left: Design overview and sectional view of the pion donut system. Bottom right: A legend detailing and correlating the parameters with part numbers for reference. Note: Aluminum components are coloured orange, lead components are blue, and the pion detector modules are depicted in purple.

the subsequent step involves physically installing 28 pion detector modules within the lead donut structure. The mechanical design must be robust enough to securely support the 28 modules in various orientations spanning a full 360° range. Further-

more, it is necessary to create an enclosure box that is both secure and light-tight. The following section will detail the specifications of this enclosure and describe the methodology for installing the modules inside the lead donut.

4.3 Pion Detector System: Mechanical Design

This section discusses the design of the light-tight enclosure box, which comprises four main components: a Lucite box, a Lucite and PMT connector, a PMT housing, and an adapter and end cap. Figure 4.8 illustrates these components from various angles. The Lucite box on the top left incorporates three critical features. Firstly, it employs fillets on the outer edges to facilitate a smoother surface, aiding in its insertion into the lead donut. Secondly, a small wedge is internally positioned to secure the Lucite and create a separation between the box and the Lucite, thereby establishing an intermediate air layer, as assumed in the simulation. Lastly, some holes are included on the exterior to assist in placing the modules within the lead donut. At the top right of the illustration, the connector segment serves as a bridge between the Lucite box and the PMT housing. This segment plays an essential role in maintaining the PMT in position and fastening it to the Lucite. The PMT housing is displayed on the bottom left, integrated into the entire enclosure box, and designed to hold the PMT securely, preventing potential wobbling and detachment from the Lucite. The bottom right presents the adapter, facilitating the connection between the PMT housing and the end cap. This end cap is designed to securely hold the PMT's voltage divider and provide the holes for the signal and high voltage outputs to the SHV and BNC connectors.

Figure 4.9 illustrates a comprehensive view of the fully assembled light-tight enclosure box, detailing how all components fit together. The illustration on the left highlights the threads designed for securely fastening the adapter to the end cap. It is important to note that glue is utilized to attach the Lucite to the PMT, and the Lucite is further wrapped in a Tyvek wrap to enhance the system's efficiency. Utilizing Tyvek wrapping around a Lucite significantly enhances light collection efficiency in Cherenkov radiation detection systems [89]. This wrapping reflects Cherenkov

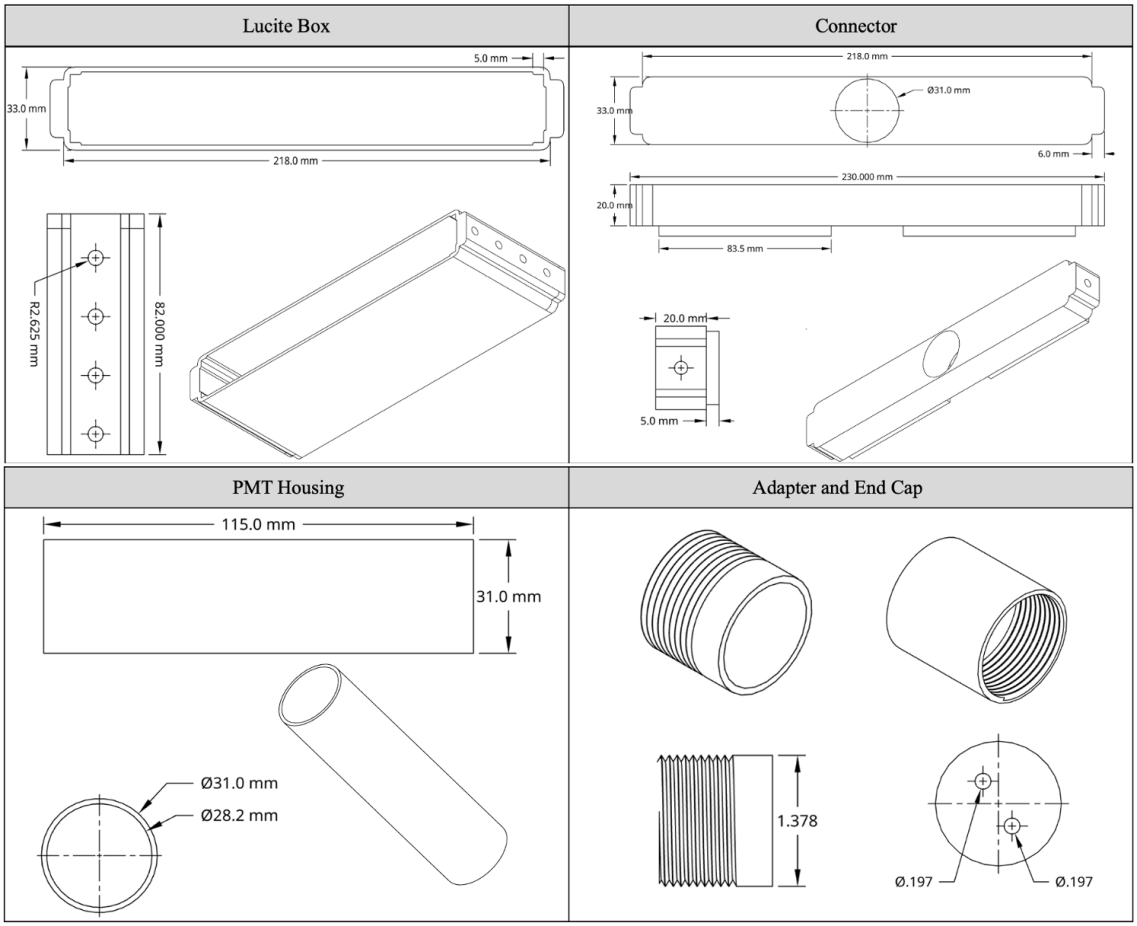

Figure 4.8: Top left: Detailed view of the Lucite box designed to accommodate the Lucite. Top right: Detailed view of the connector segment facilitating the attachment of the Lucite to the PMT housing. Bottom left: Detailed view of the PMT housing securely holds the PMT. Bottom right: Detailed view of the adapter and end cap to secure the PMT's voltage divider.

photons toward the PMT, thereby increasing the number of photoelectrons detected. Additionally, Cherenkov radiation is typically emitted at sharp angles relative to the direction of the particle. Without wrapping, a significant portion of the generated light could undergo total internal reflection, essentially getting lost and failing to reach the PMT. By reflecting this light into the lucite, Tyvek wrapping notably increases the system's efficiency, providing another opportunity for the light to reach the PMT and be detected, thus minimizing losses due to surface reflection.

In the subsequent phase of designing the light-tight enclosure box, the next step

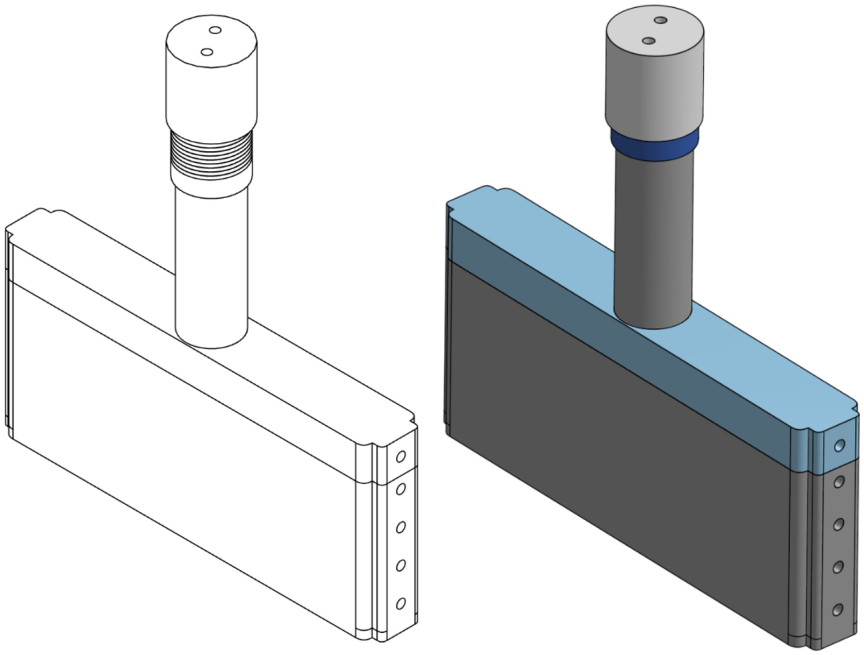

Figure 4.9: Overview of the assembled light-tight enclosure box showcasing all components together.

is to install the enclosure box within the pion detector slot in the lead donut, part #11 in Figure 4.7. Three L-brackets are utilized to secure the box to the slot: two on the sides and one at the bottom. The arrangement of these brackets is shown in the illustration at the top of Figure 4.10. The side brackets are designed to slide the module into the pion detector slot, whereas the bottom bracket is utilized to attach the module to the lead donut securely. As seen in the bottom part of Figure 4.10, the angle brackets do not interfere with either the size of the pion detector slot or the gap between the top of the enclosure box and the bottom of the lead donut arc. According to the dimensions listed in Table 4.3 and illustrated in Figure 4.7, the pion detector slot has a width of 1.635 inches, while the thickness of the pion detector enclosure box is 1.3 inches. This creates an additional gap of 0.335 inches in the slot, marked with a red star at the bottom of Figure 4.10. This gap needs to be filled. For this purpose, it is essential to take into account the tolerances incorporated in the pion donut system.

These tolerances fall into two categories: one arising from thermal deformation

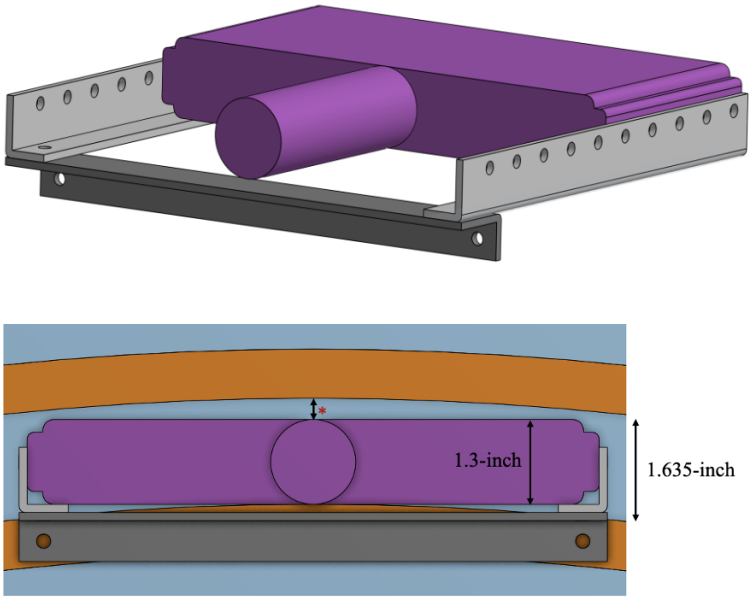

Figure 4.10: Top: Utilization of three L-brackets to facilitate installation. Bottom: The pion detector module is situated within the lead arcs, illustrating the dimensions of the pion detector cavity and the enclosure box's thickness. A red star indicates the gap between the enclosure box and the lead arc.

during the casting of lead inside the aluminum shell and the other originating from the manufacturing process of the aluminum shells themselves. However, in the end, the tolerance due to the thermal deformation is thoughtfully incorporated into the manufacturing tolerance to ensure optimal performance.

Regarding the thermal deformation, engineers have analyzed the thermal effects of pouring the lead. In the worst-case scenario, where all the lead is poured in at once, it is predicted that there will be negligible changes to the dimensions of the cavity for the pion detectors, less than a 0.080-inch change in the space between the inner and outer walls of the cavity. Moreover, the Statement of Work can specify that the vendor pours the lead more slowly to prevent significant rises in local temperatures, further reducing the potential for deformation.

The manufacturing tolerances are of two types: a diameter tolerance of 0.06 inches and a cylindricity tolerance of 0.05 inches. Cylindricity refers to a condition where a cylindrical object has two defining cylinders, inner and outer, that span its entire length. All points on the surface of this object must be contained within these two

cylinders [90]. This condition is maintained and managed over the entire length of the feature. To measure cylindricity, the object is secured firmly along its axis and then rotated. As it spins, a height gauge takes note of any surface variations at multiple points along its length. To meet the cylindricity tolerance, the cumulative variations recorded by the height gauge must be less than the specified tolerance value. This process ensures the object's symmetry and uniformity over its entire length. The impact of cylindricity on the lead donut arcs is illustrated in Figure 4.11. It can give rise to a worst-case scenario where one cylinder is expanding while the other is contracting. When taking into account the uncertainties associated with both the diameter and the cylindricity, the total potential variation equates to $((2\times0.05/2) + (2\times0.06/2)) = 0.11$ inches. Consequently, in these extreme scenarios, the additional space would range between $1.625(\text{gap}) - 0.11(\text{tolerance}) - 1.3(\text{box}) = 0.215$ in and $1.625(\text{gap}) + 0.11(\text{tolerance}) - 1.3(\text{box}) = 0.435$ in.

To ensure a flexible fitting method, two wedges are utilized. The first is secured at the center of the box, as illustrated in the middle portion of Figure 4.12. The second operates as an adjustable fitting tool, able to slide to fill any existing gap, as demonstrated at the top and bottom of Figure 4.12. This strategy aids in achieving a robust and tight installation. Note that the purple section in the figure represents the side view of the enclosure box, as detailed in Figure 4.8.

The concluding element of this section is Figure 4.13, which presents the finalized version of the pion detector module as implemented inside the pion detector slot of the lead donut. With the optimization of the pion detector system and the mechanical design complete, our attention now turns to the crucial stage of validation. It is imperative to verify that the simulated predictions align with experimental outcomes, particularly concerning the system's rotational and the quantification of photoelectrons generated across various designs.

The following sections explore two distinct experimental approaches to validate the simulation results. Section 4.4 discusses cosmic testing, which studies the system's response to cosmic rays and serves as a preliminary assessment of its functionality. Subsequently, Section 4.5 discusses beam testing conducted at the Mainz Microtron (MAMI), providing a more focused and controlled environment to verify the sim-

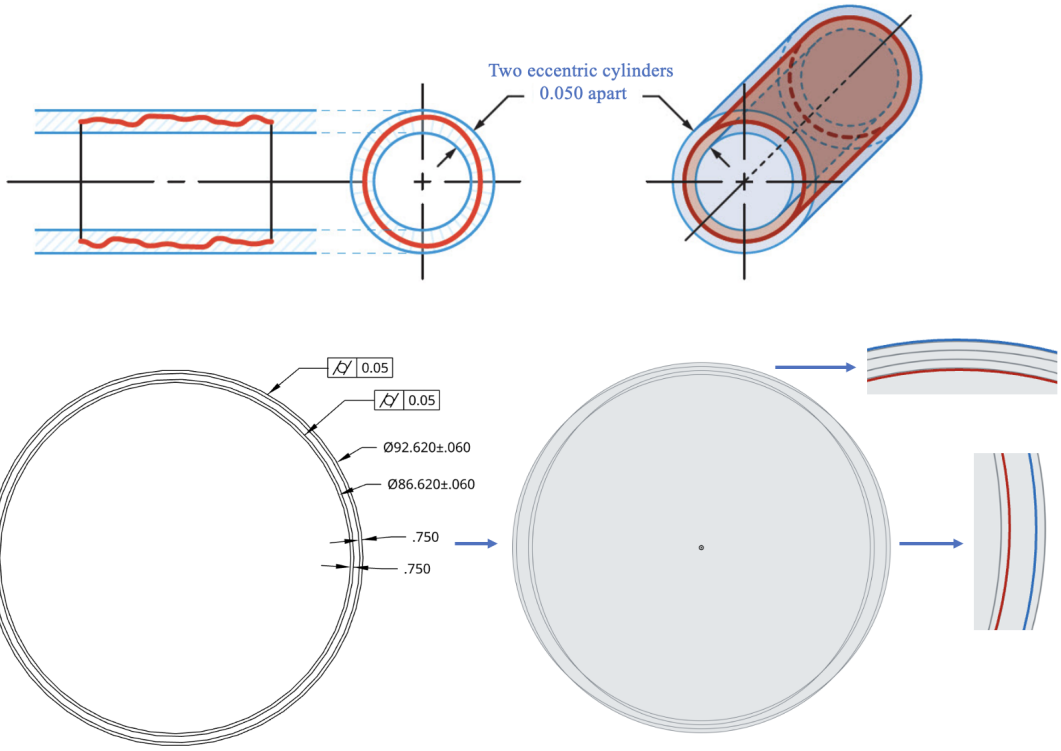

Figure 4.11: Top: Illustration of the effects of cylindricity on two concentric cylinders. Bottom: Visualization of the worst-case scenarios entailing cylindrical expansion and contraction within the Lead donut arcs, represented by the red and blue circles. The gray circles indicate the potential outcomes in these extreme scenarios [91].

ulation results. Together, these experiments ensure that the pion detector system operates as intended and that our simulations are a reliable predictor of real-world performance.

4.4 Verifying the Simulation Results: Cosmic Testing

This section presents the results of cosmic testing conducted to validate the theoretical models and simulation outcomes (Section 4.2) within the pion detector of the MOLLER experiment. A historical background and an overview of the fundamental principles underlying cosmic rays were provided in Section 2.7.1. Building

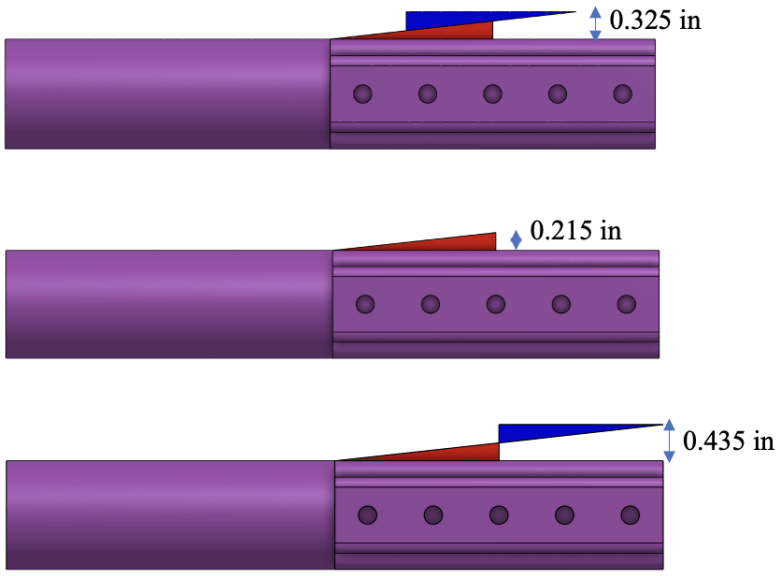

Figure 4.12: A demonstration of the flexible fitting method using two wedges. The central section illustrates the first wedge secured at the center of the box. In contrast, the top and bottom sections showcase the adjustable wedge sliding to fill gaps, effectively ensuring a robust and tight installation. Note that the purple part in the figure is the side view of the enclosure box, details of which are presented in Figure 4.8.

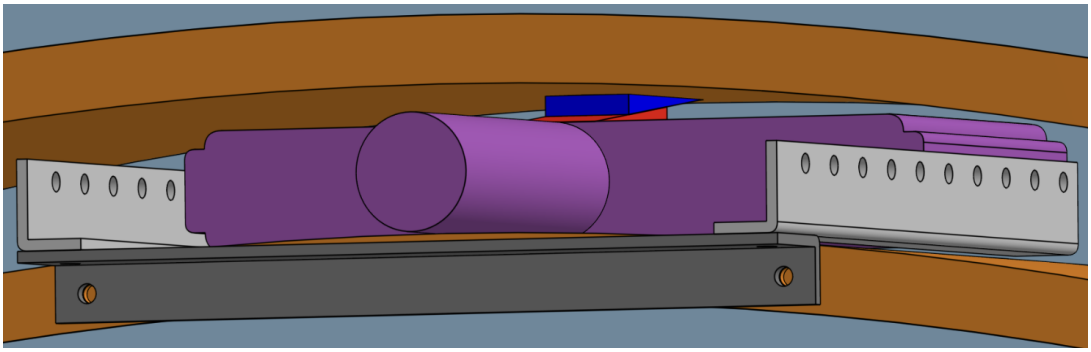

Figure 4.13: The finalized version of the implemented pion detector marks the conclusion of this section.

on this foundation, Section 4.4.1 focuses on the simulation of cosmic testing, emphasizing how these simulations replicate experimental conditions and their importance in interpreting the results. Finally, Section 4.4.2 describes the specific cosmic testing setup employed at the University of Manitoba, detailing the methodologies and

configurations used.

Therefore, the subsequent subsection will present two configurations utilized for cosmic ray testing at the University of Manitoba and a comprehensive description of the data acquisition system. The first configuration aligns with the initial design of the pion detector system (depicted in the top plot of Figure 4.6), wherein the orientation of the PMT attached to Lucite is perpendicular to the incoming cosmic ray's direction, prior to the system's rotation. The second configuration corresponds to the finalized design of the pion detector system (shown in the bottom plot of Figure 4.6), which was adopted after rotating the system. Ultimately, the outcomes of these two physical setups will be compared to the simulation results to determine simulation agreement.

4.4.1 Simulating the Cosmic Testing

During the initial phase of our cosmic ray testing, we intended to utilize the optimized Lucite dimensions referenced in Section 4.1.1 and the PMT model detailed in Section 4.1.2. However, due to the availability of materials in our laboratory, we modified the prototype to incorporate the components at hand, namely acrylic plastic (PMMA) and plastic scintillator (EJ-200) [85]. Instead of the optimal Lucite (PMMA) dimensions of 210 mm $\times$ 25.4 mm $\times$ 70 mm, we used a Lucite block with the dimensions of 300 mm $\times$ 37 mm $\times$ 100 mm. Moreover, rather than employing ET Enterprise 9125QB [58] PMTs, we utilized high-voltage Hamamatsu PMTs, model H3178-51 [92]. It should be mentioned that the decision on the PMT model had not been finalized at that time. In validating the cosmic testing outcomes, it is crucial to replicate the experimental parameters in the simulations accurately. This includes Lucite's transmission and refractive index, as well as the QE of the PMTs. Jefferson Lab has characterized the spectral transmission of Lucite from Eljen from 250 nm to 700 nm, which is crucial for our simulation parameters. Figure 4.14 presents a comparative analysis between UV acrylic and Lucite samples of various thicknesses. We utilized the transmission data for a 37 mm thick Lucite sample to simulate the PMT's perpendicular orientation to cosmic rays, configuration (1), and 100 mm data

for the parallel alignment, configuration (2). Additionally, the Lucite refractive index was included in the simulation [93], shown in the right plot of Figure 4.14. The

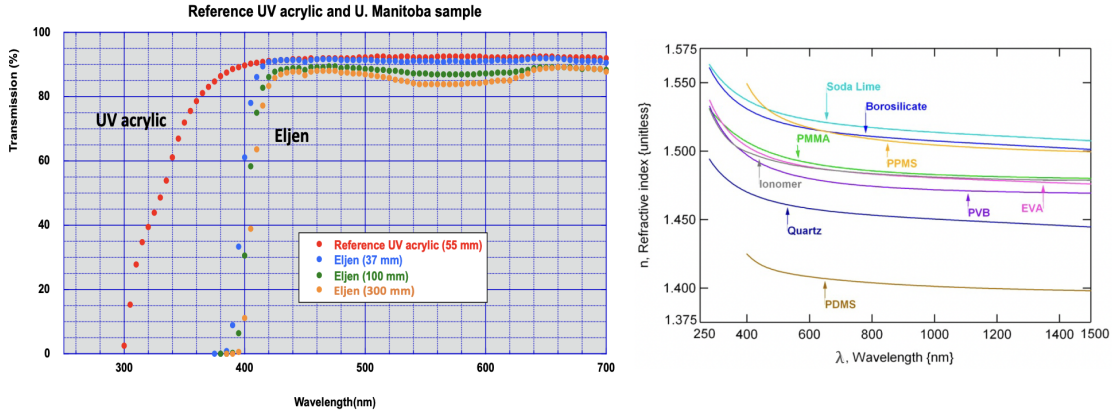

Figure 4.14: Comparative Analysis of Material Properties: The left plot displays the transmission percentages across wavelengths for UV acrylic and Lucite samples of varying thicknesses. The right plot details the refractive index values of Lucite over a broad wavelength spectrum [93].

PMT's QE was simulated using specifications from the Hamamatsu manual. The Hamamatsu PMTs, model H3178-51 [92], incorporate a bialkali photocathode and Borosilicate glass window. These components are highlighted in Figure 4.15.

Subsequent to the implemented modifications, standalone simulations with a 4 GeV muon beam (as explained in Section 2.7.1) were conducted to evaluate the performance of isolated pion detector configurations, analogous to cosmic ray testing apparatuses. It is important to understand the difference between the two types of simulations: the full MOLLER simulation and the standalone simulation. The first type encompasses all components of the MOLLER experiment, while the second type focuses solely on the pion detector system. The agreement of the results from cosmic testing with both types of simulations indicates the design's robustness.

For both configurations, the number of generated photoelectrons (#PEs) has been plotted for a comparative study. The outcomes of these standalone simulations are depicted in Figure 4.16. The ratio of #PEs in two simulation configurations is calculated as $\frac{54.85 \pm 0.14}{15.02 \pm 0.03} = 3.65 \pm 0.01$, which should be compared to the ratio of #PEs in two experimental configurations. The cosmic testing setup and results are detailed in

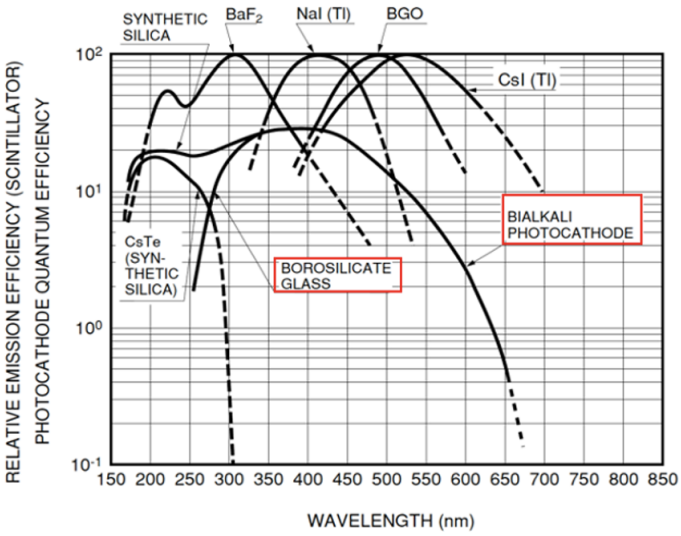

Figure 4.15: Efficiency curves for various scintillator materials and photocathode types across the wavelength spectrum. This plot illustrates the relative emission efficiency of scintillators and the QE of photocathodes, spanning wavelengths from 150 nm to 850 nm. Specifically highlighted are the efficiency curves for Bialkali photocathodes and Borosilicate glass, commonly utilized in Hamamatsu PMTs, as indicated by the red boxes for ease of reference [92].

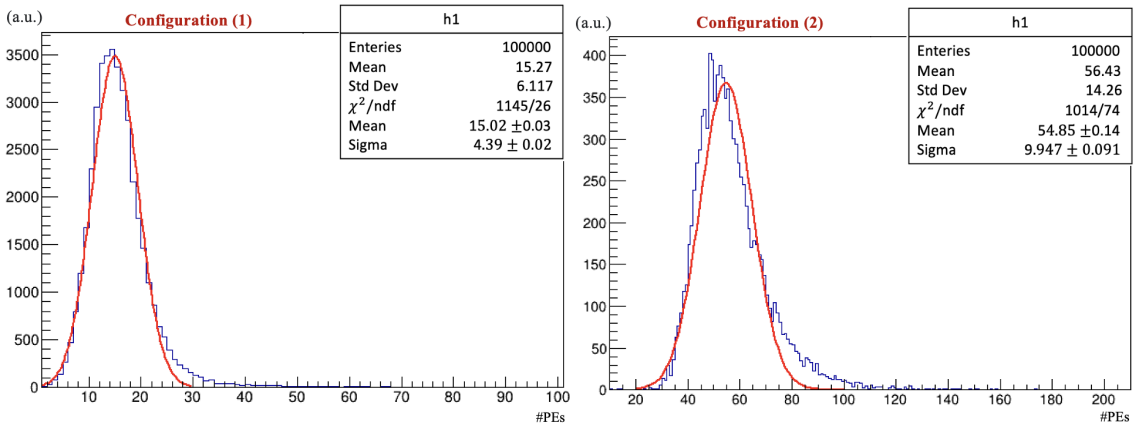

Figure 4.16: Comparison of the generated photoelectron distributions for two distinct pion detector configurations under a 4 GeV muon beam. Configuration (1) exhibits a narrower distribution of #PEs with a mean of approximately 15.02 and a standard deviation of 4.39, whereas Configuration (2) shows a broader spread with a mean of 54.85 and a standard deviation of 9.95. These distributions are indicative of the #PEs in detector setups.

the next subsection.

4.4.2 Cosmic Testing Setup

As mentioned before, acrylic plastic (PMMA), plastic scintillator (EJ-200) [85], high-voltage Hamamatsu PMTs, model H3178-51 [92] were utilized in the cosmic testing. Two plastic scintillators (EJ-200), which were matched in size to the Lucite, and Lucite are mechanically coupled to the high-voltage PMTs using optical grease for optimal optical transmission, with the flexibility of reconfiguring the setup if necessary. However, an adhesive will be used for the MOLLER experiment, as detailed in Section 4.2.

As depicted in the left-hand side of setups in Figures 4.17 and 4.18, the Lucite is placed between the scintillators. In Figure 4.17, the orientation of the PMT attached to the Lucite is perpendicular to the direction of incoming cosmic rays, which we will refer to as configuration (1). Conversely, in Figure 4.18, the PMT attached to the Lucite is aligned with the direction of incoming cosmic rays, referred to as configuration (2). The detection process begins with the scintillators' signals being fed into a discriminator to establish a threshold (approximately 1 V). An AND gate then ensures that only coincident signals from both scintillators are considered. The coincident signal from the scintillators and the signal from the Lucite are subsequently processed by the CAEN VX1725S digitizer [94]. The digitizer captures the electrical charge pulses produced by the detector, extracts the quantities of interest, and digitizes them. The digitized data are then transmitted to the data acquisition system through the VME to USB 2.0/Optical Link Bridge (CAEN VX3718 [95]). The CoMPASS software [96], which is explained later, is employed to control the acquisition, perform analysis, and manage the storage of the collected data. This method guarantees that a cosmic ray traversing both scintillators will also pass through the Lucite, effectively isolating the cosmic signal and improving measurement precision by eliminating background noise.

A general explanation of signal detection using the CAEN VX1725S digitizer [94] and CoMPASS software [96] has been provided. For detailed information on these

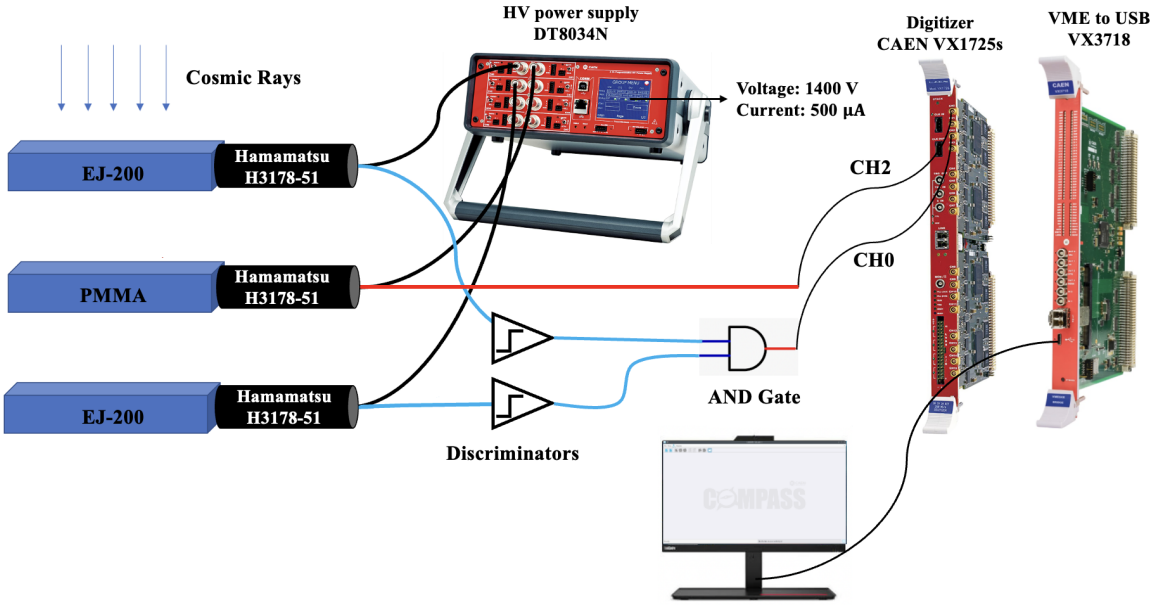

Figure 4.17: Schematic diagram of the cosmic testing setup at the University of Manitoba, with cosmic rays entering perpendicular to the PMT attached to the PMMA, configuration(1)

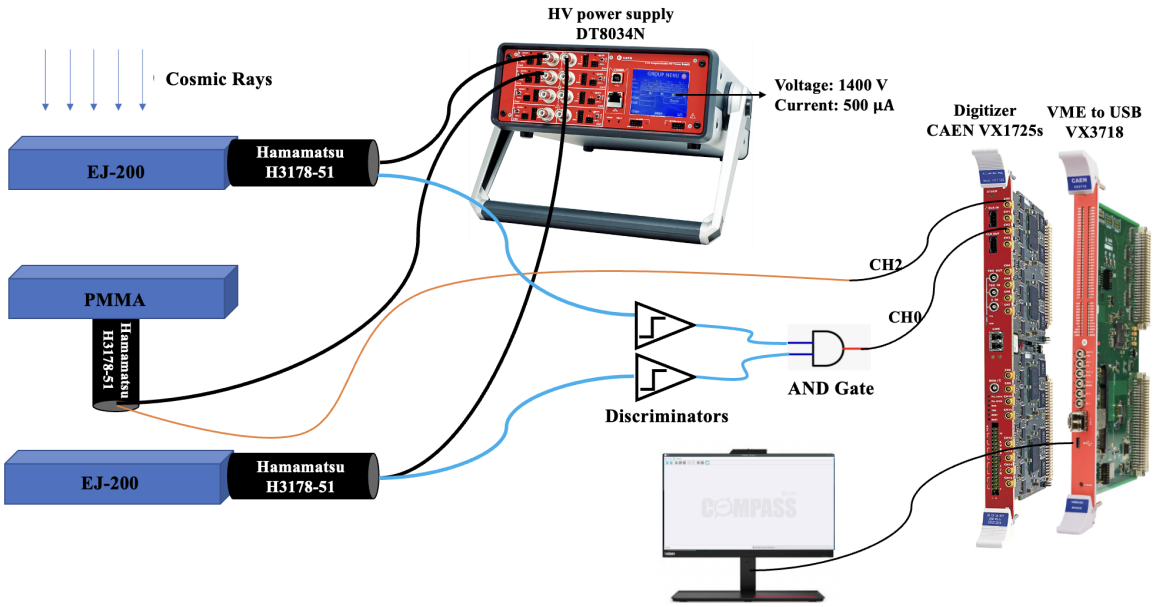

Figure 4.18: Schematic diagram of the cosmic testing setup at the University of Manitoba, with cosmic rays entering in alignment with the PMT attached to the PMMA, configuration(2)

components, refer to Table 4.4 and Figure 4.19, where the settings are shown and illustrated, respectively. Table 4.4 shows the essential settings for both channel 0 (coincidence's signal) and channel 2 (Lucite's signal) with the description as follows:

Table 4.4: CoMPASS Factory Settings for Channels 0 and 2

CoMPASS Factory Settings	**Channel 0**	**Channel 2**
Gate	300 ns	300 ns
Record length	256 ns	256 ns
Pre-gate	48 ns	48 ns
Short gate	80 ns	80 ns
Pre-trigger	128 ns	128 ns
Polarity	negative	negative
DC Offset	20.0%	10.0%
Threshold	100 LSB	10 LSB
Energy coarse gain	40 fC/LSB	2.5 fC/LSB
Input dynamic	2.0 Vpp	0.5 Vpp
Discriminator mode	CFD	CFD
CFD delay	4 ns	4 ns
CFD fraction	25%	25%
Coincident mode	Ch_0 And any	

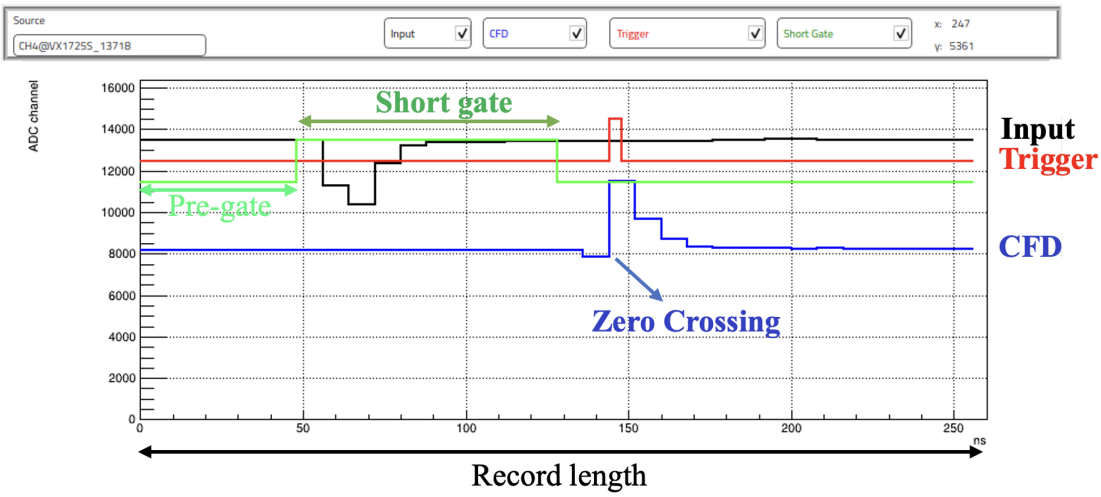

Figure 4.19: Output signal from the digitizer.

Record length: Record length is the length of the acquisition window expressed in ns. It is set to 256 ns as shown in the x-axis of Figure 4.19.

Pre-trigger: Pre-trigger sets the portion of the waveform acquisition window to be saved before the trigger. Its value is also expressed in ns and shown in Figure 4.19.

Polarity: Polarity selects whether the input signal to be processed is negative or positive. By setting Negative, the algorithm will invert the input's digital samples, and the input will always appear positive in the waveform inspector.

DC Offset: The DC offset adjusts the baseline level of the input signal by applying a specific voltage offset to the channel. This offset is expressed as a percentage of the full-scale range of the digitizer. Adjusting the DC offset effectively shifts the baseline of the input signal up or down within the dynamic range. For the signal from Lucite, which is comparatively small, a lower DC Offset is selected to optimize the visibility of the signal within the dynamic range.

Input Dynamic Range: The input dynamic option selects the digitizer's input dynamic range, measured in volts peak-to-peak (Vpp), which represents the entire amplitude range from the highest to the lowest point of the input signal that the digitizer can handle. The available options for the CAEN VX1725S are 0.5 Vpp and 2 Vpp. A 0.5 Vpp range was chosen for the signal from the Lucite because the signal is relatively small and can be challenging to detect. Therefore, a better resolution is required for accurate detection. As previously mentioned, the CAEN VX1725S digitizer [94] is a 14-bit device. The Analog Digital Converter (ADC) divides the input voltage range into discrete levels called counts. For a 14-bit digitizer, the number of counts is $2^{14} = 16384$, as illustrated on the y-axis of Figure 4.19. Consequently, the Least Significant Bit (LSB), the smallest voltage increment that the ADC can resolve, for channel 0 is $\frac{2}{16384} \approx 0.12$ mV, and for channel 2, it is $\frac{0.5}{16384} \approx 0.03$ mV. This finer resolution enables Lucite's signal to be more distinct and distinguishable.

Threshold: The threshold value is configurable from 0 to the maximum count of the ADC channels, expressed in LSB. For the coincidence signal, the threshold is set at 100 LSB, while for the Lucite signal, it is set at 10 LSB. Since the Lucite signal is triggered on the coincidence signal, a high threshold is unnecessary; a lower threshold is adequate to ensure signal detection.

Constant Fraction Discriminator (CFD): The CFD is essential for achieving precise timing measurements in signal processing. Unlike a leading-edge discriminator

that triggers at a specific threshold level, the CFD triggers at a fixed fraction of the pulse's peak amplitude. This method ensures that the trigger timing is consistent regardless of the pulse size, thereby overcoming the issue of timing walk, a variation in trigger timing caused by fluctuations in pulse amplitude. By delaying the signal and triggering at a set fraction (25% in this setup), the CFD provides a stable timing signal that is less affected by the pulse amplitude, leading to more accurate timing measurements. The utility of the CFD is evident in Figure 4.19, where the blue signal indicates the CFD's output and the red signal marks the precise trigger point, occurring when the rising edge of the input signal, displayed in black, reaches the pre-determined fraction of its maximum height.

Energy Coarse Gain: The energy coarse gain is used to rescale the measured signal charge and is expressed in terms of charge sensitivity, $\frac{\text{fC}}{(\text{LSB}\times\text{V}_{\text{pp}})}$, where V_{pp} represents the Input Dynamic Range. This setting allows the user to define the LSB regarding the charge data. For example, if the measured charge Q is 100 counts and the coarse gain is set to $40\frac{\text{fC}}{\text{LSB}}$, the calculated integrated charge would be 4pC.

Gate: Gate is the time window during which the charge of the signal is integrated to measure the total energy deposited by the incident particle. The Gate Width determines how long this window stays open.

Short Gate: Short Gate represents a time interval shortly after the initial rise of the pulse. It is shown in the green line in Figure 4.19.

Pre-gate: The pre-gate represents the starting position of both the gate and short gate, as indicated by the light green line in Figure 4.19.

Coincident mode: All channels are acquired in a logical AND operation with channel 0. The coincidence configuration includes channel 0 AND channel 1, channel 0 AND channel 2, extending to all available channels. Notably, only channels 0 and 2 had signals connected.

After configuring these detailed software settings for the digitizer, the energy distribution spectra obtained from the experimental setup, as processed by the software, are presented in Figure 4.20. The top plot displays the energy distribution for Lucite in configuration (1), demonstrating a specific energy range and count distribution. Conversely, the bottom plot represents configuration (2), showing a distinct distri-

bution pattern that spans a broader range of ADC channels. In the plots presented

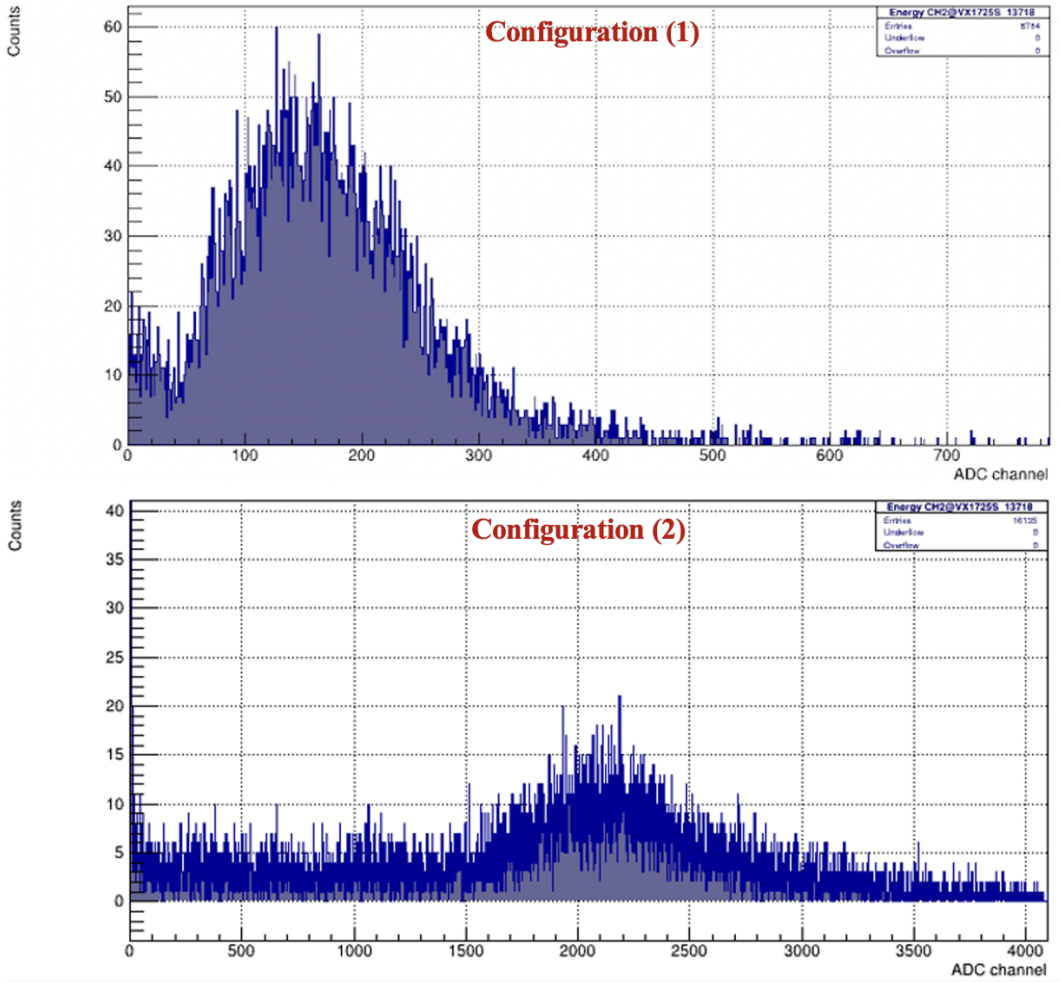

Figure 4.20: Energy distribution spectra of Lucite for two different configurations. Configuration (1) is represented in the top plot, demonstrating a specific energy range and count distribution. Configuration (2) is shown in the bottom plot, where a distinct distribution pattern is observed across a broader range of ADC channels.

in Figure 4.20, the regions at the beginning of the signals represent the pedestals, which indicate the baseline electronic noise and offsets in the absence of actual signal events. During the signal analysis, these pedestal values are subtracted to isolate the photon-generated signals. This correction ensures accurate quantification of the number of photons produced, as it removes any baseline fluctuations that could otherwise distort the measurement. The CoMPASS software generates ROOT output

files that serve as the basis for analysis. This analysis involves the removal of the pedestal from the signal, focusing on the region of interest, and reconstructing the energy distribution, as depicted in Figure 4.21. A Poisson function, appropriate for fitting the distribution of the number of generated photoelectrons, is applied to the data for configuration (1) and configuration (2).

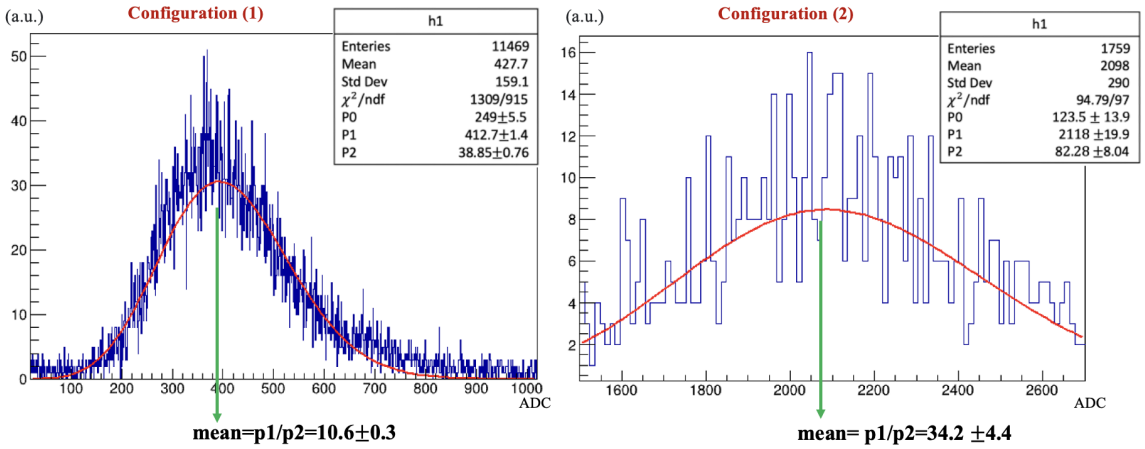

Figure 4.21: Energy distribution for Lucite was captured under two experimental configurations and fitted with a Poissonian function to estimate the number of generated photoelectrons. Configuration (1), illustrated in the left plot, suggests the generation of approximately ten photoelectrons. In contrast, Configuration (2), depicted in the right plot, indicates the generation of roughly 34 photoelectrons.

As outlined in Section 4.1.2, the emission of photoelectrons from the cathode within PMTs is a stochastic process governed by probabilistic principles. The emission events are random occurrences, making the Poisson distribution an appropriate model for such binary (yes-or-no) counting experiments. The Poisson distribution is described by the following function:

$$f(k;\lambda) = \Pr(X = k) = \frac{\lambda^k e^{-\lambda}}{k!}, \tag{4.1}$$

where k is the number of occurrences ($k = 0, 1, 2, \ldots$), λ is the expected rate of occurrences, e is Euler's number ($e \approx 2.71828\ldots$) [97].

In the ROOT analysis, a Poisson-like function is defined by the parameters P_0, P_1, and P_2, as shown in the legends of the plots in Figure 4.21. The parameter

P_0 normalizes the distribution, scaling it along the vertical axis. The parameter P_1 represents the mean number of occurrences (photoelectrons generated) within the given interval, analogous to λ in a standard Poisson distribution (Equation 4.1). The parameter P_2 adjusts the horizontal axis scale. Below is the implementation of the function in the ROOT analysis framework, using C++ [98]:

```
TF1 *f1 = new TF1("f1",
    "[0]*TMath::Power(([1]/[2]), x)*TMath::Exp(-([1]/[2]))/
         TMath::Gamma(x/[2] + 1)", 0., 10.);
```

Here, $[0] = P_0$ is the normalizing parameter, $[1]/[2] = P_1/P_2$ corresponds to the mean λ, and $[2] = P_2$ influences the distribution's spread. The variable x denotes the observed value, and the Gamma function is used to calculate the factorial of $x/[2]+1$.

The results of the fits for configuration (1) and configuration (2) are depicted in Figure 4.21. In configuration (1), the fit parameters are $P_0 = 249 \pm 5.5$, $P_1 = 412.7 \pm 1.4$, and $P_2 = 38.85 \pm 0.76$. The mean value of the distribution, calculated as mean $= \frac{P_1}{P_2}$, is 10.6 ± 0.3. In configuration (2), the fit parameters are $P_0 = 123.5 \pm 13.9$, $P_1 = 2118 \pm 19.9$, and $P_2 = 82.28 \pm 8.04$. The mean value for this configuration, calculated similarly, is 34.2 ± 4.4.

These fits highlight several key points. First, the normalization parameter P_0 serves as the normalizing factor, indicating the overall scale of the detected events. Configuration (1) shows a higher normalization value than Configuration (2), reflecting the higher frequency of detected events in the perpendicular orientation. The parameter P_1, which is analogous to the expected rate of occurrences λ in a standard Poisson distribution, is significantly higher in Configuration (2). This suggests that the alignment of the PMT with the direction of cosmic rays results in a greater average number of photoelectrons being generated. Meanwhile, P_2 adjusts the horizontal axis, affecting the spread of the distribution. Configuration (2) exhibits a larger P_2 value, indicating a broader spread in the distribution of the photoelectron counts. The mean value derived from the ratio $\frac{P_1}{P_2}$ is substantially different between the two configurations. Configuration (2) has a mean value approximately three times higher than Configuration (1). This indicates that aligning the PMT with the cosmic ray direction significantly enhances the detection efficiency and increases the mean count

of the generated photoelectron.

The ratio of #PEs in two experimental configurations is calculated as $\frac{34.2\pm4.4}{10.6\pm0.3} = 3.2\pm0.4$, which is in agreement with the ratio obtained from simulation configurations, $\frac{54.85\pm0.14}{15.02\pm0.03} = 3.65\pm0.01$. The #PEs observed in the simulations surpass those in cosmic testing. While a reasonable match in #PEs was anticipated, the discrepancy could be due to factors not included in the standalone simulations, such as Lucite's surface polish, the transparency of the optical grease, and the angular dependency of cosmic rays. Addressing these variables is time-consuming; hence, additional experiments were conducted at the Mainz Microtron, details of which will be provided in the following section.

This finding also aligns with the results from the comprehensive MOLLER simulation. In the simulation, the ratio of photoelectrons originating from the pion generator to those from the Møller electron generator increased from $5.5\% \pm 0.3\%$ to $16.8\%\pm0.6\%$. This increase in the ratio validates the experimental results, confirming that the experimental observations are consistent with the simulation predictions and that the simulation's results in other configurations can also be trusted. A comparison was conducted between the outcomes of cosmic ray testing and those anticipated for the complete MOLLER experiment, which employs all optimized components.

4.5 Verifying the Simulation Results: Beam Testing

To ensure the robustness and reliability of the results from the cosmic testing phase, a series of beam tests were performed. This section details the beam testing procedures and analyzes the data collected to verify the results from the cosmic tests and simulations. Subsection 4.5.1 describes the beam testing setup. It explains how the equipment and detectors were arranged and operated to closely replicate the conditions of the cosmic tests and simulations. The results from these beam tests are then presented, offering crucial comparative analysis with the simulation data. The discussion includes $\#PEs$ observed, the signal distributions, and the implications

of these observations for the accuracy of the simulations. Finally, Subsection 4.5.2 compares the results from beam tests with those from cosmic tests and simulation predictions, underscoring the precision of the simulations and identifying potential areas for improvement.

4.5.1 Beam Testing Setup

During beam testing, as depicted in Figure 4.22, a pion detector module, similar to that used in cosmic testing, is aligned with the 855.1 MeV electron beam. Upstream of the pion detector, a scintillator coupled to a PMT is positioned. The outputs from the pion detector and the scintillator are fed into a discriminator. The discriminator applies to filter the signals, allowing only those exceeding a pre-established threshold to be processed, thereby reducing background noise. The filtered signals are then directed into a CAEN N93B dual timer [99], an important component for timing control within the experiment, which introduces a precise timing gate, ensuring that the signal digitization by the CAEN V965 QDC [100] takes places within an accurately defined time frame.

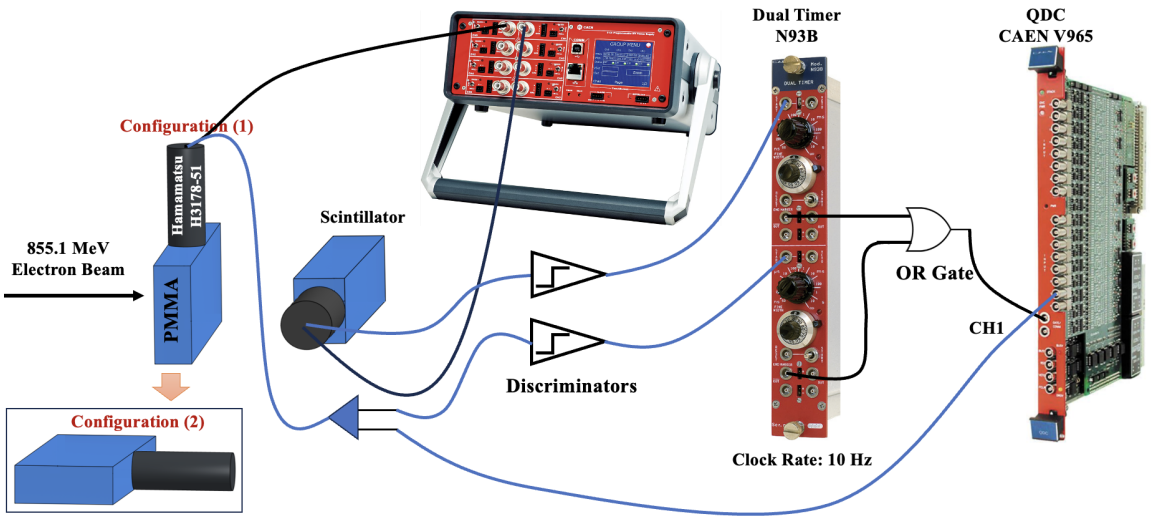

Figure 4.22: Schematic diagram of the beam testing setup at the Mainz Microtron (MAMI B), depicting the electron beam entering perpendicular to the PMT attached to the PMMA, denoted as configuration (1). The bottom left corner illustrates configuration (2) at a reduced scale to avoid repetition of figure components.

One aspect of the experimental arrangement involves integrating a clock trigger to determine the pedestal value. This pedestal represents the baseline of the ADC output in the absence of actual particle signals and establishes the zero point. It also helps distinguish between the intrinsic electronic noise of the system and the actual signals resulting from particle interactions. Operating at a frequency distinct from the beam signal, precisely at 10 Hz, as opposed to the beam clock of 5 kHz, the clock trigger ensures that pedestal measurements are independent of any beam-induced signals. While the beam induces a signal every 0.2 ms, the clock trigger alternates a pedestal measurement gate at 100 ms intervals. This scheduling guarantees that pedestal measurements occur exclusively when no particle interactions are present. The scintillator's signal is clock-triggered, and the detector's signal is time-delayed to fall within the established timing gate, as demonstrated in Figure 4.23. Then, an OR logic gate within a coincidence module combines the filtered signals from the trigger scintillator and the pion detector. This gate activates in response to any signal from the trigger scintillator or the pion detector, allowing for the differentiation of original particle events from the baseline pedestal readings, thereby enabling precise data acquisition and analysis.

In Figure 4.22, configuration (2) is demonstrated in the bottom left corner, wherein the electron beam enters in alignment with the PMT attached to the Lucite. The initial phase of our experiment involved testing configuration (2). For detailed information on the setting, refer to Table 4.5. As seen in the table, the duration for each dataset is set to 100 seconds, with a high voltage of 1700 V applied to the scintillator and 1500 V to the pion detector. The ADC with the resolution of 25 fC/LSB is used. The results of this test, along with the corresponding simulation, are presented in Figure 4.24. The plot on the left side of the figure 4.24 exhibits two distinct peaks: the first and smaller peak represents the pedestal. In comparison, the larger subsequent peak corresponds to the signal from the detector. The x-axis denotes the number of ADC channels. With a 12-bit ADC, there are $2^{12} = 4096$ potential ADC channels. The figure, however, focuses on a zoomed-in view of the signal, thereby showing fewer ADC channels for enhanced detail.

The method employed to fit a Poisson distribution to the pulse-height spectrum is

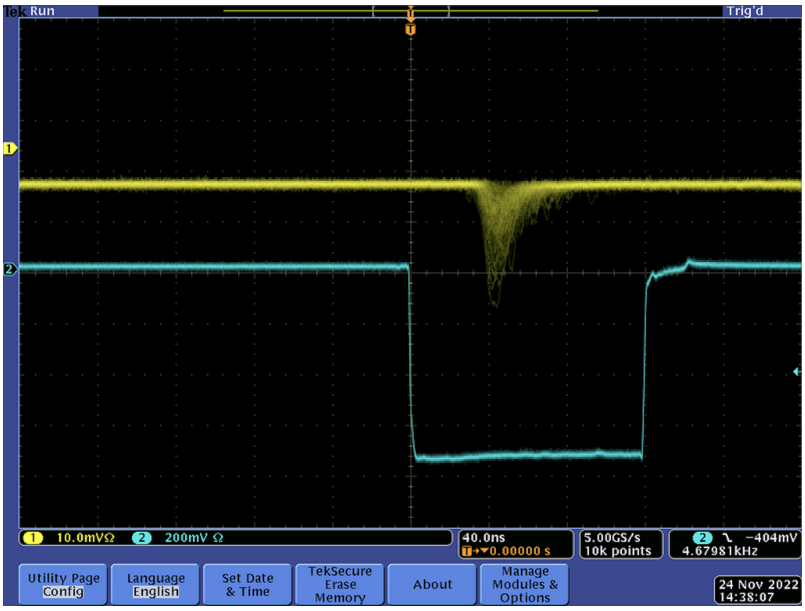

Figure 4.23: Screenshot of the oscilloscope screen showing the time-delayed detector signal (yellow) relative to the beam clock (blue). The detector's signal is carefully timed to fall within the timing gate.

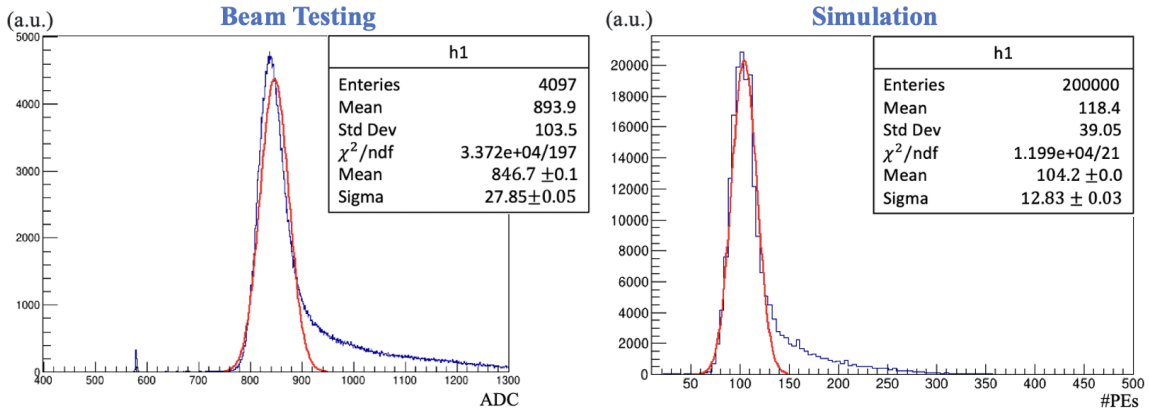

Figure 4.24: Comparative analysis of the signal obtained from beam testing (left) and the data generated from the simulation (right) for configuration (2). The left plot shows the distribution of ADC channels with a small pedestal peak and a pronounced signal peak. The right plot illustrates the $\#PEs$ from the simulation with a similar two-peak structure, pedestal peak at zero.

the same as in Section 4.4.2, but calculating $\#PEs$ is different. Under the assumption that the observed standard deviation (σ) in the fit is governed by Poisson statistics, where the variance (σ^2) is equivalent to the mean (λ), σ is thus expressed as $\frac{\sqrt{N}}{N}$.

Table 4.5: Beam Testing Settings

Settings	**Values**
Run Time	100 s
Beam Rate	5 kHz
Pedestal Rate	0.01 kHz
Scintillator PMT Voltage	1700 V
Lucite PMT Voltage	1500 V
ADC Resolution	25 fC/ADC Channel

Here, N represents the mean or average number of photoelectrons detected. The width of the pulse-height spectrum, a measure of the standard deviation, provides insight into the spread of the distribution of photoelectrons. If the spread is only due to the counting statistics intrinsic to the Poisson process, then the standard deviation of the spectrum is indicative of N, and the relationship $\sigma^2 = N$ is true. Given that N can be estimated from the fractional standard deviation (s), where s is defined as the ratio of σ to the net peak difference (peak of signal - peak of pedestal) from the fit, then N is inferred from $N = \frac{1}{s^2}$. This fractional standard deviation (s) is instrumental for accurately estimating the average number of photoelectrons.

This estimation is important for obtaining the minimum $\#PEs$, as the measured standard deviation (σ) might be inflated by factors such as electronic noise or pulse height variations due to the particle track's interaction location or angle. Given the utilization of a pencil electron beam, the pulse height variability resulting from the position or incident angle of the track is expected to be minimal. Using the method outlined, the minimum $\#PEs$ generated during beam testing can be calculated as $\left(\frac{(846.7-578.2)}{27.85}\right)^2 \approx 93$. Conversely, the $\#PEs$ produced in the corresponding simulation equals the mean value of the Gaussian fit, which is approximately 104. There is a reasonable agreement between the beam testing results and the simulation outcomes.

Further comparisons involved conducting experiments in configuration (1) in Figure 4.22 and comparing $\#PEs$ with those from the corresponding simulations. The minimum $\#PEs$ generated during the beam test is approximately 28, and in the corresponding simulation, it is approximately 30, as summarized in Table 4.6. A reasonable agreement between the beam testing results and the simulation outcomes is

observed in this configuration as well. The plots of this configuration are not shown to avoid repeating similar plots.

The ratio of the minimum number of generated $\#PEs$ between the two configurations for the experimental data was found to be 3.32 ± 0.39, while for the simulations was 3.51 ± 0.02. These values indicate consistency between the experimental results and the simulations. A summary of the results from the simulations, cosmic testing, and beam testing in terms of $\#PEs$ for both configurations and the ratios are presented in the subsequent subsection.

4.5.2 Comparison of Results from Simulations, Cosmic Testings, and Beam Testings

This subsection compares the $\#PEs$ obtained from cosmic testings, beam testings, and their respective simulations. The comparison is a crucial validation step for the simulation models by comparing simulated outcomes with empirical data. The $\#PEs$ and their ratios across different configurations are listed in Table 4.6.

Table 4.6: Comparison of the number of photoelectrons $\#PEs$ across different configurations and tests.

$\#PEs$	Cosmic Testing	Simulation of Cosmic Testing	Beam Testing	Simulation of Beam Testing
Config(1)	10.6 ± 0.3	15.02 ± 0.03	28.2 ± 0.2	29.91 ± 0.02
Config(2)	34.2 ± 4.4	54.85 ± 0.14	92.9 ± 1.6	104.20 ± 0.03
Ratio($\frac{(2)}{(1)}$)	3.2 ± 0.4	3.65 ± 0.01	3.29 ± 0.06	3.485 ± 0.003

Table 4.6 demonstrates a general consistency between the results from cosmic testing, beam testing, and their corresponding simulations. Although there is no exact one-to-one correspondence between the experimental outcomes and the simulations, the $\#PEs$ ratio between two different configurations remains constant within the experimental uncertainties. Furthermore, this ratio aligns with the ratio of $\#PEs$ from the pion generator to those from the Møller electron generator in the complete MOLLER experiment, calculated as $\frac{16.8 \pm 0.6}{5.5 \pm 0.3} = 3.055 \pm 0.199$.

Another comparison between the beam test and the simulations was the position dependency of the $\#PEs$. During the beam test, we directed the beam at five different positions across the pion detector, as seen on the right-hand side of Figure 4.25, and compared the number of generated #PEs with respect to these positions. The same process was implemented in the simulations to obtain the $\#PEs$. Figure 4.25 illustrates this comparison normalized at the centre position. The results indicate the acceptance of the detector to pions, showing that it does not receive the same amount of light from pions at different positions on the detector. Consequently, the detector does not equally sample all pions, giving more weight to the asymmetry in the center.

The agreement between the beam test results and the simulations demonstrates that the simulations correctly replicate the detector's response. This accuracy is essential because if the simulations did not match the beam test results, we could not confidently use them to interpret the pion asymmetry measurements. We measure an asymmetry for pions that are distributed across the front of the detector, combining the weighted asymmetry. The optical model of the detector is sufficiently accurate to achieve agreement between center and edge positions. However, in our simulations, more weight is assigned to the events at the outer edges of the detector than the beam test, leading to small discrepancies at the edges. This observation explains the discrepancy between the one-to-one results from cosmic testing and beam testing as detailed in Table 4.6. Cosmic testing primarily samples the photoelectron counts at the detector edges, whereas beam testing does not exhibit this characteristic.

In conclusion, this chapter has comprehensively outlined the development of the pion detector system, from its foundational principles to its practical construction. Key aspects have been meticulously detailed, such as the selection criteria for the active medium and PMTs, along with the mechanisms for distinguishing Cherenkov radiation from scintillation in pion detection. The optimization process of the pion detector system and its mechanical design were thoroughly explored. Moreover, the chapter explored validating the simulation results through cosmic and beam testings, including detailed analyses at the Mainz Microtron (MAMI) and comparative studies of the results from simulations, cosmic testings, and beam testings.

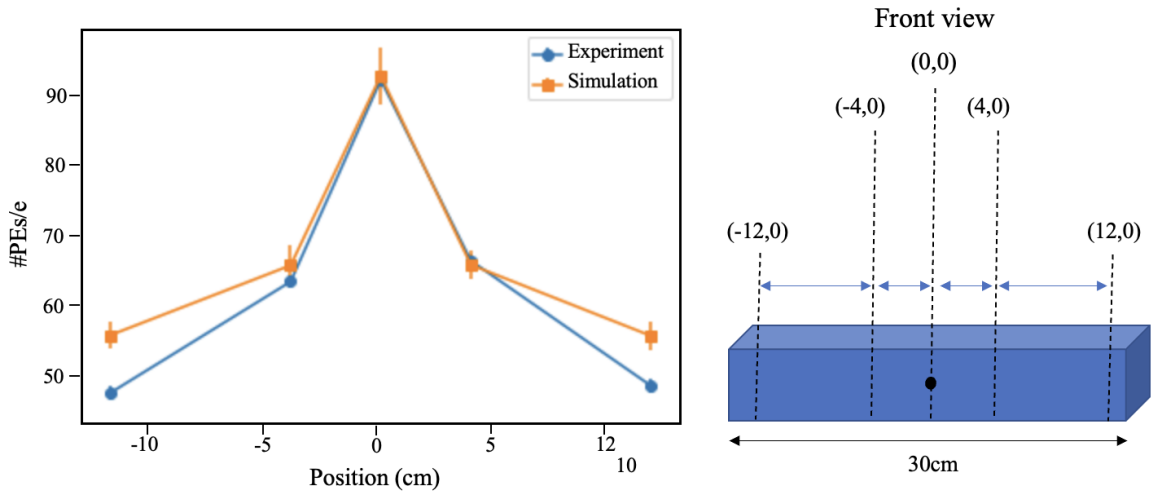

Figure 4.25: Position dependency of (#PEs): Left: The number of photoelectrons (#PEs) generated at different positions on the pion detector for both the beam test and the simulation. Right: Front view of the pion detector showing the five positions where the beam was directed: -12 cm, -4 cm, 0 cm (center), 4 cm, and 12 cm.

As we progress, Chapter 5 will shift focus to the post-experimental phase, introducing Bayesian Analysis as a sophisticated method for applying corrections to the data collected from the MOLLER experiment. This analytical approach, first employed in analyzing data from the Qweak experiment [16], offers a robust framework for refining experimental results and enhancing the accuracy of our interpretations. The upcoming chapter will elucidate the methodology and utility of Bayesian Analysis in the context of high-precision experimental physics.

Chapter 5

Bayesian Analysis Methodology

Bayesian statistics is a method of data analysis founded on Bayes' theorem. In this approach, prior knowledge about parameters in a model is updated based on observed data. The combination of prior knowledge and data collected through observation determines a posterior probability distribution. Prior knowledge is expressed as a prior probability distribution, and the likelihood function is constructed from the data collected through observation. As a result, the probability of future events is predicted by the posterior. The stages involved in Bayesian analysis, from determining the prior distribution and data models to deducing inference, are described in this chapter. Specifically, the impact of Bayesian analysis in enhancing the precision of measurements in the Qweak and MOLLER experiments, which are two examples of PVES experiments, is outlined.

5.1 Introduction to Bayesian Analysis

Statistics comprises two primary methodologies: frequentist and Bayesian approaches. Understanding the distinctions between these approaches is crucial, as it significantly influences data analysis and the interpretation of scientific results. The core difference between frequentists and Bayesians lies in their interpretation of probability. Frequentists define probability in terms of repeated measurements. For instance, when a measurement is repeated multiple times, each trial might yield a

different value due to statistical uncertainties. Over numerous trials, the frequency of any particular value defines the probability of observing that value. Thus, probabilities are associated with the frequencies of repeated events.

In contrast, Bayesian statistics fundamentally differs by directly defining probabilities as measures of belief or certainty about the occurrence of an event or the truth of a hypothesis. In Bayesian analysis, probability serves as the universal language for describing the likelihood of hypotheses and making decisions under uncertainty. Direct probabilistic inference enables Bayesian to provide more informed estimates and predictions, a conceptual difference that often leads to divergent methods in statistical data analysis. For example, weather forecasting uses Bayesian methods to predict the probability of various weather conditions based on prior data and current observations.

The foundation of Bayesian statistics was first described in 1763 by Reverend Thomas Bayes and later published by Richard Price [101]. In 1825, Pierre Simon Laplace published the Bayes' theorem [102]. In the past 50 years, the ideas of inverse probability and Bayes' theorem have become prominent tools in applied statistics, although they are long-standing in mathematics. Bayesian methods of data analysis are now widely used across different fields of science such as ecology [103], social and behavioral sciences [104], genetics [105], medicine [106], educational research [107], epidemiology [108], organizational sciences [109],[110], modeling [111], nuclear physics [112],[113], and experimental data analysis [114].

5.2 Theory

In this section, Bayes' theorem is derived, and its essential elements are explained. Furthermore, the formalization of prior distributions is discussed, emphasizing the role that priors play in shaping the posterior distribution. The process of determining the likelihood distribution and selecting methods for sampling from the posterior distribution is also examined. This discussion culminates in analyzing the applicability of Bayesian methods within PVES experiments.

5.2.1 Bayes' theorem

The Bayesian approach studies conditional probability. When two events A and B are dependent or conditional, the basic conditional probability is expressed as:

$$P(B|A) = \frac{P(B \cap A)}{P(A)}, \tag{5.1}$$

where $P(B|A)$ denotes the probability of event B given the occurrence of event A, $P(B \cap A)$ represents the probability of intersection of events A and B, and $P(A)$ is the probability of event A occurring. Noting that $P(A|B) \neq P(B|A)$ and $P(B \cap A) = P(A \cap B)$, It can be written similarly:

$$P(A|B) = \frac{P(A \cap B)}{P(B)}. \tag{5.2}$$

Based on Equation 5.1, Equation 5.2 can be rewritten as:

$$P(A|B) = \frac{P(B|A)P(A)}{P(B)}. \tag{5.3}$$

Equation 5.3 is known as Bayes' rule. Extending these principles to the context of data and model parameters, where A is the observation of a specific dataset y and B is the realization of the model with parameters θ, Bayes' rule can be expressed as:

$$P(\theta|y) = \frac{P(y|\theta)P(\theta)}{P(y)}. \tag{5.4}$$

Here, $P(\theta|y)$ is the conditional probability of the model parameters θ given the data y, representing the posterior distribution [1]. $P(y|\theta)$ is the likelihood function, the probability of the data given the model parameters. $P(\theta)$ is the prior distribution, reflecting subjective beliefs or existing knowledge about the parameters. The denominator $P(y)$ serves as a normalizing constant to ensure the posterior distribution sums

[1] Discrete events have distinct probabilities, while continuous events are described by a probability density function.

to one or integrates to one over all θ[2]. The three fundamental steps of the typical Bayesian workflow are:

1. Utilize the prior distribution, typically chosen before data collection, to represent existing knowledge about a parameter in a statistical model.

2. Employ the observed data to determine the likelihood function.

3. Combine the prior distribution and likelihood function to form the posterior using Bayes' theorem.

The posterior distribution integrates prior knowledge with the observed data, providing updated insights and facilitating inferences.

5.2.2 Formalizing Prior Distributions

Prior distributions have a determining role in Bayesian statistics. They represent the initial beliefs or knowledge about model parameters before observing the data. Prior distributions can take various forms, ranging in levels of informativeness from highly informative to non-informative. Three basic categories of priors can be used to categorize the level of (un)certainty: informative, weakly informative, and diffuse. An informative prior conveys a high degree of certainty about the model parameters. When strong existing knowledge or data is available to constrain the parameters, an informative prior is a suitable choice and will have a comparatively larger impact on the posterior. In this case, with a normally distributed prior, a small variance is typically expected. A weakly informative prior provides some guidance without being overly specific, maintaining an intermediate level of certainty. For a normally distributed prior, this would mean a larger variance than an informative prior, allowing the observed data to have a more substantial influence on the posterior. Finally, a diffuse prior reflects a large uncertainty or neutrality about the model parameter, making it suitable for situations without prior knowledge of the parameters. Here, the posterior distribution is predominantly influenced by the observed data.

[2]For discrete random variables, the posterior distribution sums to one. For continuous random variables, the posterior distribution integrates to one.

The choice of prior distribution is a critical step in Bayesian analysis, as it encapsulates prior beliefs and knowledge, influencing the resulting posterior distribution.

5.2.3 Determining the Likelihood Function

The likelihood function is a fundamental concept in frequentist and Bayesian inference, indicating how strongly the observed data support various potential values of unknown parameters. Frequentists treat unknown parameters as fixed, defining the likelihood as a conditional probability distribution of the data given these fixed parameters. In contrast, Bayesian inference considers the observed data as fixed and the parameters as variable, with the likelihood being a function of these parameters. To explain the likelihood function and the difference between frequentist and Bayesian, we refer to the example of optical photon counting [115]. In the frequentist perspective, assuming a single observation $D_i = (f_i; \sigma f_i)$, the probability distribution of the measurement, given the photon flux f (the mean number of photons measured per second) with Gaussian uncertainties, is expressed as:

$$P(D_i|f) = \frac{1}{\sqrt{2\pi\sigma f_i^2}} e^{\left[\frac{-(f_i-f)^2}{2\sigma f_i^2}\right]}. \tag{5.5}$$

Here, f_i and σf_i represent the observed flux and uncertainty in the i^{th} measurement, respectively. In the frequentist approach, the best estimate of photon flux that maximizes likelihood is determined using maximum likelihood estimation [116]. This involves finding the value of f that maximizes $P(D_i|f)$, typically done by setting the derivative of the probability function to zero. A set of all measurements can be combined to construct the likelihood L:

$$L(f) = \prod_{i=1}^{N} P(D_i|f). \tag{5.6}$$

For computational simplicity, the log-likelihood is often used, as maximizing this also maximizes the likelihood:

$$-\ln[L] = \frac{-1}{2}\sum_{i=1}^{N}\left[\ln(2\pi(\sigma f_i)^2) + \frac{(f_i - f)^2}{\sigma f_i^2}\right]. \tag{5.7}$$

By setting the derivative of Equation 5.7 to zero, $\frac{\partial \ln[L]}{\partial f}|_{f=\hat{f}} = 0$, the estimated value of f that maximizes the likelihood is:

$$\hat{f}_{Frequentist} = \frac{\sum_{i=1}^{N} f_i/\sigma f_i^2}{\sum_{i=1}^{N} 1/\sigma f_i^2}. \tag{5.8}$$

In the case of equal uncertainties (σf_i), $\hat{f}$ simplifies to the mean of the observed data:

$$\hat{f}_{Frequentist} = \frac{1}{N}\sum_{i=1}^{N} f_i. \tag{5.9}$$

In Bayesian analysis, probabilities are both the starting point and the outcome. The same likelihood function used in the frequentist approach is applied in Bayesian analysis, but its role is different. It is used to update the prior distribution to a posterior distribution. Referring to Equation 5.5, the posterior distribution in Bayesian terms is:

$$P(f|D_i) = \frac{P(D_i|f)P(f)}{P(D_i)}. \tag{5.10}$$

$P(f|D_i)$ is the posterior distribution, $P(D_i|f)$ is the likelihood, and $P(f)$ is the prior distribution, which can be informative, weakly informative, or diffuse. To demonstrate how Bayesian analysis is applied to the example of optical photon counting, a Gaussian prior distribution is considered, characterized by a mean of f_0 and a variance of σ_f^2:

$$P(f) = \frac{1}{\sqrt{2\pi\sigma f_0^2}} e^{\left[\frac{-(f-f_0)^2}{2\sigma f_0^2}\right]}. \tag{5.11}$$

Using Bayes' theorem (Equation 5.10), this prior distribution is updated with the

observed data $D_1 = (f_1; \sigma^2_{f_1})$ to obtain the posterior distribution $P(f|D_1)$:

$$P(f|D_1) = \frac{P(D_1|f)P(f)}{P(D_1)}. \tag{5.12}$$

The resulting posterior distribution, which remains Gaussian, features updated parameters. These include the mean f_1 and the variance $\sigma^2_{f_1}$, which can be determined as follows:

$$f_1 = \frac{\left(\frac{f_1}{\sigma f_1^2}\right) + \left(\frac{f_0}{\sigma f_0^2}\right)}{\left(\frac{1}{\sigma f_1^2}\right) + \left(\frac{1}{\sigma f_0^2}\right)}, \tag{5.13}$$

$$\sigma f_1 = \left(\left(\frac{1}{\sigma f_1^2}\right) + \left(\frac{1}{\sigma f_0^2}\right)\right)^{-1}. \tag{5.14}$$

This posterior distribution, $P(f|D_1)$, then serves as the prior distribution for the next step in the Bayesian analysis when new data $D_2 = (f_2; \sigma^2_{f_2})$ is observed. The new posterior distribution is obtained by updating the prior distribution with the likelihood of the new data:

$$P(f|D_2) = \frac{P(D_2|f)P(f|D_1)}{P(D_2)}, \tag{5.15}$$

where $P(f|D_2)$ is the new posterior distribution, $P(D_2|f)$ represents the likelihood of the new data given the parameter f, and $P(f|D_1)$ is the prior distribution, which was the posterior distribution from the previous step. This iterative updating process continues as new data is collected, continually refining the estimate of f. Consequently, when $D_i = (f_i; \sigma^2_{f_i})$ is observed, $P(f|D_{(i-1)})$ is updated to obtain the posterior distribution $P(f|D_i)$ as follows:

$$P(f|D_i) = \frac{P(D_i|f)P(f|D_{i-1})}{P(D_i)}. \tag{5.16}$$

Equation 5.16 is comparable to Equation 5.10; the primary distinction is that here, the prior distribution explicitly serves as the posterior distribution from the previous step. In the final step of the Bayesian analysis, the resulting posterior distribution

characterized by a mean $\hat{f}_{\text{Bayesian}}$ and variance $\sigma^2_{\text{Bayesian}}$ as follows:

$$\hat{f}_{\text{Bayesian}} = \frac{\sum_{i=1}^{N}\left(\frac{f_i}{\sigma f_i^2}\right) + \left(\frac{f_0}{\sigma f_0^2}\right)}{\sum_{i=1}^{N}\left(\frac{1}{\sigma f_i^2}\right) + \left(\frac{1}{\sigma f_0^2}\right)}, \tag{5.17}$$

$$\sigma f^2_{\text{Bayesian}} = \left(\sum_{i=1}^{N}\left(\frac{1}{\sigma f_i^2}\right) + \left(\frac{1}{\sigma f_0^2}\right)\right)^{-1}. \tag{5.18}$$

The posterior mean $\hat{f}_{\text{Bayesian}}$ represents the updated estimate of the photon flux f, incorporating both the observed data and the prior knowledge. The posterior variance $\sigma f^2_{\text{Bayesian}}$ combines the uncertainties from both the prior distribution and the data, weighted according to their respective precisions. In the case of no prior knowledge, the variance of the prior distribution approaches infinity, $\sigma f_0^2 \to \infty$. Consequently, Equation 5.17 simplifies to Equation 5.8. Therefore, in the absence of prior information, the variance is determined solely by the data. The comparison between Equation 5.17 and Equation 5.8 illustrates how the two approaches yield distinct interpretations and results when employing the same likelihood function.

In practice, the posterior distribution is not always as simple as a Gaussian function. For more complex problems, the posterior distribution may require sophisticated model-fitting techniques and computational methods. The next subsection will discuss model fitting in the Bayesian context.

5.2.4 Model fitting

Statistical models are designed to simplify reality, enhancing our understanding of the key elements of the system. In the frequentist framework, model fitting primarily focuses on estimating results using the maximum likelihood estimation method [116]. In the Bayesian framework, the emphasis is on estimating the posterior distribution of model parameters. Direct inference on the posterior distribution in Equation 5.4 is feasible in low dimensions and with simple distributions. However, the posterior distribution is usually very complicated and high-dimensional. This means that the exact evaluation of the posterior distribution is practically infeasible, which necessi-

tates the use of approximation technique. Historically, the computational challenges associated with Bayesian inference have led to a preference for frequentist methods until the development of more efficient computational methods.

The literature proposes various methods to address these challenges. Approximate Bayesian Computation (ABC) methods [117], Integrated Nested Laplace Approximations (INLA) [118], and Variational Bayesian methods [119] are referred to as non-Markov Chain Monte Carlo (MCMC) methods. These methods tend to approximate only the marginal posterior distributions and do not adequately address the approximation of joint posterior distributions. While these techniques can be fast and computationally efficient, they are often specific to certain problems or limited to families of known analytical distributions. Alternatively, MCMC methods, which will be explained in more detail, attempt to approximate the joint posterior distribution. These methods are more computationally intensive but are generally applicable to a wider range of problems. Therefore, this thesis focuses on employing MCMC methods within Bayesian analysis.

In 1990, Gelfand and Smith introduced the MCMC method [120], particularly suitable for Bayesian analysis [121]. The method stands out for its computational efficiency. It has become a widely used algorithm in Bayesian statistics, where the Monte Carlo part denotes the sampling process, and the Markov Chain part describes the mechanism for obtaining these samples. Monte Carlo methods are computational algorithms designed to estimate numerical values for various problems, such as evaluating integrals using repeated random sampling. Consider the task of estimating an expected value defined by the following equation:

$$E[f(X)] = \int_{-\infty}^{+\infty} f(x) \frac{1}{\sqrt{2\pi}} e^{-x^2/2} \, dx, \tag{5.19}$$

where X follows a standard normal distribution. Computing this integral analytically may be challenging; thus, we can employ a Monte Carlo method to approximate $E[f(X)]$. By generating n random samples $x_1, \ldots, x_n$ from the standard normal distribution, we can estimate $f(x_i)$ for each sample and approximate $E[f(X)]$ using

the following estimator:

$$E(f(X)) \approx \mu_n = \frac{1}{N} \sum_{n=1}^{N} f(x_n). \tag{5.20}$$

While obtaining samples from the standard normal distribution is straightforward, complications arise when the required samples originate from a complex distribution, say an unknown posterior distribution. MCMC methods address this issue by providing a means to sample from distributions. The underlying principle is constructing a Markov Chain that converges to the stationary distribution, a concept that will be explained subsequently.

A discrete Markov Chain is defined by a sequence of random variables, $X_0, X_1, X_2, \ldots$, that can take values in the state space $\mathcal{X}$. The probability distribution of the state at step n is denoted by $P(X_n)$, where $X_n \in \mathcal{X}$. The fundamental properties of Markov Chains is the Markov property, which is expressed as:

$$P(X_{n+1} \in A \mid X_0, X_1, \ldots, X_n) = P(X_{n+1} \in A \mid X_n) \quad \forall A \subseteq \mathcal{X}. \tag{5.21}$$

This formula implies that the probability distribution for the next state is determined only by the current state. In other words, the conditional probability $P(X_{n+1} \mid X_n)$ depends solely on X_n, not on the preceding states $X_0, X_1, \ldots, X_{n-1}$. This property simplifies the analysis by reducing the dependency of future states on the entire history to just the current state. However, the key to the method's success is not the Markov property but rather the fact that the approximate distributions are improved at each step in the simulation, ultimately converging to the target distribution.

The Markov chain is defined by some initial parameter values and transition probabilities. The choice of transition is crucial as it determines the efficacy of the MCMC method. Typically, a predetermined distribution is used to propose new values, which are then accepted or rejected based on specific criteria. Upon acceptance of new values, the Markov chain transitions to a new state; if rejected, it remains unchanged. Various choices for transitions include the Gibbs sampler [122], Metropolis-Hastings random walk sampler [123], slice sampler [124], and No-U-Turn Sampler [125], each

with unique properties. A warm-up or burn-in phase is often necessary in MCMC algorithms to ensure the chain moves toward a productive area of the parameter space. This involves discarding initial samples not representative of the effective parameter values.

One of the first and most popular MCMC methods is the Metropolis algorithm that was first introduced by Metropolis et al. [126] and then extended as the Metropolis-Hastings (MH) algorithm by Hastings [127]. In this method, sampling is obtained from the posterior distribution of the parameter (θ) given the prior and likelihood, i.e., $P(\theta|y) = \frac{P(y|\theta)P(\theta)}{P(y)}$. We know how to write $P(\theta|y)$ but do not know how to apply sampling to this distribution due to its complexity. The MCMC method is applied to determine which values of θ to be accepted or rejected. The MH algorithm accepts a value as a new sampling point with the following probability:

$$\alpha(\theta_{i+1}|\theta_i) = \min(1, \frac{P(\theta_{i+1})P(y|\theta_{i+1})}{P(\theta_i)P(y|\theta_i)}) = \min(1, H), \tag{5.22}$$

where H is called the Hastings ratio. According to the formula above, the probability of transitioning from the current position θ_i to the new point θ_{i+1} depends on the posterior value at the new point to the old point, $(P(\theta_{i+1}|y)/P(\theta_i|y))$. First, the jump will be accepted if the ratio is more than 1, i.e., when the posterior probability increases. Second, the target posteriors' ratio guarantees that the chain will eventually move to areas with high probabilities, which is more effective than wandering around the entire domain. Additionally, the sampling process is designed so that we expect to draw from a distribution that becomes increasingly closer to $p(\theta|y)$ at each step. This ensures that the approximate distributions improve progressively, converging to the target posterior distribution.

Having established the foundational principles and operational mechanics of the MH algorithm, we now turn our attention to the practical application of MCMC methods, particularly through a variety of software packages designed to facilitate these complex computations.

5.2.5 Software Tools and Practical Considerations for MCMC Methods

According to the different methods, a range of software packages implements MCMC methods, often providing options for customization. This allows analysts to focus on specifying prior distributions and models without considering technical programming aspects. BUGS, as the original general-purpose Bayesian inference engine, uses Gibbs and Metropolis sampling. WinBUGS233 is the Windows-based version of the software, and OpenBUGS234 is the open-source version available on Linux and Mac. Gibbs sampling and Hamiltonian Monte Carlo (HMC) are two features of the open-source Bayesian modeling and inference system PyMC. Using HMC, the open-source Bayesian inference engine Stan can be used with R, Python, Julia, MATLAB, and Stata. In this research, Stan with Python is used. Stan [128], a powerful Bayesian modeling language released in 2012, offers HMC with No U-Turn Sampler (NUTS) [125], an algorithm providing efficient fits for complex models.

HMC [129] is a variant of the MH algorithm that enhances sampling efficiency by utilizing principles from Hamiltonian dynamics. The core idea behind HMC is to introduce auxiliary momentum variables and utilize Hamiltonian dynamics to propose new states, thereby achieving a more efficient exploration of the target distribution. The Hamiltonian function $H(\theta, p)$ is defined as the sum of the potential energy $U(\theta)$ and the kinetic energy $K(p)$:

$$H(\theta, p) = U(\theta) + K(p). \tag{5.23}$$

Here, θ represents the position variables, which correspond to the parameters of interest, and p denotes the momentum variables, which are auxiliary variables introduced to aid the sampling process. The potential energy $U(\theta)$ is typically defined as the negative log-posterior, given by $U(\theta) = -\log P(\theta|y)$, where $P(\theta|y)$ is the posterior distribution of the parameters θ given the data y. The kinetic energy $K(p)$ is generally defined as $K(p) = \frac{1}{2}p^T M^{-1} p$, where M is the mass matrix, which is often chosen to be the identity matrix for simplicity. The evolution of the position and momentum

variables is governed by Hamilton's equations:

$$\frac{d\theta}{dt} = \frac{\partial H}{\partial p} = M^{-1}p \quad \text{and} \quad \frac{dp}{dt} = -\frac{\partial H}{\partial \theta} = -\nabla U(\theta). \tag{5.24}$$

These equations describe how the position and momentum change over time. HMC employs the leapfrog integration method [129] to numerically solve Hamilton's equations and propose a new state. The MH acceptance criterion is applied to decide whether to accept or reject the new state. In summary, by incorporating Hamiltonian dynamics, HMC can make larger, more informed steps in the parameter space compared to traditional MCMC methods. This results in more efficient sampling, particularly in high-dimensional spaces.

The efficiency gains of HMC come with certain complexities. Firstly, HMC necessitates the computation of the gradient of the log-posterior. For complex models, this computation can range from being time-consuming to outright infeasible. Secondly, HMC requires users to determine two critical hyperparameters: the step size and the number of steps to simulate the Hamiltonian dynamics. Inappropriate selection of these hyperparameters can lead to inefficiencies, making the sampling process suboptimal. NUTS is an extension of HMC, specifically designed to adaptively tune the step size and the number of steps during the burn-in period, and continues to adapt throughout the MCMC run.

The core concept of NUTS is to simulate the Hamiltonian dynamics until the system's trajectory begins to reverse direction, heading back toward its starting point. Mathematically, this reversal is detected when the momentum vector p aligns in the direction pointing back to the initial position θ_0. This condition can be expressed as $(\theta - \theta_0)^T p < 0$. The aim is to execute as large a move as possible without retracing steps, as moving back toward the starting point is unproductive for exploration. NUTS effectively constructs trajectories that prevent this reversal by performing simulations in both forward and backward directions in time. It starts with a single step, either forward or backward, then continues to double the trajectory length: two, four, and so on. This exponential expansion continues until it detects that either end of the trajectory begins to curve back toward the origin. In NUTS, the algorithm

checks for U-turns at each step, ensuring the trajectory does not reverse. This is mathematically represented by checking $(\theta_j - \theta_0)^T p_j > 0$ and $(\theta_j - \theta_{j-1})^T p_j > 0$, where θ_j and p_j represent the position and momentum at step j. In the final step, NUTS employs a selection process from the ensemble of points accumulated during the trajectory-doubling phase. This selection is executed in such a way that the detailed balance is preserved. Detailed balance ensures that the probability of transitioning from one state to another is the same as the probability of transitioning back from the second state to the first. This property guarantees that, over time, the Markov chain will sample from the correct target distribution. By preserving detailed balance, NUTS ensures that the samples it generates are representative of the target distribution, meaning that they accurately reflect the underlying statistical properties of the model being studied. The probability of selecting a point θ from the trajectory is proportional to $\exp(-H(\theta, p))$, where $H(\theta, p)$ is the Hamiltonian evaluated at the position θ and momentum p. As a result, NUTS offers a powerful and efficient alternative to conventional HMC, significantly reducing the complexity of hyperparameter tuning and improving the practical usability of MCMC methods for complex Bayesian models.

This basic introduction to HMC and NUTS summarizes their roles in Bayesian analysis. For more detailed mathematical explanations, readers are referred to reference [125]. This thesis focuses on applying Bayesian analysis to PVES experiment data rather than probing into the mathematical details or modifying Bayesian algorithms. Choosing the most suitable and user-friendly software packages and programming languages is important. Stan utilizing Python (PyStan [128]) is the preferred tool in Bayesian analysis, as mentioned before, serving as a front-end. Stan still uses C++ in the backend for rapid computations. Building upon these foundational concepts, the following sections will examine the implementation of Bayesian analysis in two specific PVES experiments: Qweak [16] and MOLLER [21].

5.3 Enhancing Precision of Extracted Quantities in the Qweak Experiment

In this section, a brief introduction to the Qweak [16] experiment, a PVES study aimed at measuring the weak charge of the proton, is provided first. The Qweak apparatus was not explained in Chapter 3 because the main scope of the thesis is the MOLLER experiment [21]. The Qweak results [47] are included here to demonstrate the application of Bayesian analysis. Then, the inputs, parameters, and the model for the Bayesian analysis are discussed. Finally, the results from the Bayesian analysis are compared with those from the previously conducted optimization process, the Monte Carlo minimization method, to illustrate differences in how each approach handles uncertainty and refines measurement precision.

5.3.1 Qweak Experiment

The Qweak experiment [16] was a precision measurement experiment designed to determine the weak charge of the proton. This was done by measuring the parity-violating asymmetry in elastic electron-proton scattering at low momentum transfer. The same as the MOLLER experiment [21], the aim is to explore new physics beyond the Standard Model of particle physics. Figure 5.1 shows a schematic of the Qweak experiment, illustrating the key components and their arrangement for measuring the weak charge of the proton.

In this experiment, a polarized electron beam with an energy of 1.165 GeV and a current of 150 μA is directed toward a 35 cm liquid hydrogen target. The polarization of the beam, approximately 85%, is a critical factor in the experiment as it allows for the measurement of parity-violating asymmetry in the scattering process. As the electrons interact with the protons in the hydrogen target, they are scattered elastically. The primary collimator shapes the electron beam before it reaches the target. The scattered electrons then pass through a toroidal magnet designed to focus the scattered electrons. The eight fused silica (quartz) detectors are used to identify the scattered electrons, completing the detection setup. Figure 5.2 shows the

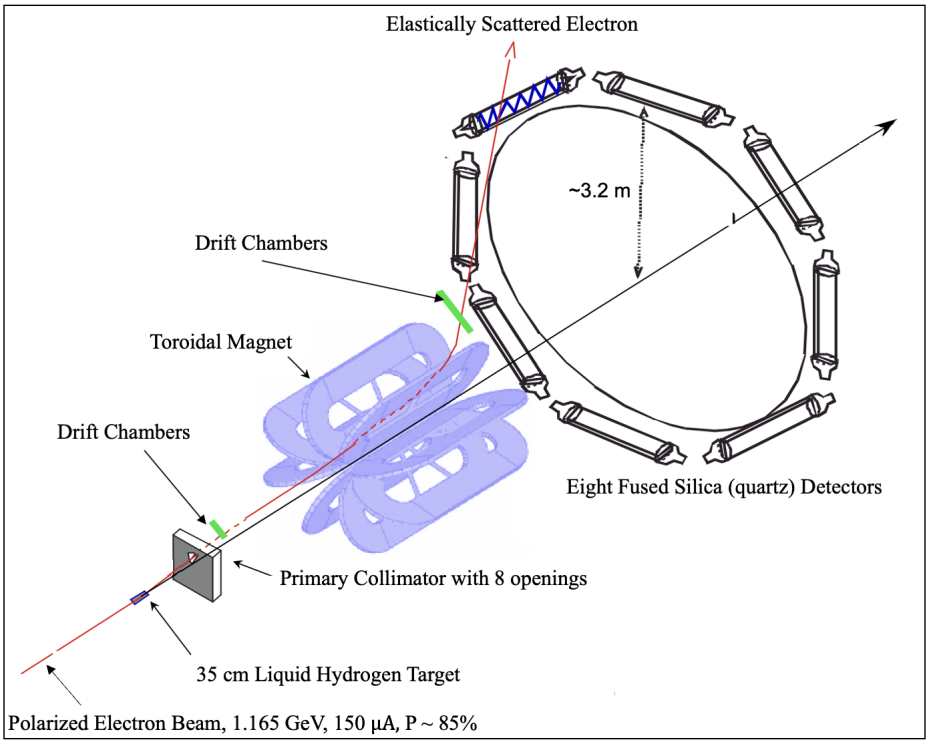

Figure 5.1: Schematic of the Qweak Experiment: A polarized electron beam targets liquid hydrogen to measure proton weak charge, guided by a primary collimator and toroidal magnet. Electron paths are tracked by drift chambers, identified by quartz detectors [130].

frontal view of eight main detectors (MD) arranged around the target.

In an ancillary measurement of the Qweak experiment, the beam energy was increased to 3.35 GeV to measure a small (approximately 0.1%) contamination from pions and other charged hadrons at higher energies. A 10.2 cm thick lead wall was placed in front of the lowermost detector (MD7), labeled as main detector 7 (MD7). This lead wall attenuates electrons more than pions due to their differing interactions with the dense material, effectively enhancing the pion dilution in the asymmetry measured by MD7. Consequently, MD7 has the role of the pion detector, similar to the dedicated pion detector in the MOLLER experiment 3.4.3.2. The unique response of MD7 to the electron and pion mix, providing a different linear combination of particle contributions compared to the other seven detectors, is critical for isolating the asymmetries attributed to scattered electrons from those due to pions. The abil-

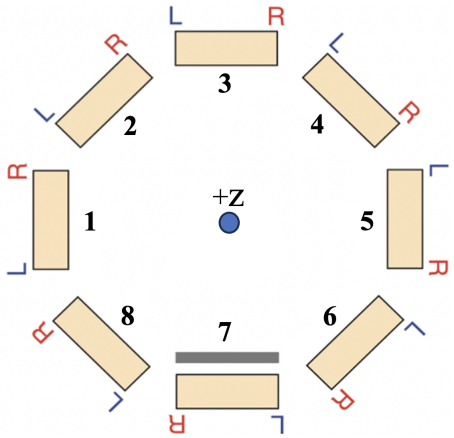

Figure 5.2: Frontal View of Detector Array in Qweak Experiment: The eight-detector configuration with a lead wall in front of MD7 to enhance pion detection.

ity to analyze these distinct linear combinations and measure the pion background fraction is essential for the experiment to separate and quantify the individual contributions to the overall measured asymmetry. This analysis is further complicated by the beam's polarization state. Ideally, data would have been collected using a longitudinally polarized beam and employing a detector system capable of rejecting all scattered particles except for electrons. The measured asymmetries would then reflect only the parity-violating asymmetry from the scattered electrons. However, the experimental conditions were not ideal, due to a partially transverse electron beam and a significant background from pions. To further the analysis, it was necessary to isolate the parity-violating asymmetry from the scattered electrons by distinguishing between longitudinal and transverse asymmetries and separating the contributions of electrons from pions. This separation process is described in detail subsequently.

The beam polarization angle quantifies the orientation of the beam electrons' polarization vectors relative to the beam axis in the horizontal plane. A polarization angle of 0° ($\theta_P = 0°$) is defined as parallel to the beam axis, pointing downstream. These vectors are decomposed into a longitudinal component along the beam axis and a transverse component perpendicular to the beam axis in the horizontal plane, leading to associated longitudinal or transverse asymmetries. In the ancillary measurement of the Qweak experiment [47], beam polarization was dictated by another

experimental hall, resulting in the Qweak primary target receiving a beam with mixed polarization. As depicted in Figure 5.3, the polarization angle of the beam, θ_P, was $-19.7^\circ \pm 1.9^\circ$, with a positive angle denoting rotation from the beam axis (+z-axis) towards the beam right (+x-axis). Consequently, a substantial undesired transverse component (about 33%) was introduced. The dataset containing this mixed polarization is referred to as mixed data (108 hours of data-taking), as it includes the physics asymmetry of interest, and the data was acquired under these conditions. Several runs with purely transverse polarization were necessary to properly account for the transverse component in the mixed dataset. These runs, with a beam polarization angle of $92.2^\circ \pm 1.9^\circ$ [131], were essential for analyzing and correcting the transverse background. This dataset is known as transverse data (4.3 hours of data-taking).

As mentioned in Chapter 2, when we talk about the asymmetry components in all the subsequent sections, it means that the asymmetry arises from the polarization components.

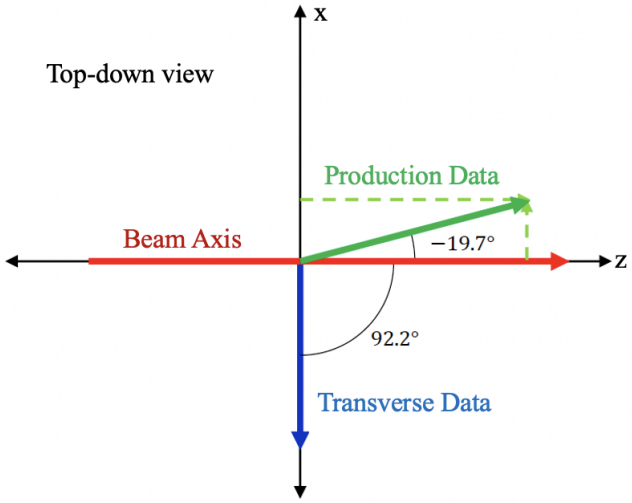

Figure 5.3: Top-down view of the beam polarization: Illustrating the red arrow to indicate the downstream direction of the beam axis, with the mixed data (green dashed arrow) showing a combination of longitudinal and transverse polarization at a -19.7° angle. The transverse data (solid blue arrow) indicates an almost pure horizontal polarization at a 92.2° angle relative to the beam axis [132].

The Qweak experiment [47] utilized two data acquisition modes similar to those described for the MOLLER experiment in Section 3.5: the high beam-current in-

tegrating mode and the low beam-current counting mode. The apparatus was predominantly operated in integrating mode, where the beam current could reach up to 180 μA. In this mode, the light yield from individual events was integrated over a helicity window. Event mode data, typically collected at beam currents of a few μA, were essential for separating the contributions from electrons and pions within the integrated data. Utilizing eight MDs and two types of runs (mixed and transverse), sixteen asymmetry values were determined from the integrating data-taking mode. These asymmetry values, denoted by A_{ij}, were calculated using the normalized yield difference as follows:

$$A_{ij} = \frac{Y_{ij}^{+} - Y_{ij}^{-}}{Y_{ij}^{+} + Y_{ij}^{-}}, \tag{5.25}$$

where $Y^{\pm}$ represents the integrated signal yield corresponding to the right-handed/left-handed ($\pm$) helicity states (see Section 2.2). Here, i indicates the detector number, and j represents the run type.

In event mode, the pulse height for each event is individually recorded. Pions, minimum ionizing particles at these energies, exhibit minimal showering when passing through the 10.2 cm thick lead wall in front of MD7, resulting in a modest energy deposit in the quartz detectors. In contrast, electrons, due to their lower mass, are more readily attenuated by the lead, as detailed in Section 2.6.5 and illustrated in Figure 2.11. Interactions with the lead result in energy loss via emitted gamma rays, which may convert into electron-positron pairs. These secondary particles, possessing sufficient energy, can further emit photons, thus propagating an electromagnetic shower rich in electrons and positrons. This cascade amplifies the signal of an incident electron, leading to a greater light deposition through Cherenkov radiation in the MDs for electron events compared to pion events. A soft neutral background, which arose from the secondary scattering of primary scattered electrons or pions, contributed additional signals within the MDs. This background effect was quantified in event mode and subsequently corrected in each MD by applying a scaling factor, $(1 - f_{\mathrm{NB}}^{i})$.

Comprehensive details on the measurement techniques fall beyond the scope of this thesis chapter but are thoroughly documented in Chapter 4 of Reference [132], a foundational thesis for the Qweak experiment. Considering all the measurement

processes, the measured asymmetries were parameterized as follows [132]:

$$A_{ij}^{\text{meas}} = (1 - f_{\text{NB}}^{i})\Big[(1 - f_{\pi}^{i})(A_{e}^{L}\cos\theta_{P}^{j} + A_{e}^{T}\sin\theta_{P}^{j}\sin\phi^{i}) + f_{\pi}^{i}(A_{\pi}^{L}\cos\theta_{P}^{j} + A_{\pi}^{T}\sin\theta_{P}^{j}\sin\phi^{i})\Big], \tag{5.26}$$

where f_{π}^{i} represents the fractional yield of pions detected by the MD i (where i is the number of detectors), the longitudinal asymmetry attributed to electrons (pions) is denoted by $A_{e(\pi)}^{L}$, and the transverse asymmetry by $A_{e(\pi)}^{T}$. The polarization angle for run type j (where j is the run type) is given by θ_{P}^{j}, and the neutral background yield fraction for MD i is f_{NB}^{i}. The azimuthal angle placement of the MDs is defined by ϕ^{i}, with specific values such as $\phi^{1} = 0^{\circ}$ and $\phi^{2} = 45^{\circ}$, among others. The results of these measurements are concisely summarized in two tables: Table 5.1 presents the data for the mixed dataset, and Table 5.2 details the transverse dataset. These tables provide the necessary data inputs for the subsequent analytical methods.

Table 5.1: Summary of Measurement Results: Mixed Dataset

	MD1	MD2	MD3	MD4	MD5	MD6	MD7	MD8
A_{meas}	-2.233 ±0.570	-2.233 ±0.570	-3.183 ±0.560	-2.573 ±0.580	-2.093 ±0.580	0.167 ±0.580	1.077 ±0.950	-1.483 ±0.570
f_{π}	0.096 ±0.029	0.096 ±0.029	0.096 ±0.029	0.096 ±0.029	0.096 ±0.029	0.096 ±0.029	0.81 ±0.05	0.096 ±0.029
f_{NB}	0.063 ±0.006	0.063 ±0.006	0.063 ±0.006	0.063 ±0.006	0.063 ±0.006	0.063 ±0.006	0.51 ±0.09	0.063 ±0.006
θ	-19.7° ±1.9°	-19.7° ±1.9°	-19.7° ±1.9°	-19.7° ±1.9°	-19.7° ±1.9°	-19.7° ±1.9°	-19.7° ±1.9°	-19.7° ±1.9°
ϕ	0°	45°	90°	135°	180°	225°	270°	315°

As shown in the tables, the fractional yield values for pions and the neutral background are consistent across both datasets because the number of photoelectrons generated in a material does not depend on the polarization direction. However, these values are significantly higher in MD7, designed to block electrons and predominantly detect pions. Additionally, the values of θ, ϕ, and their associated uncertainties remain constant for all MDs.

To extract the component asymmetries, A_{e}^{L}, A_{e}^{T}, A_{π}^{L}, and A_{π}^{T}, from the measured

Table 5.2: Summary of Measurement Results: Transverse Dataset

	MD1	MD2	MD3	MD4	MD5	MD6	MD7	MD8
A_{meas}	2.587 ± 2.870	6.147 ±2.850	6.587 ±2.800	2.727 ±2.880	-4.493 ±2.900	-1.193 ± 2.880	18.617 ±4.640	-3.993 ±2.860
f_π	0.096 ±0.029	0.096 ±0.029	0.096 ±0.029	0.096 ±0.029	0.096 ±0.029	0.096 ±0.029	0.81 ±0.05	0.096 ±0.029
f_{NB}	0.063 ±0.006	0.063 ±0.006	0.063 ±0.006	0.063 ±0.006	0.063 ±0.006	0.063 ±0.006	0.51 ±0.09	0.063 ±0.006
θ	92.2° ±1.9°	92.2° ±1.9°	92.2° ±1.9°	92.2° ±1.9°	92.2° ±1.9°	92.2° ±1.9°	92.2° ±1.9°	92.2° ±1.9°
ϕ	0°	45°	90°	135°	180°	225°	270°	315°

asymmetries in Equation 5.26, two methods are described. The first method is a Many-Worlds Monte Carlo minimization approach, implemented in [132] and [47], and used in original extraction. I have not personally conducted any work on this method. My only contribution has been to acquire the code and inputs to regenerate the results independently for comparison and validation purposes. The second method is the new Bayesian analysis, which is the primary subject of this chapter. The subsequent subsections detail these two methods, respectively.

5.3.2 Many-Worlds Monte Carlo minimization Method

To extract the component asymmetries, A_e^L, A_e^T, A_π^L, and A_π^T, from the measured asymmetries in Equation 5.26 using the Many-Worlds Monte Carlo minimization approach [132], a value for each input quantity was randomly selected from a Gaussian distribution about their mean with widths equal to their uncertainties. These random values were then used to calculate the asymmetry in each MD and for each polarization configuration via the following equation:

$$\begin{aligned} A_{\text{calc}}^{ij} = (1-\tilde{f}_{\text{NB}}^i)\Big[&(1-\tilde{f}_\pi^i)(A_e^L\cos\tilde{\theta}_P^j + A_e^T\sin\tilde{\theta}_P^j\sin\tilde{\phi}^i) \\ &+ \tilde{f}_\pi^i(A_\pi^L\cos\tilde{\theta}_P^j + A_\pi^T\sin\tilde{\theta}_P^j\sin\tilde{\phi}^i)\Big], \end{aligned} \tag{5.27}$$

where a tilda over a quantity indicates a randomly selected value for that quantity. The function δ, where

$$\delta^2_{\text{dof}} = \sum \left(A^{ij}_{\text{meas}} - A^{ij}_{\text{calc}} \right)^2 , \tag{5.28}$$

was then minimized with respect to the unknown component asymmetries. This resulted in one possible set of values for each component asymmetry, A_e^L, A_e^T, A_π^L, and A_π^T. The randomization and minimization process was repeated 10^6 times, giving 10^6 extracted values for each of the four component asymmetries and 10^6 values for the calculated asymmetries. The root mean squared of the resulting distributions are taken as their uncertainties. The results from this analysis method are summarized in Table 5.3. In the following subsection, the implementation of Bayesian analysis using the same inputs and unknowns is explained.

Table 5.3: Asymmetries Components and Uncertainties (Monte Carlo minimization [47])

Asymmetry	**Value (ppm)**	**Uncertainty (ppm)**
A_e^L	-5.25	1.49
A_e^T	12.3	3.6
A_π^L	25.4	9.0
A_π^T	-60.1	19.3

5.3.3 Bayesian Analysis Method

The Bayesian framework comprises data, parameters, and a model. As detailed in Section 5.2, the model uses prior knowledge and measured data to update beliefs about the parameters reflected in the posterior distribution.

For the Bayesian analysis of data from the Qweak experiment [47], the same data (A_{meas}, f_π, f_{NB}, θ, ϕ) and parameters (A_e^L, A_e^T, A_π^L, A_π^T) as discussed in the previous subsection are used. No prior knowledge is assumed, indicating that the posterior is influenced by the measured data. Moreover, Equation 5.27 is implemented as the model, as outlined in Subsection 5.2.4. The code for this analysis is available in [133]. The outcomes of the Bayesian analysis, which determine the asymmetry components and their uncertainties, are concisely summarized in Table 5.4. Comparing Table 5.4

Table 5.4: Asymmetries Components and Uncertainties (Bayesian analysis)

Asymmetry	**Value (ppm)**	**Uncertainty (ppm)**
A_e^L	-4.9	0.7
A_e^T	12.0	2.0
A_π^L	22.8	5.9
A_π^T	-55.9	14.5

with Table 5.3 shows that the Monte Carlo minimization method consistently resulted in larger absolute values and uncertainties across all measured asymmetries relative to Bayesian analysis. In the subsequent subsection, we will explore the comparative study of Bayesian and Monte Carlo minimization methods to validate and clarify these findings further.

5.3.4 Bayesian Analysis Vs Monte Carlo minimization

To evaluate the performance of the Bayesian analysis technique, asymmetry components derived using both approaches were substituted into Equation 5.26. The resulting asymmetry values, referred to as fitted asymmetry, are presented for all MDs across two datasets. The corresponding values, along with their associated uncertainties, are shown in the plots of Figure 5.4. This facilitates a direct comparison of the two statistical methods in terms of their fit to the measured data. In both datasets, the Bayesian analysis method (red circles) provides a closer fit to the measured asymmetry (blue squares) than the Monte Carlo minimization method (black triangles). This indicates the Bayesian method's robustness in parameter estimation, which may be attributed to its systematic incorporation of prior information and subsequent data-driven updates. The error bars, representing uncertainties in the measured asymmetries, are consistently smaller in the Bayesian approach compared to the Monte Carlo minimization method. Furthermore, the Bayesian method's error bars show less variation across detector numbers, suggesting a more stable estimation process, whereas the Monte Carlo method's uncertainties appear more varied.

The chi-squared (χ^2) statistic, as discussed in chapter 27 of Reference [134], is intimately connected to the concept of goodness of fit. The goodness of fit is a statis-

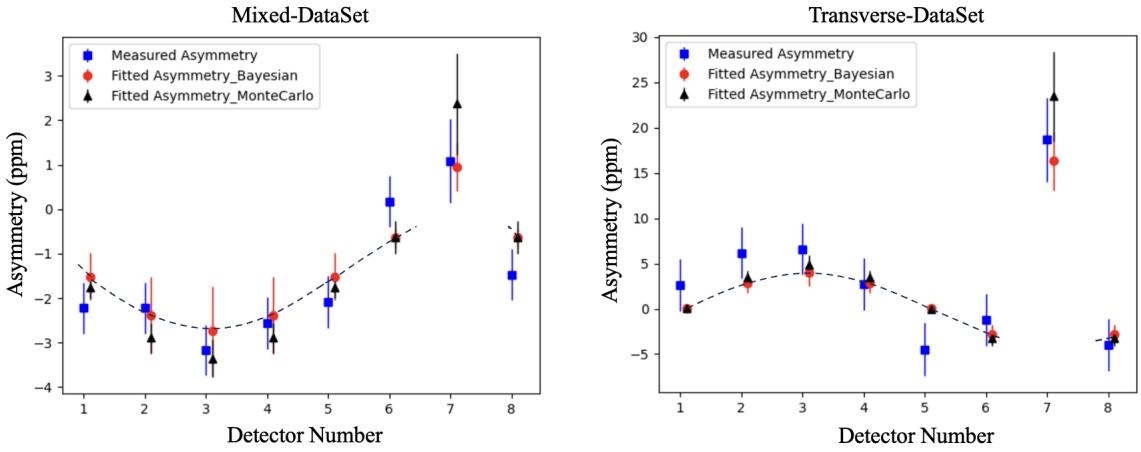

Figure 5.4: Comparative analysis of measured and fitted asymmetry values across detectors. Plots illustrate the asymmetry measurements (depicted as blue squares) and compare them with the asymmetry values derived through Bayesian inference (shown as red circles) and Monte Carlo simulations (represented by black triangles). The data spans eight detectors and encompasses two distinct datasets, with error bars indicating the measurement uncertainty for each data point. Dashed lines in both data sets show the fitted sine wave in the Bayesian analysis, which is different from those obtained using the Monte Carlo method [47].

tical measure that enables us to examine how well the distribution of residuals, or the differences between observed and fitted values, aligns with the expected distribution of experimental uncertainties. We commence by assuming that each observed data point, denoted as Y, is drawn from a distribution with a mean μ and variance σ^2, symbolically expressed as $Y \sim D(\mu, \sigma^2)$. When we conduct a fitting procedure, we generate residuals e_i for each data point, which are defined as the difference between the measured value y_i and the fitted value $\hat{y}_i$:

$$e_i = y_i - \hat{y}_i. \tag{5.29}$$

These residuals are expected to follow a distribution with zero mean and variance equal to the square of the standard deviation of the measurements:

$$e \sim D(0, \sigma_e^2). \tag{5.30}$$

To gauge the goodness of fit, we normalize the residuals by the standard deviation σ and subsequently square this quantity to define the χ^2 as follows:

$$\chi^2 = \sum_{i=1}^{N} \left(\frac{e_i}{\sigma_e} \right)^2 . \tag{5.31}$$

The normalized residuals $\frac{e}{\sigma_e}$ are expected to follow a standard normal distribution $D(0,1)$. The sum of the squares of these normalized residuals gives rise to a χ^2 distribution. Notably, the mean of the χ^2 distribution is equal to its degrees of freedom, not the total number of observations. This is because the degrees of freedom account for the number of parameters estimated in the model. Each parameter estimation reduces the number of independent pieces of information by one, leading to a lower effective number of observations used in the calculation.

We have determined the χ^2 values for both Bayesian analysis and Monte Carlo minimization methods:

$$\chi^2_{\text{Bayesian}} = 1.2,$$
$$\chi^2_{\text{Monte Carlo}} = 1.3.$$

The comparative analysis of these χ^2 values verified that the Bayesian method provides a better fit to the experimental data of the Qweak experiment. This aligns with the conclusions presented in Figure 5.4.

To understand why the Bayesian method shows a better fit to the experimental data of the Qweak experiment and smaller uncertainties, the extracted asymmetry components from the two methods are compared in Figure 5.5. The symmetric shape of the posterior distributions obtained through the Bayesian method contrasts with the asymmetry and pronounced tails observed in the Monte Carlo results. These tails in the Monte Carlo method indicate the presence of greater sensitivity to statistical fluctuations, contributing to larger uncertainties in the extracted asymmetry values. In contrast, the Bayesian approach inherently incorporates prior distributions and experimental data in each iteration, resulting in posterior distributions that are better constrained and centered around the most probable values. This integration of prior

knowledge with the observed data during the iterative process of Bayesian inference naturally leads to the suppression of extreme outliers and the production of more symmetric distributions with reduced uncertainties.

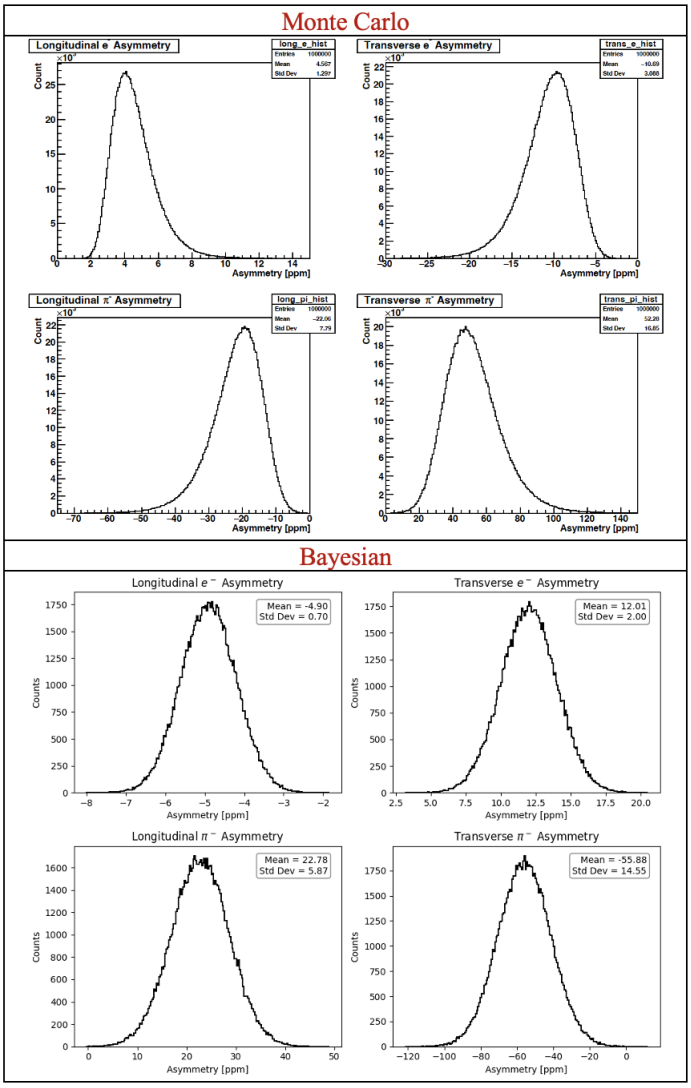

Figure 5.5: Comparative analysis of measured and fitted asymmetry values across detectors. Plots illustrate the asymmetry measurements (depicted as blue squares) and compare them with the asymmetry values derived through Bayesian inference (shown as red circles) and Monte Carlo simulations (represented by black triangles). The data spans eight detectors and encompasses two distinct datasets, with error bars indicating the measurement uncertainty for each data point.

While the Bayesian analysis method yielded a better fit to the Qweak experimental

data as an example of PVES experiments, it is important to recognize that this does not universally establish Bayesian analysis as the superior method. Different analysis methods have unique advantages and are better suited to specific data types and research questions. The selection of an appropriate statistical method should be guided by the data characteristics, experimental design, and the specifics of each investigative scenario.

Although the choice of statistical method plays a significant role in analyzing experimental data, a thorough understanding of uncertainties and their interdependencies is equally important for achieving reliable results. In PVES experiments, capturing the full range and complexity of uncertainties is crucial for accurate data analysis. The covariance matrix quantifies the uncertainty and relationships between variables by measuring how changes in one variable are associated with changes in another. For experiments aimed at detecting small asymmetry signals, a comprehensive understanding of these relationships is essential to accurately determining parameters. The covariance matrix is calculated as follows:

$$\mathrm{Cov}(X,Y) = \frac{1}{n-1}\sum_{i=1}^{n}(X_i - \bar{X})(Y_i - \bar{Y}) \tag{5.32}$$

where $\mathrm{Cov}(X,Y)$ is the covariance between two variables X and Y, X_i and Y_i are individual observations from variables X and Y respectively, $\bar{X}$ and $\bar{Y}$ are the means of X and Y, and n is the number of observations. For a set of variables, the covariance matrix is a square matrix giving the covariance between each pair of elements. For a dataset with m variables, the covariance matrix Σ is an $m \times m$ matrix where each element Σ_{ij} is the covariance $\mathrm{Cov}(X_i, X_j)$ between the i^{th} and j^{th} variables. It is calculated as:

$$\Sigma = \begin{bmatrix} \mathrm{Cov}(X_1,X_1) & \mathrm{Cov}(X_1,X_2) & \cdots & \mathrm{Cov}(X_1,X_m) \\ \mathrm{Cov}(X_2,X_1) & \mathrm{Cov}(X_2,X_2) & \cdots & \mathrm{Cov}(X_2,X_m) \\ \vdots & \vdots & \ddots & \vdots \\ \mathrm{Cov}(X_m,X_1) & \mathrm{Cov}(X_m,X_2) & \cdots & \mathrm{Cov}(X_m,X_m) \end{bmatrix} \tag{5.33}$$

The covariance matrix in the case of the Qweak experiment [47], for the longitudinal and transverse electron asymmetry (A_e^L and A_e^T) and longitudinal and transverse pion asymmetry (A_π^L and A_π^T), would be as follows:

$$\Sigma = \begin{bmatrix} \mathrm{Cov}(A_e^L, A_e^L) & \mathrm{Cov}(A_e^L, A_e^T) & \mathrm{Cov}(A_e^L, A_\pi^L) & \mathrm{Cov}(A_e^L, A_\pi^T) \\ \mathrm{Cov}(A_e^T, A_e^L) & \mathrm{Cov}(A_e^T, A_e^T) & \mathrm{Cov}(A_e^T, A_\pi^L) & \mathrm{Cov}(A_e^T, A_\pi^T) \\ \mathrm{Cov}(A_\pi^L, A_e^L) & \mathrm{Cov}(A_\pi^L, A_e^T) & \mathrm{Cov}(A_\pi^L, A_\pi^L) & \mathrm{Cov}(A_\pi^L, A_\pi^T) \\ \mathrm{Cov}(A_\pi^T, A_e^L) & \mathrm{Cov}(A_\pi^T, A_e^T) & \mathrm{Cov}(A_\pi^T, A_\pi^L) & \mathrm{Cov}(A_\pi^T, A_\pi^T) \end{bmatrix} \tag{5.34}$$

In this matrix, each element represents the covariance between the respective asymmetry parameters, reflecting their interdependencies. For instance, $\mathrm{Cov}(A_e^L, A_e^T)$ quantifies the extent to which the longitudinal and transverse electron asymmetries vary together within the experimental data. The covariance matrices for the Monte Carlo minimization and Bayesian methods are as follows:
Covariance Matrix with Uncertainty - Monte Carlo minimization analysis:

$$\begin{pmatrix} 1.5 \pm 1.2 & -1.2 \pm 1.1 & -10.3 \pm 6.5 & 9.0 \pm 5.1 \\ -1.2 \pm 1.1 & 6.1 \pm 3.0 & 10.9 \pm 6.4 & -26 \pm 13 \\ -10.3 \pm 6.5 & 10.9 \pm 6.4 & 97 \pm 44 & -83 \pm 34 \\ 9.0 \pm 5.1 & -26 \pm 13 & -83 \pm 34 & 221 \pm 68 \end{pmatrix}$$

Covariance Matrix with Uncertainty - Bayesian analysis:

$$\begin{pmatrix} 0.4 \pm 0.2 & -0.6 \pm 0.4 & -2.9 \pm 1.1 & 6.0 \pm 2.9 \\ -0.6 \pm 0.4 & 3.2 \pm 1.2 & 6.1 \pm 2.9 & -17.9 \pm 8.5 \\ -2.9 \pm 1.1 & 6.1 \pm 2.9 & 26.7 \pm 9.6 & -57 \pm 28 \\ 6.0 \pm 2.9 & -17.9 \pm 8.5 & -57 \pm 28 & 165 \pm 83 \end{pmatrix}$$

It is evident that the two matrices are in agreement within their respective uncertainties. This agreement indicates that both methods are capturing the underlying physics model effectively. However, a notable difference is observed in the magnitude of the components and their associated uncertainties: the values in the Monte Carlo minimization matrix are generally larger than those in the Bayesian analysis matrix.

To examine the reasoning behind the larger uncertainties associated with the Monte Carlo method, a visual analysis of the distribution of each component in the covariance matrix across all iterations is performed. Histograms of all 16 elements of the Monte Carlo covariance matrix provide a graphical representation that can reveal the underlying distribution and variance within the data. These histograms allow for a more intuitive understanding of where the larger values and broader uncertainty ranges originate, as depicted in the histograms in Figure 5.6.

The histograms derived from the Monte Carlo covariance matrix elements reveal pronounced tails and differences between the mean and the mode, suggesting skewed distributions rather than symmetric ones. These features indicate a non-negligible probability of extreme values far from the mean, which is not the mode in many cases. This discrepancy highlights that the central tendency of the data is not uniformly distributed around a single peak but exhibits significant variations. Such outliers in the tails and the different mean and mode values can inflate the variance, leading to larger confidence intervals and, consequently, greater overall uncertainty in parameter estimates. However, the Bayesian analysis focuses on reproducing the mode with symmetric uncertainty, reflecting the underlying Gaussian assumptions about how uncertainties are represented. Furthermore, the shape and spread of these histograms provide insights into correlations between parameters. When two elements display similarly skewed distributions with tails extending in the same direction, this suggests potential correlations. These interdependencies are crucial for understanding the covariance matrix's off-diagonal elements and play a significant role in interpreting the overall experiment. These correlations can be directly obtained from the Bayesian analysis and be compared with the histograms' shapes shown in Figure 5.6. The contour plots from the Bayesian analysis, as depicted in Figure 5.7, illustrate the correlations between different pairs of parameters. Similar to the pronounced tails and skewed distributions observed in the histograms, these contour plots display elongated shapes and asymmetries, indicating strong correlations.

It is evident that A_e^L is negatively correlated with A_e^T, similar to the negative correlation observed between A_π^L and A_π^T. As previously discussed, pure longitudinal polarization results in pure longitudinal asymmetry and deviations from this ideal

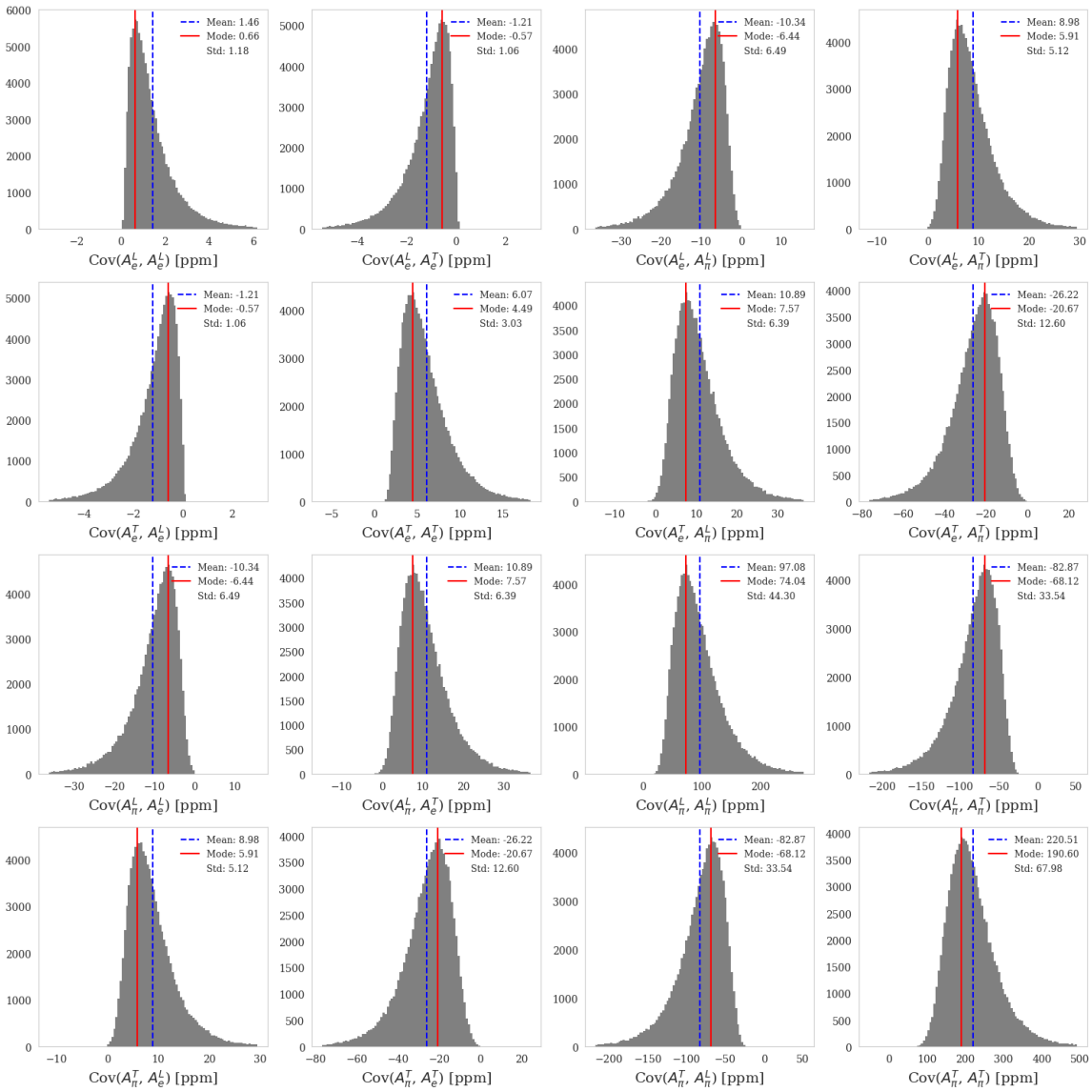

Figure 5.6: Histograms representing the distribution of the 16 elements of the Monte Carlo covariance matrix across all iterations. Each panel displays the distribution for a different covariance element, denoted as $\mathrm{Cov}(A_i, A_j)$ in parts per billion (ppb). The mean, mode, and standard deviation for each distribution are indicated by the dashed blue line, solid red line, and the values listed in the legends, respectively.

state give rise to transverse asymmetry, thereby causing these negative correlations. Additionally, there is a strong negative correlation between A_e^L and A_π^L, as well as between A_e^T and A_π^T. In contrast, A_e^T is positively correlated with A_π^L, and A_e^L is positively correlated with A_π^T. The visual observations in Figures 5.6 and 5.7 underscore

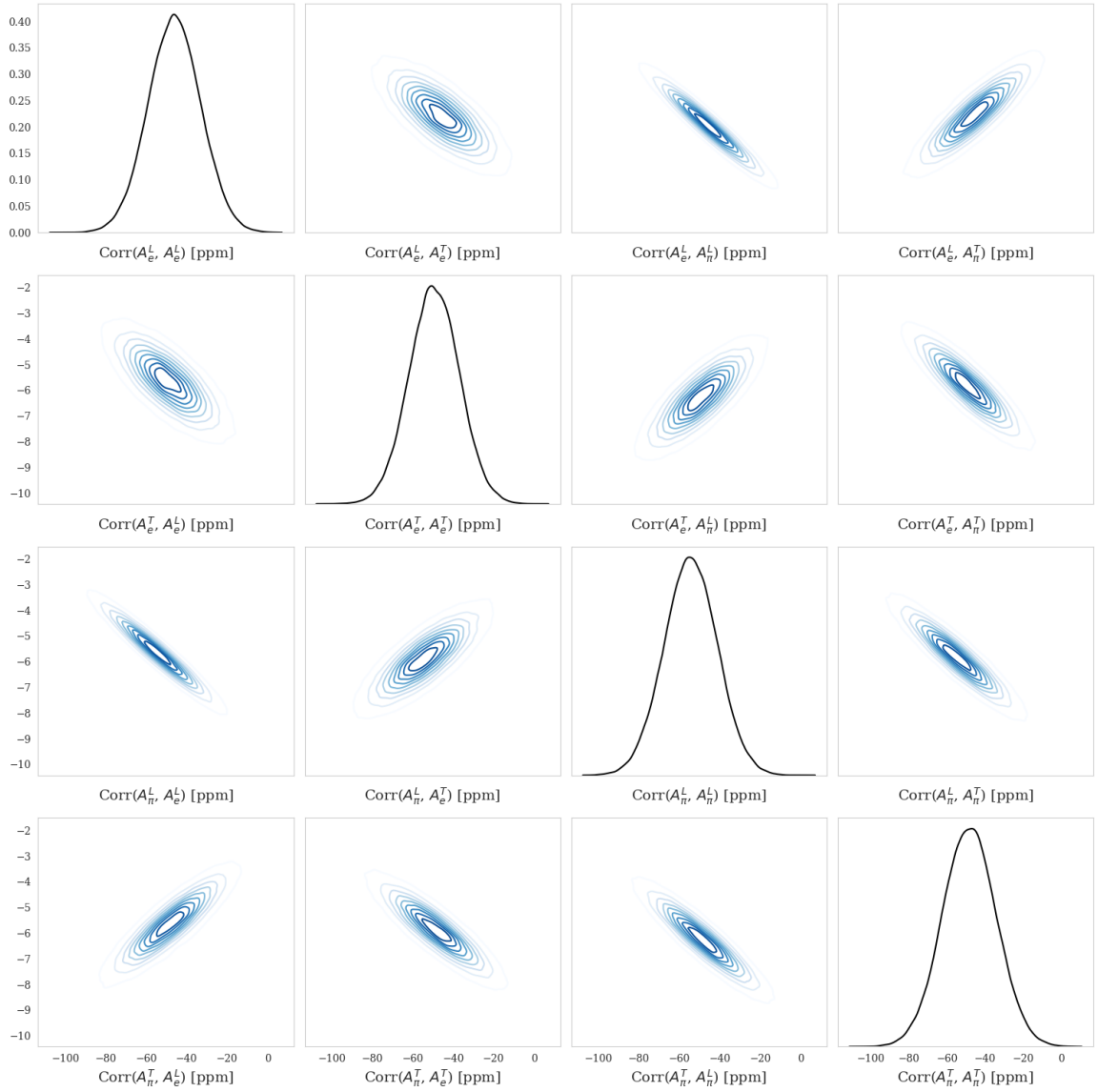

Figure 5.7: Correlation plots and distribution histograms for parameter estimates from Bayesian analysis, displaying pairwise relationships between A_e^L, A_e^T, A_π^L, and A_π^T. Each row and column correspond to these parameters, with histograms on the diagonal showing the distributions of individual parameters and contour plots off-diagonal with decile lines visualizing the density distribution from 10% to 90% .

the importance of comprehensive analysis and interpretation of covariance matrix and correlation elements, which are essential for grasping different methods' performance and its derived uncertainties in the context of PVES experiments.

5.4 Enhancing Precision of Extracted Quantities in the MOLLER Experiment

This section examines the steps of applying Bayesian analysis to the MOLLER experiment, a methodological transition from the Qweak experiment's frequentist approach. The emphasis is on adapting and refining the Bayesian framework to address the unique challenges and configurations of the MOLLER experiment [21]. This effort requires a detailed comparison of the experimental setups, underlying assumptions, and analytical methodologies of the two experiments. By navigating these intricacies, the section establishes a foundation for a comprehensive evaluation of the inputs, parameters, and models that form the basis of the Bayesian analysis, preparing the way for a thorough interpretation of the MOLLER experiment's outcomes.

5.4.1 Underlying Assumptions: MOLLER Experiment versus Qweak Experiment

There are differences between the Qweak [47] and MOLLER [21] experiments when applying Bayesian analysis. These differences arise from different experimental geometries and configurations, data types (mock asymmetry values in MOLLER versus measured asymmetry values in Qweak), and polarization angles.

The primary distinction lies in the differing design and geometry between the two experiments. Unlike the Qweak experiment [47], which employs eight MDs with MD7 serving as the pion detector, the MOLLER experiment [21] features a main detector array for ring 5 comprised of 84 modules distinct from the pion detector, which consists of 28 modules. Consequently, the Bayesian analysis must incorporate asymmetry values from both sets of detectors. As a result, the configuration of Tables 5.1 and 5.2 is notably altered. Originally comprising eight columns to correspond with the Qweak experiment's eight MDs, these tables would now expand to accommodate the MOLLER experiment's design, featuring a total of 112 columns, which include 84 for the main detector ring 5 and an additional 28 for the pion detector. Note that in this thesis, the analysis will focus on the main detector ring 5 and the pion detector.

In future work, it will be expanded to include all six rings of the main detectors, comprising 224 modules, the pion detector, and the ShowerMax, each including 28 modules.

The second distinction lies in the polarization angles, which remain consistent in the geometric definition as outlined in Section 5.3.1: longitudinal components are aligned with the beam axis, and transverse components are oriented perpendicular to the beam in the horizontal plane, leading to the respective longitudinal or transverse asymmetries. However, the actual polarization angles vary between the experiments. As detailed in Section 5.3.1, the Qweak experiment [47] received a beam with mixed polarization, depicted in Figure 5.3. The beam's polarization angle, denoted as θ_P, was measured at $-19.7^\circ \pm 1.9^\circ$, forming the basis for the mixed dataset. In a subsequent run, the beam polarization angle was set to $92.2^\circ \pm 1.9^\circ$, constituting the transverse dataset. The MOLLER experiment will assume pure longitudinal polarization to generate the longitudinal dataset and pure transverse polarization to form the transverse dataset. An uncertainty of one degree is incorporated to account for any deviations. This one-degree uncertainty in polarization angles is necessary to suppress transverse polarization effects by averaging asymmetries across the full azimuth range. However, imperfect cancellation of these effects could result in significant systematic uncertainties. A transverse polarization component can introduce azimuthal modulation in the measured asymmetry, potentially amplifying these systematic uncertainties. To mitigate this, polarization components will be monitored continuously in the experimental hall by measuring the transverse scattering asymmetry with an accuracy below 1° within a few hours. Therefore, in the Bayesian analysis for the MOLLER experiment, the longitudinal polarization angle is set to $0^\circ \pm 1^\circ$, and the transverse polarization angle is set to $90^\circ \pm 1^\circ$, as depicted in Figure 5.8.

Another distinction arises from the complexity of the model used in the Bayesian framework for the MOLLER experiment. The Qweak experiment employed a relatively straightforward model by assuming an almost entirely horizontal transverse orientation for the spin of the electron beam [47]. In contrast, the MOLLER experiment necessitates a more intricate model that accounts for spin variations. As a result of considering spin variation in the horizontal plane, the spin angles in the

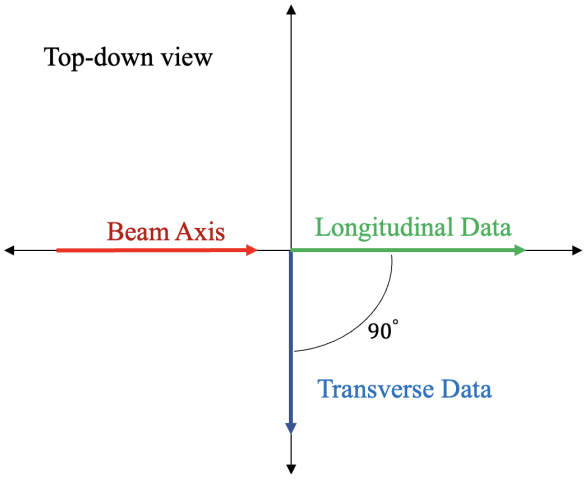

Figure 5.8: Top-down view of beam polarization: The red arrow indicates the downstream direction of the beam axis, the green arrow represents pure longitudinal polarization, and the blue arrow depicts pure transverse polarization.

longitudinal data-taking, when the polarization angle is set to $0° \pm 1°$, span from $-\pi$ to $+\pi$, represented by $[-\pi, +\pi]$. In the transverse data-taking, when the polarization angle is set to $90° \pm 1°$, the spin angle is close to zero, as it is in the same plane as the polarization vector, represented by $0° \pm 1°$.

The next distinction involves the generators considered in the Bayesian analysis. In the Qweak experiment, the inputs include the effects of all types of generators, including Møller electron, pion, elastic, and inelastic interactions. However, for the Bayesian analysis of the MOLLER experiment in this thesis, only Møller electron and pion generators are considered. This means that the inputs used in this analysis do not account for the effects of elastic and inelastic generators. Incorporating all generators into the Geant4 simulations represents a future step for this line of research, which will provide a more comprehensive understanding of the experimental data and enhance the precision of the Bayesian analysis applied to the MOLLER experiment.

The last distinction is that while the Qweak experiment [47] has been completed, and its data are available for further analysis, the MOLLER experiment [21] has not yet been conducted, and thus no empirical data are available. In the context of the MOLLER experiment, it is necessary to generate synthetic data, referred to as mock asymmetry values. To create this mock data, we simulate random variables based on

known mean values and their associated uncertainties. The methodologies for determining the mean values of asymmetry components are as follows: The asymmetry components for Møller and pion generators across various detectors (main detector ring 5 and pion detector) are simulated. These components have been categorized into longitudinal and transverse components (vertical and horizontal) for both Møller and pion asymmetries at the main and pion detectors. The equations presented below show how these various asymmetry components are combined to contribute to the final simulated asymmetry values, denoted as A_{ij}^{true}, considering all inputs:

$$\begin{aligned} A_{ij}^{\text{true}} =& (1 - f_\pi^i)\Big(A_e^L(i,j)\cos(\theta_P^j) + \big(A_e^{TV}(i,j)\sin(\phi_P^j) + A_e^{TH}(i,j)\cos(\phi_P^j)\big)\sin(\theta_P^j)\Big) \\ &+ f_\pi^i\Big(A_\pi^L(i,j)\cos(\theta_P^j) + \big(A_\pi^{TV}(i,j)\sin(\phi_P^j) + A_\pi^{TH}(i,j)\cos(\phi_P^j)\big)\sin(\theta_P^j)\Big), \end{aligned} \tag{5.35}$$

where A_{ij}^{true} represents the final expected asymmetry values from the simulations for each of the 84 modules in the main detector and the 28 modules in the pion detector. The terms $1 - f_\pi^i$ and f_π^i denote the Møller and pion yield fractions, respectively, for each detector module i. These fractions, which vary between the main and pion detectors, are calculated by dividing the number of generated photoelectrons from the pion generator by the total number of generated photoelectrons from both the pion and Møller generators at the detector modules. The longitudinal and transverse asymmetry values (vertical and horizontal) are denoted by $A_e^L(i,j), A_\pi^L(i,j)$, $A_e^{TV}(i,j), A_e^{TH}(i,j), A_\pi^{TV}(i,j)$, and $A_\pi^{TH}(i,j)$, respectively. The angle θ_P^j represents the polarization angle for dataset j. The angle ϕ_P^j is the angle in the azimuthal plane (x-y plane) from the x-axis to the projection of the spin vector onto this plane. The index i indicates the number of modules in the main (pion) detector, while the index j corresponds to the dataset, whether longitudinal or transverse.

These A_{ij}^{true} values provide precise estimates and are used as the mean values for generating mock asymmetry values. To calculate the uncertainties associated with these mean values, one might initially consider the propagation of uncertainty. However, for the mock data, we need to calculate uncertainty reflecting the measured asymmetry values in the actual experiment. This uncertainty is determined based

on the rate of particles per detector module and the run time, given by $\frac{1}{\sqrt{\text{rate}\times\text{run time}}}$. Therefore, the uncertainties for the main and pion detectors can be formulated as:

$$\sigma_{\text{Main detector}} = \frac{1}{\sqrt{\text{Total rate at main detector} \times \text{time window}}},$$
$$\sigma_{\text{Pion detector}} = \frac{1}{\sqrt{\text{Total rate at pion detector} \times \text{time window}}},$$

where the total rate is the sum of the rates from the Møller and pion generators, and the time window refers to the period for one measurement, assuming stable conditions in the beam, accelerator, and experiment. This represents minimal uncertainty since there will be excess uncertainty in other terms, but that does not affect the analysis. These asymmetry uncertainties apply to both longitudinal and transverse datasets. Although the time window remains consistent, the total run time is divided differently: 90% is allocated to the longitudinal measurement, and 10% to the transverse measurement. The reason for the 90% allocation is that the main measurement of the experiment is the longitudinal asymmetry. In contrast, the transverse asymmetry is used to correct the longitudinal asymmetry for transverse effects. This allocation ensures that the primary focus remains on the longitudinal measurement, with sufficient data to make necessary corrections using the transverse measurement. Note that this assumption is based on the Qweak experiment and Reference [74] for MOLLER. However, other assumptions could have been made.

Now, mock asymmetry values, A_{mock}, can be generated using a normal distribution where the simulated true asymmetry values, A_{true}, are used as the means. The calculated uncertainties, denoted as σ, are used as the standard deviations. This process can be mathematically represented as follows:

$$A_{\text{mock}} \sim \mathcal{N}(A_{\text{true}}, \sigma) \tag{5.36}$$

This approach introduces variation in the mock data, making them distinct from the true values. This variation is generated to simulate actual experimental conditions where idealized assumptions of simulations no longer hold.

Figure 5.9 illustrates the generated mock asymmetry for the longitudinal and

transverse datasets at the pion detector, showing the variation in mock asymmetry values compared to the true values. Similarly, Figure 5.10 presents the comparison for the main detector. In the two figures, the upper plots compare true asymmetry values and mock asymmetry averages. Green diamonds indicate the true asymmetry values, while blue squares represent the mock asymmetry averages. These averages are calculated from the random values within the range of uncertainty, which is depicted by the shaded areas around the mock values. The shaded areas represent the range of individual measurements, while the blue squares show the averages of all these measurements. Below each asymmetry comparison plot are the normalized residual plots, which highlight the deviation of the mock averages from the true values for each detector module. A normalized residual value close to zero suggests a mock average closely matching the true value. Conversely, normalized residual values significantly different from zero indicate a notable discrepancy. The histograms adjacent to the normalized residual plots detail the distribution of these deviations. They are a useful tool for assessing the overall consistency of the mock data in relation to the true data. The mean and RMS values of the histograms quantify the central tendency and the spread of the normalized residual values, with values close to zero and an RMS near one suggesting that the mock averages are well-aligned with the true values.

For both the pion and main detectors, the longitudinal measurements exhibit better RMS values than the transverse ones, which aligns with our expectations given the higher quantity of longitudinal measurements. Specifically for the pion detector, the mean of normalized residual values stands at -0.20 for both types of measurements. However, the RMS of 1.21 for transverse measurements indicates a broader spread than the RMS of 1.07 for the longitudinal measurements. In the case of the main detector, the longitudinal measurements present a mean normalized residual value of 0.07 and an RMS of 0.96, suggesting tighter agreement than the transverse measurements, which have a mean of -0.15 and an RMS of 0.91.

Now that we have mock asymmetry values, we can feed these values in the fol-

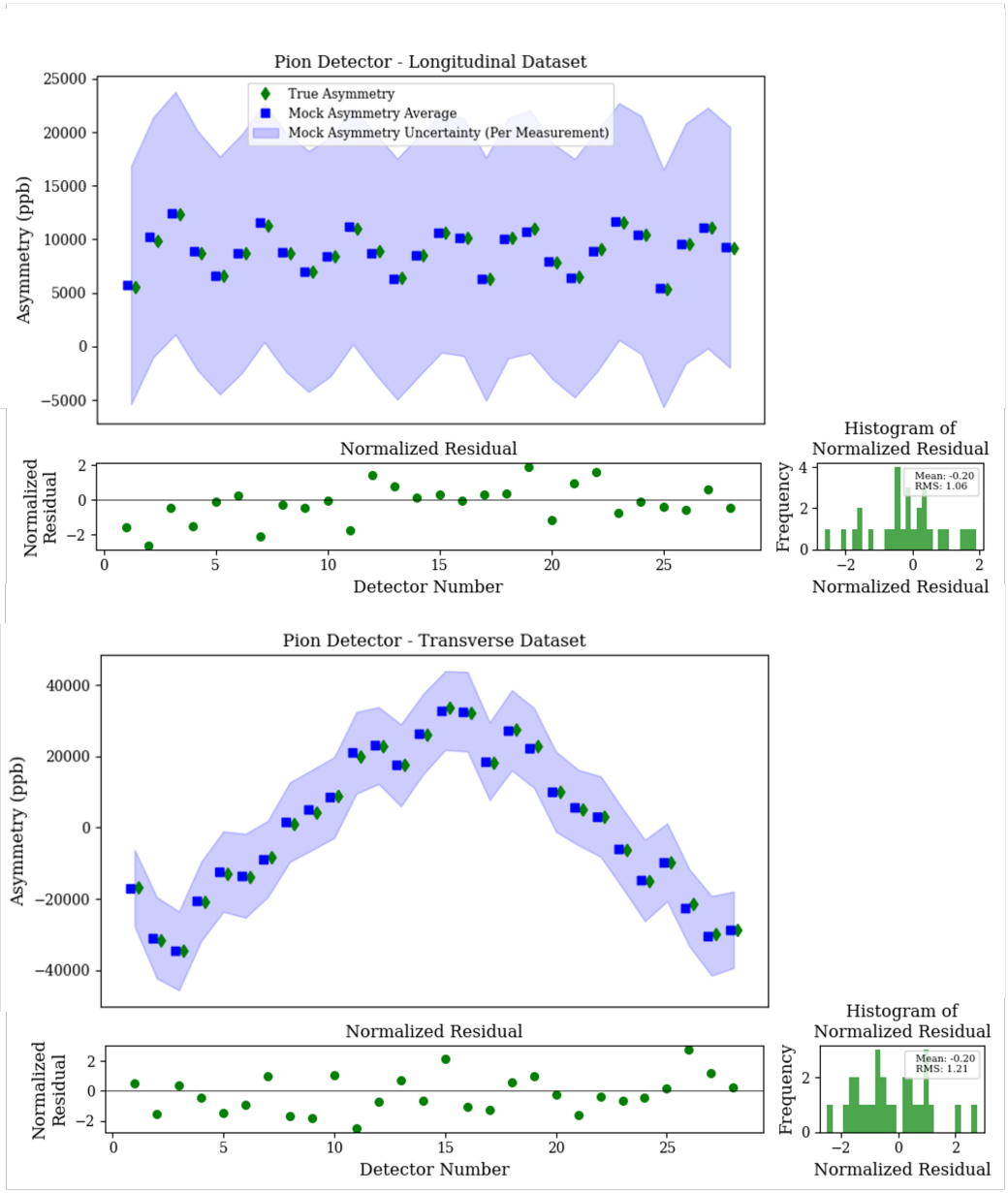

Figure 5.9: True and average mock asymmetry in the pion detector. The longitudinal and transverse datasets are displayed in the top and bottom plots. Green diamonds show true asymmetry values from simulations, blue squares represent the average of mock asymmetry values from analysis, and shaded areas indicate the measured uncertainty for each measurement. Normalized residual plots and histograms illustrate the deviation between the datasets for each module.

lowing equation and extract asymmetry components, A_e^L, A_e^T, A_π^L, and A_π^T.

$$\begin{aligned} A_{ij}^{\text{mock}} &= (1 - f_\pi^i)\Big(A_{ij} A_e^L \cos(\theta_P^j) + C_{ij} A_e^T \sin(\theta_P^j)\Big) \\ &\quad + f_\pi^i \Big(B_{ij} A_\pi^L \cos(\theta_P^j) + D_{ij} A_\pi^T \sin(\theta_P^j)\Big), \\ A_{ij} &= N_{A_e^L(i,j)}, \\ B_{ij} &= N_{A_\pi^L(i,j)}, \\ C_{ij} &= N_{A_e^{TV}(i,j)} \sin(\phi_P^j)(i,j) + N_{A_e^{TH}(i,j)} \cos(\phi_P^j)(i,j), \\ D_{ij} &= N_{\quad} \sin(\phi_P^j)(i,j) + N_{\quad} \cos(\phi_P^j)(i,j) \end{aligned} \tag{5.37}$$

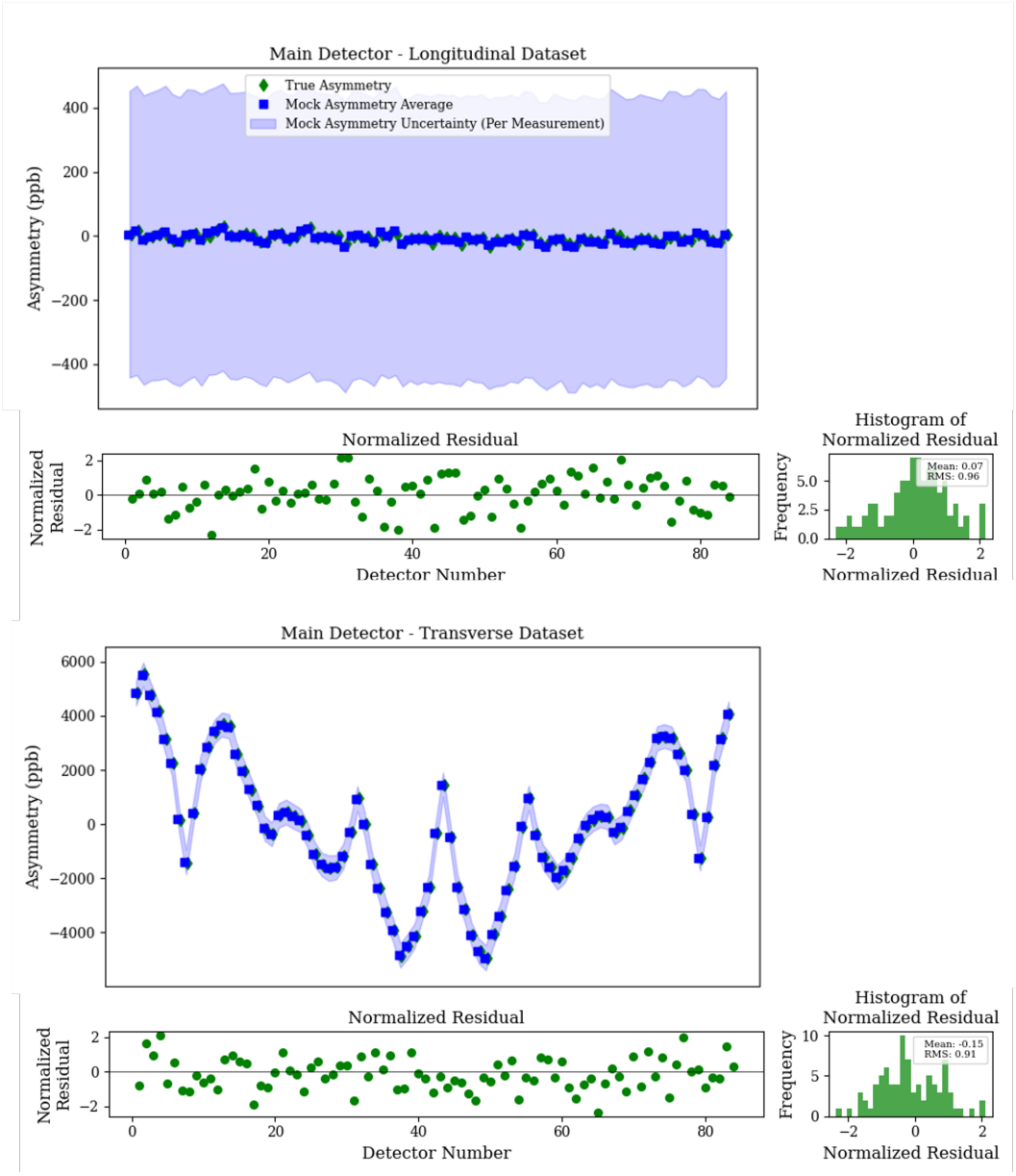

Figure 5.10: True and mock asymmetry in the main detector. The top plot shows longitudinal data, and the bottom plot shows transverse data. Green diamonds mark true asymmetry values, while blue squares represent the average mock asymmetry values. Shaded areas indicate the measured uncertainty for each measurement. The normalized residual plots and the histograms beside them quantify the agreement and consistency across detector modules.

where $A_{i,j}^{\text{mock}}$ represents the generated mock asymmetry values for the pion and main detector modules. A_e^L, A_e^T, A_π^L, and A_π^T represent the Møller and pion asymmetry components that need to be extracted. The terms A_{ij}, B_{ij}, C_{ij}, and D_{ij} are referred to as kinematic coefficients, which best replicate the seven-fold symmetry nature of the experiment and the existence of identical-particle scatterings discussed before, in contrast to the behaviour observed in Qweak. $N_{A_e^L}$, $N_{A_\pi^L}$, $N_{A_e^{TV}}$, $N_{A_e^{TH}}$, $N_{A_\pi^{TV}}$, and $N_{A_\pi^{TH}}$ are normalized asymmetry values obtained by normalizing A_e^L, A_π^L, A_e^{TV}, A_e^{TH}, A_π^{TV}, and A_π^{TH} in Equation 5.35. The key point is that the normalizing factors for obtaining the normalized asymmetry values should be independent of the experiment's kinematics. To calculate normalizing factors, A_e^L from Equation 2.11, A_e^T from Equation 2.24, and A_π^L and A_π^T from Equation 2.36 are simulated within the acceptance range of the experiment, and the maximum values obtained are considered as the normalizing factors. Other parameters align with those in Equation 5.35.

With the foundational approach and specific methodologies applied in the MOLLER experiment's Bayesian analysis established, we now transition to a more detailed examination of the statistical interpretations and the specifics of modelling precision. The following section explores the application of these principles and their practical implications for enhancing correction precision.

5.4.2 Applying Bayesian Analysis

As explained, the Bayesian framework comprises data, parameters, and a model. In the case of the MOLLER experiment, referring to Equation 5.37, the data include f_π^i, θ_P^j, ϕ_P^j, A_{ij}, B_{ij}, C_{ij}, and D_{ij}. The parameters are the asymmetry components that should be extracted, A_e^L, A_e^T, A_π^L, and A_π^T. The model is defined by Equation 5.37 and has no prior knowledge. It is applied separately for the pion and main detectors and for longitudinal and transverse measurements. Consequently, the asymmetry components are extracted using four equations: two for the pion detector (for longitudinal and transverse measurements) and two for the main detector (for longitudinal and transverse measurements).

In addition to the inputs discussed previously, the technical inputs are summarized

in Table 5.5. This table provides a comprehensive summary of the technical inputs

Table 5.5: Technical Inputs for the Bayesian Analysis of the MOLLER Experiment.

Input Data	**Value**	**Explanation**
Total Run Time (N)	8256 hours	One Measurement Per Hour
Longitudinal Run Time (N_L)	7430 hours	One Measurement Per Hour
Transverse Run Time (N_T)	825 hours	One Measurement Per Hour
num_MainDet	84	Number of Main Detector Modules
num_PionDet	28	Number of Pion Detector Modules
$\theta_P(L)$	normal $(0°, 1°)$	Longitudinal Polarization Angle (Polar Angle)
$\theta_P(T)$	normal $(90°, 1°)$	Transverse Polarization Angle (Polar Angle)
$\phi_P(L)$	normal $(0°, \pi)$	Longitudinal Polarization Angle (Azimuthal Angle)
$\phi_P(T)$	normal $(0°, 1°)$	Transverse Polarization Angle (Azimuthal Angle)

utilized in the Bayesian analysis of the MOLLER experiment. These inputs include detailed specifications such as the total run time, specific run times for longitudinal and transverse measurements, and the number of modules in the main and pion detectors. Additionally, the table lists the statistical distribution of experimental parameters, like the polarization angles. These parameters are essential for accurately modeling the experiment's conditions and are important for the subsequent analysis and extraction of asymmetry components.

To conceptualize how these parameters are incorporated into the actual experiment, consider the following scenario: there are two runs in the experiment. The first run takes 7,430 hours, and the second takes 825 hours. In the first run, the polarization angle is set to the longitudinal configuration with a deviation of one degree. In the second run, the polarization angle is set to the transverse configuration degrees with the same uncertainty of one degree. In both runs, there is one measurement per hour. In the end, the parameters we measure are called mock asymmetry values for both the pion and main detectors in two datasets (longitudinal and transverse).

Then, the mock asymmetry values and other inputs are substituted for the analysis into the Bayesian model (Equation 5.37). The number of iterations for the longitudinal component is 7,430, and for the transverse component is 825, with 10,000 samples per iteration. The results of the extracted asymmetry components and associated uncertainties are summarized in Table 5.6 and compared with the inputs of the analysis.

Table 5.6: Comparison of asymmetry values and uncertainties: Inputs versus Outputs

	A_e^L (ppm)	A_e^T (ppm)	A_π^L (ppm)	A_π^T (ppm)
Inputs	-28.00	13845	28400	-53667
Outputs	-28.40 $\pm$ 0.51	13823.0 $\pm$ 9.6	28486 $\pm$ 75	-53762 $\pm$ 190

Table 5.6 compares the input asymmetry values to the Bayesian model and the outputs obtained from the Bayesian analysis. For A_e^L, the input value of -28.00 ppm closely matches the output value of -28.40 ppm with an uncertainty of $\pm$0.51 ppm, indicating strong agreement. However, for A_e^T, the input value is 13,845 ppm, and the corresponding output is 13,823.0 ppm with an uncertainty of $\pm$9.6 ppm, showing a slight discrepancy outside the uncertainty range. The A_π^L input of 28,400 ppm is slightly exceeded by the output of 28,486 ppm with an uncertainty of $\pm$75 ppm, and the A_π^T input of -53,667 ppm is well-approximated by the output of -53,762 ppm, with a larger uncertainty of $\pm$190 ppm. Overall, the close alignment between most inputs and outputs within the uncertainty ranges validates the effectiveness of the Bayesian model in accurately reproducing the asymmetry values, confirming the reliability and precision of the analysis.

Another way to verify the results is by substituting the asymmetry components along with other parameters into the right-hand side of Equation 5.37, computing A_{ij}^{fitted}, and deriving another set of asymmetry values, referred to as the fitted asymmetry values, as done in Qweak and demonstrated in Figure 5.4.

Figure 5.11 provides a comparative analysis of fitted and mock asymmetry averages for the pion detector in the MOLLER experiment, displaying both longitudinal (top plot) and transverse (bottom plot) datasets. The blue squares in each plot indi-

cate the average of mock asymmetry values, while the red circles represent the average of fitted asymmetry values obtained through Bayesian analysis. The middle plot of each dataset is for understanding the precision of the fitted and mock asymmetry averages. Due to the scale of the asymmetry values, the error bars are too small to be visible in the top plots of each dataset. To address this, the middle plots subtract the mock asymmetry average from both the mock and fitted asymmetry values, effectively re-centring the data around zero. This re-centering allows for a more precise visualization of the error bars, illustrating the precision of the measurements. The blue dots in these plots represent the residual mock asymmetry values, which are all at zero as they are subtracted by themselves. The red circles with error bars show the residual fitted asymmetry values, where the error bars represent the uncertainty in the mock and fitted values. In the bottom plot of each dataset, the histogram of the normalized residuals (the difference between the average of fitted and mock asymmetry values, normalized by the uncertainty in the mock asymmetry values) is presented, which helps assess the fit quality. For the longitudinal dataset, the residuals are centred around a mean of 0.01 with an RMS of 1.06, indicating a good fit as the residuals are mainly distributed close to zero. In the case of the transverse dataset, the residuals have a mean of -0.20 and an RMS of 1.21, showing a slight offset but still maintaining a reasonable fit quality.

Similarly, Figure 5.12 presents a comparison of fitted and mock asymmetry averages for the main detector in the MOLLER experiment, encompassing longitudinal (top plot) and transverse (bottom plot) datasets. In each plot, blue squares represent the mock asymmetry averages, and red circles denote the averages obtained from fitted asymmetry values using Bayesian analysis. In the middle plots for each dataset, the residuals are shown by subtracting the mock asymmetry averages from both the mock and fitted averages, thus realigning all mock residuals to zero for clarity. This approach is specifically employed to make the relatively small error bars visible, which are otherwise obscured due to the scale of the asymmetry values. The histograms in the bottom plots provide a statistical view of the normalized residuals. For the longitudinal dataset, these residuals cluster around a mean of -0.00 with an RMS of 0.96, suggesting a tight fit to the model. The transverse dataset displays a

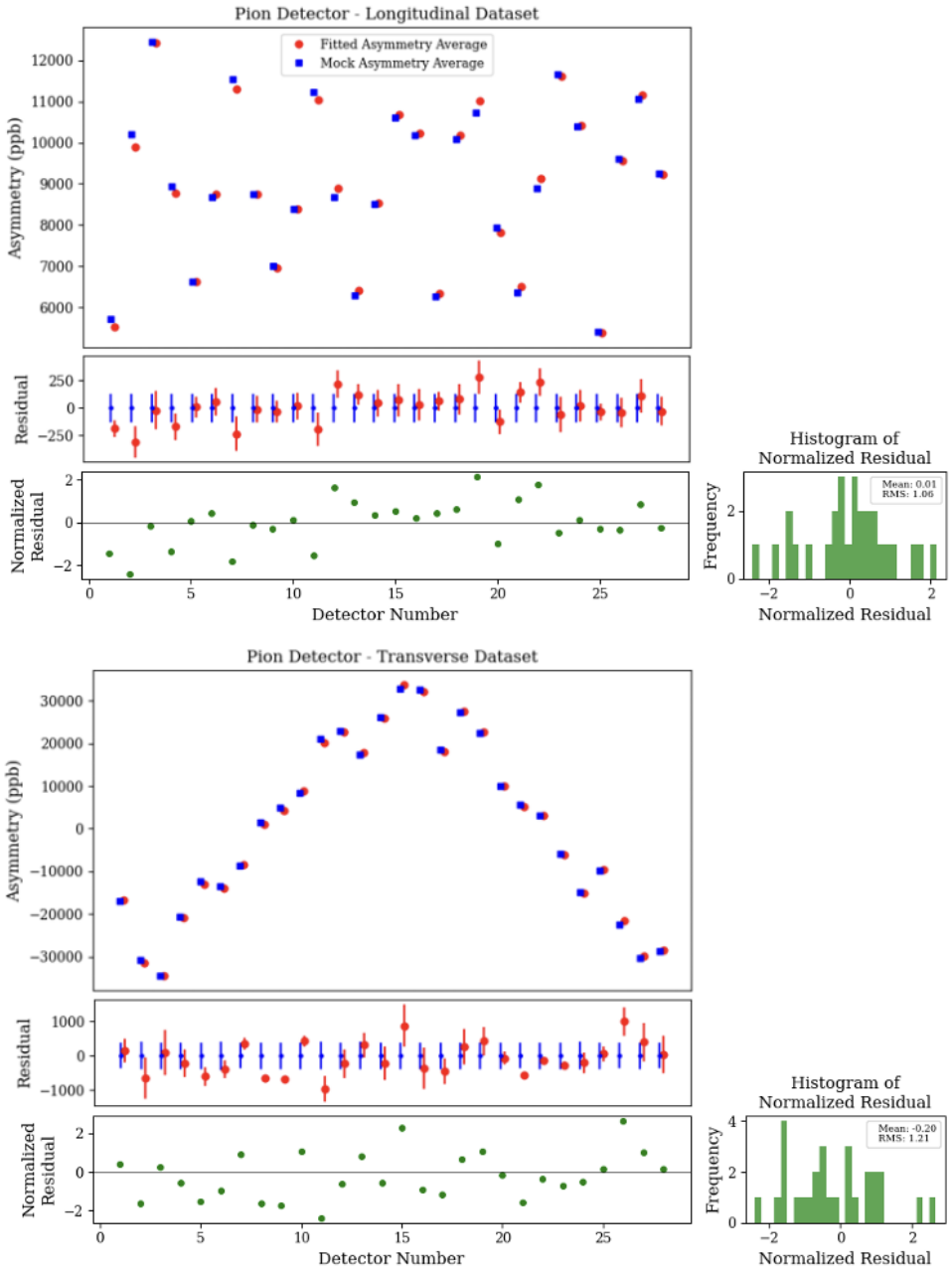

Figure 5.11: Comparison of average fitted and mock asymmetry values in the MOLLER experiment's pion detector, using longitudinal and transverse datasets (top and bottom plots, respectively). Blue squares represent mock averages, and red circles show fitted averages with error bars for uncertainty. Middle plots highlight residuals to underscore small error bars. Bottom plots display normalized residuals and histograms, evaluating fit quality through means and RMS values.

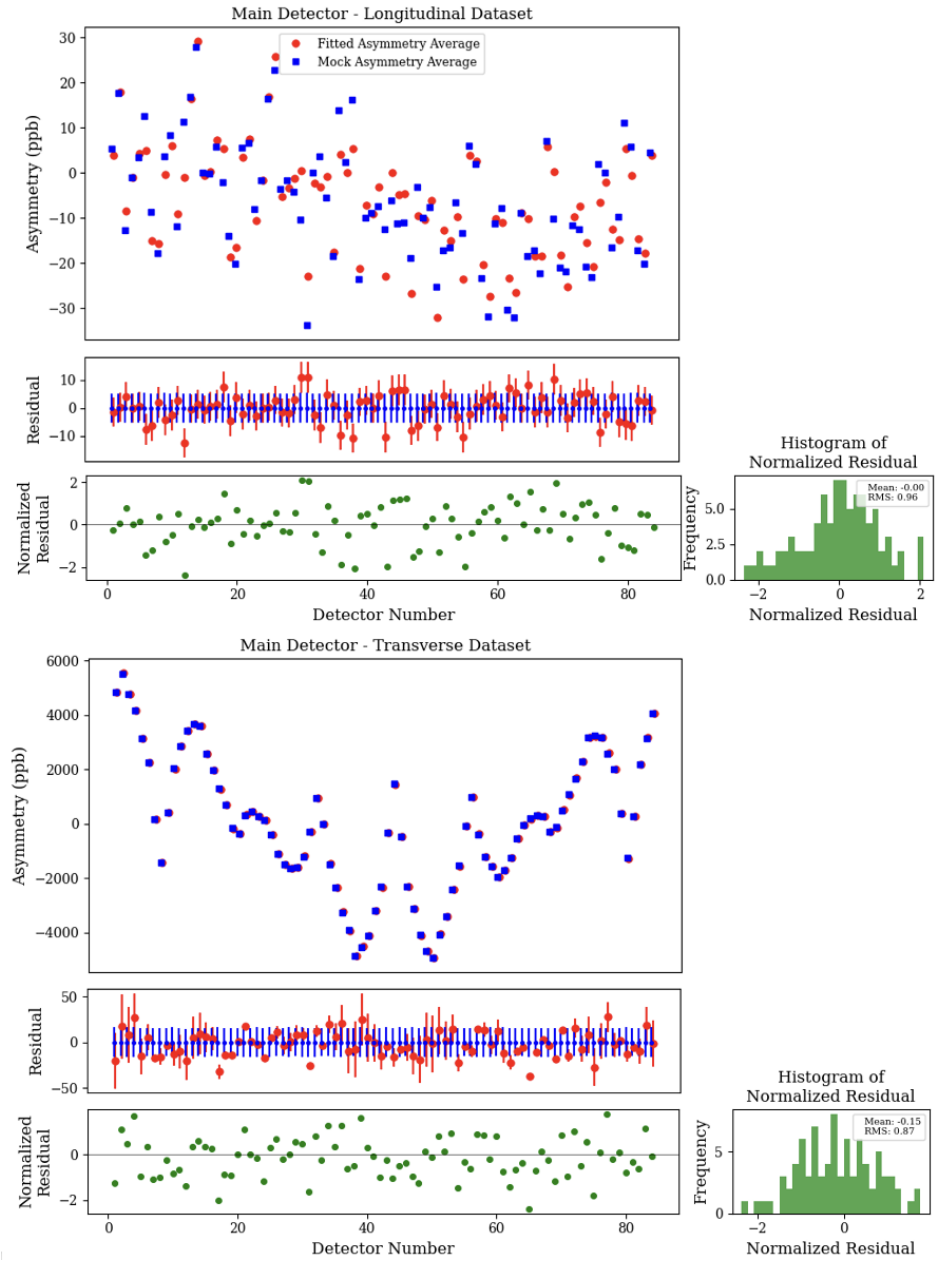

Figure 5.12: Comparison of average fitted and mock asymmetry values in the MOLLER experiment's main detector across longitudinal and transverse datasets (top and bottom plots, respectively). Blue squares and red circles depict mock and fitted averages, with error bars for uncertainties. Middle plots focus on residuals, showing differences between mock and fitted values to enhance error bar visibility. Bottom plots feature normalized residuals and histograms, assessing fit quality through means and RMS values.

slightly wider spread with a mean of -0.15 and an RMS of 0.87, indicating minor deviations but still maintaining overall consistency. These distributions are instrumental in evaluating the robustness and accuracy of the Bayesian fitting process applied to the asymmetry measurements of the main detector. These plots serve as a critical component for validating the Bayesian framework, ensuring the model's robustness in accurately predicting asymmetry components before they are applied to actual experimental data.

The final aspect of the Bayesian analysis for the MOLLER experiment [21] involves determining the correlations between asymmetry components, similar to those illustrated in Figure 5.7 for the Qweak experiment. As explained in Subsection 5.3.4, the off-diagonal elements represent the correlation between these components, indicating the extent and direction of their linear relationships. As seen in Figure 5.13, there is no correlation between the estimated parameters A_e^L, A_e^T, A_π^L, and A_π^T. This absence of correlation demonstrates how the MOLLER setup and kinematics successfully separate the main detector signals and the pion detector signals and provide independent, uncontrolled access to both.

In this chapter, the theoretical and practical landscapes of Bayesian analysis have been explored, emphasizing its impact on interpreting data from the Qweak and MOLLER experiments. The detailed examination of Bayesian methods in the context of the Qweak and MOLLER experiments has highlighted the versatility of Bayesian analysis in handling complex statistical models and underscored its efficacy in enhancing measurement precision. By integrating prior information with empirical data, a robust framework for making informed inferences is offered by Bayesian analysis, thereby contributing to a deeper comprehension of the underlying phenomena in PVES experiments.

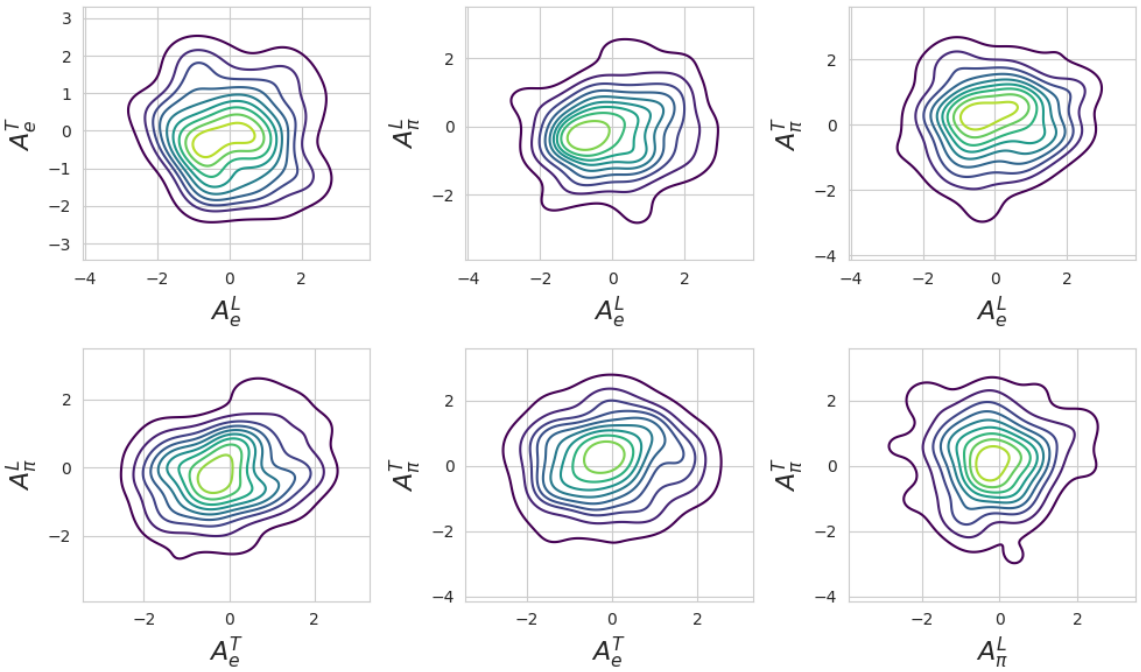

Figure 5.13: Correlation plots showing pairwise relationships between the off-diagonal elements A_e^L, A_e^T, A_π^L, and A_π^T in the Bayesian analysis of the MOLLER experiment. Each plot displays contour lines representing the density distribution from the 10% to the 90%.

Chapter 6

Summary and Future Directions

6.1 Summary

The Measurement of a Lepton Lepton Electroweak Reaction (MOLLER) experiment focuses on measuring the parity-violating asymmetry (A_{PV}) in electron-electron scattering events. The experiment aims to achieve this with a precision of 2.4% (0.54 ppb) using an 11 GeV electron beam in Hall A at the Thomas Jefferson National Accelerator Facility (JLab). The precision measurement of A_{PV} requires careful consideration and correction for background processes. Distinguishing between signal events and background events is crucial for obtaining this level of accuracy in the MOLLER experiment. This differentiation is addressed through signal corrections, which can be performed experimentally or non-experimentally.

The experimental method employs background detectors designed to capture the background particles rather than the main signal. In the context of MOLLER, background processes can affect the measurement by introducing dilution factors and asymmetries that need to be accounted for in the final analysis. These parameters contribute to the correction of A_{PV} using the following formula:

$$A_{PV} = R_{tot} \frac{\frac{A_{expt}}{P_b} - \sum_i f_i^{bkgd} A_i^{bkgd}}{1 - \sum_i f_i^{bkgd}}, \tag{6.1}$$

where R_{tot} is an overall normalization factor, P_b is the beam polarization, and A_{expt}

is the experimentally measured asymmetry, which is required to be corrected for background processes, characterized by fractional dilution factors, f_i^{bkgd}, and asymmetries, A_i^{bkgd}. The implementation of background detectors enhances the signal-to-background ratio. However, uncontrollable factors during measurements, such as beam direction deviations or spin alignment discrepancies caused by source imperfections, accelerator flaws, external magnetic fields, or subsystem misalignments, necessitate post-measurement corrections, referred to as non-experimental signal correction, to compensate for these deviations.

Bayesian analysis focuses on its application in improving the extraction of asymmetry components in Parity-Violating Electron Scattering (PVES) experiments, such as Qweak and MOLLER. The proposed Bayesian models aim to infer background asymmetries from observed quantities, thereby enabling more accurate corrections to the results.

Continuing with exploring experimental details and their impacts, the following subsection will examine the specific results obtained from the pion detector system. Subsequently, in Section 6.1.2, the outcomes from the Bayesian analysis will be reviewed, which has been instrumental in refining the interpretation of the data obtained.

6.1.1 Pion Detector System Development

The pion detector system, as described in Chapter 4, plays an integral role in the signal correction process for the MOLLER experiment. The implementation of this system was underpinned by key material and equipment selections that significantly influenced its effectiveness.

The choice of Lucite as the active medium, as outlined in Section 4.1.1, was predicated on its suitable properties for the detection environment in the MOLLER experiment. Lucite, with its high optical clarity and compatibility with ultraviolet light, proved to be an optimal material for capturing the Cherenkov radiation generated by passing particles. Its selection followed comprehensive analyses that evaluated various materials on criteria such as radiation hardness, light transmission, and mechanical

robustness. The final decision to use Lucite was reinforced by its successful historical use in similar experimental setups, where it demonstrated sustained performance under high-radiation conditions.

In conjunction with the active medium selection, choosing Photomultiplier Tubes (PMTs) was critical for the detection system's efficacy. Section 4.1.2 details the selection process, culminating in adopting the ET Enterprise 9125B model for the experiment. This PMT was chosen for its suitable spectral range, high quantum efficiency, and compatibility with the expected operational conditions. Its characteristics, including the cathode sensitivity and anode current capabilities, matched the high accuracy requirements for detecting low-level light signals. Integrating these PMTs with the Lucite detectors forms the foundation of the MOLLER experiment's pion detection system, ensuring reliable and precise measurements of background signals from charged pions.

Implementing the pion detector system was guided by a series of optimizations, each enhancing the π/e ratio. The optimized design of the pion detector system, which underwent substantial evolutionary changes as outlined in Section 4.2, demonstrated a significant performance improvement. The finalized configuration resulted in an increased π/e ratio of $61.5\% \pm 1.7\%$, as compared to the initial ratio of $0.10\% \pm 0.01\%$ (Table 4.2). This substantial improvement reflects the successful filtration of signals from low-energy particles attributed to the integrated design of the pion detector system with the lead donut.

The mechanical design of the pion detector system is a critical aspect of the MOLLER experiment, ensuring functionality and reliability in a demanding experimental environment. The design process, as detailed in Section 4.3, involved the development of a light-tight enclosure box composed of four main components: a Lucite box, a connector for the Lucite and PMT, a PMT housing, and an end cap. Each component was thoroughly engineered to meet specific requirements, such as facilitating smooth insertion into the lead donut, maintaining the PMT in position, and securing the PMT's voltage divider. These components were showcased in Figure 4.8, highlighting their detailed design and assembly. The final assembly was demonstrated in Figure 4.9, showing the light-tight enclosure box with all components fitted

together.

Installation of the enclosure box into the pion detector slot within the lead donut is achieved using three L-brackets, as depicted in Figure 4.10. Adjustments for manufacturing tolerances and thermal deformation were carefully managed to maintain the precision of the mechanical fit, with the tolerance analysis illustrated in Figure 4.11. The mechanical design phase culminated in the finalized implementation of the pion detector module within the lead donut, as shown in Figure 4.13, signifying a major design milestone in the project. This comprehensive approach from initial design to final implementation underscores the precise attention to detail and engineering expertise that underpins the successful deployment of the pion detector system in the MOLLER experiment.

Moreover, the cosmic ray tests, as discussed in Sections 4.4, confirmed the simulated predictions, thus verifying the effectiveness of the system's design. The experimental results from cosmic testing showed that the pion detector system yielded a threefold increase in the number of detected photoelectrons in its optimized configuration (beam direction aligned to the PMT orientation - configuration (2)) compared to the initial configuration (beam direction perpendicular to the PMT orientation - configuration (1)). This agreed with the simulation results, reinforcing the reliability of the system's design for background signal detection.

Beam testing at the Mainz Microtron (MAMI), detailed in Section 4.5, provided an additional layer of experimental validation for the pion detector system. Using an 855.1 MeV electron beam, the pion detector prototype was tested in configurations analogous to the experimental setup of cosmic tests. The findings from the beam tests demonstrated an enhanced number of photoelectrons detected, consistent with the simulation predictions and cosmic testing results. Specifically, configuration (2) of the pion detector confirmed a notable increase in signal detection efficiency, verifying the design optimizations. The beam tests confirmed the accuracy of the simulation models, enhancing trust in the pion detector's capability to correct signals in the real-world experimental setting effectively.

These findings underscore the pion detector system's successful development, yielding promising results and substantiating its utility as an effective background

detector. Its contribution advances the MOLLER experiment's signal correction process, marking a notable step forward in pursuing high-precision measurements in particle physics.

6.1.2 Bayesian Analysis Methodology

The foundational concepts of Bayesian analysis are introduced in Chapter 5 and contrasted in Section 5.1 with the frequentist approach, which traditionally defines probability in terms of repeated measurements and long-term frequencies of events. In contrast, Bayesian statistics interprets probability as a measure of belief or certainty regarding the occurrence of an event or the truth of a hypothesis. This fundamental difference alters how probabilities are used in statistical analysis. Bayesian analysis uses probability as a universal language for describing the likelihood of hypotheses and making decisions under uncertainty. It allows for direct probabilistic inference, providing more informed estimates and predictions. This shift from a frequentist to a Bayesian approach represents a conceptual divergence that significantly impacts methods in statistical data analysis.

Bayes' theorem, as detailed in Section 5.2, forms the core of Bayesian analysis, linking prior distributions and likelihood functions to update beliefs in light of new evidence, resulting in the posterior distribution. The theorem transforms subjective beliefs (priors) and objective data (likelihood) into a combined model (posterior), which is then used for statistical inference and decision-making. The complexity of the posterior distribution, often high-dimensional and analytically intractable, necessitates advanced computational techniques for effective model fitting. Markov Chain Monte Carlo (MCMC) methods are particularly highlighted for their ability to sample from complex posterior distributions, thus enabling practical Bayesian inference. PyStan utilizes Hamiltonian Monte Carlo (HMC) and the No U-Turn Sampler (NUTS), each aiding in efficient and effective sampling and model fitting.

Section 5.3 explores the application of Bayesian analysis to enhance the precision of extracted quantities in the Qweak experiment. This section compares the results of Bayesian analysis with those from a previously employed Monte Carlo minimization

method. Two main analytical approaches are discussed: the Many-Worlds Monte Carlo Minimization Method and the Bayesian Analysis Method. The former uses randomized inputs based on Gaussian distributions of measured values to compute asymmetries and minimize deviations from these values, providing a set of possible values for each asymmetry component. In contrast, the Bayesian analysis method utilizes a model incorporating prior knowledge and measured data to update beliefs about parameters through the posterior distribution. This method is noted for potentially providing more precise estimates and smaller uncertainties due to its systematic incorporation of data and prior information. Comparative analysis indicates that Bayesian analysis generally yields closer fits to the measured data and more constrained uncertainty estimates. This comparison is visually supported by plots in Figure 5.4, which compare fitted values against actual measurements across various detectors. The robustness of Bayesian parameter estimation is emphasized compared to the Monte Carlo method.

Section 5.4 of the chapter explores enhancing the precision of extracted quantities through Bayesian analysis in the MOLLER experiment, following the methods used in the Qweak experiment. This section addresses the need to adapt and refine the Bayesian framework to meet the specific challenges and configurations of the MOLLER experiment. It involves a detailed comparison of the underlying assumptions, experimental setups, and analytical methodologies between the two experiments to lay a foundation for a comprehensive evaluation of the inputs, parameters, and models used in Bayesian analysis.

Key differences between the Qweak and MOLLER experiments in applying Bayesian analysis include experimental geometries, the types of data used (mock asymmetry values in MOLLER versus measured asymmetry values in Qweak), variations in polarization angles, and approaches to spin variation. In this context, Bayesian analysis generates mock asymmetry data based on simulated true asymmetry values and associated uncertainties. These mock data are crucial for validating the Bayesian model under simulated conditions before applying it to experimental data. The analysis then uses these mock asymmetries to refine the model and extract precise asymmetry components, demonstrating the method's efficacy in providing detailed insights into

experimental outcomes. Figures 5.9 to 5.12 illustrate various comparisons between true, mock, and fitted asymmetry values for both the pion and main detectors in the MOLLER experiment, using Bayesian analysis. These figures provide a comprehensive visual and quantitative analysis of the Bayesian model's application in the MOLLER experiment, illustrating its capacity to handle complex datasets and its effectiveness in achieving precise measurements under simulated experimental conditions.

Overall, Section 5.4 thoroughly explores the application of Bayesian analysis in a high-precision experimental context, showcasing how methodological refinements and careful consideration of experimental details contribute to the advancement of scientific understanding in particle physics experiments.

6.2 Future Directions

6.2.1 Future Directions of the Pion Detector System Development

A primary focus in the future direction of the pion detector system for the MOLLER experiment will be replacing the current PMT base with a switchable version. This upgrade is crucial as it allows the system to transition between integrating and event data-taking modes. Upon integrating the switchable PMT base, a comprehensive reevaluation of the system using actual experimental components is proposed. This includes employing the specified Lucite dimensions, the selected PMT models, and the finalized light-tight enclosure box in practical tests. To validate their performance, the intent is to conduct rigorous cosmic and beam tests with these fundamental components. The results of these tests will be compared not only with the outcomes from previous simulations but also with data from cosmic and beam testing. This iterative testing and comparison process is designed to enhance the system's accuracy and efficiency, ensuring that the pion detector system fully meets the high-precision requirements of the MOLLER experiment.

Subsequently, following the implementation of the MOLLER experiment and the

collection of measurements, data analysis of the actual data would be an important part. The results can be compared with the results from the simulations, cosmic tests and beam testing, and also the Bayesian analysis can be applied to the measured values instead of the mock values.

6.2.2 Future Directions of Bayesian Analysis

Future studies in Bayesian analysis should consider adjusting the assumptions used for generating mock data in the MOLLER experiment. Integrating elastic and inelastic scattering processes into the existing Moller and pion generators can generate more realistic mock data. This allows the Bayesian analysis to accommodate a broader range of scattering events and provide a more accurate reflection of expected experimental outcomes.

Additionally, modifications to the experimental setup, such as incorporating the effects of all six rings of the main detector and the showermax detector, could enhance the model's accuracy. By aggregating the asymmetry values from all modules of the main detectors and the showermax detector and incorporating these into the Bayesian model, the analysis would capture a more comprehensive picture of the scattering events.

Exploring a variety of polarization angles could further refine the analysis. Current models utilize limited polarization angles; however, experimenting with a broader range of angles could uncover impacts on the asymmetry measurements not previously accounted for, potentially revealing new insights into the spin-dependent interactions at play.

These enhancements will not only improve the accuracy of the Bayesian models but also expand our understanding of the underlying physical processes in PVES experiments, aiming to refine the predictive capabilities of our models to ensure they are robust and reflective of the complex dynamics encountered in high-precision experimental physics.

Bibliography

[1] David Griffiths. *Introduction to elementary particles*. John Wiley & Sons, 2020.

[2] Tsung-Dao Lee and Chen-Ning Yang. Question of parity conservation in weak interactions. *Physical Review*, 104(1):254, 1956.

[3] KS Kumar, Sonny Mantry, WJ Marciano, and PA Souder. Low-energy measurements of the weak mixing angle. *Annual Review of Nuclear and Particle Science*, 63:237–267, 2013.

[4] MJ Ramsey-Musolf. Low-energy parity-violation and new physics. *Physical Review C*, 60(1):015501, 1999.

[5] Jens Erler, Charles J Horowitz, Sonny Mantry, and Paul A Souder. Weak polarized electron scattering. *Annual Review of Nuclear and Particle Science*, 64:269–298, 2014.

[6] C Yi Prescott, WB Atwood, RLA Cottrell, Hi Destaebler, Edward L Garwin, A Gonidec, Roger H Miller, LS Rochester, T Sato, DJ Sherden, et al. Parity non-conservation in inelastic electron scattering. *Physics Letters B*, 77(3):347–352, 1978.

[7] W Heil, J Ahrens, HG Andresen, A Bornheimer, D Conrath, K-J Dietz, W Gasteyer, H-J Gessinger, W Hartmann, J Jethwa, et al. Improved limits on the weak, neutral, hadronic axial vector coupling constants from quasielastic scattering of polarized electrons. *Nuclear Physics B*, 327(1):1–31, 1989.

[8] Paul A Souder, R Holmes, D-H Kim, KS Kumar, ME Schulze, K Isakovich, GW Dodson, KW Dow, M Farkhondeh, S Kowalski, et al. Measurement of parity violation in the elastic scattering of polarized electrons from c 12. *Physical review letters*, 65(6):694, 1990.

[9] J_ Ashman, B Badelek, Guenter Baum, J Beaufays, CP Bee, C Benchouk, IG Bird, SC Brown, MC Caputo, HWK Cheung, et al. A measurement of the spin asymmetry and determination of the structure function g1 in deep inelastic muon-proton scattering. *Physics Letters B*, 206(2):364–370, 1988.

[10] David B Kaplan and Aneesh Manohar. Strange matrix elements in the proton from neutral-current experiments. *Nuclear Physics B*, 310(3-4):527–547, 1988.

[11] DT Spayde, T Averett, D Barkhuff, DH Beck, EJ Beise, C Benson, H Breuer, R Carr, S Covrig, J DelCorso, et al. Parity violation in elastic electron-proton scattering and the proton's strange magnetic form factor. *Physical Review Letters*, 84(6):1106, 2000.

[12] KA Aniol, DS Armstrong, Todd Averett, Maud Baylac, Etienne Burtin, John Calarco, GD Cates, Christian Cavata, Zhengwei Chai, CC Chang, et al. Parity-violating electroweak asymmetry in e p scattering. *Physical Review C*, 69(6): 065501, 2004.

[13] DS Armstrong, J Arvieux, Razmik Asaturyan, Todd Averett, SL Bailey, Guillaume Batigne, DH Beck, EJ Beise, Jay Benesch, Louis Bimbot, et al. Strange-quark contributions to parity-violating asymmetries in the forward g0 electron-proton scattering experiment. *Physical review letters*, 95(9):092001, 2005.

[14] FE Maas, P Achenbach, K Aulenbacher, S Baunack, L Capozza, J Diefenbach, K Grimm, Y Imai, T Hammel, D Von Harrach, et al. Measurement of strange-quark contributions to the nucleon's form factors at q 2= 0.230 (g e v/c) 2. *Physical review letters*, 93(2):022002, 2004.

[15] PL Anthony, RG Arnold, C Arroyo, K Bega, J Biesiada, PE Bosted, G Bower,

J Cahoon, R Carr, GD Cates, et al. Precision measurement of the weak mixing angle in moeller scattering. *Physical review letters*, 95(8):081601, 2005.

[16] T Allison, M Anderson, D Androić, DS Armstrong, A Asaturyan, T Averett, R Averill, J Balewski, J Beaufait, RS Beminiwattha, et al. Precision measurement of the weak charge of the proton. *Nature*, 557(7704):207–211, 2018.

[17] Sea Abrahamyan, Z Ahmed, H Albataineh, K Aniol, DS Armstrong, W Armstrong, T Averett, B Babineau, A Barbieri, V Bellini, et al. Measurement of the neutron radius of pb 208 through parity violation in electron scattering. *Physical review letters*, 108(11):112502, 2012.

[18] D Adhikari, H Albataineh, D Androic, K Aniol, DS Armstrong, T Averett, C Ayerbe Gayoso, S Barcus, V Bellini, RS Beminiwattha, et al. Accurate determination of the neutron skin thickness of pb 208 through parity-violation in electron scattering. *Physical review letters*, 126(17):172502, 2021.

[19] D Adhikari, H Albataineh, D Androic, KA Aniol, DS Armstrong, T Averett, C Ayerbe Gayoso, SK Barcus, V Bellini, RS Beminiwattha, et al. Precision determination of the neutral weak form factor of ca 48. *Physical Review Letters*, 129(4):042501, 2022.

[20] Dominik Becker, K Gerz, S Baunack, KS Kumar, and FE Maas. P2-the weak charge of the proton. In *AIP Conference Proceedings*, volume 1563, pages 78–81. American Institute of Physics, 2013.

[21] J Benesch, P Brindza, RD Carlini, JP Chen, E Chudakov, S Covrig, MM Dalton, A Deur, D Gaskell, A Gavalya, et al. The moller experiment: An ultra-precise measurement of the weak mixing angle using møller scattering. *arXiv preprint arXiv:1411.4088*, 2014.

[22] PA Souder. Parity violation in deep inelastic scattering with the solid spectrometer at jlab. In *International Journal of Modern Physics: Conference Series*, volume 40, page 1660077. World Scientific, 2016.

[23] Andrzej Czarnecki and William J Marciano. Polarized møller scattering asymmetries. *International Journal of Modern Physics A*, 15(16):2365–2375, 2000.

[24] SC Bennett and Carl E Wieman. Measurement of the 6 s→ 7 s transition polarizability in atomic cesium and an improved test of the standard model. *Physical Review Letters*, 82(12):2484, 1999.

[25] GP Zeller, KS McFarland, T Adams, A Alton, S Avvakumov, L De Barbaro, P De Barbaro, RH Bernstein, A Bodek, T Bolton, et al. Precise determination of electroweak parameters in neutrino-nucleon scattering. *Physical Review Letters*, 88(9):091802, 2002.

[26] The SLD Electroweak, Heavy Flavour Groups, ALEPH Collaboration, DELPHI Collaboration, L3 Collaboration, OPAL Collaboration, SLD Collaboration, LEP Electroweak Working Group, et al. Precision electroweak measurements on the z resonance. *Physics Reports*, 427(5-6):257–454, 2006.

[27] Phys.org. The standard model of particle physics, 2021. URL `https://phys.org/news/2021-12-year-physicists-lies-standard.html/`.

[28] Georges Aad, Tatevik Abajyan, B Abbott, J Abdallah, S Abdel Khalek, Ahmed Ali Abdelalim, R Aben, B Abi, M Abolins, OS AbouZeid, et al. Observation of a new particle in the search for the standard model higgs boson with the atlas detector at the lhc. *Physics Letters B*, 716(1):1–29, 2012.

[29] Serguei Chatrchyan, CMS collaboration, et al. (2012). observation of a new boson at a mass of 125 gev with the cms experiment at the lhc. *Phys. Lett. B*, 716:30–61, 2012.

[30] Richard L Garwin, Leon M Lederman, and Marcel Weinrich. Observations of the failure of conservation of parity and charge conjugation in meson decays: the magnetic moment of the free muon. *Physical Review*, 105(4):1415, 1957.

[31] 4 gravitons. The (2, 0) theory: What does it mean?, 2023. URL `https://4gravitons.com/the-2-0-theory-what-does-it-mean/`.

[32] Samoil M. Bilenky and J. Hosek. GLASHOW-WEINBERG-SALAM THEORY OF ELECTROWEAK INTERACTIONS AND THE NEUTRAL CURRENTS. *Phys. Rept.*, 90:73–157, 1982. doi: 10.1016/0370-1573(82)90016-3.

[33] Gerald S. Guralnik. The history of the guralnik, hagen and kibble development of the theory of spontaneous symmetry breaking and gauge particles. *International Journal of Modern Physics A*, 24:2601–2627, 2009.

[34] Paul Langacker. *The standard model and beyond*. Taylor & Francis, 2017.

[35] MOLLER Collaboration. Conceptual design report. Technical report, Jefferson Lab, August 2020.

[36] D.M. Nikolenko, J. Arrington, L.M. Barkov, et al. Proton form factors and two-photon exchange in elastic electron-proton scattering. *Physics of Atomic Nuclei*, 78:394–403, 2015.

[37] Jean-Philippe Karr, Dominique Marchand, and Eric Voutier. The proton size. *Nature Reviews Physics*, 2(11):601–614, 2020.

[38] Curtis G Callan Jr and David J Gross. High-energy electroproduction and the constitution of the electric current. *Physical Review Letters*, 22(4):156, 1969.

[39] JD Jackson. Annual review of nuclear and particle science. 22:227, 1972.

[40] AO Barut and C Fronsdal. Spin-orbit correlations in μ- e and e– e- scattering. *Physical Review*, 120(5):1871, 1960.

[41] Lester L DeRaad Jr and Yee Jack Ng. Electron-electron scattering. iii. helicity cross sections for electron-electron scattering. *Physical Review D*, 11(6):1586, 1975.

[42] Lance Dixon and Marc Schreiber. Radiative corrections to the azimuthal asymmetry in transversely polarized møller scattering. *Physical Review D*, 69(11): 113001, 2004.

[43] Brandon Buncher and Carl E Carlson. Electron beam single-spin asymmetries in the resonance region with final hadrons observed. *Physical Review D*, 93(7): 074032, 2016.

[44] D Dreschsel and Lothar Tiator. Threshold pion photoproduction on nucleons. *Journal of Physics G: Nuclear and Particle Physics*, 18(3):449, 1992.

[45] Dieter Drechsel, Barbara Pasquini, and Marc Vanderhaeghen. Dispersion relations in real and virtual compton scattering. *Physics reports*, 378(2-3):99–205, 2003.

[46] Rainer Haidan. *Elektroproduktion pseudoskalarer Mesonen im Resonanzgebiet bei großen Impulsüberträgen*. Dt. Elektronen-Synchroton, 1979.

[47] D Androić, David S Armstrong, A Asaturyan, K Bartlett, RS Beminiwattha, J Benesch, F Benmokhtar, J Birchall, RD Carlini, JC Cornejo, et al. Parity-violating inelastic electron-proton scattering at low q 2 above the resonance region. *Physical Review C*, 101(5):055503, 2020.

[48] The remoll Collaboration. remoll: Monte carlo simulation for moller experiment. `https://github.com/JeffersonLab/remoll`, 2023.

[49] RD Birkhoff. The passage of fast electrons through matter. In *Corpuscles and Radiation in Matter II/Korpuskeln und Strahlung in Materie II*, pages 53–138. Springer, 1958.

[50] Claude Leroy and Pier-Giorgio Rancoita. *Principles of radiation interaction in matter and detection*. World Scientific, 2011.

[51] R. L. Workman and Others. Review of Particle Physics. *PTEP*, 2022:083C01, 2022. doi: 10.1093/ptep/ptac097.

[52] Spencer N Axani. The physics behind the cosmicwatch desktop muon.

[53] Particle Data Group. Review of particle physics 2023 - particle detectors at accelerators. Technical report, Lawrence Berkeley National Laboratory, 2023. URL https://pdg.lbl.gov/2023/reviews/rpp2022-rev-particle-detectors-non-accel.pdf.

[54] Stefaan Tavernier. *Experimental techniques in nuclear and particle physics*. Springer Nature, 2010.

[55] DH Jakubassa-Amundsen. Advances in bremsstrahlung: a review. *arXiv preprint arXiv:2103.06034*, 2021.

[56] Rosa Poggiani and Rosa Poggiani. Cherenkov and transition radiation detectors. *High Energy Astrophysical Techniques*, pages 65–67, 2017.

[57] Particle Data Group. Review of particle physics. https://pdg.lbl.gov/2020/reviews/rpp2020-rev-atomic-nuclear-prop.pdf, 2020.

[58] ET Enterprises Ltd. 9125b series - 30 mm photomultiplier. https://et-enterprises.com/products/photomultipliers/product/p9125b-series, 2023.

[59] CERN Timeline. Victor hess discovers cosmic rays, 2023. URL https://timeline.web.cern.ch/victor-hess-discovers-cosmic-rays-0.

[60] Victor Franz Hess. New results of cosmic-ray research. *Terrestrial Magnetism and Atmospheric Electricity*, 41(4):345–350, 1936.

[61] HyperPhysics. Hadrons. HyperPhysics, Georgia State University, 2023. URL http://hyperphysics.phy-astr.gsu.edu/hbase/Particles/hadron.html.

[62] KA Olive, Kaustubh Agashe, Claude Amsler, Mario Antonelli, JF Arguin, DM Asner, H Baer, HR Band, RM Barnett, Tullio Basaglia, et al. Review of particle physics. *Chinese physics C*, 38(9):1–1676, 2014.

[63] Lorenzo Bonechia, Raffaello D'Alessandroa, and Andrea Giammancoc. Reviews in physics.

[64] Thomas K Gaisser. Atmospheric neutrinos. *arXiv preprint arXiv:1910.08851*, 2019.

[65] University of Mainz Institute for Nuclear Physics. The mainz microtron mami, 2023. URL `https://www.blogs.uni-mainz.de/fb08-nuclear-physics/`.

[66] Marco Dehn, Kurt Aulenbacher, Hans-Joachim Kreidel, Fabian Nillius, BS Schlimme, Valeri Tioukine, et al. Recent challenges for the 1.5 gev mami-c accelerator at jgu mainz. In *7th Int. Particle Accelerator Conf.(IPAC'16), Busan, Korea, May 8-13, 2016*, pages 4149–4151. JACOW, Geneva, Switzerland, 2016.

[67] University of Mainz Institute for Nuclear Physics. Technical data of the mainz microtron, 2023. URL `https://www.blogs.uni-mainz.de/fb08-nuclear-physics/accelerators-mami-mesa/the-mainz-microtron/technical-data/`.

[68] Jefferson Lab. remoll: REMOte MOLLer simulation, 2023. URL `https://github.com/JeffersonLab/remoll`.

[69] F Krauss, CJ Lin, S Navas, P Richardson, and T Sjöstrand. 39. monte carlo particle numbering scheme.

[70] Jefferson Lab. remoll: Readme variables. `https://jeffersonlab.github.io/remoll/README.variables.html`, 2023.

[71] GEANT4 Collaboration. Geant4 - a simulation toolkit. `https://geant4.web.cern.ch`, 2023.

[72] ROOT Collaboration. Root - a data analysis framework. `https://root.cern`, 2023.

[73] David Earl Wiser. *INCLUSIVE PHOTOPRODUCTION OF PROTONS, KAONS, AND PIONS AT SLAC ENERGIES.* The University of Wisconsin-Madison, 1977.

[74] MOLLER Collaboration. Technical design report. Technical report, Jefferson Lab, July 2023. URL https:virginia.box.com/shared/static/b0ho4zkos5xwdh2q2ukabq4ilekg2pps.pdf.

[75] Nathan B Clayburn, JL McCarter, JM Dreiling, M Poelker, DM Ryan, and Timothy J Gay. Search for spin-polarized photoemission from gaas using light with orbital angular momentum. *Physical Review B—Condensed Matter and Materials Physics*, 87(3):035204, 2013.

[76] Reza Kazimi, Alicia Hofler, Joseph M Grames, Yan Wang, John Hansknecht, Michael F Spata, Tomasz E Plawski, Matt Poelker, and Arne Freyberger. Operational results of simultaneous four-beam delivery at jefferson lab. Technical report, Thomas Jefferson National Accelerator Facility (TJNAF), Newport News, VA, 2019.

[77] Caryn Palatchi. Laser and electron beam technology for parity violating electron scattering measurements. Technical report, Thomas Jefferson National Accelerator Facility (TJNAF), Newport News, VA, 2019.

[78] R Suleiman, P Adderley, J Grames, J Hansknecht, M Poelker, and M Stutzman. High current polarized electron source. In *AIP Conference Proceedings*, volume 1970, page 050007. AIP Publishing LLC, 2018.

[79] Jay Benesch and Yves Roblin. Redesigning the jefferson lab hall a beam line for high precision parity experiments. *Journal of Instrumentation*, 16(12):T12007, 2021.

[80] Gabriel Palacios-Serrano, P Adderley, JF Benesch, DB Bullard, JM Grames, C Hernandez-Garcia, AS Hofler, D Machie, M Poelker, ML Stutzman, et al. High voltage design and evaluation of wien filters for the cebaf 200 kev injector upgrade. Technical report, Thomas Jefferson National Accelerator Facility (TJNAF), Newport News, VA, 2021.

[81] Fabio Sauli. The gas electron multiplier (gem): Operating principles and applications. *Nuclear Instruments and Methods in Physics Research Section A: Accelerators, Spectrometers, Detectors and Associated Equipment*, 805:2–24, 2016.

[82] Christian W Fabjan and Herwig Schopper. *Particle Physics Reference Library: Volume 2: Detectors for Particles and Radiation*, volume 2. Springer Nature, 2020.

[83] Wikipedia contributors. Acrylic, 2023. URL `https://en.wikipedia.org/wiki/Acrylic`.

[84] Z Ahmed, K Allada, KA Aniol, DS Armstrong, J Arrington, P Baturin, V Bellini, J Benesch, R Beminiwattha, F Benmokhtar, et al. New precision limit on the strange vector form factors of the proton. *Physical review letters*, 108(10):102001, 2012.

[85] Eljen Technology. Acrylic plastic products, 2023. URL `https://eljentechnology.com/20-products/acrylic-plastic`.

[86] Photomultiplier tubes basics and applications. `https://www.hamamatsu.com/us/en/product/optical-sensors/pmt.html`.

[87] Shv jack standard solder cup terminal connector pe4239. `https://www.pasternack.com/shv-jack-standard-solder-cup-terminal-connector-pe4239-p.aspx`, .

[88] Bnc female standard solder cup terminal connector pe4014. `https://www.pasternack.com/bnc-female-standard-solder-cup-terminal-connector-pe4014-p.aspx`, .

[89] Ruiguang Wang, Haoqi Lu, and Changgen Yang. Water cherenkov detector of the juno veto system. In *XXVIII International Conference on Neutrino Physics and Astrophysics*, page 246, 2018.

[90] Unknown. ylindricity. https://fractory.com/cylindricity-gdt-explained/, 2023.

[91] Unknown. ylindricity. https://www.gdandtbasics.com/cylindricity, 2023.

[92] Hamamatsu Photonics. Photomultiplier tube assembly h3178-51. Online, 2023. Available: https://www.hamamatsu.com/jp/en/product/optical-sensors/pmt/pmt-assembly/head-on-type/H3178-51.html.

[93] David C Miller, Michael D Kempe, Cheryl E Kennedy, and Sarah R Kurtz. Analysis of transmitted optical spectrum enabling accelerated testing of cpv designs. In *High and Low Concentrator Systems for Solar Electric Applications IV*, volume 7407, pages 101–112. SPIE, 2009.

[94] CAEN. Vx1725 / vx1725s - 16/8 channel 14-bit 250 ms/s digitizer. Online, 2023. Available: https://www.caen.it/products/vx1725/.

[95] CAEN. Vx3718 - vme64 to usb 2.0/optical link bridge. Online, 2023. Available: https://www.caen.it/products/vx3718/.

[96] CAEN. Compass - multiparametric daq software for physics applications. Online, 2023. Available: https://www.caen.it/products/compass/.

[97] Poisson distribution. *Wikipedia*, 2023. URL https://en.wikipedia.org/wiki/Poisson_distribution.

[98] ROOT Forum. Fitting a poisson distribution to a histogram. https://root-forum.cern.ch/t/fitting-a-poisson-distribution-to-a-histogram/12078, 2023.

[99] CAEN. N93b - dual timer. https://www.caen.it/products/n93b/, 2023.

[100] CAEN. V965 - qdc charge to digital converter. https://www.caen.it/products/v965/, 2023.

[101] Thomas Bayes. Lii. an essay towards solving a problem in the doctrine of chances. by the late rev. mr. bayes, frs communicated by mr. price, in a letter to john canton, amfr s. *Philosophical transactions of the Royal Society of London*, (53):370–418, 1763.

[102] PS Laplace. Essai philosophique sur les probabilities, courcier imprimeur, paris; reprints of this work and of laplace's much larger theorie analytic des probabilities are available from editions culture et civilisation, 115 ave. *Cabriel Lebron*, 1160, 1814.

[103] Aaron M Ellison. Bayesian inference in ecology. *Ecology letters*, 7(6):509–520, 2004.

[104] Rens Van de Schoot, Sonja D Winter, Oisín Ryan, Mariëlle Zondervan-Zwijnenburg, and Sarah Depaoli. A systematic review of bayesian articles in psychology: The last 25 years. *Psychological Methods*, 22(2):217, 2017.

[105] Matthew Stephens and David J Balding. Bayesian statistical methods for genetic association studies. *Nature Reviews Genetics*, 10(10):681–690, 2009.

[106] Deborah Ashby. Bayesian statistics in medicine: a 25 year review. *Statistics in medicine*, 25(21):3589–3631, 2006.

[107] Marieke Thurlings and Perry den Brok. Learning outcomes of teacher professional development activities: a meta-study. *Educational review*, 69(5):554–576, 2017.

[108] Charlotte Rietbergen, Thomas PA Debray, Irene Klugkist, Kristel JM Janssen, and Karel GM Moons. Reporting of bayesian analysis in epidemiologic research should become more transparent. *Journal of Clinical Epidemiology*, 86:51–58, 2017.

[109] JK Kruschke, H Aguinis, and H Joo. " the time has come: Bayesian methods for data analysis in the organizational sciences": Erratum. 2014.

[110] Sanne C Smid, Daniel McNeish, Milica Miočević, and Rens van de Schoot. Bayesian versus frequentist estimation for structural equation models in small sample contexts: A systematic review. *Structural Equation Modeling: A Multidisciplinary Journal*, 27(1):131–161, 2020.

[111] Andre A Rupp, Dipak K Dey, and Bruno D Zumbo. To bayes or not to bayes, from whether to when: Applications of bayesian methodology to modeling. *Structural Equation Modeling*, 11(3):424–451, 2004.

[112] Shirin Golchi and Richard Lockhart. A frequency-calibrated bayesian search for new particles. *The Annals of Applied Statistics*, 12(3):1939–1968, 2018.

[113] L Yang, CJ Lin, YX Zhang, PW Wen, HM Jia, DX Wang, NR Ma, F Yang, FP Zhong, SH Zhong, et al. Bayesian analysis on interactions of exotic nuclear systems. *Physics Letters B*, 807:135540, 2020.

[114] Bruno Lecoutre. The bayesian approach to experimental data analysis. *Essential Statistical Methods for Medical Statistics. Elsevier, Oxford*, pages 308–344, 2011.

[115] Jake VanderPlas. Frequentism and bayesianism: a python-driven primer. *arXiv preprint arXiv:1411.5018*, 2014.

[116] Alexander Ly, Maarten Marsman, Josine Verhagen, Raoul PPP Grasman, and Eric-Jan Wagenmakers. A tutorial on fisher information. *Journal of Mathematical Psychology*, 80:40–55, 2017.

[117] Scott A Sisson, Yanan Fan, and Mark Beaumont. *Handbook of approximate Bayesian computation*. CRC Press, 2018.

[118] Facundo Munoz, M Grazia Pennino, David Conesa, Antonio López-Quílez, and José M Bellido. Estimation and prediction of the spatial occurrence of fish species using bayesian latent gaussian models. *Stochastic Environmental Research and Risk Assessment*, 27(5):1171–1180, 2013.

[119] David M Blei, Alp Kucukelbir, and Jon D McAuliffe. Variational inference: A review for statisticians. *Journal of the American statistical Association*, 112 (518):859–877, 2017.

[120] AE Gelfand and AFM Smith. Sampling-based approaches to computing marginal distributions. *Journal of the American Statistical Association*, 85: 398–409, 1990.

[121] Charles J Geyer. Markov chain monte carlo maximum likelihood. 1991.

[122] George Casella and Edward I George. Explaining the gibbs sampler. *American statistician*, pages 167–174, 1992.

[123] Siddhartha Chib and Edward Greenberg. Understanding the metropolis-hastings algorithm. *American statistician*, pages 327–335, 1995.

[124] Antonietta Mira, Jesper Møller, and Gareth O Roberts. Perfect slice samplers. *Journal of the Royal Statistical Society: Series B (Statistical Methodology)*, 63 (3):593–606, 2001.

[125] Matthew D Hoffman, Andrew Gelman, et al. The no-u-turn sampler: adaptively setting path lengths in hamiltonian monte carlo. *J. Mach. Learn. Res.*, 15(1): 1593–1623, 2014.

[126] Nicholas Metropolis, Arianna W Rosenbluth, Marshall N Rosenbluth, Augusta H Teller, and Edward Teller. Equation of state calculations by fast computing machines. *The journal of chemical physics*, 21(6):1087–1092, 1953.

[127] W Keith Hastings. Monte carlo sampling methods using markov chains and their applications. 1970.

[128] Bob Carpenter, Andrew Gelman, Matthew D Hoffman, Daniel Lee, Ben Goodrich, Michael Betancourt, Marcus A Brubaker, Jiqiang Guo, Peter Li, and Allen Riddell. Stan: A probabilistic programming language. *Journal of statistical software*, 76, 2017.

[129] Steve Brooks, Andrew Gelman, Galin Jones, and Xiao-Li Meng. *Handbook of markov chain monte carlo*. CRC press, 2011.

[130] R. Carlini. The qweak experiment: A search for new physics at the tev scale via a measurement of the proton's weak charge. Talk presented at the 19th Particles and Nuclei International Conference (PANIC11), July 2011. URL https://web.mit.edu/panic11/talks/tuesday/PARALLEL-3G/1-1330/carlini/222-0-PANIC11-Qweak_Talk-R_Carlini.pdf.

[131] M. Dalton. 3 pass polarization angle. https://qweak.jlab.org/elog/Ancillary/227, Dec 2015. QweakELOG.

[132] James Franklyn Dowd. *Probe of Electroweak Interference Effects in Non-Resonant Inelastic Electron-Proton Scattering*. PhD thesis, College of William Mary, 2018. URL https://scholarworks.wm.edu/etd/1550153997/.

[133] Elhamm1. Bayesian analysis. https://github.com/Elhamm1/Bayesian-Analysis, 2024.

[134] Robley D Evans. The atomic nucleus. mcgraw-hill. *New York*, 19552:785–793, 1955.